UNIVERSITY OF Southampton

University of Southampton Research Repository

Copyright © and Moral Rights for this thesis and, where applicable, any accompanying data are retained by the author and/or other copyright owners. A copy can be downloaded for personal non-commercial research or study, without prior permission or charge. This thesis and the accompanying data cannot be reproduced or quoted extensively from without first obtaining permission in writing from the copyright holder/s. The content of the thesis and accompanying research data (where applicable) must not be changed in any way or sold commercially in any format or medium without the formal permission of the copyright holder/s.

When referring to this thesis and any accompanying data, full bibliographic details must be given, e.g.

Thesis: Author (Year of Submission) "Full thesis title", University of Southampton, name of the University Faculty or School or Department, PhD Thesis, pagination.

Data: Author (Year) Title. URI [dataset]

UNIVERSITY OF SOUTHAMPTON

FACULTY OF NATURAL AND ENVIRONMENTAL SCIENCES

Ocean and Earth Science

Sedimentological and Oceanographic Change in the Northwest Atlantic Ocean across the Eocene Oligocene Transition

by

James Francis Spray

Thesis for the degree of Doctor of Philosophy

October 2017

UNIVERSITY OF SOUTHAMPTON

ABSTRACT

FACULTY OF NATURAL AND ENVIRONMENTAL SCIENCES

Ocean and Earth Science

Thesis for the degree of Doctor of Philosophy

SEDIMENTOLOGICAL AND OCEANOGRAPHIC CHANGE IN THE NORTHWEST ATLANTIC OCEAN ACROSS THE EOCENE OLIGOCENE TRANSITION

By James Francis Spray

The Eocene-Oligocene Transition (EOT) marks the most pivotal interval in Earth's Cenozoic transition from warm, relatively ice-free 'greenhouse' conditions to a cooler 'icehouse' climate. The EOT saw the rapid growth of a large East Antarctic Ice Cap, global cooling, and a reorganisation of ocean currents at ~33-34 Ma, but little is known about how these events affected the Northern Hemisphere. The traditional view is that glaciation of the northern continents occurred much later than on Antarctica, but recent studies have, controversially, suggested that large northern ice sheets formed across the EOT. This thesis documents an investigation into this and related problems, taking advantage of rapidly deposited sediment drifts overlying the Southeast Newfoundland Ridge (SENR) recovered during Integrated Ocean Drilling Program (IODP) Expedition 342. Detrital sand and sedimentological features found in EOT-aged sediments on the SENR were interpreted at the time of their discovery to be evidence of ice rafting, and so could support the idea of bipolar glaciation. Provenance, surface texture, and sedimentological analyses presented in this thesis, however, show that icebergs did not deposit these grains. Instead, the presence of these grains is attributed interplay between deep-water currents and glacioeustatic sea level change, through the use of grain flux, grain size, stable isotope, and spectral analyses. Industrial well and seismic data, together with a palaeogeographic digital elevation model, are used to reconstruct the geometry of the SENR, and show that its sedimentary history was often linked to larger-scale oceanographic changes along the Newfoundland Margin. These findings support the hypothesis that significant Northern Hemisphere glaciation did not occur across the EOT.

Table of Contents

Table of Tables

Table of Figures

Table of Figures

Table of Figures

Academic Thesis: Declaration Of Authorship

I, JAMES FRANCIS SPRAY, declare that this thesis and the work presented in it are my own and have been generated by me as the result of my own original research.

Sedimentological and Oceanographic Change in the Northwest Atlantic Ocean Across the Eocene Oligocene Transition

I confirm that:

1. This work was done wholly or mainly while in candidature for a research degree at this University;
2. Where any part of this thesis has previously been submitted for a degree or any other qualification at this University or any other institution, this has been clearly stated;
3. Where I have consulted the published work of others, this is always clearly attributed;
4. Where I have quoted from the work of others, the source is always given. With the exception of such quotations, this thesis is entirely my own work;
5. I have acknowledged all main sources of help;
6. Where the thesis is based on work done by myself jointly with others, I have made clear exactly what was done by others and what I have contributed myself;
7. None of this work has been published before submission.

Signed: .....

Date: .....

Acknowledgements

First and foremost, I would like to acknowledge the instrumental support of my supervisors: Paul Wilson, Steven Bohaty, and Andrew Davies. Without their unwavering dedication, enthusiasm, and patience, this thesis simply would not have been possible. Paul, I am indebted to you for keeping me on the right path; the value of your experience at every step cannot be overstated. To Steve, I will never cease to be amazed by your encyclopaedic knowledge of all things palaeoclimatic, and I look back with great fondness at time spent in Bremen, dealing with sediments and beer steins alike. To Andy, I cannot express enough my appreciation for your invaluable guidance, for your kind words and encouragement, and for the wonderful experiences I had both at Neftex and on our field trip.

I am, and forever will be, immensely grateful for the endless love and support of my family, and of my wonderful fiancée, Brenna, without whom my sanity would have crumbled long ago. To Brenna, how you have managed to plan our wedding while also writing your own thesis I will never know, and I thank you for your commendable patience shown during the many important conversations derailed by thoughts of icebergs and ocean currents drifting through my head. To my friends and fellow students I am also deeply thankful, to Richard, Anieke, Joel, and Chloe, and to many other friends in Southampton and elsewhere.

In Southampton, I would like to thank the many people who have helped me along my way. In particular, I am grateful for the guidance of Megan Spencer, Agnes Michalik, Richard Pearce, Matthew Cooper, and James Hunt in the many laboratories in which I found myself, and for help and advice given by Ian Bailey, Ian Harding, Peter Talling, Diederik Liebrand, Claire Huck, and my fellow students. Further afield, I am indebted to the incredible help and hospitality of Brian Romans, and to Helen Coxall, Walter Hale, Kristen Chilton, and many others. This thesis was made possible due to the continuing efforts of the IODP, which provided my samples. It was funded by a NERC CASE studentship between the UKIODP and Neftex (now Halliburton Neftex®).

Chapter 1 Introduction

1.1 The Eocene Oligocene Transition (EOT)

The Eocene-Oligocene Transition (33-34 Ma) is arguably the most significant climate change event of the Cenozoic, marking the tipping point in a longer transition of Earth's climate from a relatively warm, ice-free 'greenhouse' state to a cooler 'icehouse' state. Over an interval of ~300 kyr, a large, sustained ice cap rapidly formed on East Antarctica (DeConto and Pollard, 2003; Katz et al., 2008) and global temperatures cooled (Liu et al., 2009). Deep-water circulation patterns also changed across the interval, with North Atlantic Deep Water (NADW) being formed in the high northern latitudes and exported through the North Atlantic (Davies et al., 2001; Miller et al., 2009). In the Southern Hemisphere, the Antarctic Circumpolar Current (ACC) also developed over the EOT (Cristini et al., 2012). The glacioeustatic sea level fall associated with Antarctic ice formation is suggested to have exposed and eroded large areas of shallow carbonate, and shallow carbonate deposition was replaced by pelagic burial at depth, leading to deepening of the Carbonate Compensation Depth (CCD) (Merico et al., 2008).

The rapid pace of climate change across the EOT was brought about by atmospheric CO_2 concentrations dropping below a critical threshold, resulting in an initial growth of Antarctic ice (Figure 1.1). This then initiated strong positive feedback effects associated with ice sheet height and coalescence; leading to rapid further ice growth (DeConto and Pollard 2003; Coxall et al. 2005). Atmospheric CO_2 levels decreased slowly through the late Eocene (Pagani et al., 2005; Zachos et al., 2008), until glaciation was triggered during an orbital configuration encouraging cool austral summers. Specifically, this orbital trigger consisted of an extended interval of low eccentricity that coincided with a low amplitude modulation node in obliquity, (Figure 1.1) (Coxall et al., 2005). This hypothesis of a combination of CO_2 decline and orbital forcing has largely replaced the idea that the EOT occurred as a response to the tectonic opening of the Drake Passage and/or the Tasman Gateway and oceanographic isolation of Antarctica, by the Antarctic Circumpolar Current (ACC). This process would still have affected the extent of ice formation across the EOT,

though it is now believed that CO_2 and orbital forcing dictated the timing (Cristini et al., 2012; Katz et al., 2011).

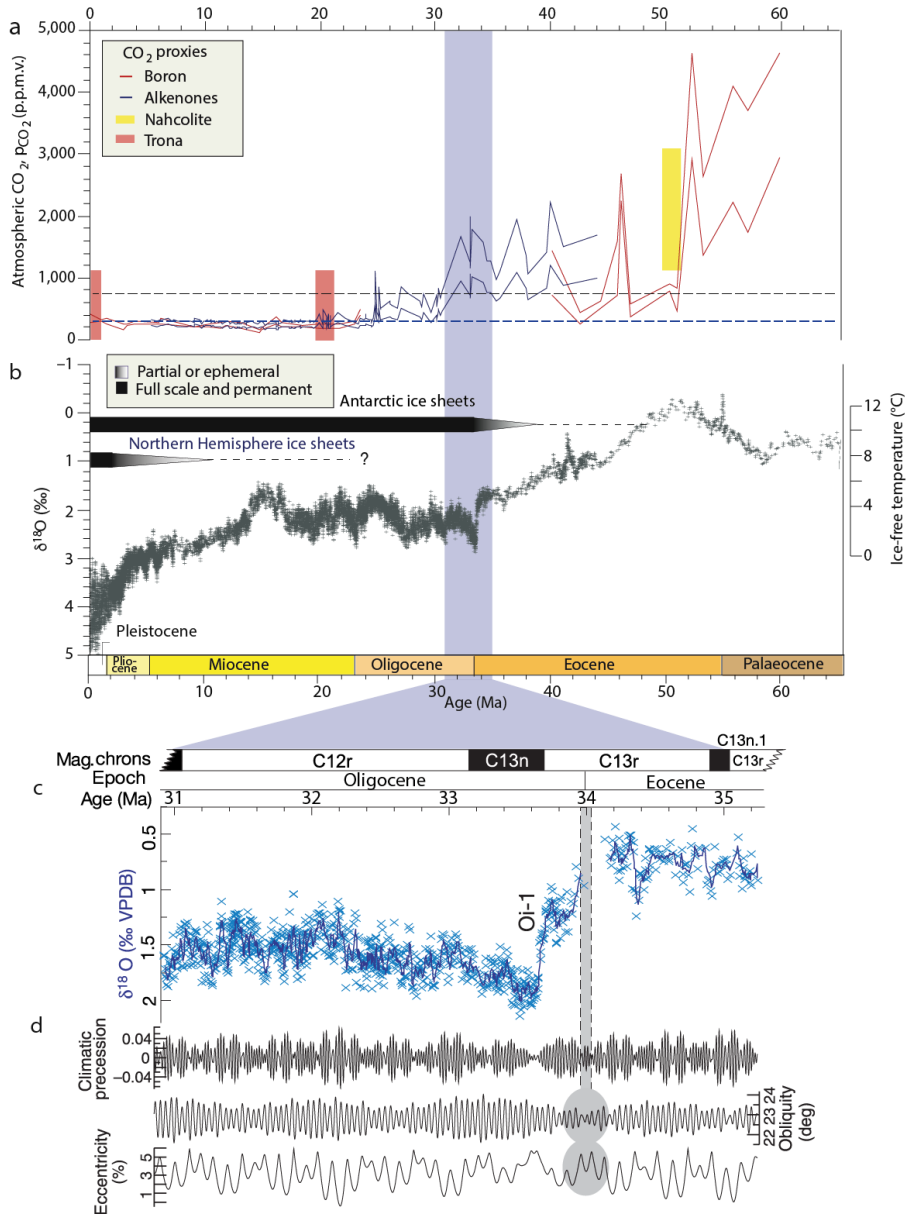

Figure 1.1: a) Proxy reconstructions of atmospheric CO_2 decline through the Cenozoic, black and blue dashed lines indicate modelled thresholds for Southern and Northern hemisphere glaciation respectively (DeConto et al., 2008), b) global composite of available benthic foraminiferal oxygen isotope records across the Cenozoic, c) benthic foraminiferal oxygen isotope record across the EOT from ODP Site 1218, and d) orbital parameters, highlighting 'trigger' interval of low amplitude eccentricity and obliquity modulation. Figure modified from Zachos et al., (2008) and Coxall et al., (2005).

1.1.1 Review of EOT stratigraphy and terms

The EOT climate event should not be confused with the stratigraphic Eocene Oligocene Boundary (EOB), which separates the latest Eocene (Priabonian) and earliest Oligocene (Rupelian). The EOB is identified by the extinction of the planktic foraminiferal genus *Hantkenidae*, and its Global Stratotype Section and Point (GSSP) is defined at Massignano, Italy (Silva and Jenkins, 1993). It is dated to 33.9 Ma as of 2012 (previously 33.7 Ma) (Berggren et al., 1995; Gradstein et al., 2012). The EOT, by comparison, is identified by a globally recognisable increase in benthic foraminiferal oxygen and carbon isotope records ($\delta^{18}O_{bf}$, $\delta^{13}C_{bf}$).

As the resolution of EOT $\delta^{18}O_{bf}$ stratigraphy has increased, particularly through the generation of high-resolution equatorial Pacific (Ocean Drilling Program (ODP) Site 1218) and Southern Ocean (ODP Sites 689, 738, 744 and 748) $\delta^{18}O_{bf}$ records, a distinct step-like structure to the interval has been revealed, with two pronounced rapid increases seen either side of a 'plateau' (Bohaty et al., 2012; Coxall et al., 2005) (Figure 1.2). These steps, referred to herein as EOT-1 (precursor step in Miller et al., (2008)) and the Oi-1 shift (Oligocene isotope shift 1) respectively, together constitute a ~1.5‰ increase in $\delta^{18}O_{bf}$ across the transition. A transient $\delta^{18}O_{bf}$ shift, termed EOT-2, has also been tentatively invoked between EOT-1 and the Oi-1 event, however this was based on a low-resolution record that displays high levels of noise (Katz et al., 2008) (Figure 1.2). The Oi-1 event, which is the most commonly identified step of the EOT, coincides with the C13r/c13n magnetochron reversal (Figures 1.1, 1.2).

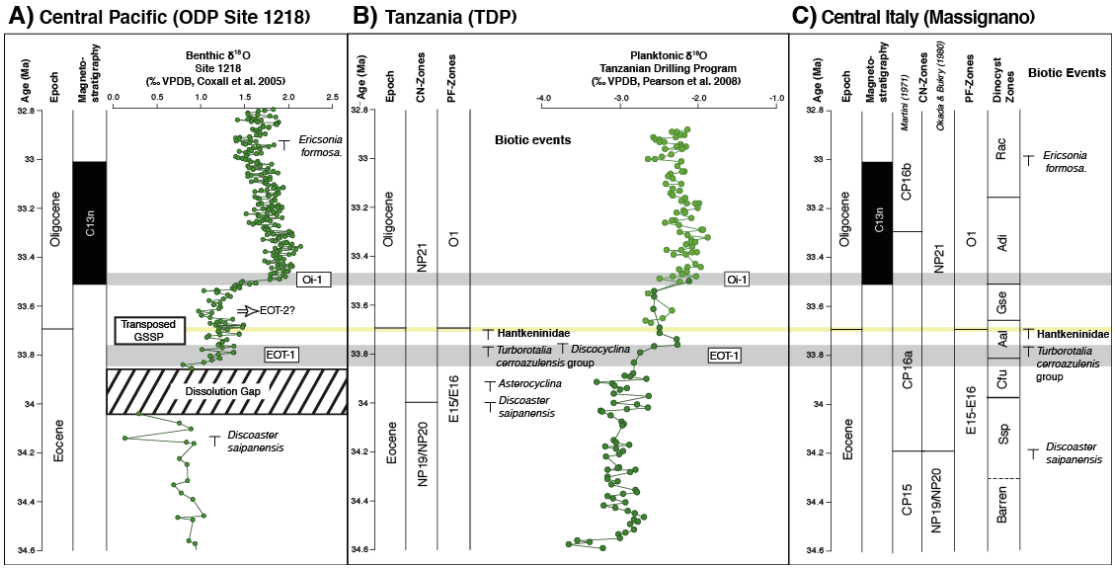

Figure 1.2: Expanded oxygen isotope stratigraphy across the EOT, showing the placement of the EOB, EOT-1, EOT-2 and the Oi-1 shift. a) Benthic foraminiferal oxygen isotope record from ODP Site 1218, b) planktic foraminiferal oxygen isotope record from Tanzania Drilling Project (TDP), c) Microfossil, nannofossil, and dinocyst zones for from the Global Stratotype Section and Point (GSSP) for the Eocene-Oligocene Boundary at Massignano. Figure modified from Houben et al., (2012).

The relative combinations of ice-growth versus global deep water cooling to the observed shift in $\delta^{18}O_{bf}$ are unclear, despite various attempts to address this problem (Coxall et al., 2005; Katz et al., 2008; Scher et al., 2011). Some data sets suggest that cooling was more prevalent in the EOT-1 step and ice growth was responsible for most of the Oi-1 shift (Bohaty et al., 2012; Houben et al., 2012; Katz et al., 2008; Lear et al., 2008). The changes in global temperature, glaciation, sea-level change, and oceanography across the EOT are explored in greater detail below.

1.1.2 Temperature change across EOT

Several lines of evidence suggest that global temperatures had been declining through the Late Eocene leading up to the EOT, driven by declining atmospheric CO_2- in the absence of large volumes of Antarctic ice, increasing $\delta^{18}O_{bf}$ can be interpreted as decreasing deep water temperatures, and $U^{K'}_{37}$ and TEX_{86}^{H} data suggest global sea surface temperatures (SSTs) declined over the same period (Anagnostou et al., 2016; Inglis et al., 2015; Lear et al., 2008; Liu et al., 2009).

The formation of a large volume of ice across the EOT makes the interpretation of deep-water temperature from $\delta^{18}O_{bf}$ more complex; an independent palaeothermometer is needed to separate the two components. The ratio of magnesium to calcium in foraminiferal calcite (Mg/Ca) has been shown to vary with water temperature, but quantifying temperature change using this proxy for the EOT has proved difficult. Analysis of benthic Mg/Ca records across the EOT from deep-water sediments in the Pacific and Atlantic indicates little temperature change, but this interpretation is complicated by contemporaneous deepening of the CCD; changes in carbonate saturation affect the partitioning of Mg in foraminiferal calcite, which distorts Mg/Ca and can mask temperature change (Coxall et al., 2005; Lear et al., 2004, 2000). Benthic foraminiferal Mg/Ca temperature reconstructions across the EOT from the Tanzania Drilling Project (TDP), where the shallower palaeodepth makes the record here less susceptible to CCD changes, suggest a global cooling of ~2.5 °C, and Southern Ocean Mg/Ca data from intermediate water depths also record a 2-3 °C cooling (Bohaty et al., 2012; Lear et al., 2008).

Further attempts to separate ice volume and temperature change across the EOT have focused on resolving the ice volume component through analysis of sea level change in shallow marine settings. Sequence stratigraphic analysis of EOT intervals from New Jersey and Alabama suggest a 1-2 °C cooling across the EOT-1 step and 1-4 °C across the Oi-1 shift, whereas sedimentological and biotic analysis of marginal marine sections in Italy suggests that the cooling across the EOT was focused on the EOT-1 step, and that the Oi-1 shift featured no significant temperature change (Houben et al., 2012; Miller et al., 2009). An earlier study combining sequence stratigraphy and Mg/Ca at St. Stevens Quarry, Alabama, found a ~2.5°C cooling across EOT-1, and a further ~2°C cooling across the Oi-1 shift (Katz et al., 2008), though there are issues associated with estimating ice volume using sequence stratigraphy, as discussed in Section 1.1.4 below.

1.1.3 Glaciation changes across the EOT

Though a small ice cap may have been present on the Antarctic continent in the Late Eocene, $\delta^{18}O_{bf}$ estimates (separated from temperature as described above) suggest that it expanded to a volume similar to modern day values (70-100% of modern Antarctic ice volume) across the EOT (Coxall et al., 2005; Lear et al., 2008; Scher et al., 2014). The appearance of ice-rafted debris (IRD) in Southern Ocean marine sediments across the EOT, alongside a change in clay mineralogy in Southern Ocean drill sites, has also been interpreted to signify the ice cap growing large enough to reach the Antarctic coastline (Ehrmann, 1998; Scher et al., 2011).

While Antarctic ice growth across the EOT has been widely studied, much less is known about the state of the Northern Hemisphere climate over the same time period. The established view is that ice caps only formed in the Northern Hemisphere much more recently, with a Greenland ice cap since ~7 Ma, and further glaciation in North America and Scandinavia occurring ~2.6 Ma (Bailey et al., 2013; Larsen et al., 1994). The discovery of coarse detrital grains and dropstones in marine sediments of EOT-age from East Greenland, however, has led to intense debate over the extent of glaciation in the Northern Hemisphere during the interval. Eldrett et al., (2007) interpreted the dropstones as evidence only of a coastal outlet alpine glacier, whereas Tripati et al., (2008) inferred that IRD implied bipolar glaciation (DeConto et al., 2008; Edgar et al., 2007; Eldrett et al., 2007; Tripati et al., 2008). Tripati et al., (2005) interpreted that a Late Eocene benthic foraminiferal oxygen isotope record from the equatorial Pacific implied a volume of ice growth that was too large to be explained by Antarctic glaciation, and hence posited that the IRD was from a large Greenland ice cap responsible for the remainder of the isotope shift. Edgar et al (2007) challenged this interpretation however, pointing out that the isotope shift had been calculated using outliers, required an unreasonably large ice budget, and that a benthic oxygen isotope record for the same interval from the tropical Atlantic showed a smaller shift, which could be accounted for by cooling and Antarctic ice growth alone. Coupled ocean-atmosphere-ice models also indicate that the CO_2 threshold for large-scale Northern Hemisphere glaciation (280 p.p.m.v.) was much lower than for Antarctica (750 p.p.m.v.), and proxy CO_2 estimates for the interval are higher than the Northern Hemisphere threshold (DeConto et al., 2008; Gasson et al., 2013) (Figure 1.1).

1.1.4 Sea level change across the EOT

The formation of a large continental ice cap across the EOT caused a significant glacioeustatic sea level fall, leading to widespread erosion of shallow shelf sediments, and deposition of eroded material into deeper waters. Estimates of this glacioeustatic sea level fall vary, but most lie between about 50 and 75 m (Miller et al., 2008, 1997). The first attempt to use sequence stratigraphy to create a global (eustatic) record of sea level change for the Cenozoic, dubbed the 'Exxon Curve', failed to identify a significant fall in sea level across the EOT (Haq et al., 1987; Miller et al., 2008), but contemporary studies reported a potentially global disconformity in the earliest Oligocene, attributed to sea level fall, and a sea level fall at the EOB has since been described by Hardenbol as Pr4/Ru1 (Haq et al., 1987; Hardenbol et al., 1999; Olsson et al., 1980).

A new estimation of Cenozoic global sea level change was created from sediments offshore of New Jersey, on the east coast shelf of the USA, correlated with corresponding wells drilled onshore and with seismic data (Fulthorpe et al., 2008; Miller et al., 1997; Pekar et al., 1997) (Figure 1.3). Changes in palaeowater-depth were tracked through the composite Cenozoic record by analysing benthic foramniferal biofacies, combined with the process of two-dimensional backstripping- a method of extracting a eustatic sea level record from strata by reconstructing the morphology of the depositional surface at the time of deposition (Pekar and Kominz, 2001). A combination of strontium isotope stratigraphy, biostratigraphy, and magnetostratigraphy has determined the age model to an accuracy of 0.7-0.1 Myr (Kominz et al., 2008; Pekar et al., 1997; Pekar and Kominz, 2001).

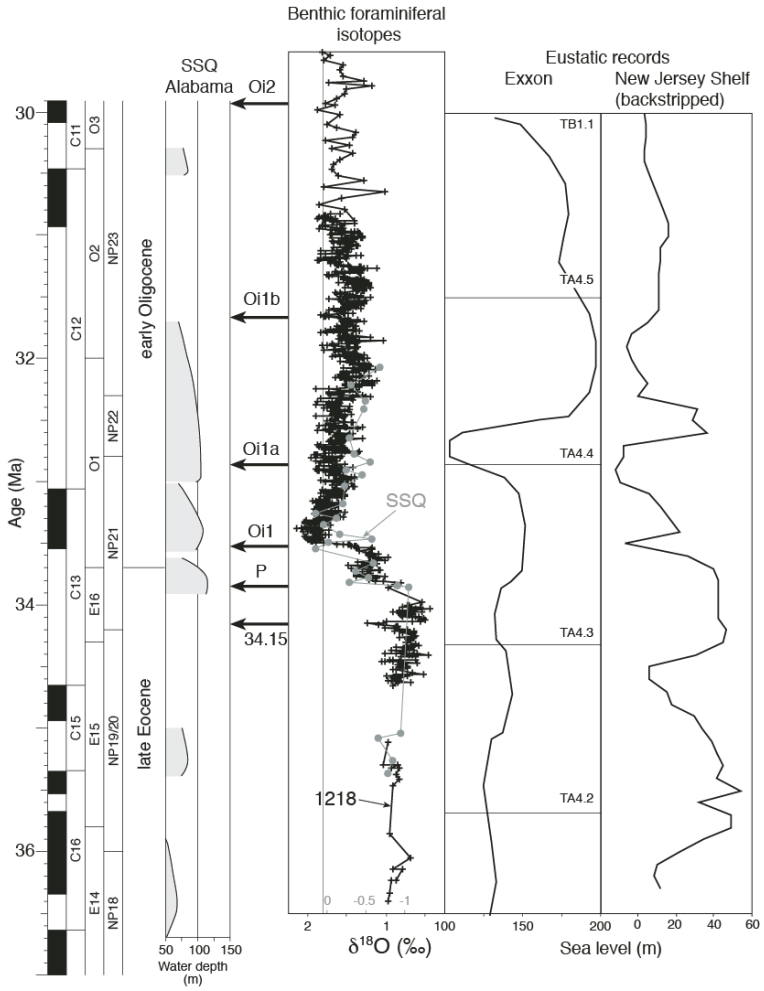

Figure 1.3: Comparison between water depth estimates from St Steven's Quarry, the eustatic sea level record of the Exxon working group (Haq et al., 1987), and the backstripped New Jersey Shelf eustatic record(Miller et al., 2005). Benthic foraminiferal isotope records from the Pacific ODP Site 1218 (Coxall et al., 2005), and from SSQ are also shown. Figure modified from Miller et al., (2008).

The New Jersey shelf lies on a passive margin, and is considered a far field site with respect to the establishment of a large Antarctic ice cap over the EOT (Kominz et al., 2008; Pekar et al., 1997; Pekar and Kominz, 2001). The predicted eustatic fall across the EOT of ~55 m was correlated to the Oi-1 oxygen isotope shift (Miller and Mountain, 1996; Pekar et al., 2002). Similar analysis has also been carried out at another EOT section at St. Steven's Quarry (SSQ), in Alabama, USA (Miller et al., 2008, 1993). There has been no attempt made to backstrip the SSQ eustatic sea level record, and so the estimated water depth change of 50-150m is likely an overestimation; the record is broadly in agreement with the estimation of a ~55m drop across Oi-1 (Miller et al., 2008, 2005). The lack of sequence stratigraphic change at SSQ over the

EOT-1 isotope step suggests that the main cause of this first $\delta^{18}O_{bf}$ shift was temperature change, not sea level/ice volume (Miller et al., 2008) (Figure 1.3).

Because the New Jersey and SSQ Cenozoic sea level records come from passive margins, the traditional assumption is that the sea level change experienced at these locations, *relative sea level* (RSL), is approximate to *eustatic* sea level; elsewhere, local tectonic influences, among other factors, can also affect RSL (Table 1.1). This assumption has been challenged; however- Moucha et al., (2008) demonstrate that on timescales of 10 Myr the flow of mantle can affect RSL even on supposedly passive, stable continental platforms such as the New Jersey margin. This process, termed dynamic topography, appears to have been responsible for ~100 m of topographic change across the last 30 Myr on the New Jersey margin, but for RSL change on the timescale of the EOT (<1 Myr) is unlikely to have been a significant factor compared to glacioeustasy (Moucha et al., 2008; Rowley, 2013). RSL change across the EOT could also have been influenced by isostacy (the response of the Earth's crust to loading). Glacio-isostatic adjustment (GIA), for example, refers to local uplift/subsidence that occurs following the removal/addition of a large volume of glacial ice to the lithosphere (Peltier and Fairbanks, 2006; Shennan et al., 2002). Though GIA, combined with other isostatic influences such as hydro-isostasy, is generally thought to be minimal for far-field sites, more modern studies have shown it can alter RSL on the order of 5 m over 21 Kyr in these areas, though this is in response to more extensive, bipolar glaciation, unlike the typically envisaged glacial conditions of the EOT (Milne and Mitrovica, 2008).

Record	Location	RSL Fall (m)	Back-stripped?	Interpretation
(Miller et al. 2005)	New Jersey Shelf, US	~55	Yes	Eustatic
(Miller et al., 2008)	SSQ Alabama, US	35-60	Estimated	Eustatic, all interpreted across Oi-1
(Turgut and Eseller, 2000)	Eastern Thrace Basin, Turkey	~70	No	Inferred to be eustatic
(Houben et al., 2012)	Vicentinian Alps, Italy	70-80	No	Eustatic, 20 m for EOT-1, 50-60 m for Oi-1
(Pinous et al., 1999)	Western Kazakhstan	26-50	No	Inferred to be eustatic
(Gale et al., 2006)	Isle of Wight, UK	~15	No	Eustatic, but effect reduced by local subsidence
(Hegewald and Jokat, 2013)	Chukchi Shelf, Arctic	~200	Yes	Inferred to be tectonic, but likely has eustatic component

Table 1.1: Quantitative estimations for RSL change across the EOT.

1.1.5 Oceanographic changes across the EOT

The pattern of deep water being formed in the North Atlantic as well as the Southern Ocean is thought to have started around the time of the EOT (Davies et al., 2001). The intensification of bottom currents in the North Atlantic across the interval is supported by the subsequent formation of thick sediment drifts at several locations along continental margins at this time (e.g. the Southeast Faeroes drift); with bottom currents increasing accumulation rates above typical pelagic values by transporting and depositing of large volumes of sediment (Davies et al., 2001; Howe et al., 2001; Via and Thomas, 2006; Wold, 1994) (Figure 1.4). The EOT interval is also marked in sedimentary sequences along the margins of the North Atlantic by erosional unconformities, which are interpreted to represent the intensification of bottom current intensity (Tucholke and Vogt, 1979). The A^U horizon, for example, points to erosion along the US East Coast margin, with a contemporary unconformity, termed R4, also present in several drifts in the Northeast Atlantic (Campbell and Mosher,

2016; Mountain and Tucholke, 1985) (Figure 1.4). A number of drifts along the western margin of the North Atlantic predate the EOT however, including the drifts on the Southeast Newfoundland Ridge, which are suggested to have started developing in the Eocene (Boyle et al., 2017; Campbell and Mosher, 2016; Norris et al., 2014). Hobhein et al. (2012) identified a drift deposit (Judd Falls Drift, Figure 1.4) of Mid-Eocene age in the Faeroe-Shetland Basin, which they argued implied that North Atlantic Deep Water (NADW) formation began at this time. Their interpretations have been challenged however, both as to whether the body is in fact a drift, and as to whether it records deep or shallow sedimentary processes (Hohbein et al., 2013, 2012; Stoker et al., 2013).

One hypothesis for circulation change across the EOT involves tectonic processes, rather than climate forcing; specifically, the deepening of the Greenland–Iceland–Faeroes Ridge, which had previously separated the Greenland-Norwegian Sea (a major area of deep water formation) from the North Atlantic Ocean, is estimated to have occurred contemporaneously to the EOT (Via and Thomas, 2006). Miller et al (2009) however, have argued that global cooling, beginning in the middle Eocene and continuing across the EOT, resulted in the formation of deep water (Borrelli et al., 2014; Campbell and Mosher, 2016). The growth of the East Antarctic ice sheet to the continent's coastlines across the EOT, as evidenced by the appearance of ice-rafted debris in Antarctic shelf sediments, may have also indirectly brought about circulation changes in the North Atlantic by increasing Antarctic Bottom Water (AABW) formation, increasing latitudinal gradients and increasing thermohaline circulation (Expedition 318 Scientists, 2010; Goldner et al., 2014; Miller et al., 2009; Scher et al., 2011).

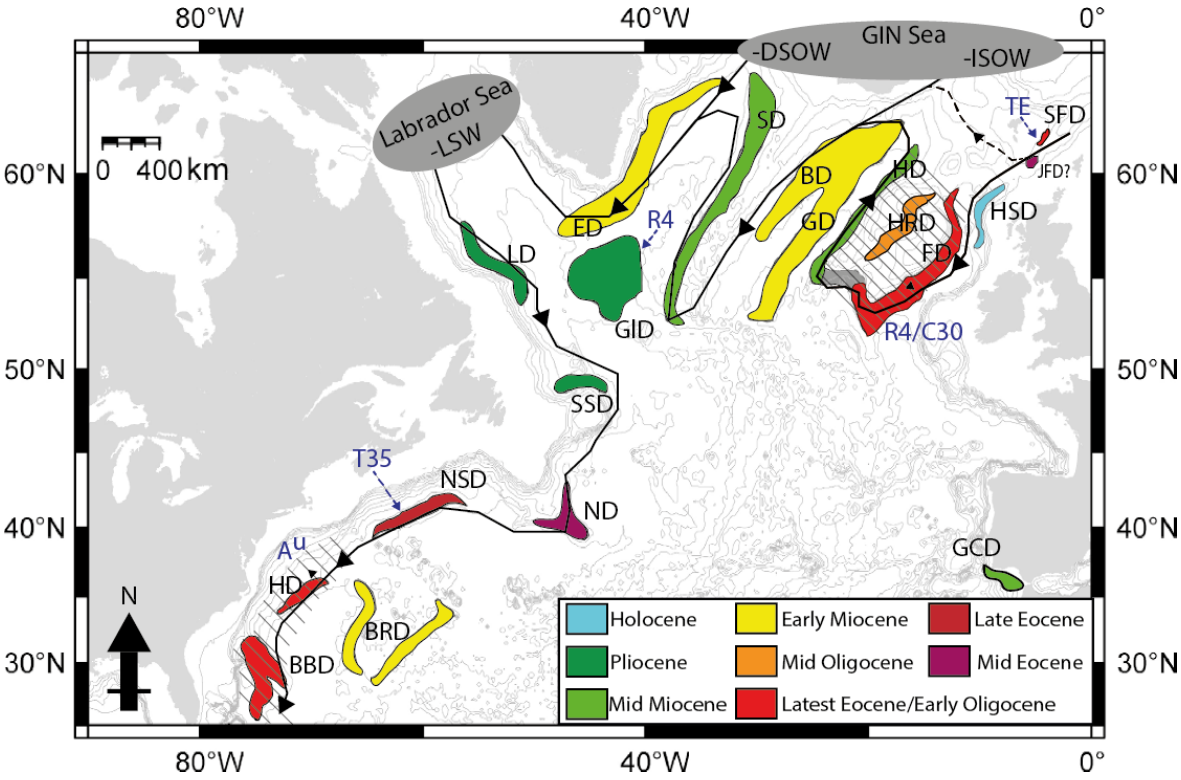

Figure 1.4: Key North Atlantic sediment drifts, alongside flow path of modern NADW and areas of deep water formation: Denmark Strait Overflow Water (DSOW) and Iceland-Scotland Overflow Water (ISOW), both form in the Greenland-Iceland-Norway (GIN) Sea, whereas Labrador Sea Water (LSW) is formed in the Labrador Sea (Bell et al., 2015; Yashayaev and Clarke, 2008). Blue text and dashed lines show erosional unconformities across the Latest Eocene-Earliest Oligocene: TE (Davies et al., 2001), R4/C30 (Miller and Tucholke, 1983; Stoker et al., 2001), T35 (Campbell and Mosher, 2016), and A^U (Tucholke and Mountain, 1979a). Drifts are: SFD= Southeast Faeroes Drift (Davies et al., 2001), JFD= Judd Falls Drift (Hohbein et al., 2012), HSD= Hebrides Slope Drift (Masson et al., 2002), FD= Feni Drift, HRD= Hatton-Rockall basin Drift (Roberts, 1975), GD= Gardar Drift, BD= Bjorn Drift, SD= Snorri Drift, ED= Eirik Drift (Müller-Michaelis et al., 2013), GlD= Gloria Drift, LD= Labrador/Orphan Drift (Piper, 2005), SSD= Sackville Spur Drift (Kennard et al., 1990), ND= Newfoundland Drift (Boyle et al., 2017), NSD= Nova Scotia Drift (Campbell and Mosher, 2016), HD= Hatteras Drift (Locker and Laine, 1992), BRD= Bermuda Rise Drift (Ayer and Laine, 1982), BBD= Blake Bahama outer ridge Drift (Faugères and Stow, 2008). Unless specified, ages are from (Wold, 1994). Modified from Faugères et al., (1999).

1.1.6 Importance of the EOT to the hydrocarbon industry

In addition to being an important interval palaeoclimatically speaking, the EOT is also of interest in the hydrocarbon exploration sector. At far field sites that are free from significant tectonic influence, glacioeustatic sea level fall across the EOT would have led to the development of lowstand system tracts, characterised by marked

progradation of clastic systems into deeper water, and the exposure and erosion of shallower marginal sediments (Walsh and Nittrouer, 2003) (Figure 1.5). This progradation can lead to the formation of sandstone bodies in the deeper parts of a basin, with the potential to act as hydrocarbon reservoirs (Boulila et al., 2011; Vail, 1977; Wade and Pälike, 2004). These sandstone bodies may exist as either perched/shelf-edge deltas or as deep marine turbidite fans. The sustained increase in the size of the Antarctic ice cap across the EOT also led to increased magnitudes of ice volume fluctuations going into the Oligocene, paced by obliquity (40 ka) and eccentricity (110, 405 ka) cycles seen in $\delta^{18}O_{bf}$ records (Abels et al., 2007; Wade and Pälike, 2004). Sea level change driven by these orbitally controlled cycles has been detected, for example, in shallow marine clastic sedimentation changes in the North Sea basin in the Early Oligocene (Abels et al., 2007). During the Oligocene, the longer orbital periods (405 ka eccentricity, 1.2 Ma obliquity) appear to have driven 3rd order sea level variability, which may have greatly influenced sedimentation patterns globally, providing a framework for sedimentary facies prediction (Boulila et al., 2011; Wade and Pälike, 2004).

The interpreted increase in bottom current intensity in the North Atlantic across the EOT could also be of considerable interest to the field of hydrocarbon exploration. Contour currents can create sandstones that can act as reservoirs by winnowing away finer sediment, leaving a better sorted, higher net-to-gross deposit (Howe et al., 2001). Intense contour currents are also capable of transporting, sorting, and re-depositing large volumes of sand to form hydrocarbon reservoirs, for example in the Campos Basin, offshore Brazil, or the Gulf of Cádiz (Hernandez-Molina et al., 2014; Viana et al., 1998a) (Figure 1.4). Furthermore, fine-grained contourite drift deposits, which tend to exhibit low permeability, can act to seal in sandstone reservoirs below (Duarte and Viana, 2007).

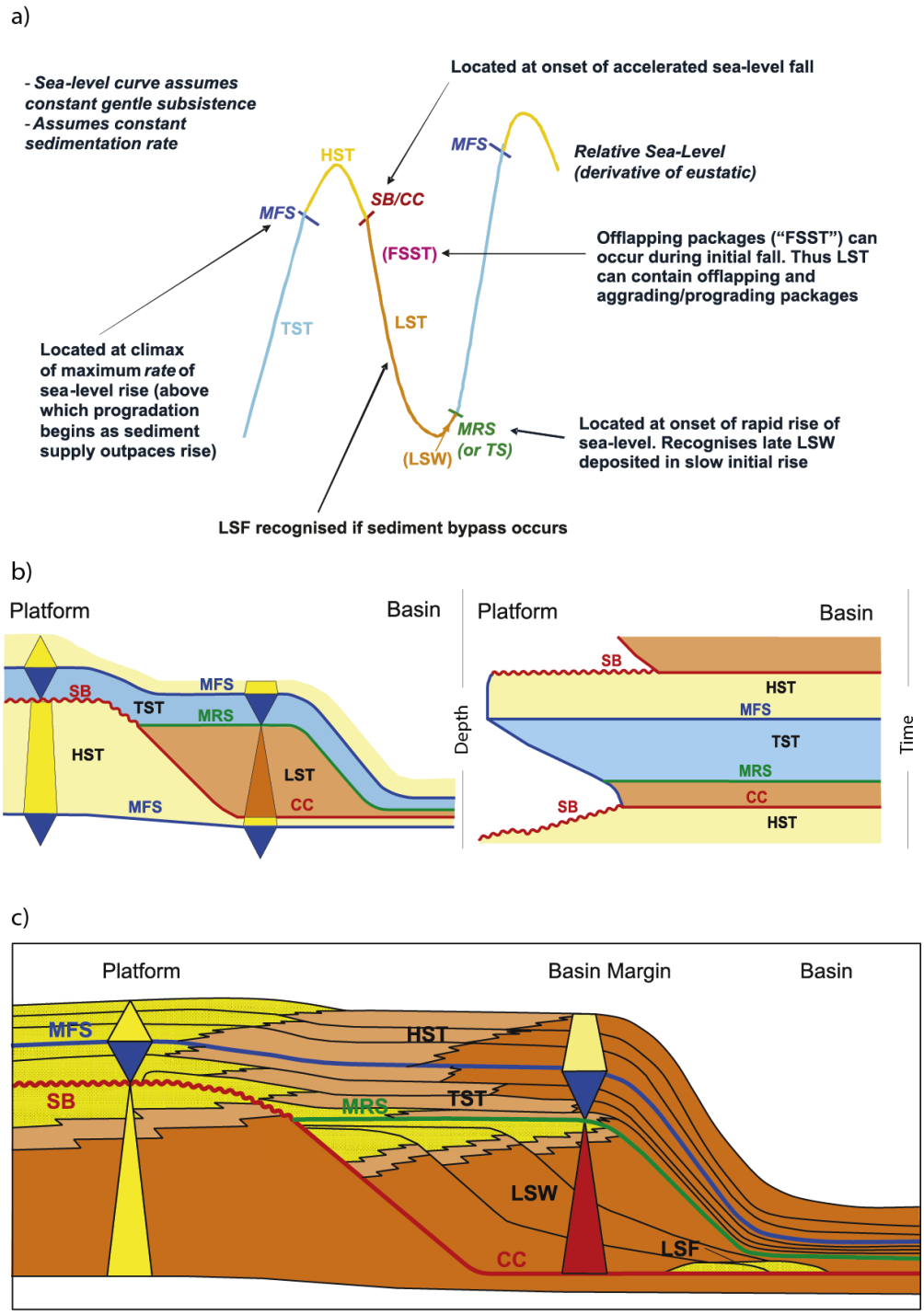

Figure 1.5: a) Summary of the sequence of sedimentary tracts expected during an idealised cycle of sea level change. b) Differences in sedimentation in space and time during the sea level cycle shown in a), showing differences in erosion/deposition between platform/shelf and basin. c) An idealised sedimentary succession deposited as a result of the sea level cycle shown in a); as sea level falls during the lowstand system tract, erosion occurs on the platform and coarse material is deposited into the basin. TST= Transgressive System Tract, HST= Highstand Systems Tract, LST= Lowstand Systems Tract, FSST= Falling-Stage Systems Tract, MFS= Maximum Flooding Surface, SB/CC= Sequence Boundary/Correlative Conformity, MRS= Maximum Regression Surface, LSW= Lowstand Systems Wedge, LSF= Lowstand Systems Fan. Panels adapted from Simmons (2012).

1.2 Studying the EOT in the North Atlantic

Our understanding of climatic change across the EOT has been greatly advanced by the generation of high-resolution proxy records from ODP Site 1218 in the equatorial Pacific (Coxall et al., 2005). Currently, however, there is no comparable record for the North Atlantic. An analogous high-resolution North Atlantic interval across the EOT would not only allow the global climatic changes across the interval to be compared to any changes in glacial and oceanographic conditions in the region, but might also obviate the calcite saturation effect on Mg/Ca encountered in the Pacific (Coxall et al., 2005; Lear et al., 2008, 2004). Obtaining a suitable stratigraphic section from the North Atlantic has proved difficult however, in part because the preponderance of erosional unconformities (Tucholke and Vogt, 1979; Tucholke and Mountain, 1986) (Figure 1.4).

1.2.1 The Southeast Newfoundland Ridge

This thesis focuses on a new EOT sedimentary section that overlies the Southeast Newfoundland Ridge (SENR), a volcanic bathymetric feature that protrudes from the base of the Grand Banks, along the Newfoundland Margin (Figure 1.6). Thick Palaeogene sedimentary drift deposits were penetrated on the SENR during IODP Expedition 342, which recovered a high resolution EOT sequence at Site U1411 (41°37.09'N, 48°59.99'W, water depth 3300 meters below sea level (mbsl) (Norris et al., 2014). The crest of the SENR lies at ~3000-3500 mbsl, compared to the abyssal plain of the Newfoundland Basin to the north, which features depths greater than 5000 mbsl.

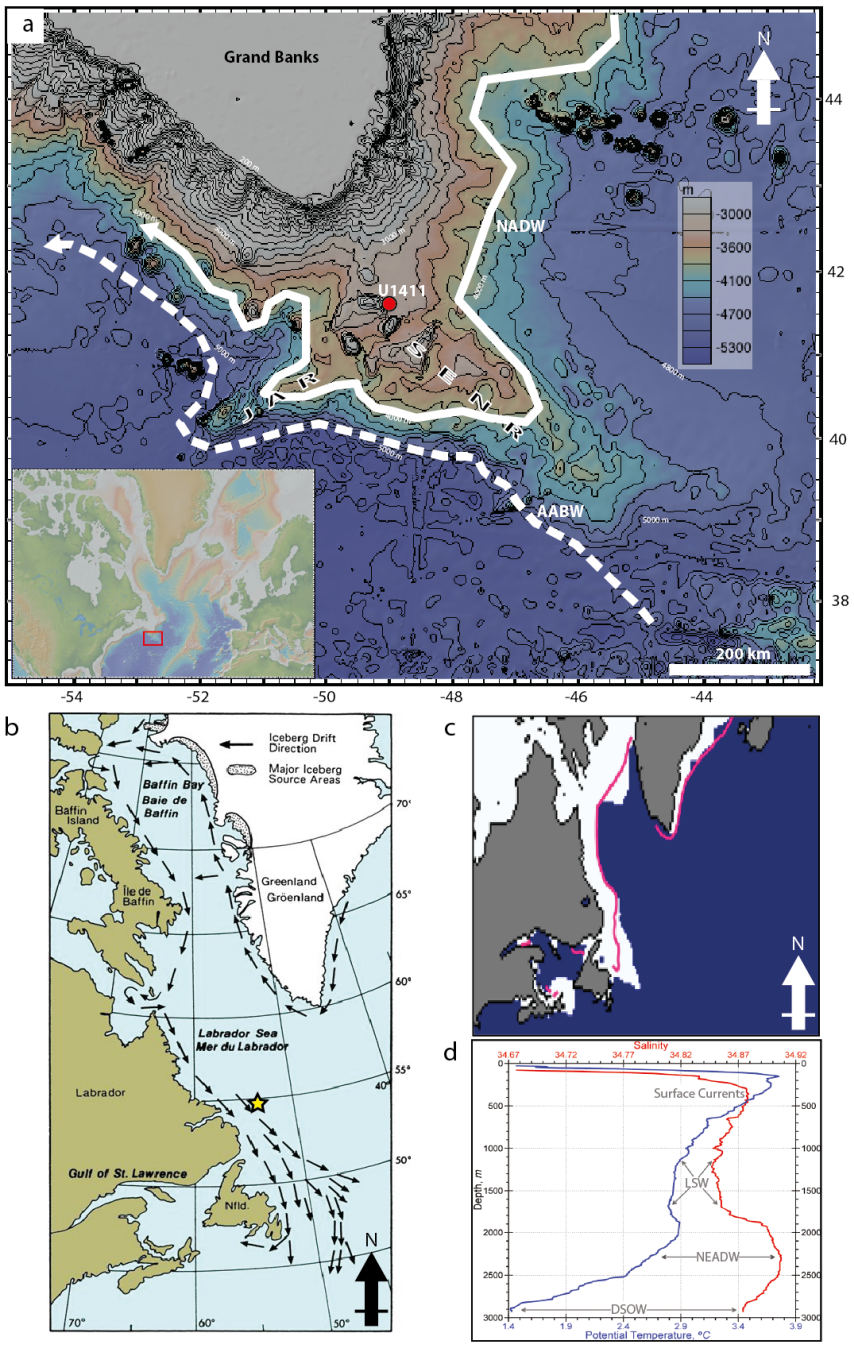

Figure 1.6: a) Bathymetry of the SENR and JAR, IODP Site U1411, and the modern flow-path of the NADW and AABW. Inset shows the situation of the SENR in the wider North Atlantic. Bathymetric base map is from GeoMapApp (http://www.geomapapp.org). b) Main areas of iceberg formation in the modern North Atlantic, along with prevailing surface currents, image courtesy of the Canadian Coast Guard. c) Modern 'winter' extent of Northern Hemisphere sea ice in 2015. Median April ice edge from 1981-2010 denoted by pink line, Image courtesy of the National Snow and Ice Data Center, University of Colorado, Boulder. d) Depth profile of NADW components in the Labrador Sea (see star in b for location). North East Atlantic Deep Water (NEADW) is largely composed of Iceland-Scotland Overflow Water (ISOW). Adapted from Yashayaev and Clarke (2008).

The basement of the SENR is oceanic; the ridge is thought to have been formed by magma supplied by a mantle plume lying under the rifting zone between the Barremian and earliest Aptian (chrons M4-M0)(Tucholke et al., 2007; Tucholke and Ludwig, 1982). Fragments of diagenetically altered coral recovered from IODP Site 1407, of Albian age, imply that the SENR was exposed to meteoric waters shortly after its formation (Norris et al., 2014). The oceanic origin of the SENR basement contrasts with the Newfoundland Basin directly to the north, which overlies transitional continental crust, with the continent-ocean boundary (COB) marked by the J-anomaly to the East. The J-Anomaly is the oldest identified oceanic crust magnetic anomaly in the region, and is thought to have formed between anomalies M0 and M1, giving it a Barremian-Aptian age (108-113 Ma) (Austin et al., 1989; Tucholke et al., 1989; Tucholke and Ludwig, 1982). Where the SENR crosses this anomaly, a smaller ridge, the J-Anomaly Ridge (JAR), extends to the southwest.

The Newfoundland margin itself has been passive throughout the Cenozoic, it separated from the Iberian margin through multiple phases of rifting that ended in the Late Aptian (112 Ma) Since these events the Newfoundland margin and basin has been tectonically inactive (Austin et al., 1989; Peron-Pinvidic et al., 2010; Péron-Pinvidic et al., 2007).

1.2.2 Modern cryosphere-oceanographic setting at SENR

Today, the SENR lies in path of icebergs, dominantly calving from the Greenland Ice Cap, transported through the Labrador Sea (Figure 1.6b). Famously, the ocean liner *R.M.S Titanic* struck a large iceberg in 1912 with fatal consequences and now lies in ~3800 m of water at (41.73° N, 49.95° W) on the SENR (Cochonat et al., 1989).

The area around Newfoundland and the Gulf of St. Lawrence also lies close to the current maximum extent of the annual Northern Hemisphere sea ice regime (Wang et al., 1994) with sea ice both forming locally along the Labrador and Newfoundland coastlines (and to a lesser extent in the Gulf of St. Lawrence) (Deser et al., 2002; Mysak et al., 1990; Prinsenberg et al., 1997; Saucier et al., 2003). Drifting sea ice is also concentrated along the coastline and is transported towards the study site, controlled by a complex interplay between freshwater delivery, atmospheric conditions, sea surface temperature, and surface currents (Figure 1.6c).

The SENR also lies in the flow-path of the modern deep western boundary current (DWBC), which exports NADW from its areas of formation, in the Labrador Sea and Greenland-Iceland-Norwegian Sea, southwards along the North American margin. Today, the DWBC skirts the SENR at depths <4500 m, here the upper part of the current is dominated by NADW. The upper portion of the NADW consists of Labrador Sea Water (LSW), with Iceland-Scotland Overflow Water (ISOW) at intermediate depths and Denmark Strait Overflow Water (DSOW) making up the deepest component of the NADW (Figure 1.6d, Figure 1.4). To the south of the ridge, the modern day DWBC also incorporates AABW at depths > 4500 m (Clarke et al., 1980; Dickson and Brown, 1994; McCave and Tucholke, 1986) (Figure 1.6a). The situation of the SENR in the flow path of the DWBC is the reason that thick sediment drifts have accumulated here through the Cenozoic, providing high-resolution palaeoclimatic archives.

The modern day DWBC has a mean southerly flow of ~5-10 cm s^{-1} (Gardner et al., 2017; Richardson et al., 1981). Modern day measurements along base of the continental slope in the Labrador Sea document bottom current speeds faster than 20 cm s^{-1}, however, and bottom currents of ~10 cm s^{-1} have been measured in the Newfoundland basin. Bottom current speeds of 30 cm s^{-1} have also been recorded on the SENR (Clarke et al., 1980; Cochonat et al., 1989; Rabinowitz and Eittreim, 1974). At present, the Gulf Stream, bringing warm water northwards from the equator, also converges with the DWBC near the SENR, with the complex interaction between the two causing highly variable, strong currents (up to 70 cm s^{-1}) at depths >5000 mbsl (Richardson et al., 1981).

1.2.3 Initial findings of IODP Expedition 342

A high resolution EOT interval was recovered during IODP Expedition 342 at Site U1411, located on the northern flank of the SENR, near to the crest of the ridge (Figure 1.6). The immediate area features several Cretaceous-aged seamounts, around which the thick Cenozoic sediment drifts described above have accumulated.

The site lies in ~3300 m water depth, with the sea floor at the base of the ridge a further ~1500 m deeper. Linear sedimentation rates across the EOT within the sediment drift drilled are up to ~5 cm/kyr, due to increased sediment delivery by the action of bottom currents (Norris et al., 2014). The interval is largely dominated by homogenous clay and silt, which contains exceptionally well-preserved foraminifers, providing the potential for the generation of high-quality, high-resolution stable isotope records. One striking feature of the Site U1411 EOT interval is the presence of disseminated, well-sorted, fine sand-to-coarse silt detrital grains. These are sometimes present in loosely compacted pockets or clasts on core split-surfaces of mm-cm scale in size. Shipboard, the origin of these detrital clasts was the subject of considerable debate. Eventually, they were tentatively hypothesised to be related to ice rafting (Norris et al., 2014).

If these grains are indeed iceberg-rafted IRD then, given the distal nature of the study site (with respect to Greenland and the Arctic), it could represent important evidence for extensive Northern Hemisphere glaciation across the EOT—an outcome which would necessitate a re-thinking of our current understanding of ice-sheet growth in a high-CO_2 world (DeConto et al., 2008). A confirmed iceberg IRD record could also be coupled with a benthic foraminiferal oxygen isotope record for the interval, allowing for an accurate estimate of the timing and volume of any potential Northern Hemisphere ice growth.

In the same vein, if these grains represent sea ice-rafted debris (SIRD), then this would point to a more extensive sea ice regime than currently thought, possibly even close to its present day extent. The existence of large areas of sea ice have important implications for understanding the oceanography and climate of the late Eocene and Early Oligocene, from the albedo effect (insolation being reflected from the ice surface), to the process of brine rejection during sea ice formation, which is an important factor in bottom water formation as it forms dense water that contributes to deep water masses. Primarily this occurs in the Southern Ocean, but also contributes to deep water formation in the Arctic, and regionally can affect circulation in the Northern Hemisphere (Aagaard et al., 1985; Curry et al., 1995; Schumacher et al., 1983; Shcherbina et al., 2003). Sea ice export into the North Atlantic can also deliver large volumes of fresh water and can affect climate variability (Prins et al.,

2008), (Parkinson, 2000). Understanding whether ice rafting has delivered material to a site is also important when attempting to characterise the flow speed for bottom currents, for example using the sortable silt fraction (Hass, 2002).

Generally, when assessing a potential IRD record, only lithic grains larger than a certain size fraction (usually >63 μm or >150 μm) are counted, to avoid the possibility that smaller grains transported by bottom currents or wind could be mistaken for IRD (Darby, 2014; Hebbeln, 2000). Recent work has shown however that strong bottom currents can erode, transport and deposit sandy material (Rebesco et al., 2014). It is therefore necessary to consider that the presence of detrital sand at Site U1411 may also reflect deposition by strong bottom currents. If the lithic grains do represent bottom current activity, then this also may have important ramifications in understanding the climatic and oceanographic development of the North Atlantic during the EOT- the appearance of these fine sands may indicate a strengthening of deep water formation and export in the region (Hohbein et al., 2012).

1.3 Aims/Objectives

The expanded EOT-age drift sequence at Site U1411 on the SENR offers a perfect opportunity to study the response of the North Atlantic to global climatic change across this key event. In particular, this thesis aims to tackle the following aims:

- To determine whether the presence of detrital sand (including the compacted detrital clasts) on the SENR represents evidence of pervasive ice rafting in the North Atlantic across the EOT.

- To relate sedimentological evidence of changes in North Atlantic oceanographic circulation and/or sea level fluctuation to the palaeoclimate signals contained in stable isotopic analysis of the interval.

- To frame the sedimentological development of the Cenozoic drift sequence on the SENR within the context of the larger environment of the Newfoundland Margin.

1.4 Thesis structure

This thesis is composed of this introductory chapter, three main science chapters (2, 3 and 4) entitled as follows, and a conclusions chapter (Chapter 5):

Chapter 2: The extent of glacial ice-rafted debris in the North Atlantic at the Eocene Oligocene Transition.

Chapter 3: Changes in oceanography and sea level across the Eocene Oligocene Transition recorded on the Southeast Newfoundland Ridge: interpreting the detrital record of Site U1411.

Chapter 4: Cenozoic Changes in sea level, sedimentation, and morphology in the Newfoundland Basin and Southeast Newfoundland Ridge.

Chapter 2 The extent of glacial ice-rafted debris in the North Atlantic across the Eocene Oligocene Transition

2.1 Introduction

The traditional view of Cenozoic glaciation is that the extent of the Antarctic ice cap rapidly expanded across the EOT, but the Northern Hemisphere did not experience significant glaciation for another several million years. The discovery of coarse detrital grains in marine sediments of EOT-age from East Greenland, interpreted to be ice-rafted debris (IRD) however, has led to speculation over the extent of glaciation in the Northern Hemisphere during the interval (DeConto et al., 2008; Edgar et al., 2007; Eldrett et al., 2007; Tripati et al., 2005). Tripati et al (2005) interpreted that a Late Eocene benthic foraminiferal oxygen isotope record from the Pacific implied a volume of ice growth that was too large to be explained by Antarctic glaciation, and hence posited that the IRD represented a significant Greenland ice cap responsible for the remainder of the isotope shift. Edgar et al (2007) challenged this observation, however, pointing out that the isotope shift in question had been calculated using outliers, and that an Atlantic oxygen isotope record for the same interval showed a smaller shift, which could be accounted for by Antarctic ice growth alone.

Recent provenance work suggests a Central East Greenland source for the IRD in question, but the nature and extent of ice rafting into the North Atlantic at the time is unknown (Tripati et al., 2008). To date, IRD has only been identified at one location, Ocean Drilling Program (ODP) Site 913 (drilled during ODP Leg 151), and it is proximal to the suspected source of ice (Eldrett et al., 2007). Assuming that a large Greenland ice sheet across the EOT would produce icebergs large enough to transport debris out into the North Atlantic, it would seem prudent therefore to examine EOT intervals from other, more distal sites in the North Atlantic, to determine whether the Site 913 record is representative of a larger Northern Hemisphere ice cap, or rather a localised tidewater glacier. The discovery of iceberg-rafted sediment at sites spanning the North Atlantic across the EOT would lend support to the controversial idea of bipolar glaciation at this time. Conversely, the absence of any evidence of ice rafting at these sites would support the view that any Northern Hemisphere glaciation across

the EOT was limited to localised tidewater glaciers, and that an extensive glacial regime did not become established until much later in the Cenozoic.

This chapter compares the lithology of the Site 913 EOT interval to three EOT sections from the North Atlantic: Integrated Ocean Drilling Program (IODP) Sites U1406 and U1411 (both IODP Expedition 342), and ODP Site 647 (ODP Leg 105). All of these EOT sections feature coarse detrital grains, and each site features ice-rafted sediments in its Pleistocene section, suggesting it was affected by iceberg rafting at the time of our current understanding of Northern Hemisphere glaciation (Norris et al., 2014; Scott et al., 1989). Furthermore, Sites 647, U1411 and U1406 lie at successively more distal points in the flow-path of modern day surface currents that today transport icebergs through the North Atlantic (Figure 2.1) (Andrews, 2000; Pickart, 1992; Raymo, 1994). Specifically, this chapter compares the lithology of the cores from each of the sections, determines provenance where possible, and compares the nature of coarse lithic grains through surface texture analysis.

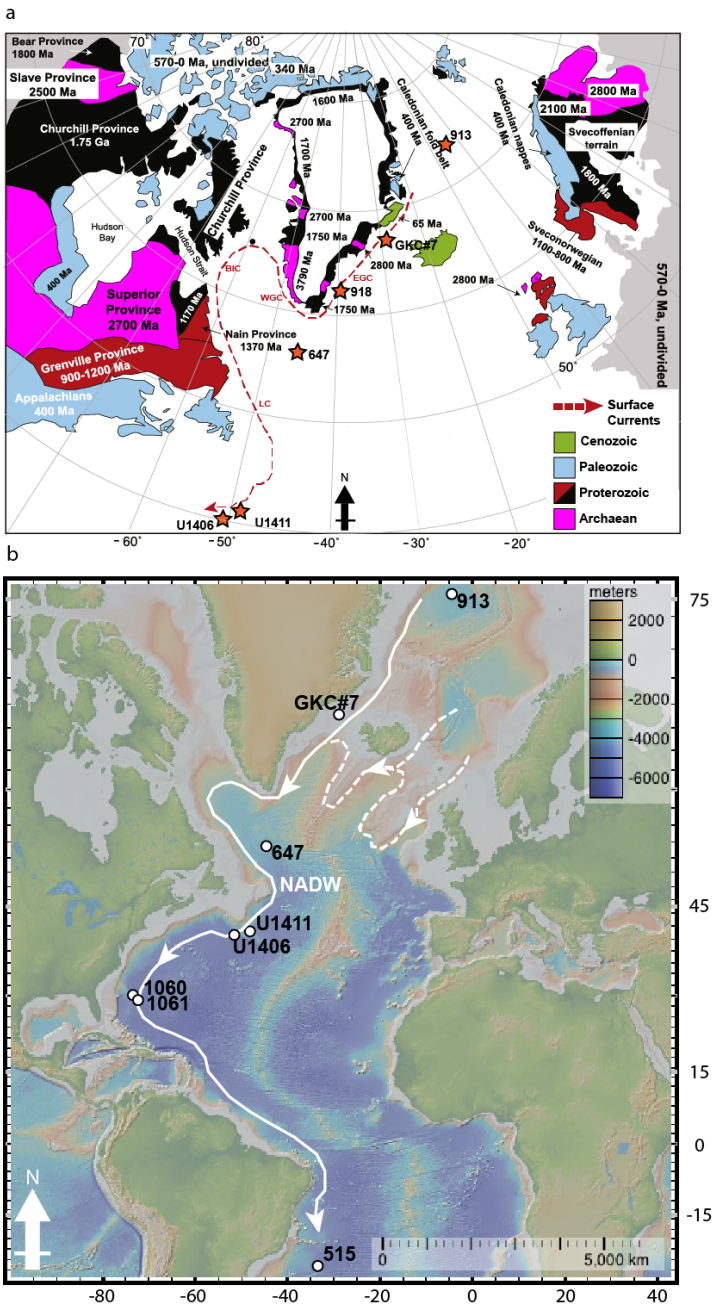

Figure 2.1: a) terrane data for the North Atlantic provinces (modified from Bailey et al., 2012). Modern surface currents responsible for exporting icebergs are also shown- EGC= East Greenland Current, WGC= West Greenland Current, BIC=Baffin Island Current, LC= Labrador Current (Moffa-Sánchez et al., 2014). b) Locations of the sites featured in this chapter, in relation to the transport of North Atlantic Deep water (Dickson and Brown, 1994). Bathymetric base map for b) is from GeoMapApp (http://www.geomapapp.org).

Examining the archived core half sections from the EOT sections listed above can provide clues as to whether they represent a period of ice rafting. For example, in combination with understanding the palaeobathymetry of the depositional environment, the presence or absence of graded changes in grain size can rule out the possibility that coarse detrital grains may be the result of turbidite flows, rather than

ice rafting (Eldrett et al., 2007; Tripati et al., 2008). Furthermore, when dropstones or other large lithic clasts are present in an interval that also features laminations, if these lamina have been deformed by the impact of the sinking clast, this can indicate that they have been ice-rafted (Bennett et al., 1996; Eldrett et al., 2007; Price, 1999). In addition to making comparisons between the four EOT sections discussed above, the EOT sections were also compared to the Pleistocene section from U1411, which was deposited under a time of known Northern Hemisphere glaciation (Raymo, 1994), and to cores from three low-latitude drift deposits in the North Atlantic (DSDP Site 515, and ODP Sites 1060 and 1061) (Figure 2.1). These low-latitude sections were examined to discover whether the features seen in the high latitude sections could also form in settings removed from the potential influence of ice rafting. These sites were chosen because they were similar in their sedimentology and sedimentation rates to the Site U1411 and 647 EOT intervals.

Surface textures on quartz grains can be used to determine transport mechanisms, including iceberg, sea ice, aeolian, and fluvial transport (Mahaney et al., 2001; Mahaney and Kalm, 2000; Newsome and Ladd, 1999; St. John et al., 2015; Strand et al., 2003; Williams and Morgan, 1993). Conchoidal fractures, for example, are mechanically formed textures formed by grinding, and tend to occur in glacial environments. In contrast, silica dissolution (a chemical texture) is more commonly seen in grains that have been transported through marine environments (Krinsley and Donahue, 1968; Krinsley and Doornkamp, 2011; Mahaney and Kalm, 2000). Quartz grains from glacial environments appear relatively fresh and unweathered, i.e., they have been recently fractured from their original source material (Krinsley and Doornkamp, 2011). They display fractures and gouges from glacial grinding, but remain relatively angular. Calving icebergs can carry these grains across the ocean for great distances without the grains undergoing any further contact with one another. In contrast, grains from subaqueous environments tend to be more weathered; they have had longer and more complex transport histories. They often feature dissolution and precipitation- which can overprint earlier textures, and are more rounded than their glacial counterparts due to traction with other grains (Krinsley and Doornkamp 2011; Mahaney, Stewart, and Kalm 2001). IRD carried by sea ice can closely reflect subaqueous grains, because the material carried by sea ice is often entrained in coastal areas, river mouths, and shallow shelves (Eicken et al. 2005; Reimnitz et al.

1998; Reimnitz et al. 1993; Barnes, Reimnitz, and Fox 1982; John et al. 2015; Nürnberg et al. 1994; Dethleff and Kuhlmann 2010; Lisitzin 2002).

A previous study has already analysed the surface textures of quartz grains from the coarse detrital fraction present at ODP Site 913, interpreting them to have been iceberg rafted from a glacial source (Tripati et al., 2008). One of the six samples analysed in the Tripati study was from the top 12 cm of section one of a core, however, and another was from a core catcher; this increases the risk of contamination by younger material, especially as the cores from Site 913 were recovered through rotary drilling. Furthermore, the study used an unconventionally wide grain size range (>125 μm, no upper limit), despite the observations made by Krinsley and Doornkamp (2011) that quartz grains above and below 200 μm display different ranges of textures (Krinsley and Doornkamp, 2011). There has, however, been little further research into the sensitivity of different surface textures to grain size, with no agreed size range between different studies, though many use a lower limit of 200-250 μm. (Immonen, 2013; Immonen et al., 2009; St. John, 2008; St. John et al., 2015; Stickley et al., 2009; Strand et al., 2003).

2.1.1 Aims

The primary aim of this chapter is to determine whether there is any evidence of a Northern Hemisphere (Greenland) ice cap across the EOT large enough to initiate iceberg rafting in the North Atlantic, as seen in periods of true bipolar glaciation in the Pliocene and Pleistocene. Surface textural analysis of coarse detrital grains from several locations in the North Atlantic is also featured, to determine whether there is any evidence of iceberg rafting regardless of source.

As part of this aim, specific attention is paid to investigating the origin of compacted lithic clasts that were identified at one of the intervals (Site U1411); at the time of their discovery during IODP Exp. 342 they were tentatively been interpreted to be ice-rafted dropstones.

A further aim of this chapter is to determine how sensitive the textural analysis of detrital grains is to changes in grain size.

2.2 Geological materials and methods

2.2.1 Study sites

Site U1406:

Site U1406 is located at 40°20.99′N, 51°38.99′W, and was drilled during IODP Expedition 342 at a water depth of 3799 mbsl (meters below sea level). It penetrates a succession of pelagic sediments perched atop an isolated seamount on the J-Anomaly Ridge (Norris et al., 2014) (Figure 2.1). Across the EOT, it has a carbonate content of 40-80% and a relatively low linear sedimentation rate (~0.7 cm/kyr), compared to other drift bodies on the Southeast Newfoundland Ridge (SENR). As Site U1406 was drilled near to the summit of a seamount on the ridge, it is effectively isolated from downslope movements.

Site U1411:

Site U1411 was drilled offshore of Newfoundland during IODP Expedition 342. It recovered a drift deposit plastered onto a seamount on the SENR, located at 41°37.09′N, 48°59.99′W at a depth of 3300 mbsl (Norris et al., 2014) (Figure 2.1). The EOT interval at Site U1411 consists of a thick, largely homogeneous drift of silty clay and clay-rich nannofossil ooze, with a high sedimentation rate of ~3 cm/kyr. Fine-grained detrital sand was identified shipboard, particularly in the form of loosely compacted lithic detrital clasts (mm-cm in scale). These were initially tentatively interpreted to be ice-rafted in origin, as no other process was envisaged to account for their transport to the site based on their size (Norris et al., 2014).

Site 647:

ODP Site 647 was drilled at a location of 53°19.88'N, 45°15.72'W during Leg 105, at a water depth of 3861.8 mbsl (Srivastava et al., 1987). It lies in the Labrador Sea, to the south of the Gloria Drift (Figure 2.1). The EOT section is composed of hemipelagic clay-rich deposits, with a similar average linear sedimentation rate (~3.6 cm/kyr) to Site U1411.

Site 913:

ODP Site 913 lies offshore of East Greenland (Figure 2.1) at a position of 75°29.35′N, 6°56.82′W, and was drilled during Leg 151 at a water depth of 3319 mbsl (Myhre et al., 1995). Average linear sedimentation rates range from 0.65-2.53 cm/ka for the interval, though there are some hiatuses (Eldrett et al., 2004; Myhre et al., 1995). A previous study on this interval concluded that outsized clasts found in the sediment were dropstones (Eldrett et al., 2007). The presence of lamina at this site aided the diagnosis of said dropstones, as their deformation can be diagnostic in separating an ice-rafted clast from a product of bioturbation that has been formed post-deposition (Eldrett et al., 2007).

Low Latitude Sites:

ODP Sites 1060 and 1061 lie on the Blake-Bahama Outer Ridge, at locations of 30°45.59'N, 74°27.99'W and 29°58.49'N, 73°35.99'W respectively. They were drilled during ODP Leg 172 (Figure 2.1). Site 1060 lies at a depth of 3493 mbsl, and Site 1061 lies at a depth of 4046 mbsl; both sites feature drift deposits of Pliocene-Quaternary age with average linear sedimentation rates of 5-25 cm/kyr, these formed under the influence of North Atlantic Deep Water (NADW) (Yokokawa, 2001). DSDP Site 515 was drilled in the Brazil Basin, at a location of 26°14.33'S, 36°30.17'W and a water depth of 4250m, where it is bathed by Antarctic Bottom Water (AABW, Figure 2.1). The targeted drift deposit at this site is of mid-Miocene to mid-Pleistocene age, and has an average linear sedimentation rate of ~2 cm/kyr (Barker et al., 1983).

2.2.2 Core descriptions

The archive core sections of the sites listed above were examined to confirm that the Site 913 EOT interval represents a record of glacially derived ice rafting, and to explore the interpretation made during Expedition 342 that the detrital grains, and in particular mm-cm scale compacted detrital clasts identified at Site U1411, are also ice rafted. The Site 647 EOT and low latitude cores were also examined to look for similar features. A digital hand lens was used to capture images of features of interest for all of the intervals studied.

2.2.2.1 Investigation of Site U1411 compacted detrital clasts

Elemental mapping:

Two compacted detrital clasts (both ~1 mm in diameter) were removed intact from the working halves of the Site U1411 EOT interval to further explore their nature. Inspection with a binocular microscope showed they consisted of a clean, sorted collection of detrital grains, matching the shipboard description (Norris et al., 2014). They were mounted onto stubs and sputter coated in gold film in preparation for Scanning Electron Microscope (SEM) analysis. The morphology, size, and mineralogy of the disaggregated grains were analysed using a Leo 1450VP SEM with an attached light element PGT energy dispersive spectrometer (EDS) at The National Oceanography Centre, Southampton (NOCS). Elemental maps were created of the following elements: Ca, Si, K, Al, Cl, Ti, Fe, Mg, and Cr (low-level blank).

Computer Tomography (CT) Scanning of Discrete Samples:

Several half-core rounds (~2 cm in thickness) containing the clasts were CT scanned in a pilot study at the μVIS X-Ray Imaging Centre at the University of Southampton to allow their internal structure to be determined.

2.2.3 Grain comparisons

2.2.3.1 Mineralogy

Microscopy & QEMSCAN Analysis:

The mineralogy of the grains recovered from each interval were explored through light microscope analysis at NOCS; combined with previously published heavy mineral analysis for the Site 913 EOT interval (Eldrett et al., 2007; Tripati et al., 2008). The relatively small size of the grains from the Site U1411 EOT interval made light microscope analysis difficult, and so a more quantitative approach was taken. The mineralogy of the detrital fraction was explored further through QEMSCAN analysis performed at University College London (UCL). Ten 25 cm^3 samples from the Site U1411 EOT section were prepared at NOCS through de-carbonation in excess 10% acetic acid. They were washed in de-ionised water, shaken with sodium hexametaphosphate, and then wet-sieved through a 20 μm mesh. The samples were then encased in resin and polished in preparation for loading into the QEMSCAN apparatus.

2.2.3.2 Provenance

The radiogenic Pb isotope system was used to trace the provenance of sand-sized feldspar grains present in the Site U1411 detrital component. Several studies have determined the provenance of IRD in the North Atlantic using the Pb isotope signatures of feldspars. As such there is currently a detailed understanding of the Pb isotope signatures of each source region, including the source area of the IRD from the Site 913 EOT interval— East Greenland (Bailey et al., 2012; Gwiazda et al., 1996). Pb isotope data is also available of more-recently ice-rafted feldspars sourced from the Palaeogene Basalts and underlying Palaeozoic sediments of East Greenland (i.e., the source area of the Site 913 sediments) (Simon, 2007; White et al., 2016).

Pb Sample preparation

Recent studies have analysed individual feldspar grains by using laser ablation to liberate Pb (Bailey et al. 2013; Bailey et al. 2012); this method is more efficient than the traditional approach of dissolving feldspars either individually or *en masse,* and separating Pb via column chemistry (Gwiazda et al., 1996). A pilot study was conducted to explore the feasibility of using laser ablation on the Exp. 342 feldspars. However, none of the grains targeted were large enough to yield a measurable amount of Pb. For 31 samples, 350-500 feldspars were hand-picked for dissolution as composites. No feldspars that were large enough were found during the inspection of the >150 μm fraction to dissolve individually. In addition to these samples, five composite samples were prepared from the EOT section of IODP Site U1406, to confirm the interpretation made during Expedition 342 that the detrital sand from each site came from the same source (Norris et al., 2014).

In total therefore, 36 samples were prepared for the process of leaching and digestion, along with five procedural blanks. The samples were transferred into 3 ml Teflon pots and leached on a hot plate at 140°C with 6M hydrochloric acid (HCl) for two hours and left overnight. They were then washed several times with Milli-Q water, in preparation for digestion. The samples were each digested with 20 μl sub-boiled nitric acid (HNO_3) and 160 μl of 27M hydrofluoric acid (HF) on a hot plate for 24 hours. They were then evaporated to dryness and cleaned with a few drops of concentrated HCl and HNO_3 (evaporated after each step) ready for column separation.

Pb Column chemistry

Columns were rinsed with de-ionised water, before being loaded with 5-10 drops of AG1x8 anion exchange resin. Prior to the addition of the samples, each column was washed through twice over with 6M HCl and then Milli-Q, respectively, and then with 1M HBr. The dissolved samples/blanks were then transferred via clean pipette into the columns and allowed to drip through. HBr was added and allowed to drip through three times, before 6M HCl was added and the residue collected in cleaned Teflon pots, ready for isotopic analysis. Samples and blanks were screened prior to isotopic analysis, with the five blanks showing <0.001 ppb Pb.

The Pb isotopes were analysed using a multi-collector inductively coupled plasma mass spectrometer (MC-ICP-MS, Thermo Scientific Neptune) at NOCS. Where there was sufficient Pb, two separate methods of correction were used on the samples: ^{203}Tl–^{205}Tl spiking and Sample–standard bracketing. Some samples only yielded enough Pb for sample-standard bracketing (Taylor et al., 2015). The NBS 981 standard was analysed ten times, giving external precision (at two standard deviations) of 0.0017, 0.002, and 0.0056 for $^{206}Pb/^{204}Pb$, $^{207}Pb/^{204}Pb$, and $^{208}Pb/^{204}Pb$ respectively.

2.2.3.3 Quartz grain surface texture analysis

Site U1411 and U1406 EOT intervals:

The EOT-age working half-sections from Sites U1411 and U1406 were both sampled at high frequency intervals (up to 4 cm), at NOCS. This involved weighing and drying unprocessed sediment, before adding sodium hexametaphosphate and shaking to disaggregate clay. Each sample was then wet-sieved through a 63-μm mesh to isolate the coarse fraction. The coarse fraction was dry-sieved at >200 μm and large mineral grains were individually picked out. Ideally, >15 grains should be picked per sample to provide a statistically representative picture (Dunhill, 1998). However detrital grains >200 μm in size were very rare in both the U1406 and U1411 EOT sections, and at most one-to-two grains were found per sample. In total, 128 grains were found.

Site U1411 Pleistocene interval:

Detrital grains were also obtained from Pleistocene-age sediments from Site U1411 to complement the EOT-age samples. These sediments represent classic iceberg-rafted deposits, as the core surfaces feature numerous dropstones and visible coarse sediment. Samples were taken from the working core sections at the BCR, and then processed as described above at NOCS. Coarse detrital grains were abundant in these samples, and so ~20-40 grains were picked per sample. One sample was also dry-sieved at ½ϕ intervals, and 15-20 grains were picked out from each size fraction, to study the sensitivity of surface texture analysis to grain size. The ϕ scale is logarithmic, and is calculated as:

$$\phi = \log_2 D \qquad (2.1)$$

Here D is the diameter of the particle in mm (Wentworth, 1922). This scale is commonly used when analysing particle size distributions because the behaviour of fine grains changes as a result of only very small changes in grain size, but this sensitivity decreases for coarser grains.

Site 647 EOT interval:

The Site 647 EOT section was sampled at the BCR, where 12 samples were taken. The entire interval was originally obtained through rotary drilling, and so care was taken to avoid sampling from areas that contained drilling slurry, and from the tops of cores. All samples were processed as described above for Site U1411. The detrital coarse fraction in this interval was similar to the Site U1411 EOT, in that the vast majority of grains were <200 μm, as well as the fact that there were not enough large grains per sample to analyse individual samples. In total, 53 large detrital grains were identified.

Site 913 EOT interval:

Five samples of unprocessed sediment were obtained from the EOT interval at Site 913; these were then processed as described for Site U1411. The samples processed for this study each contained a large number of coarse detrital grains, and so ~20-40 grains were picked per sample for analysis. As with the Site U1411 Plio-Pleistocene section, one sample was also dry-sieved at ½ϕ intervals and grains were picked out from each size fraction (Eq. 2.1).

Texture	Study					
	St John et al., 2015	**Tripati et al., 2008; Helland and Holmes 1997**	**Immonen 2013**	**Mahaney 1993; et al., 2001;**	**Dunhill 1998**	**Williams and Morgan 1993**
Size range (um)	>250	>125; 63-600	250-600	63-2000	180-300	>500
Roundness/ Angularity	6 step scale	2 step	3 step	Angular features; rounding	4 step	6 step
Relief	High/ Med/low	High/ Med/low	High/ Med/low	High/ Med/low	High/ Med/low	High/ Med/low
Breakage Blocks	P/A	Large; imbricated	-	-	Small/ large	Small/ large
Conchoidal fractures	P/A	Small/ Large	P/A	P/A	Small/ large	Small/ large
Straight step	P/A	P/A	P/A	P/A	P/A	P/A
Arcuate step	P/A	P/A	P/A	P/A	P/A	P/A
Isolated cusps/ v impact pits	P/A	P/A	P/A	P/A	-	P/A
Other Fractures	Isolated	Micro-fractures	Planes	Plates	Surface	Smooth
Striations	P/A	P/A	Scratches	-	-	Scratches
Grooves	P/A	Straight; curved	P/A	Straight; curved	Straight; curved	Straight; curved
Edge abrasion	-	P/A	P/A	Abrasion features	Abraded surfaces	P/A
Upturned plates	-	P/A	-	P/A	P/A	-
Silica dissolution	Absent-rare; Present; Common; Pervasive	Oriented	Etching	Dissolution etching	Irregular; pitted	Large solution pits; etching
Microlayering	P/A	-	Layered breakage	-	-	-
Silica precipitation	-	Limited/ Extensive	-	P/A	P/A	Amorphous precipitation
Adhering particles	-	P/A	-	P/A	-	P/A
Chemical v-shaped pits	-	P/A	P/A	-	V-shaped etching	P/A

Table 2.1: Common textures used in SEM analysis of quartz grains. Features in bold are mechanical, those in italics are chemical. P/A signifies texture was recorded as either present or absent in the relevant study.

Scanning Electron Microscope image capture:

The individual grains from each sample were mounted onto stubs and then sputter coated with a gold film prior to imaging. A Leo 1450VP Scanning Electron Microscope was then used to photograph each grain at NOCS. As stated above, nearly all previous studies have focused on quartz, so the attached light element PGT EDS detector was used to confirm the mineralogy of each grains (Krinsley and Doornkamp, 2011).

Interpretation of grain textures:

Images taken were examined for surface textures, roundness, and relief. The suite of surface textures used in this thesis represent an amalgamation of several bodies of work, to allow for easier comparison of the results with prior studies (Table 2.1, see Figures 2.2 and 2.3 for examples). Each texture was classed as being either mechanical or chemical in its weathering origin (See Supplementary Table A1 for descriptions of each texture). Mechanical textures relate to physical damage caused by grains being ground/smashed/split, whereas chemical textures are the result of dissolution and re-precipitation of silica when immersed in water (Krinsley and Doornkamp, 2011). For every grain analysed, each of the textures detailed below was recorded as being either present or absent. Nearly all grains featured at least some degree of silica dissolution, so the ranking scheme of St John et al. (2015) was applied: rare-absent (0-2% of grain's surface), present (2-25%), common (25-75%) or pervasive (>75%). The roundness of each grain was also visually graded using Power's roundness scale (Powers, 1953), a six-category scale featuring the following classes: very angular, angular, sub-angular, sub-rounded, rounded, and well rounded. The relief of each grain was classified as being low, medium, or high, and the maximum diameter of each grain was measured in μm.

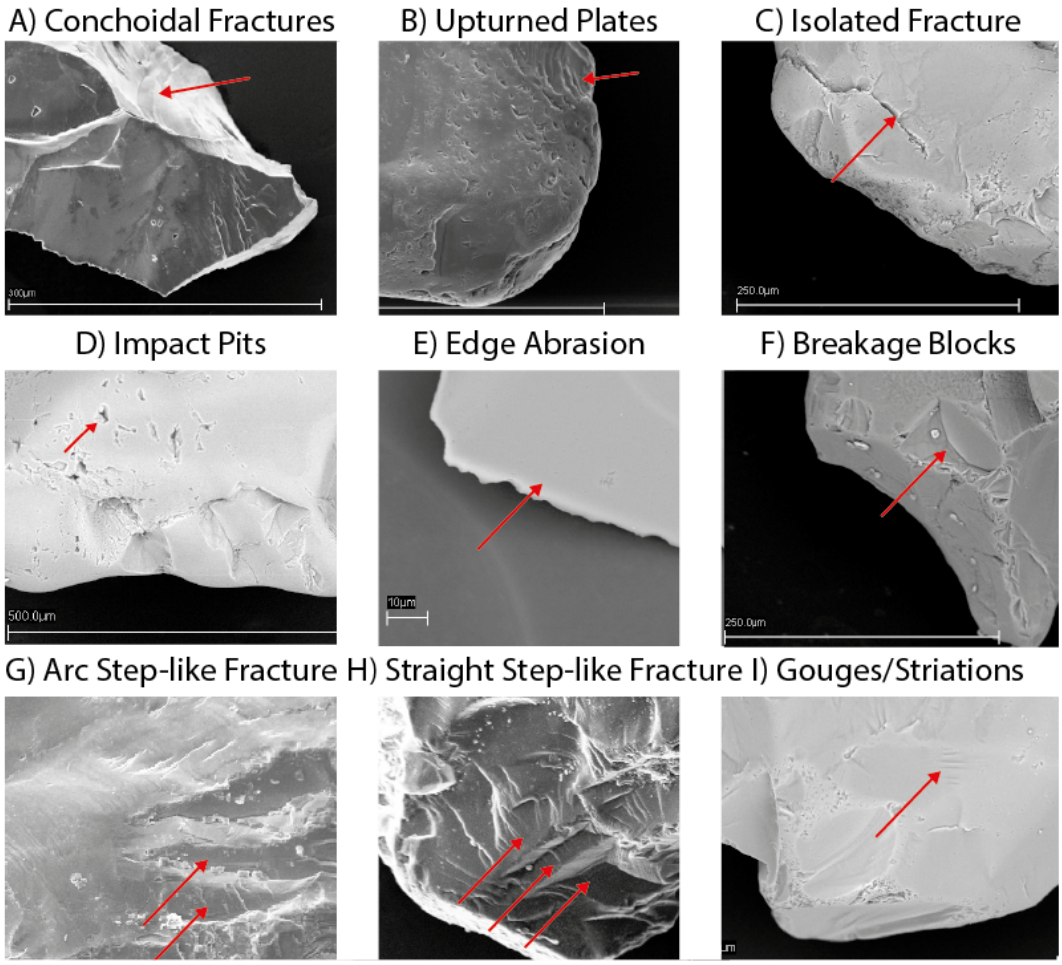

Figure 2.2: Mechanically formed quartz grain surface textures: a) conchoidal fracture; U1411 C6H4 50.5-52 cm, b) upturned plates; U1411 C6H4 26.5-28 cm, c) isolated fracture; U1411 B18H7 66.5-68 cm, d) impact pits; U1411 B15H3 50.5-52 cm, e) edge abrasion; U1411 B18H6 94.5-96 cm, f) breakage blocks; U1411 C8H2 106.5-108 cm, g) arc step-like fractures; U1411 C6H3 2.5-4 cm, h) straight step-like fractures; U1411 B15H1 98.5-100 cm, i) gouges/striations; U1411 C8H3 18.5-20 cm.

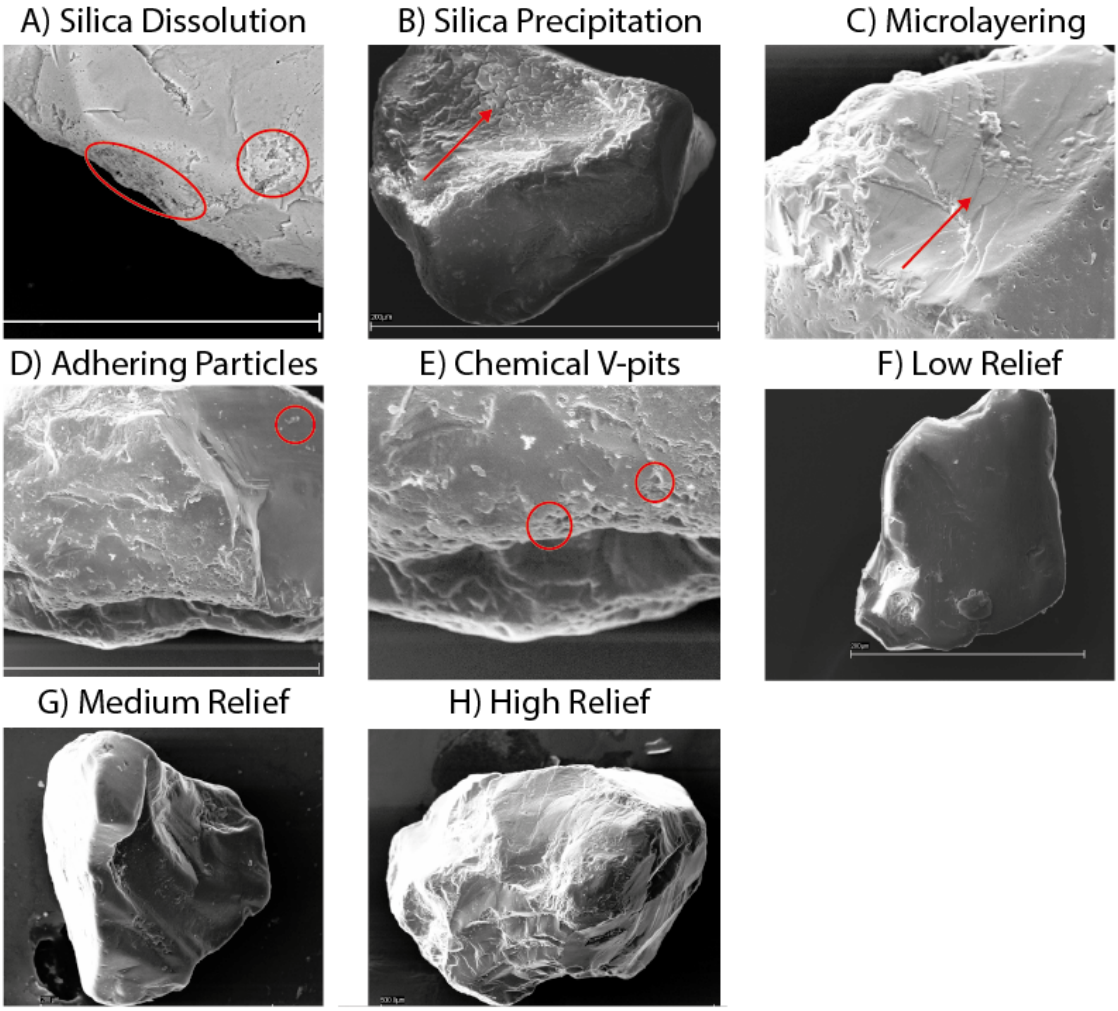

Figure 2.3: Chemically formed grain surface textures. For each image pair, the left image is from previous studies and the right is from this report: a) silica dissolution; U1411 B18H7 66.5-68 cm, b) silica precipitation; U1411 B20H4 50.5-52 cm, c) microlayering; U1411 C6H4 26.5-28 cm, d) adhering particles; U1411 C6H3 101.5-104 cm, e) chemical v-pits; U1411 C6H3 101.5-104 cm, f) low relief; U1411 B19H5 50.5-52 cm, g) medium relief; U1411 C6H7 70.5-72 cm, h) high relief; U1411 B15H1 98.5-100 cm.

Grain size comparisons:

As detailed above, one sample each from the Site U1411 Pleistocene and Site 913 EOT intervals were sampled at varying grain size intervals to explore how changes in grain size affect the expression of surface textures. The grains were binned into ½ ϕ intervals based on their maximum measured diameters. For each ϕ bin that contained >15 grains, the frequency that each surface texture featured on the grains within was calculated as a percentage.

Inter-site comparisons:

In total, 128 quartz grains were identified from the EOT sections of Sites U1411 and U1406, 166 from Site 913, 53 from Site 647, and 163 from the Plio-Pleistocene section of Site U1411. In keeping with the findings of the experiment into surface texture changes with grain size, and in keeping with previous studies, only grains from 200-600 μm were used to calculate the frequency of each texture within each site (Table 2.1).

Euclidean distances were calculated to determine how different each section was from the others, in a similar approach to a previously published inter-site grain surface comparison study (Mahaney et al., 2001). Euclidean distances were calculated using the following formula:

$$d_{ij} = \sqrt{\sum_{k=1}^{p} (X_{ik} - X_{jk})^2} \qquad (2.2)$$

Here the Euclidean distance between two sample-sets i and j is defined as d_{ij}. For a defined number of variables (in this case surface textures) given by p, the distance is calculated by summating the square of the difference in each variable between the two sample sets, $x_{ik} - x_{jk}$. It is important when calculating Euclidean distances that the variables are independent of each other (Shennan, 1988). This was not the case for the relief, silica dissolution, or roundness variables. Therefore, for the purposes of calculating Euclidean distances, each of these was treated as a single feature classed as being present or absent for each grain. An angular surface texture was considered to be 'present' for grains displaying sub-angular to very angular features, dissolution was considered to be 'present' for grains displaying common to pervasive silica dissolution, and high relief was marked as being 'present' for grains displaying high relief. For the Site 913 EOT interval and Site U1411 Pleistocene interval, Euclidean distances were also calculated between the samples within each interval, to provide a comparison to the inter-site calculations described above.

2.3 Results and discussion

2.3.1 Sedimentological differences between intervals

Site U1411 EOT interval:

Close inspection of the Site U1411 EOT core sections allowed elaboration on the shipboard descriptions of the compacted detrital clasts (Figure 2.4). Many of the clasts visible on core surface images are in fact large crushed foraminifera, which become increasingly common down-hole. Furthermore, the U1411 EOT interval features a large range of sizes and shapes of compacted detrital clasts, and the coarseness of the constituent grains of these clasts also varies. While there are no distinct silt/sand layers, many of the features are burrow-shaped, some are laterally extensive, and some occur in clusters (Figure 2.4).

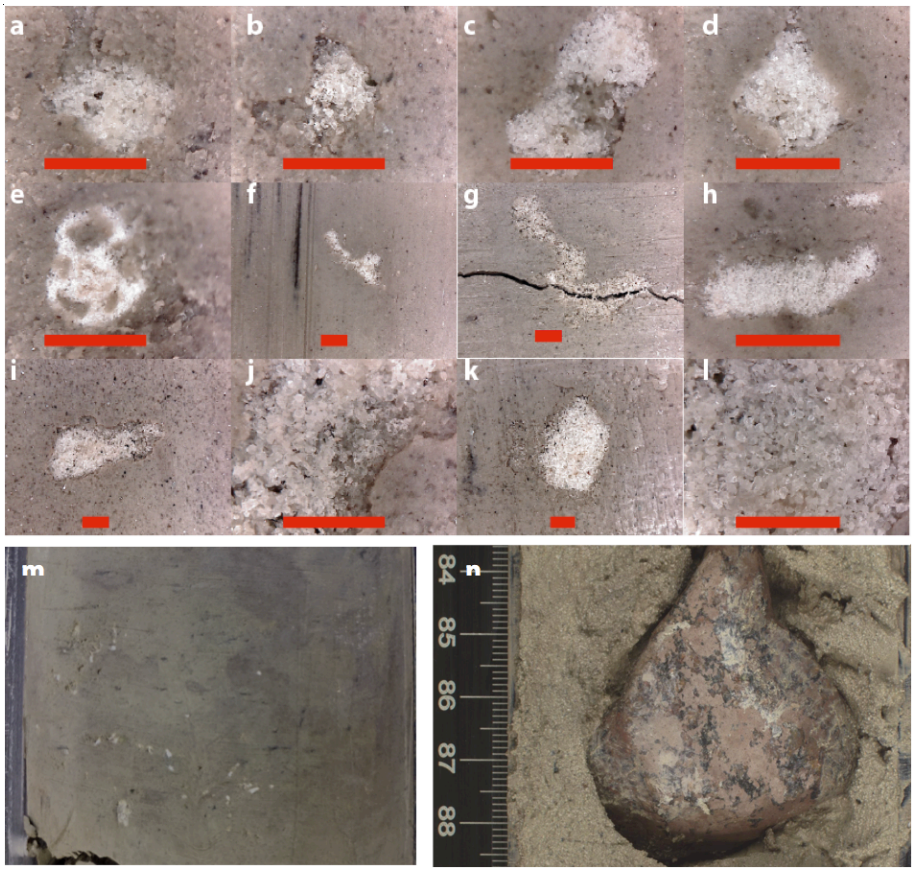

Figure 2.4: Core surface images of the Site U1411 EOT interval: a) B15H2 96.5 cm, b) B7H2 12 cm, c) B16H2 72.5 cm, d) C7H1 112.5 cm, e) B15H3 1 cm, f) B19H7 44 cm, g) B8H5 95 cm, h) B15H6 92 cm, i) B7H1 95 cm, k) B7H2 21.5 cm, m) B15H6 46 cm, n) B2H5 85 cm. Images j and l are magnified versions of i and k respectively; red scale bar is 1 mm in each image. Image m shows silty mud with bioturbation typical of the EOT interval (B15H6 46 cm); there is also a cluster of lithic clasts. Image n shows the coarse-grained, homogenised nature of the Pleistocene interval, featuring a large dropstone (B2H5 86 cm).

The EDS elemental maps (Figure 2.5) confirm that the vast majority of the compacted detrital clasts are composed of quartz grains. This is in contrast to the surrounding sediment, but in agreement with the shipboard determination of the detrital sand found disseminated in the sediments throughout the interval. Some feldspars are also apparent at relatively lower concentrations. While the background sediment contains abundant Ca (representative of calcium carbonate), this was rare inside the clasts. Their constituent grains are generally coarse silt to very fine sand, again in agreement with the shipboard description of the detrital sand.

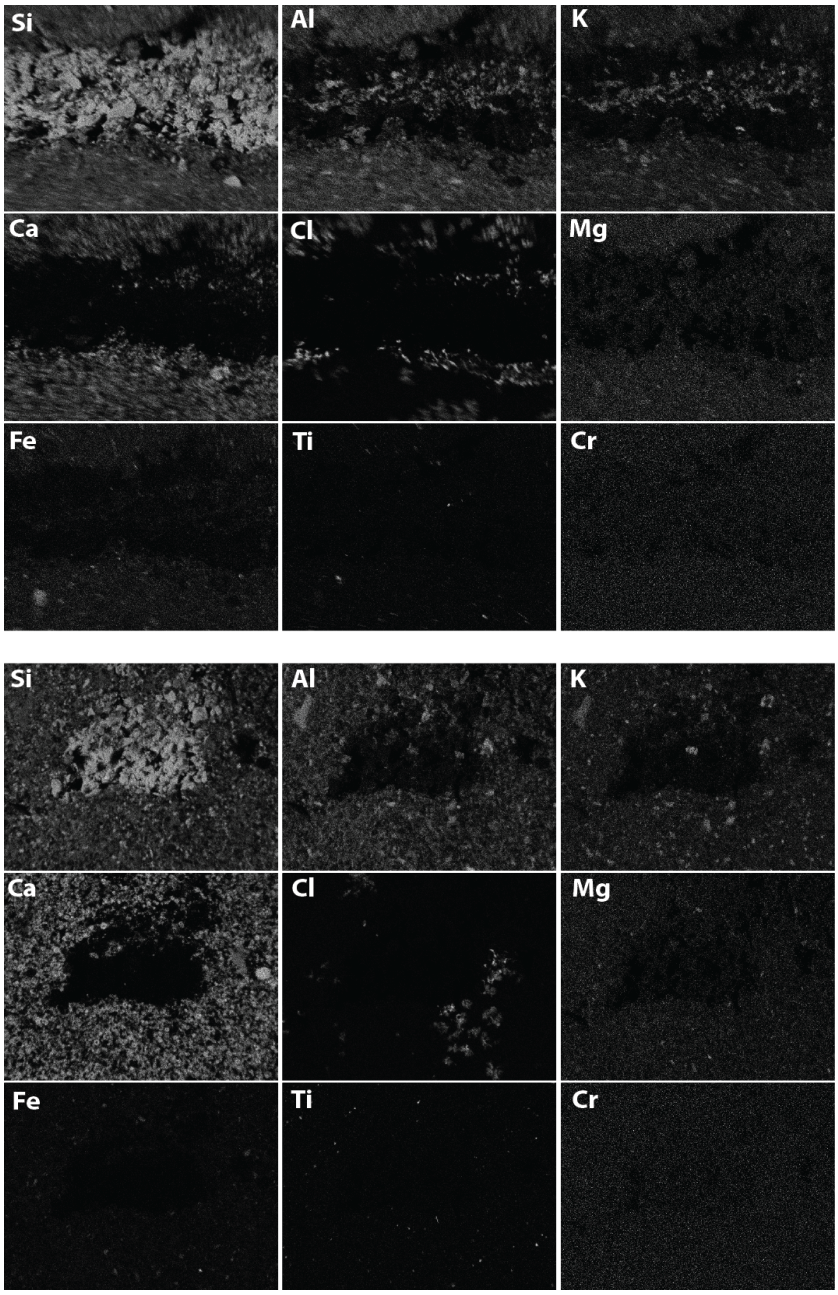

Figure 2.5: SEM elemental maps for two lithic clasts from the Site U1411 EOT interval: C10X3 124 cm (top) and B15H5 20 cm (bottom). White areas represent a stronger signal for the element in question. Field of view is 1mm wide.

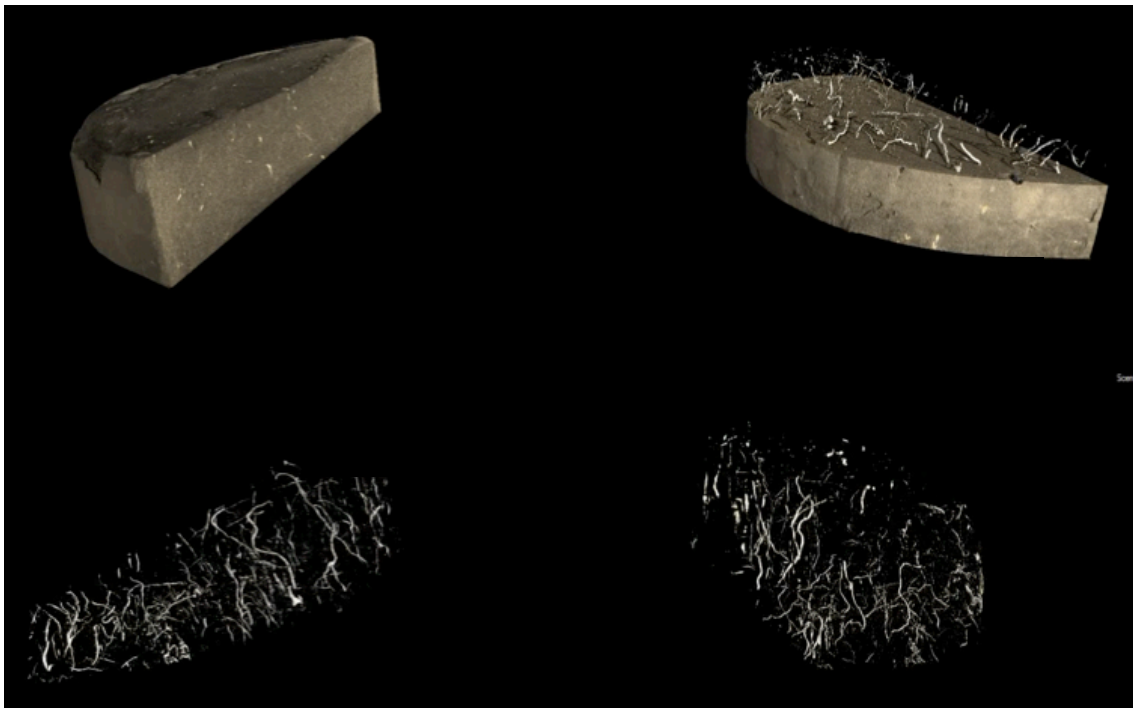

Figure 2.6: CT-Scan images of a discrete core section sample from Site U1411, B7H6 58-59.5 cm. Internal structure is revealed as background sediment is digitally removed. Diameter= 10 cm.

The CT study was able to identify internal structures within the discrete samples, because of their different density to the background clay. These structures consist of a network of sometimes inter-connected tubes running through the sample (Figure 2.6). The majority of these features are oriented vertically, and have a circular cross-section when crossing the core half surface. This finding indicates that what were initially identified as individual, ice-rafted siltstone clasts are in fact cross-cuttings of inter-connected burrows. Close inspection of the core surfaces also reveals some burrow-shaped features (Figure 2.4g). Though the core surfaces do appear bioturbated, these features occur frequently and regularly throughout the interval, rather than in pulses, as might be expected if they were the remnants of bioturbated silty-sand layers commonly seen in bi-gradational Stow sequences in contourite drifts (Stow and Faugères, 2008). There are, however, a few instances of higher-density areas of compacted detrital clasts (Figure 2.4m), and it is possible for contourites to contain meter-scale intervals of largely homogeneous mud facies (Gonthier et al., 1984). The sorted nature of the grains within the clasts (including the burrow shapes) could represent selective sorting or armouring of burrows on behalf of the organism responsible (Frey, 2012). The selective scavenging of these grains by burrowing organisms may also explain why these features occur frequently and

regularly throughout the interval, rather than in pulses, as might be expected if they were the remnants of bioturbated silty-sand layers.

Understanding that these features at Site U1411 are in fact post-depositional features is important; they range from mm-cm scale in size, and so, if transported to the study site intact, would have been too large to be transported there by anything but ice rafting. The shipboard party did find a single consolidated clast that reacted to acid by bubbling, signifying a carbonate cement (Norris et al., 2014). No other clasts with cement were observed during this study however, and no carbonate cement is evident from the SEM elemental maps. Overall the evidence presented here suggests that these features are post-depositional products of bioturbation, and not ice-rafted dropstones. The Pleistocene-age deposits from Site U1411, though similarly bioturbated, display a much coarser texture than the EOT interval. They also feature large (>5 cm) lithic clasts that, due to the isolated nature of the site's location, can only be explained as ice-rafted dropstones (Figure 2.4n) (Norris et al., 2014).

Site U1406 EOT interval:

The EOT section at Site U1406 shows a very different sedimentology to that of Site U1411 (Figure 2.4 & 2.7). The sedimentation rate is lower at U1406 (<1 cm/kyr), and the sediment is more carbonate-rich. It may be that the delivery of detrital material to this site was limited by its isolated position; the bottom current responsible for the drifts deposited on the SENR and JAR hits the bathymetric obstacle of the SENR before reaching the site (i.e., at Site U1411), where it appears much of the sediment is deposited first (Figure 2.1). As a result, the sediment is considerably paler than the dominant green/grey colouration seen throughout Site U1411 (Figure 2.7). Site U1406 lies deeper than Site U1411 (3799 vs. 3300 mbsl at present day, 3300 vs. 2580 mbsl at 50 Ma) and so it is unlikely that a shallowing Carbonate Compensation Depth (CCD) is responsible for the difference in carbonate content between the two sites (Norris et al., 2014). The degree of homogenisation (through bioturbation) is similar to U1411, with the exception of a few larger burrows. Very few compacted detrital clasts are visible at Site U1406; the few that are visible have relatively fine constituent grains.

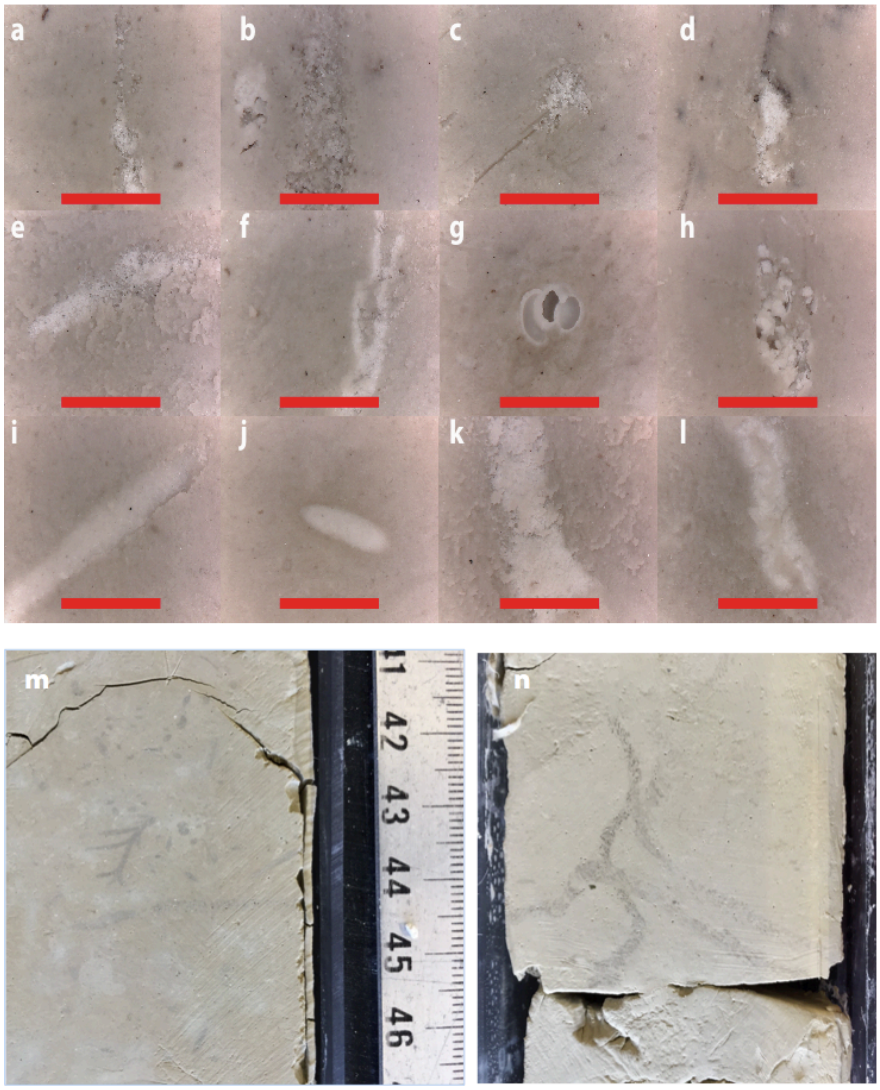

Figure 2.7: Core surface images Site U1406 EOT interval: a) A22H2 17 cm, b) A22H3 57.5 cm, c) C22H5 63.5 cm, d) A23H6 13.5 cm, e) A22H3 7.5 cm, f) A22H2 59 cm, g) C23H5 9 cm, h) A23H5 58 cm, i) B25H3 10cm, j) C23H5 58cm, k) A23H2 122cm, and l) C23H3 12 cm. Red scale bar = 1 mm. Images g and h appear to be fragments of foraminifera; i and j do not appear to have a granular texture. Images m and n (U1406B 25X 3, 41-47 cm and U1406B 24X 6, 127-133 cm) show carbonate-rich sediment with burrows.

Site 913 EOT interval:

The EOT interval at this site consists of clays with sections of interbedded silty clay layers, with intermittent bioturbation (Myhre et al., 1995). This sediment is much coarser than the drift sediments seen at the other sites discussed in this chapter, and features fine-scale laminations. The core sections from the EOT section at Site 913 interval display several large lithic clasts, including some composed of detrital grains (Figure 2.8). These grains are much coarser than those in the Exp. 342 sediments, and are more heterogeneous in composition (Figure 2.11). Some of the clasts at this site have deformed the lamina beneath them (Figure 2.8e-f), indicating that they dropped

onto the sediment surface from above. These are interpreted to be ice-rafted dropstones of loosely compacted sandstone, rather than post-depositional features.

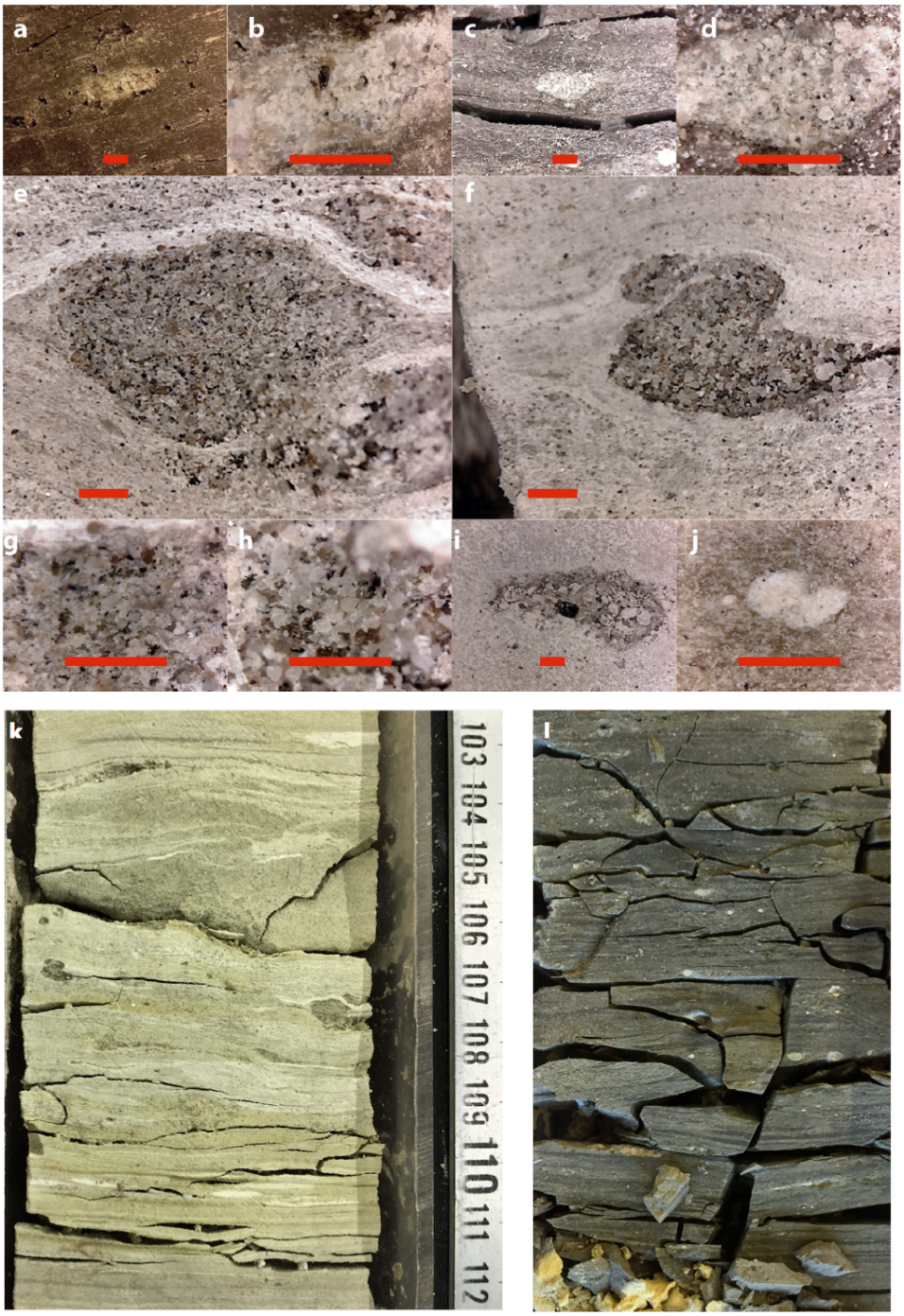

Figure 2.8: Core surface images from the Site 913 EOT interval, showing several lithic clasts, some of which have impacted the lamina below them: a) B23R1 9 cm, c) B27R5 125.5 cm, e) B27R1 108 cm, f) B27R1 107 cm, i) B27R2 35 cm, and j) B24R4 50 cm. Images b, d, g and h are magnified versions of images a, c, e and f respectively. Scale bar= 1 mm in all images. Image k (913B 27R 1, 102-112 cm) shows the fine-scaled lamina present in the interval; the clasts shown in images e and f are visible centre right and centre left respectively. Image l (913B 27R 5, 120-130 cm) also demonstrates the disturbed nature of much of the interval.

Site 647 EOT interval:

The EOT interval from Site 647 does not contain any observable clasts in the fashion of those seen in the Site U1411 or Site 913 EOT intervals. Several small (mm) white features were identified (Figure 2.9), but these do not have a grain-like texture or composition akin to those identified in the other sites, and are interpreted to be burrows filled in with diagenetic calcite (Scott et al., 1989). The core surfaces of the EOT section from Site 647 underwent significant disruption through rotary drilling, but extensive bioturbation is visible. Several intervals show fine laminae, but these are interpreted to be diagenetic features, rather than changes in lithology/grain size, (Scott et al., 1989). Overall there is no evidence of ice-rafting occurring across the EOT interval at this site. In the Pliocene sediments from this site, however, evidence of ice rafting is present in the form of large (>5 cm) lithic dropstones and detrital clasts similar to those seen at Site 913 (compare Figure 2.9i-j and Figure 2.11).

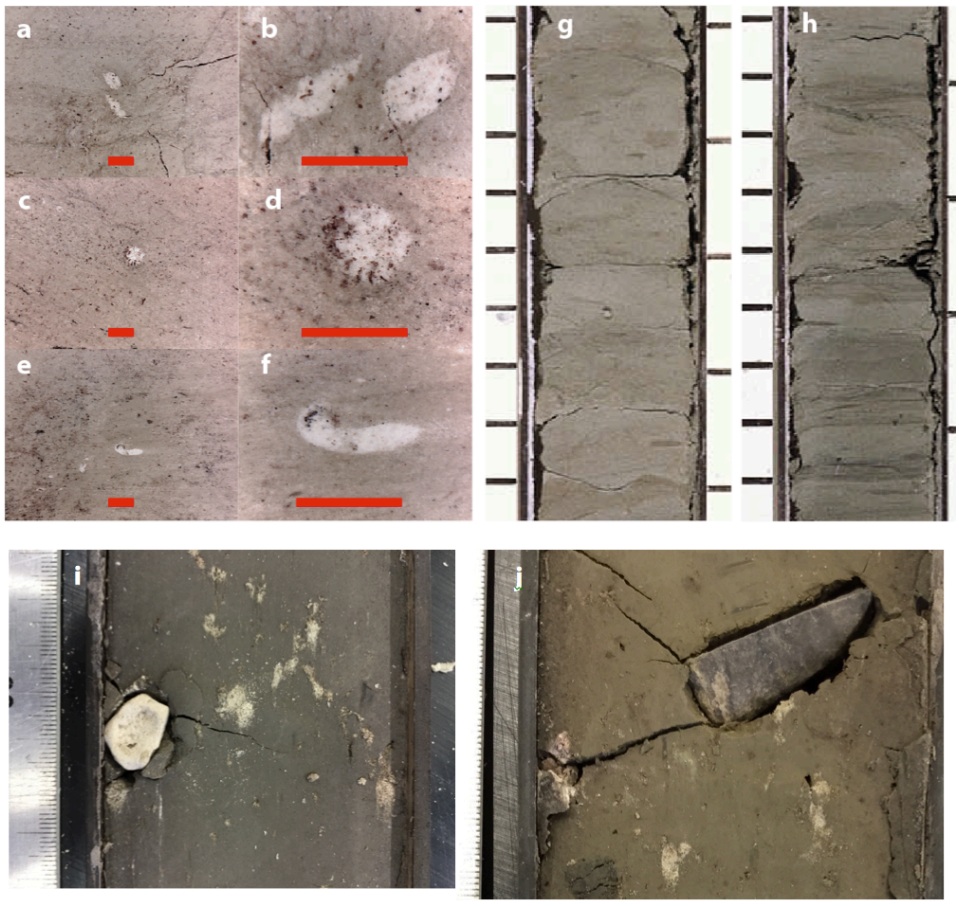

Figure 2.9: Core surface images of ODP Site 647 EOT interval: a) A31R2 69.5 cm, c) A30R2 114 cm, e) A30R1 124.5cm; images b, d, and f are magnified views of a, c, and e. Images g and h are from Core 32B Section 1, 60-80 cm and 110-130 cm respectively. Images i and j display core surfaces from the Pliocene interval of the same site (A10R4 18-24 cm and A10R3 38-43 cm respectively).

Low latitude drift deposits:

The three low-latitude sites studied (ODP Sites 1060 and 1061, and DSDP Site 515) display several features similar in appearance to those present at Site U1411, albeit at a much less common frequency. The core sections from Sites 1060 and 1061 display rare examples of isolated silt laminae, though these are not seen at Site 515 (Figure 2.10). The features from Site U1411 and the low latitude sites appear to be more closely related to each other than the Site 913 features; they are more visually homogeneous, finer-grained, and are smaller (generally <1 cm) than the clasts at Site 913, and do not appear above deformed laminae (Figure 2.11).

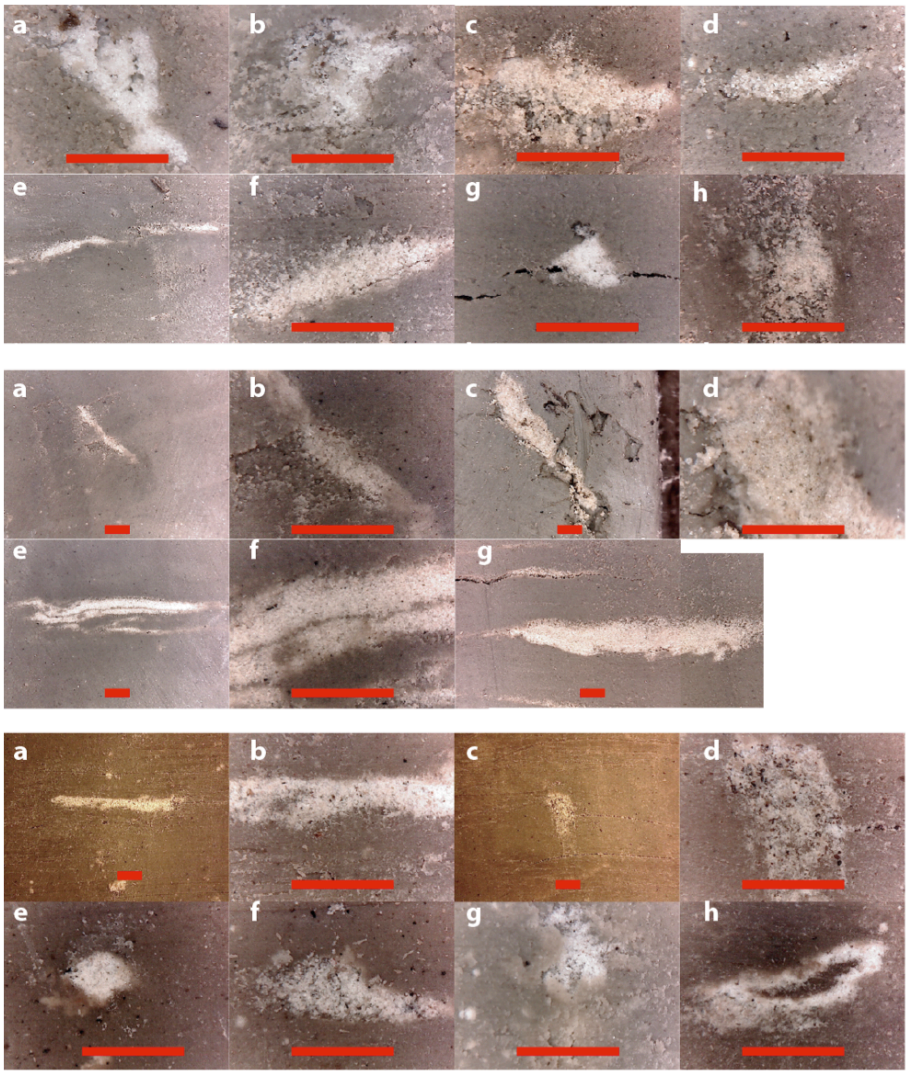

Figure 2.10: Images from low latitude drifts. Top: ODP Site 1060 a) B4H6 39 cm, b) A16H3 138 cm, c) B14H2 89 cm, d) A16H3 56 cm, e) A9H4 53 cm, g) C7H2 64.5 cm, h) B14H2 88 cm. Middle: ODP Site 1061 a) A30H4 23.5 cm, c) A19H5 19.5 cm, e) A30H4 24.5 cm, g) A13H4 47 cm. Bottom: DSDP Site 515 a) A10H3 46 cm, c) B6H7 25 cm, e) A10H3 69.5 cm, f) A10H3 40 cm, B14H2 92.5 cm, and A10H3 73 cm. For the top panel, image f is a magnified view of the previous image, as are images b, d, and f in the middle panel and images b and d in the bottom panel. The scale bar= 1 mm in each image.

Summary:

The Site 913 EOT section displays preserved fine-scale lamina in sandy sediment, visible changes in grain size, and multiple lithic clasts that deform underlying laminae (dropstones). The Site U1411 EOT section, in contrast, is a largely homogeneous drift deposit of clayey-silt and silty-clay, which features no laminae. Compacted lithic clasts composed of silt are present through the interval, but these appear to be more fine-grained and homogeneous than similar features identified at Site 913, and are interpreted to be related to bioturbation. Site U1406 is similarly fine-grained and bioturbated, but with a higher carbonate content. The Site 647 EOT interval displays a similar lithology and features a similar sedimentation rate to Site U1411, albeit it is less well preserved. There is frequent evidence of bioturbation through the interval, but no detrital clasts similar to those seen at Site U1411 or Site 913 are visible. The Site 913 cores are the only EOT-age sediments that appear to show evidence of ice rafting, with ice rafting only becoming apparent in the Site 647 and Exp. 342 cores in the Pliocene and Pleistocene.

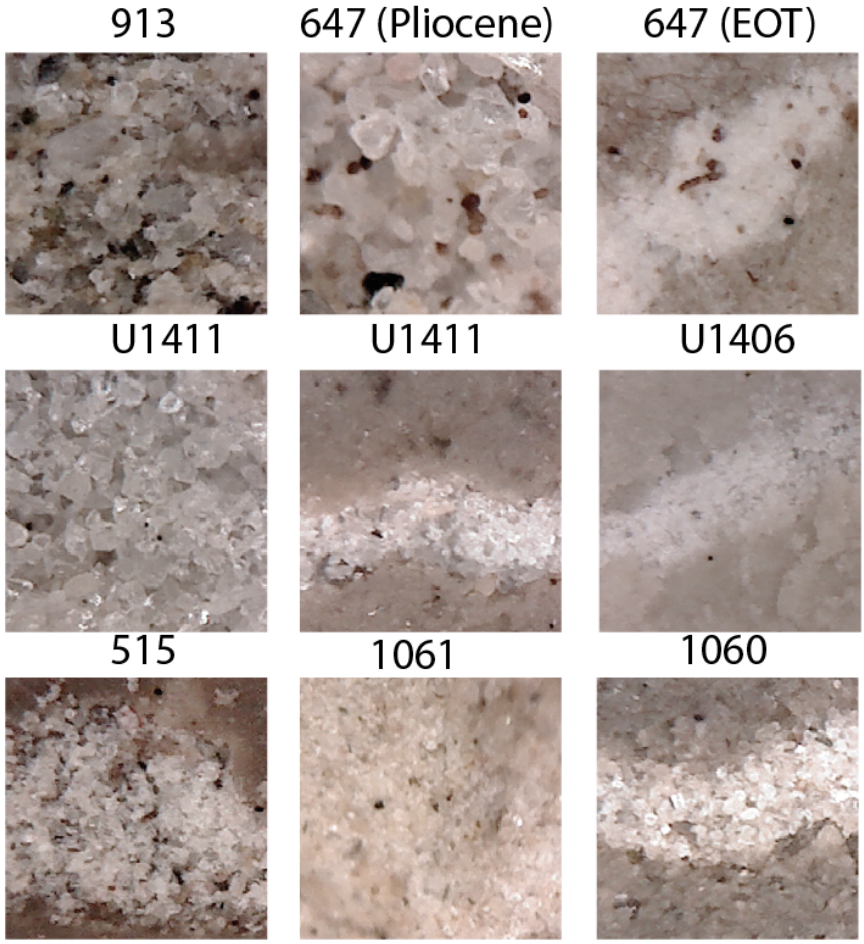

Figure 2.11: Comparison of constituent grain sizes of blebs from high latitudes (top), Expedition 342 (middle) and low latitude drift sites (bottom). Each square image is 1x1 mm: a) 913 B23R1 91 cm, b) 647 B10R1 113 cm, c) 647 A31R2 69.5 cm, d) U1411 B7H2 21.5 cm, e) U1411 B15H6 134 cm, f) U1406 A22H2 74 cm, g) 515 B6H7 25 cm, h) 1061 A19H5 19.5 cm, and 1060 A16H3 56 cm.

Interpretation of the Site U1411 compacted detrital 'clasts':

These features were revealed through detailed core surface and CT analysis to be products of bioturbation, rather than ice-rafted dropstones. It is often possible when studying evidence of bioturbation to identify trace fossils, which can then be grouped into ichnofacies related to certain depositional environments (Frey, 2012). Though most trace fossil analysis has focused on shallow marine environments, rather than the deep marine sediment cores, analysis of deep-water contourites has shown that the oxygenation and sediment supply afforded by deep water currents can allow for the formation of trace fossil assemblages more commonly seen in much shallower environments (Thistle et al., 1991; Wetzel and Uchman, 2012). The Site U1406 EOT interval analysed in this chapter, for example, shows evidence of *Chondrites*, a network of branched tunnels that slope downwards (Figure 2.7m), and *Zoophycos*, a

sub-horizontal burrow formed of successive concave laminae (Figure 2.7n) (Frey, 2012; Rodríguez-Tovar and Dorador, 2014; Uchman and Wetzel, 2011).

The Site U1411 loosely compacted lithic clasts display a wide range of different morphologies, and so are difficult to define as any one trace fossil. The burrows they form range from vertical to sub-horizontal, undulate, and sometimes display branching. Some of these branched burrows may be *Chondrites* (Figure 2.6), but others (e.g. Figure 2.4g) are perhaps more likely to *Trypanites*, the burrows of organisms such as polychaete worms, though these are usually associated with hardgrounds (Frey, 2012; Thistle et al., 1991). The mass of lithic clasts in Figure 2.4m may be *Thalassinoides* — a complex mass of interconnecting vertical and horizontal burrows (Uchman and Wetzel, 2011; Wetzel and Uchman, 2012).

2.3.2 Does the mineralogy and provenance of detrital grains from each EOT interval suggest a single, expansive source?

Light microscope analysis of the samples from Site 913 confirmed the abundance of quartz (dominant), mica, and feldspars, as well as the presence of lithic clasts (Table 2.2), in agreement with previous studies (Eldrett et al., 2007; Tripati et al., 2008). The lithic clasts (some of which are macroscopic) include gneiss, quartz, and basalt. The coarse detrital fraction also has a diverse heavy mineral component (Tripati et al., 2008). Sites U1411 and U1406 were also dominated by quartz, with mica and feldspars also present (Table 2.2). There is no discernible difference in mineralogy between these two sites. In contrast to Site 913, neither site features lithic clasts. Light microscope inspection of the Site 647 samples confirm that they are also dominated by quartz, with some calcite grains (inferred shipboard to be authigenic) also present (Scott et al., 1989). Pyrite is also abundant in every sample (Table 2.2). Rare volcanic clasts are also present.

Major minerals /lithic clasts	EOT interval			
	Site 913	**Site 647**	**Site U1411**	**Site U1406**
Quartz	Abundant	Abundant	Abundant	Abundant
Feldspar	Present	Present	Present	Present
Mica	Present	Rare-absent	Present	Present
Pyrite*	Rare-absent	Present	Present	Present
Volcanic clasts	Present	Present	Rare-absent	Rare-absent
Granite clasts	Present	Rare-absent	Rare-absent	Rare-absent
Gneiss clasts	Present	Rare-absent	Rare-absent	Rare-absent
Schist clasts	Present	Rare-absent	Rare-absent	Rare-absent
Macroscopic Dropstones	Present	Absent	Absent	Absent
Calcite*	Rare-absent	Present	Rare-absent	Rare-absent

Table 2.2: Mineralogy of detrital sand fractions from EOT-age intervals from the North Atlantic. *Inferred to be authigenic.

QEMSCAN analysis of the Site U1411 detrital fraction demonstrates that quartz is the dominant mineralogy throughout the interval (45-65%, Figure 2.12). Feldspars make up another ~15% of the detrital fraction, and mica is also present (5-10%). It appears that some clay minerals (chlorite, smectite, illite, kaolinite, etc.) survived the washing and sieving process. Pyrite (1-5%) and glauconite (<1%) are the main authigenic minerals. Garnet, amphibole, rutile/anatase, and tourmaline are the most abundant heavy minerals identified, in contrast with the Site 913 EOT interval, where chloritoid and epidote are the most abundant (Tripati et al., 2008).

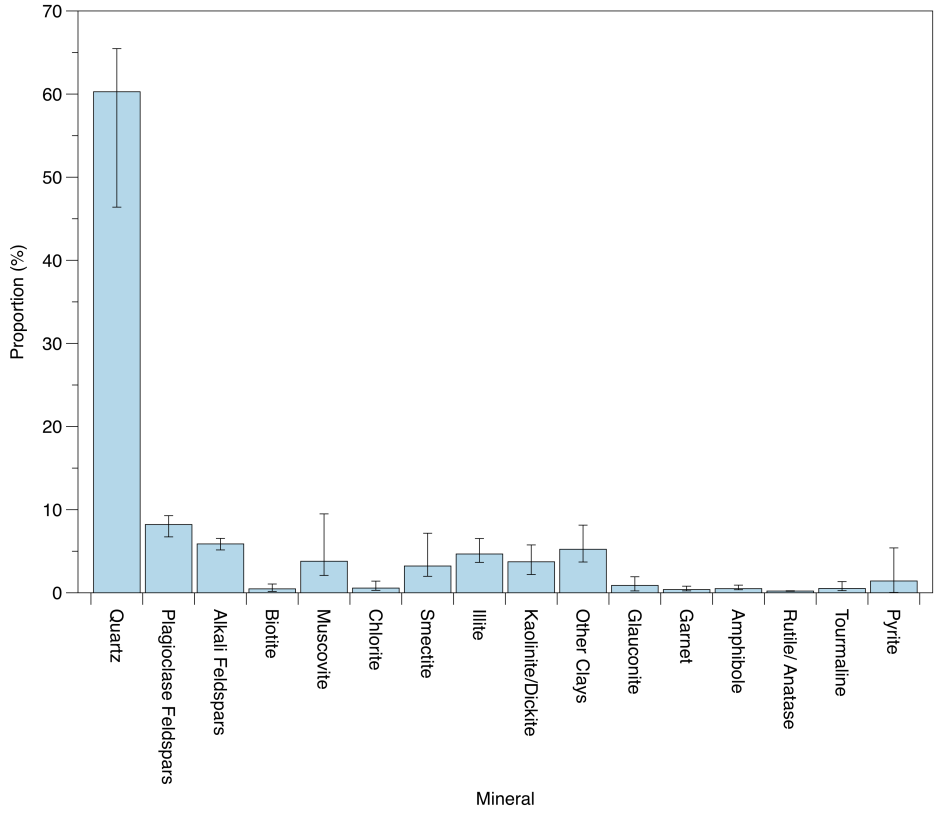

Figure 2.12: QEMSCAN analysis showing in major mineral components of the detrital fraction from the Site U1411 EOT interval (see Appendix B for data).

The Pb isotopic analysis of feldspars from Sites U1411 and U1406 (Figure 2.13) confirms that the coarse detrital fraction from two sites shares the same source. There is no obvious separation between the Late Eocene, EOT, or Early Oligocene samples, suggesting there was no significant change in the source of these detrital feldspars across the interval. Unfortunately, the scarcity of the coarse detrital grains present in the Site 647 EOT interval, combined with the large proportion of the interval's core sections that had been either already sampled or potentially contaminated during drilling, meant that it was not possible to analyse the provenance of feldspars from this site.

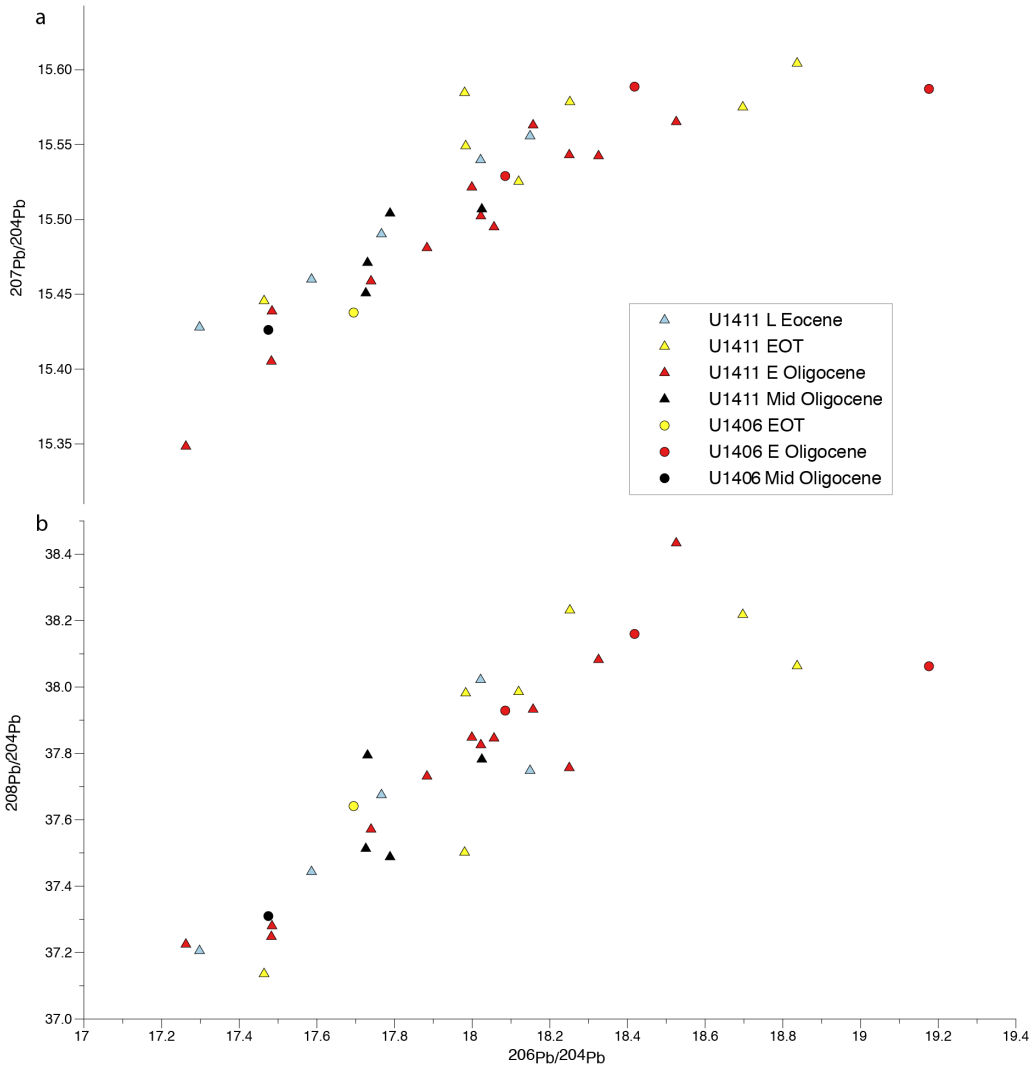

Figure 2.13: Pb isotope data from feldspars of Sites U1411 and U1406, grouped into Late Eocene, EOT, Early Oligocene and Mid-Oligocene intervals (see Appendix B for data).

When compared against published data from the North Atlantic terranes, the Expedition 342 data have little overlap with the Greenland provinces (solid lines on Figure 2.14), whereas they appear to convincingly match the local North American provinces (filled shapes), specifically a combination of the Appalachian and Grenville provinces (Figure 2.1). The Exp. 342 data also overlap with sections of the Scandinavian and British/Irish provinces (dashed lines), but given the proximity of the site to Grenville and Appalachian source material, these seem the more likely sources (see Appendix B for references). There is overlap between the Greenland Caledonides (for Caledonian fold belt, see Figure 2.1) and the Exp. 342 samples, which is perhaps unsurprising as these rocks are of a similar age to those of the Appalachian province (Bailey et al., 2012). As discussed above, however, the dominant source for the Site 913 IRD is interpreted to be Paleogene-age East Greenland basalts, potentially with a Palaeozoic component (Bernard et al., 2016; Eldrett et al., 2007;

Tripati et al., 2008). Fission-track data for the area also implies the glacial erosion of these basalts across the EOT (at the time they had a greater extent than at present) proximal to the coastline (Bernard et al., 2016). Feldspars analysed from Denmark Strait (DS) sediments by White et al (2016) come from the same interpreted source areas as Site 913, and show a clear difference to the Exp. 342 samples; the relatively negative DS samples (e.g. $^{206}Pb/^{204}Pb$ ratios of 12-14 vs. 17-19 for Exp. 342) represent the Paleogene basalts, and lie separate from the Exp. 342 samples (Figure 2.14).

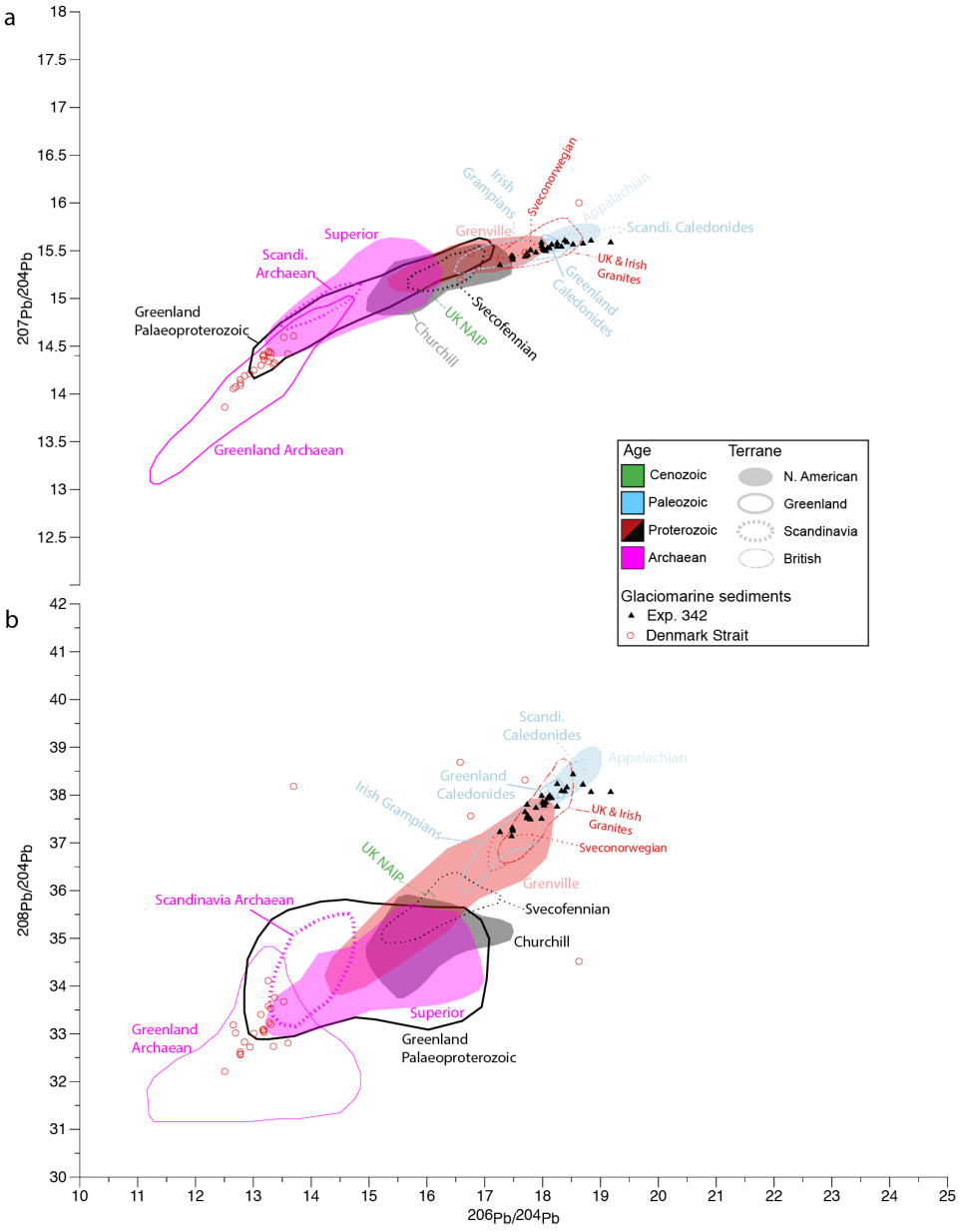

Figure 2.14: Pb isotope data from Expedition 342 feldspars (triangles), overlain on feldspar-derived terrane data from the major North Atlantic provinces displayed in Figure 2.1 (see Appendix B for references). Feldspar derived Pb isotope data from sediments representing the interpreted sources of the Site 913 EOT-age detrital fraction is also shown (open circles) (White et al., 2016).

The differences in mineralogy and provenance between the EOT intervals of Sites U1411 and U1406 versus Site 913 suggests that they do not represent an extension of ice rafting from of a hypothetical Greenland ice cap into the North Atlantic, with a local North American source for the Exp. 342 coarse detrital fraction appearing more likely. Though less material was available to analyse, the Site 647 coarse detrital fraction from the EOT also appears to be distinct from Site 913, based on the scarcity of lithic clasts in the former (Table 2.2). These findings are in keeping with the sedimentological nature of the cores from each interval (Section 2.3.1).

2.3.3 Does the surface texture analysis of quartz grains show sensitivity to changes in grain size?

In total, there were five bins for the samples from the Site U1411 Pleistocene interval, ranging from 2.5-2 to 0.5-0 ϕ, and five bins for Site 913 ranging from 3-2.5 to 1-0.5 ϕ.

Relief:

The Site 913 grains show no definitive trend with increasing grain size, with 80-90% of the grains having *medium* or *high* relief for all grain size bins (Figure 2.15a). The Site U1411 grains with *low* relief increase by ~20% from the 2.5-2 ϕ bin to 0.5-0 ϕ. The proportion of *high* relief grains fluctuates, but overall also increases by ~10%, with *medium* relief grains decreasing in frequency (Figure 2.15b).

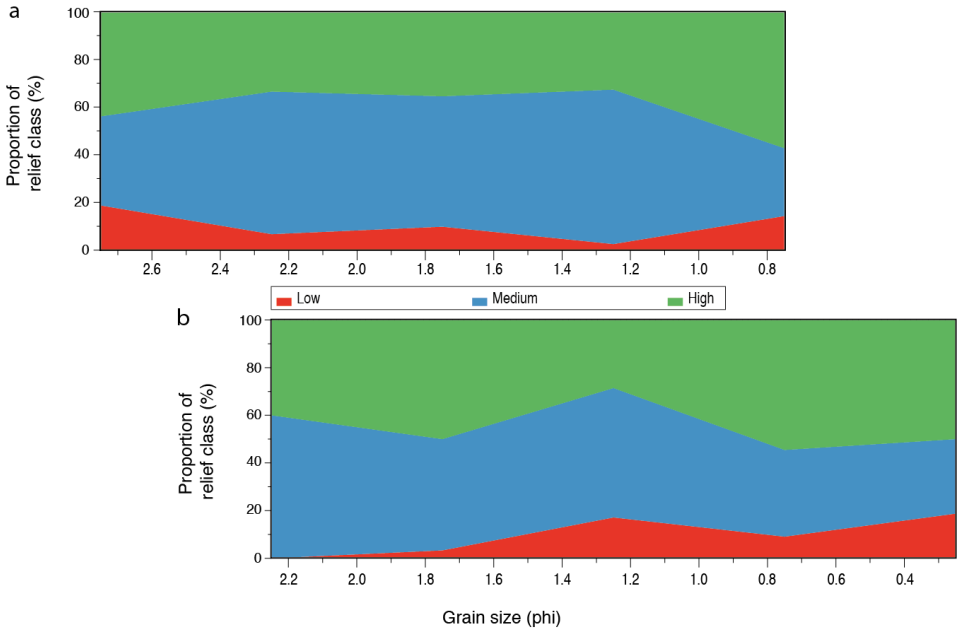

Figure 2.15: Sensitivity of grain relief classes to changes in grain size from a) ODP Site 913 EOT interval, and b) IODP Site U1411 Pleistocene interval (see Appendix A.2 for data).

Dissolution:

The degree of silica dissolution on the Site 913 grains increases with increasing grain size; this is mostly accountable to a decrease in the percentage of grains with *absent-rare* dissolution from ~45% to 10% and an increase in the percentage of grains with *common* dissolution from ~7% to ~50% (Figure 2.16a). There is, however, no immediately obvious trend in the dissolution classes of the Site U1411 grains (Figure 2.16b).

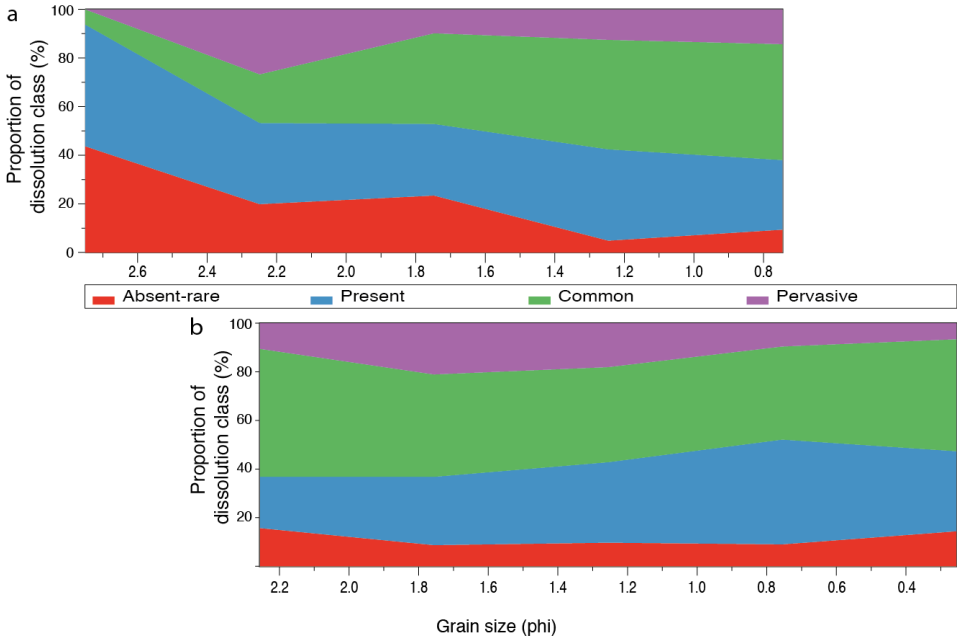

Figure 2.16 Sensitivity of silica dissolution classes to changes in grain size from a) ODP Site 913 EOT interval, and b) IODP Site U1411 Pleistocene interval (see Appendix A.2 for data).

Roundness:

The Site 913 grains increase in roundness with increasing grain size. *Very angular* and *angular* grains decrease from 100% of the 3-2.5 ϕ bin to ~50% of the 1-0.5 ϕ bin, with the greatest decrease being in *angular* grains. The remaining classes all show overall increases with increasing grain size (Figure 2.17). The Site U1411 Pleistocene grains also become more rounded with increasing grain size. *Well-rounded* and *rounded* grains, which are both absent in the smallest grain size bin (2.5-2 ϕ), both increase to ~10%, whereas *very angular* grains decrease from ~30% to being absent in the coarsest grain size bin (Figure 2.17).

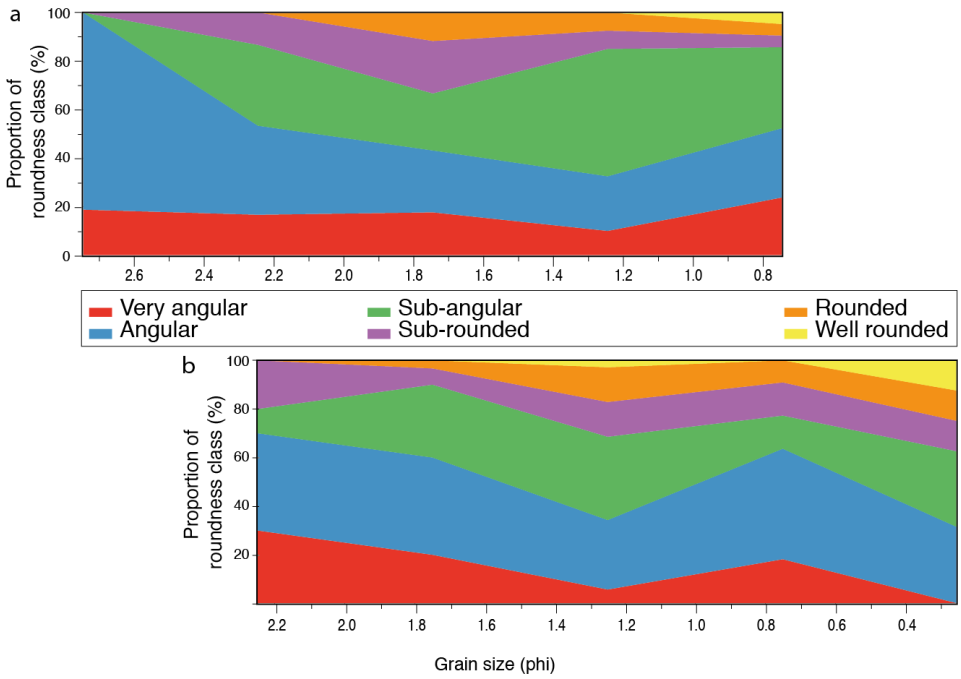

Figure 2.17: Sensitivity of roundness classes to changes in grain size from a) ODP Site 913 EOT interval, and b) IODP Site U1411 Pleistocene interval (see Appendix A.2 for data).

Surface Textures:

The majority of the surface textures identified in the Site 913 grains increase in frequency with increasing grain size (Figure 2.18). Most mechanical surface textures (solid black lines) show slight increases in frequency with increasing grain size (total increase of ~10-20% across all grain size bins), with the exception of *mechanical impact pits* (large ~50% increase), *conchoidal fractures* (very little change), and *edge abrasion* (~25% decrease). There is no unifying trend across the mechanical surface textures analysed in the Site U1411 grains, however (Figure 2.18, solid red lines), though *mechanical impact pits* and *straight step-like fractures* increase by ~50% and 20% respectively, in agreement with the trends from Site 913. *Edge abrasion* is the only texture that becomes less frequent with increasing grain size in both samples. This may reflect that, as larger grains become more rounded, edges get worn away to the point that the texture is no longer visible. The five chemical surface textures (dashed black lines) identified on the Site 913 grains recorded overall increases in frequency with increasing grain size (Figure 2.18). Of these, *microlayering* showed the lowest overall change (<5%; this feature was observed only at low frequencies across all grain size bins). The chemical surface textures of the Site U1411 grains show a similar trend to Site 913, with four of the five textures showing increasing frequency with relation to grain size (dashed red lines, Figure 2.18). *Silica dissolution* however

shows a decrease of ~5%. Chemical surface textures may be more prevalent on larger grains purely because of their larger surface area.

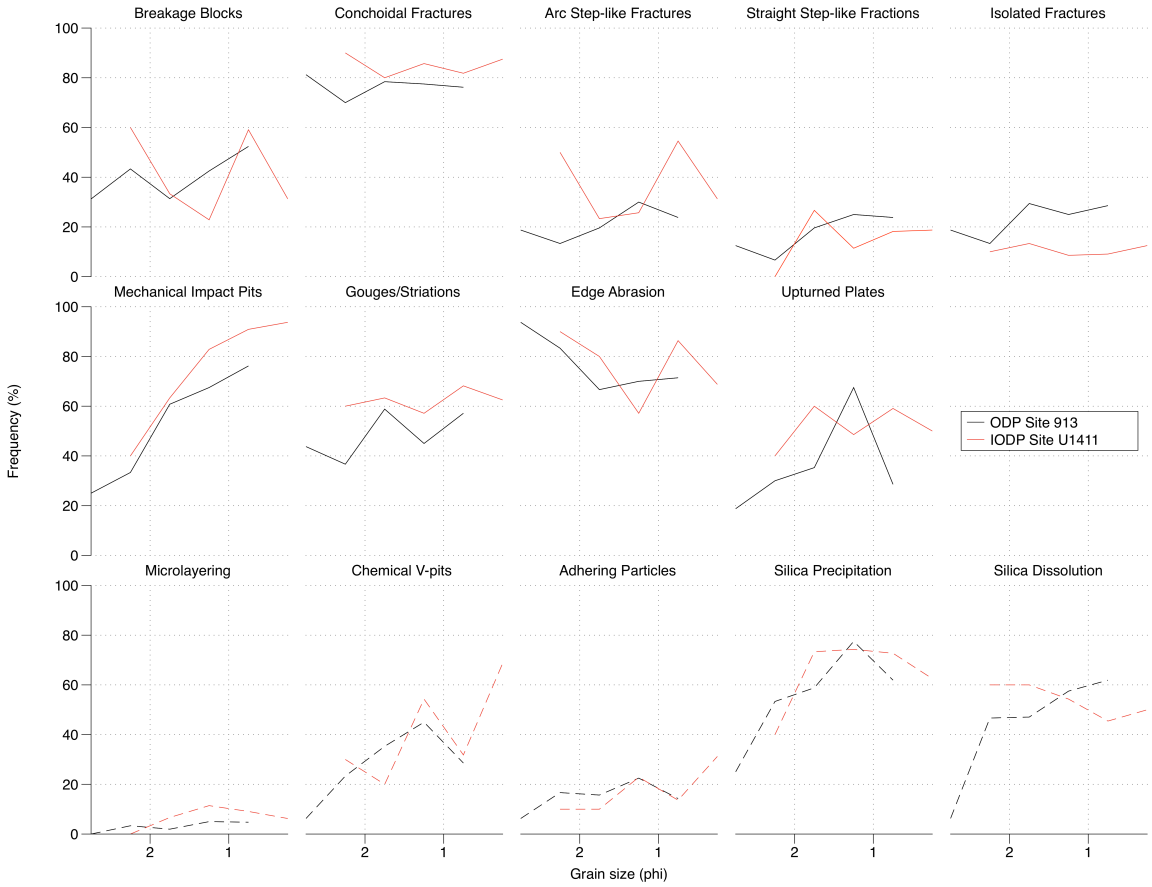

Figure 2.18: Sensitivity of mechanical (solid lines) and chemical (dashed lines) surface textures in grains from ODP Site 913 EOT interval (black lines) and IODP Site U1411 Pleistocene interval (red lines)(see Appendix A.2 for data).

Summary:

The relationships between surface textures and grain size are important, particularly as there is no universally accepted size range for quartz grain surface textural analysis in previously published literature. The results here emphasise a need for caution when comparing quartz surface texture analyses from different studies, if the size fractions in each are not consistent. Krinsley and Doornkamp (2011) suggest that quartz grains larger than 200 μm (2.32 ϕ) display surface textures in a different way to smaller grains (smaller grains are dominated by flat cleavage planes); their interpretation is borne out by the results of this chapter, particularly in terms of roundness and chemical surface textures. As such, 200 μm was used as the lower limit for the inter-site grain comparisons in this chapter. 600 μm was used as the upper limit, as featured in previous studies (Table 2.1).

2.3.4 What was the transport mechanism for the detrital sand from each interval?

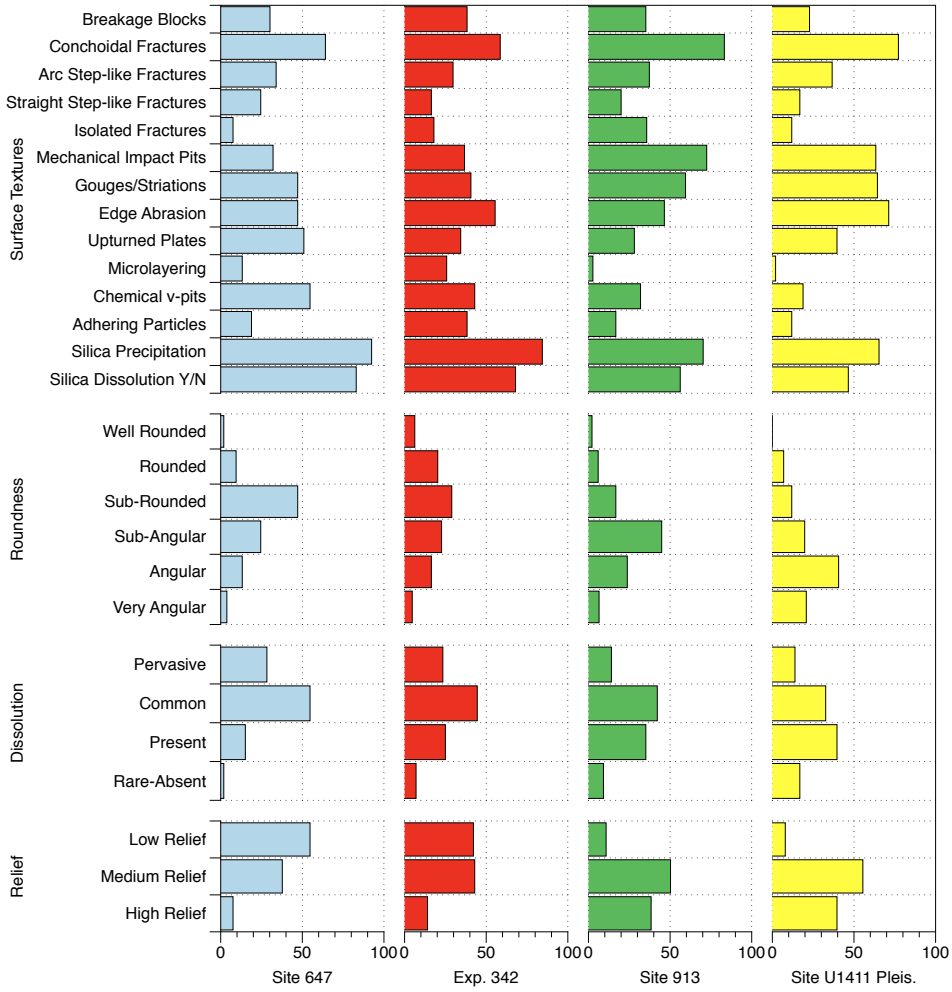

Figure 2.19: Frequency (%) of surface textures, roundness, dissolution and relief classes in quartz grains analysed from the four target intervals (see Appendix A.2 for data).

The proportions of mechanical and chemical textures from the Exp. 342 and Site 647 EOT intervals are very similar in shape, as are the Site 913 EOT and Site U1411 Pleistocene intervals (Figure 2.19). Qualitatively, the comparisons between Exp. 342 and Site 647 (Figure 2.20a iv), and between Site 913 and Site U1411 Pleistocene (Figure 2.20a i) show relatively little difference. In contrast, the majority of the mechanical textures analysed are more common in the U1411 Pleistocene and 913 EOT sections than the EOT sections from Exp. 342 and Site 647 (with the reverse being true for chemical textures, Figure 2.20a ii, iii). In each of these four comparisons (Figure 2.20a ii, iii, iv & v), *mechanical impact pits* show the greatest difference (30-40%), being most common in the 913 EOT and U1411 Pleistocene sections.

Conchoidal fractures, *arc step-like fractures*, and *gouges/striations* are also more common in the 913 EOT and U1411 Pleistocene sections than the Exp. 342 and Site 647 EOT sections.

The Exp. 342 and Site 647 EOT grains display a normal distribution of roundness classes, with *sub-rounded* grains being the most common class (Figure 2.19). They also both show profiles skewed towards higher levels of silica dissolution; for Site 647 in particular, more than half of the grains feature *common* dissolution. Both sections have high proportions of *low* and *medium* relief grains (~40-50%), and relatively few (<15%) *high* relief grains.

The Site 913 EOT and U1411 Pleistocene grains, in comparison, are skewed towards more angular grains (Figure 2.19), showing higher proportions of *sub-rounded* to *well-rounded* grains, and lower proportions of *sub-angular* to *very angular* grains (Figure 2.20b: ii, iii, iv & v). The grains from these two sections show an even distribution of silica dissolution classes. There is relatively little difference in silica dissolution between Site 913 EOT and Site U1411 Pleistocene sections (1-10%, Figure 2.20c: i & vi). Here however, the Exp. 342 and Site 913 EOT sections are also very similar (1-10% difference, Figure 2.20c: v). The Site 913 EOT and U1411 Pleistocene grains show lower proportions of *rare-absent* and *present* dissolution, and higher proportions of *common* and *pervasive* dissolution than the Exp. 342 and Site 647 EOT grains (Figure 2.20c: ii, iii, iv & v). In other words, silica dissolution is most common in the Exp. 342 and Site 647 intervals. The Site 913 EOT interval and Site U1411 Pleistocene interval have higher proportions of *high* relief grains (35-40%), and a much lower proportion (~10%) of low relief grains than the previous two intervals (Figure 2.19, Figure 2.20d).

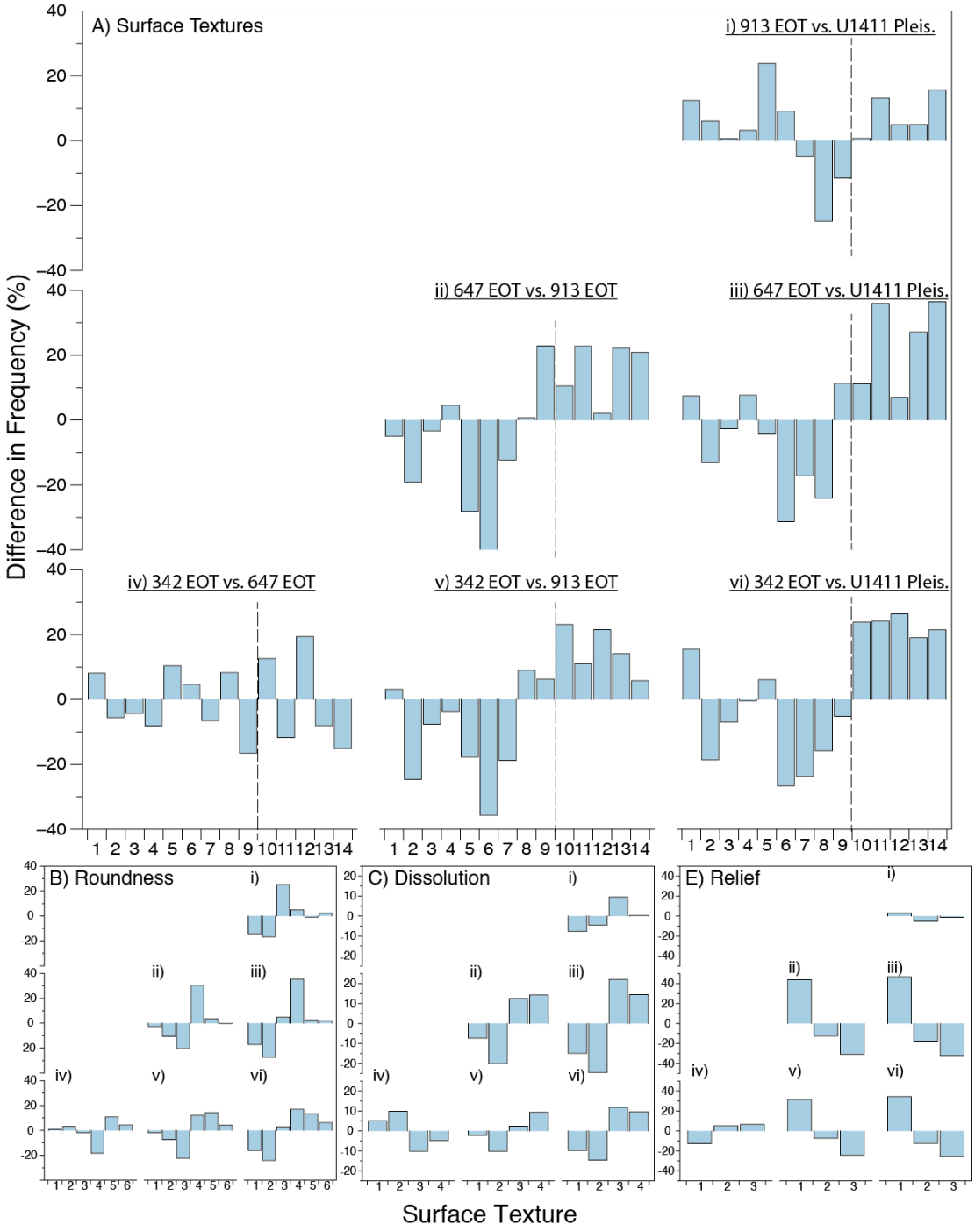

Figure 2.20: Differences in abundance of each texture between the four study intervals. a) surface textures (dashed line separates mechanical vs. chemical textures), b) roundness, c) degree of dissolution, and d) relief. In each instance numbers along x axes refer to the order that each texture is displayed in figure 2.19.

It is clear that the grain textures analysed at the Site 913 EOT and U1411 Pleistocene intervals are very similar. The grains from these intervals both resemble iceberg-rafted debris; they show high angularity, and high frequencies of mechanical surface textures. This is indicative of relatively fresh grains that have been formed in a mechanical environment (i.e. glacial crushing), and have then been transported

without undergoing significant saltation (i.e., on top of icebergs rather than in a river or ocean current) (Krinsley and Donahue, 1968; Mahaney, 1995; Mahaney et al., 2001). They display high-medium relief, and feature less extensive silica dissolution than grains from the Exp. 342 and Site 647 EOT intervals, which again may reflect less time spent in subaqueous settings conducive to dissolution. The conclusion that the grains from these sections represent glacial IRD is in agreement with previous studies on the Site 913 EOT coarse detrital material (Eldrett et al., 2007; Tripati et al., 2008).

Grain texture analysis of the Site 647 and Exp. 342 EOT intervals showed high proportions of rounded, low-medium relief grains, with more grains displaying chemical surface textures, and fewer grains displaying mechanical textures than the iceberg-rafted grains. The textural composition of these grains instead suggests that they represent material that has undergone significant transport by fluvio-marine currents (Krinsley and Donahue, 1968; Krinsley and Doornkamp, 2011; Mahaney et al., 2001). During this transport, the grains will have been exposed to more saltation (resulting in rounding), and more submersion (resulting in chemical surface textures) than relatively fresh grains that have been formed in glacial conditions and then transported by icebergs (a more passive form of transport). The difference between the Site 647 and Exp. 342 EOT grains, compared to the Site 913 EOT grains, suggests that the source of the icebergs responsible for the IRD seen at the was not large enough to affect sedimentation in the North Atlantic, unlike later, more extensive glaciations (Bailey et al., 2013; Bond et al., 1992; Lisitzin, 2002; Raymo, 1994).

Several studies comparing IRD from icebergs and sea ice have noted that sea ice IRD can also display the trends described in Sites 647 and Exp. 342 above (Dunhill, 1998; St. John et al., 2015). As sea ice tends to entrain detrital material from shallow shelves, beaches, and riverine outputs, the textures present on sea ice IRD are largely a product of their transport history prior to their entrainment into the ice, rather than them being transported by it (Darby, 2003; Dethleff and Kuhlmann, 2010; Eicken et al., 2005; Kempema et al., 1989; Lisitzin, 2002; Nürnberg et al., 1994; St. John et al., 2015). As such it is difficult to separate sea ice IRD from grains that have been transport solely by fluvial or marine currents using surface textural analysis alone. Sites U1411 and U1406, however, lie at the southernmost extent of the modern-day sea ice regime (Figure 1.6). Furthermore, though there is evidence for ephemeral sea

ice in the Arctic Ocean across the EOT, there is no documented evidence of sea ice IRD in the North Atlantic, and modelled winter month temperature estimations for the EOT at the latitude of these sites are ~20-28°C (Darby, 2014; Eldrett et al., 2009).

The calculated Euclidean distances between each target interval back up this observation, as displayed in Table 2.3. The Site 647 and Exp. 342 EOT intervals are closest in Euclidean space (41); the Site 913 EOT and Site U1411 Pleistocene intervals are also relatively close (50). The Site 647 EOT interval is separated from the Site U1411 Pleistocene interval by the greatest distance (94), and is also relatively far away from Site 913 (80); the Exp. 342 EOT interval is also relatively far away from these intervals. It is interesting that the EOT-age grains from the Newfoundland drifts differ more in terms of their surface from Pleistocene-age sediments from the same location than they do from EOT-age sediments from other locations.

Euclidean Distance	**Site 647**	**Exp. 342**	**Site 913**	**Site U1411 Pleistocene**
Site 647	0			
Exp. 342	41	0		
Site 913	80	69	0	
Site U1411 Pleistocene	94	85	50	0

Table 2.3: Euclidean distances between each interval analysed in this chapter.

The Euclidean distances between samples from within the Site 913 EOT interval, and within the Site U1411 Pleistocene interval (32-48 and 38-55 respectively, Tables 2.4 & 2.5) are similar to values between the Site 647 and Exp. 342 EOT intervals, and between the Site 913 and Site U1411 Pleistocene intervals (Table 2.3), reinforcing the idea that each pair has the same environmental history (Mahaney et al., 2001).

Euclidean Distance	**913EOT-1**	**913EOT-2**	**913EOT-3**	**913EOT-4**	**913EOT-5**
913EOT-1	0				
913EOT-2	48	0			
913EOT-3	48	46	0		
913EOT-4	39	43	42	0	
913EOT-5	42	46	41	32	0

Table 2.4: Euclidean distances between each sample from the ODP Site 913 EOT interval

Euclidean Distance	U1411P-1	U1411P-2	U1411P-3	U1411P-4	U1411PP-5
U1411P-1	0				
U1411P-2	38	0			
U1411P-3	46	47	0		
U1411P-4	41	55	44	0	
U1411P-5	42	56	47	44	0

Table 2.5: Euclidean distances between each sample from the IODP Site U1411 Pleistocene interval

2.4 Conclusions

The results of this exploration of North Atlantic EOT-age detrital sediments suggest that, while the EOT interval at Site 913 does represent an example of glacially sourced ice rafting, that there is no evidence for a larger ice-rafting regime extending into the North Atlantic (i.e., there is no evidence for significant bipolar glaciation across the EOT). The Site 913 interval likely represents ice rafting from a local tidewater glacier on East Greenland, the influence of which did not extend into the North Atlantic.

The detrital grains and clasts identified at Sites U1411 and U1406 were originally interpreted shipboard to be a further record of IRD across the EOT (Norris et al., 2014). The surface textures of quartz grains from this site however suggest that they were transported in a sub-aqueous environment, and differ from those found at Site 913. It is generally accepted that sand grains cannot be transported significant distances by ocean currents, and the bathymetric locations of Site U1411 and U1406 suggest that they were unlikely to be directly affected by downslope movements (Mackiewicz et al., 1984; McCave and Hall, 2006; Molnia, 1983; Ruddiman, 1977). These grains are found in drift deposits however, and the provenance data presented here suggest a local source, so it is possible that they were transported a short distance to the site locally by the same current responsible for the rest of the drift.

Furthermore, CT-scanning has shown that the detrital clasts seen at these sites, originally thought to have been ice-rafted clasts similar to those seen at Site 913, are actually a product of post-depositional bioturbation (Norris et al., 2014).

Though it was not possible to analyse the provenance of the detrital grains from the Site 647 EOT interval, the mineralogy, sedimentology, and the surface textures of these grains suggest that, similar to Site U1411, this EOT interval does not provide any evidence of ice-rafting, either from the same source as Site 913 or elsewhere.

Chapter 3 Changes in oceanography and sea level across the Eocene Oligocene Transition recorded on the Southeast Newfoundland Ridge: interpreting the detrital record of Site U1411

3.1 Introduction

The Eocene-Oligocene Transition (33-34 Ma) marks the most significant climate change event of the Cenozoic; over an interval of ~300 kyr, Earth's climate transitioned from a 'greenhouse' to an 'icehouse' state as a large, sustained ice cap was rapidly established on Antarctica (DeConto and Pollard, 2003; Katz et al., 2008). Associated with this change were a global cooling and a reorganisation of the carbon cycle in the oceans. The associated glacioeustatic sea-level fall is suggested to have exposed and eroded large areas of shallow carbonate, and shallow carbonate deposition was replaced by pelagic burial at depth, leading to deepening of the Carbonate Compensation Depth (CCD) (Merico et al., 2008).

Climate change at the EOT was likely brought about by a combination of decreasing atmospheric CO_2 throughout the late Eocene (Pagani et al., 2005; Zachos et al., 2008), coupled with an orbital trigger — in this case low amplitude cyclic variation of high latitude insolation due to the changing obliquity of earth's axis (Coxall et al., 2005). Together these forces triggered the growth of Antarctic ice, which then initiated strong positive feedback effects associated with ice sheet height and coalescence; these lead to rapid further ice growth (Coxall et al., 2005; DeConto and Pollard, 2003). This hypothesis has largely replaced the idea that the opening of Drake Passage and/or the Tasman Gateway triggered glaciation through the oceanographic isolation of Antarctica, though this process would still have affected the extent of ice formation (Cristini et al., 2012; Katz et al., 2011).

The benthic foraminiferal oxygen isotope ($\delta^{18}O_{bf}$) stratigraphy of the EOT has been studied in detail, and several records have revealed a distinct step-like structure, with two pronounced sharp increases either side of a plateau (Coxall et al., 2005; Miller et al., 2008; Scher et al., 2011). These steps, referred to here as EOT-1 (precursor step in

(Miller et al., 2008)) and the Oi-1 event respectively, together constitute a ~1.5‰ increase in $\delta^{18}O_{bf}$ across the transition. The relative combinations of ice-growth versus global cooling are unclear, despite various attempts to address this problem (Coxall et al., 2005; Katz et al., 2008; Scher et al., 2011). Some data sets suggest that cooling was more prevalent in the EOT-1 step and ice growth was responsible for most of the Oi-1 shift (Houben et al., 2012; Katz et al., 2008; Lear et al., 2008). As detailed in the introduction to this thesis, the glacioeustatic sea level fall associated with the ice formation during this shift is estimated to be ~70 m (Miller et al., 2008).

As well as glacioeustatic changes, the development of conditions similar to the modern-day pattern of thermohaline circulation, with deep water being formed in the North Atlantic as well as the Southern Ocean, is also thought to have started around the time of the EOT. This is supported by the onset of many sediment drifts and widespread evidence of erosion by bottom-currents (Davies et al., 2001; Howe et al., 2001; Via and Thomas, 2006; Wold, 1994). Contrary to this, a number of drifts along the western margin of the North Atlantic originate from the Late Eocene, including the drifts on the Southeast Newfoundland Ridge (SENR) (Boyle et al., 2017; Campbell and Mosher, 2016; Norris et al., 2014). One hypothesis is that this change in circulation was brought about by tectonic processes, through the deepening of the Greenland–Iceland–Faeroes Ridge, which had previously separated the Greenland-Norwegian Sea (a major area of deep water formation) from the North Atlantic Ocean, rather than being brought about by the climatic events of the EOT itself (Via and Thomas, 2006). Others have argued that global cooling, beginning in the Mid-Eocene and continuing across the EOT as described above, resulted in the formation of deep water, and that the growth of the Antarctic ice sheet to the continent's coastlines across the EOT (as evidenced by the appearance of ice-rafted debris in Antarctic shelf sediments) also increased Antarctic Bottom Water formation. This deep water formation increased latitudinal gradients, which increased thermohaline circulation (Campbell and Mosher, 2016; Expedition 318 Scientists, 2010; Goldner et al., 2014; Miller et al., 2009; Scher et al., 2011).

IODP Sites U1411 and U1406 are perched respectively on the SENR and on a seamount on the adjacent J-Anomaly Ridge. Both sites contain EOT-age intervals of drift-deposited sediment, at a location that is ideally placed to capture changes in

sedimentation driven by sea level change and/or changes in bottom current intensity in the North Atlantic Ocean (Figure 3.1) (Boyle et al., 2017; Norris et al., 2014). The sediments at both of these sites contained detrital sand grains, which were tentatively interpreted by the shipboard party as being ice-rafted debris (Norris et al., 2014). Data presented in Chapter 2 of this thesis, however, suggested that this was not the case, and so it seems likely therefore that this detrital sand represents either sedimentation changes associated with glacioeustatic sea level change, the intensification of deep water currents, or possibly a combination of the two.

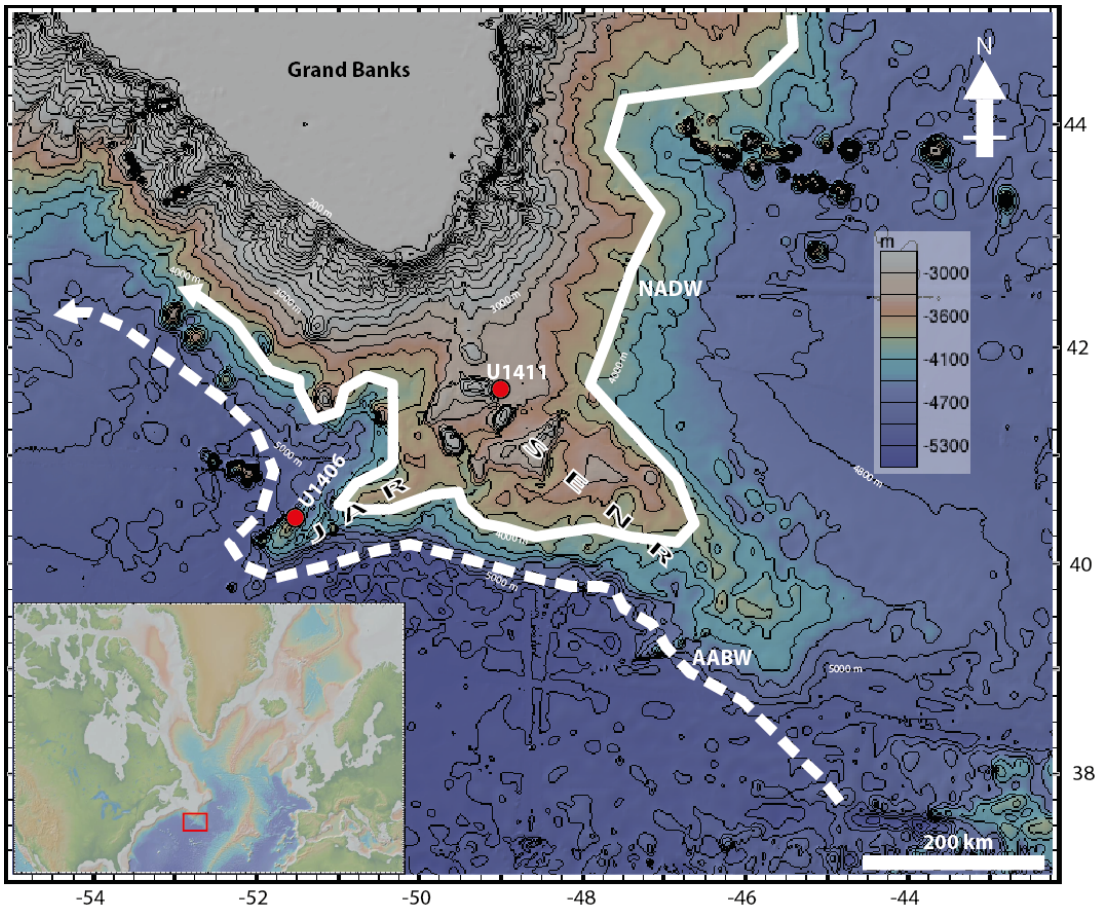

Figure 3.1: Bathymetry of the Southeast Newfoundland Ridge (SENR) and J-Anomaly Ridge (JAR), showing the locations of IODP Sites U1411 and U1406, and the flow-path of modern North Atlantic Deep Water (NADW) and Antarctic Bottom Water (AABW); inset shows the location of the ridges in the North Atlantic. Bathymetric base map is from GeoMapApp (http://www.geomapapp.org).

Identifying the controlling factor of this detrital sand could not only build upon our understanding of palaeoclimatic change across the EOT, but could also help to predict the formation of hydrocarbon reservoirs relevant to oil and gas exploration. If the presence of the grains is controlled by eustatic sea level change, then clastic sedimentation patterns may also have been altered in nearby shallow marine settings

and along the continental shelf, likely resulting in increased sediment transport to the deep ocean (Abreu and Haddad, 1998; Katz et al., 2013; Miller et al., 2008; Miller and Mountain, 1996). Specifically, a drop in eustatic sea level can lead to the development of a significant lowstand system tract, characterised by marked progradation of clastic systems into deeper water (Walsh and Nittrouer, 2003) (Figure 1.5). This progradation can lead to the formation of sandstone bodies in deeper parts of a basin, with the potential to act as hydrocarbon reservoirs (Wade and Pälike, 2004). These sandstone bodies may exist as either perched/shelf-edge deltas or as deep marine turbidite fans. The increase in the size of Antarctic ice caps across the EOT also led to marked variability in ice volume going into the Oligocene, paced by obliquity (40 ka) and eccentricity (110, 405 ka) cycles seen in $\delta^{18}O_{bf}$ records (Abels et al., 2007; Wade and Pälike, 2004). Sea level change driven by these orbital-controlled cycles has been detected in shallow marine clastic sedimentation changes in the North Sea basin in the Early Oligocene (Abels et al., 2007). During the Oligocene, the longer orbital periods (405 ka eccentricity, 1.2 Ma obliquity) appear to drive third-order sea level variability, which may have greatly influenced sedimentation patterns globally, providing a framework for sedimentary facies prediction (Wade and Pälike, 2004).

If, however, the grains are instead controlled by bottom current variability, then this could also be of some interest to hydrocarbon exploration. Contour currents can create sandstones that can act as reservoirs by winnowing away finer sediment, leaving a better sorted, higher net-to-gross deposit (Howe et al., 2001). Understanding the palaeoclimatic significance contained in the presence of the detrital sand is therefore vital in understanding the sedimentological and/or oceanographic changes occurring in the North Atlantic across the EOT.

3.1.1 Aims

This study aims to determine the source and controlling influences of the detrital sand fraction across the EOT at Sites U1411 and U1406, and to determine whether this component represents either a process separate from the deposition of the fine-grained drift deposits that cover the area.

3.2 Methods

3.2.1 Detrital sand grain flux

Standard methods for quantifying the abundance of detrital grains can be split into two broad categories: i) counting grains in splits of certain size fractions as commonly used for Heinrich event studies in North Atlantic sediments of Late Pleistocene age (Lang et al., 2014), and ii) estimating by eye the percentage of detrital grains for a certain size fraction in each sample. This method has been used to assess the abundance of IRD in Eocene-aged sediments in the Arctic, and in an EOT study of proximal ice-rafting off Greenland (Eldrett et al., 2007; Moran et al., 2006).

Both methods were trialled, and although ii) was found to be significantly quicker, it was also deemed less sensitive, due to the relatively small percentages of lithic material estimated in each sample (1-5%). In Arctic sediments, carbonate is almost absent. However, Site U1411 is carbonate-rich (~5-60%) and so this method is less appropriate. Counting methods also sometimes involve dissolving carbonate to facilitate easier counting; the practice was not adopted here, however, as the exceptionally preserved foraminifers represent an incredibly valuable record of EOT climatic change. As such method i) was used.

The unprocessed samples were prepared at the National Oceanography Centre, Southampton (NOCS). Each was weighed, dried, and then clays were de-flocculated by adding sodium hexametaphosphate and placing on a shaker table. Each sample was then washed through a 63-μm mesh sieve to remove clay and silt. Prior to counting, samples were split to a workable size and dry-sieved at 63 μm and 150 μm because initial experimentation with dry sieves revealed that the majority of the grains were <150 μm. A variable-zoom binocular light microscope was used to inspect each sample at each size fraction (63-150 and >150 μm) and detrital grains were recorded using a mechanical counter. Although detrital grains were typically absent above 150 μm, pyrite was found in abundance; it was deemed to be authigenic due to the fact that foraminiferal tests in the sediment often featured diagenetic pyrite (Norris et al., 2014). In total, 492 samples were counted from the original EOT sampling interval at eight cm (~2-3 kyr) resolution, ranging from 127.475 m to 171.365 m CCSF, with a further 167 samples also counted in the Latest Eocene from 171.5 m CCSF to 196.115

m CCSF at a resolution of 16cm (~4-6 kyr). Authigenic pyrite grains were ignored when counting the samples. The weight of both the coarse (>63 μm) and 63-150 μm fractions was also recorded for each sample, to determine whether each was dominantly influenced by detrital input or by pelagic carbonate accumulation.

The same detrital grains identified at Site U1411 during Exp. 342 were also reported to appear at the EOB at Site U1406. As introduced in Chapter 2, the EOT interval at this site features a lower sedimentation rate and higher carbonate component than at Site U1411. A low-resolution count was conducted through the EOT interval, with 28 samples counted at intervals of ~1 m (~140 ka), covering a period of ~32.3 Ma to ~36 Ma (206-234 m CCSF). A record of the weight % of the coarse fraction was also generated at NOCS, as described above for Site U1411.

The grain counts for both sites were converted to flux (grains cm^{-2} kyr^{-1}) using the following equation (3.1):

$$Flux = gc \cdot lsr \cdot dbd \quad (3.1)$$

Here *gc* is grain concentration (grains g^{-1}), *lsr* is linear sedimentation rate (cm kyr^{-1}), and *dbd* is dry bulk density (g cm^{-3}). The linear sedimentation rates for each site were calculated using un-tuned magnetostratigraphic age models based on the shipboard identifications of magnetic reversals (Norris et al., 2014).

3.2.2 Bulk carbonate stable isotope analysis

A bulk carbonate carbon and oxygen isotope record was developed at NOCS, using a Europa Geo 20-20 stable isotope mass spectrometer equipped with an automatic carbonate preparation system (Wilson & Bohaty, unpublished data). Bulk samples were prepared by subsampling unprocessed sediment, drying and weighing it, then grinding it to a fine powder using a pestle and mortar. Samples were run throughout ~127 to 175 m CCSF at a variable resolution of 8-20 cm, and at a lower resolution to a depth of ~ 196 m CCSF. All isotope ratio values are reported relative to the Vienna Pee Dee Belemnite (VPDB) standard.

3.2.3 Grain size distribution analysis

Twenty-three unprocessed samples from ~128 to 192 m CCSF were analysed for grain size distribution. These samples were dried, weighed, and then carbonate was removed from each sample by adding excess ten percent acetic acid and leaving it for 24 hours. Samples were then shaken to determine whether any carbonate remained, before being washed repeatedly with Milli-Q water; a centrifuge was used to avoid any of the fine material being lost between each wash. The samples were not treated to remove biogenic silica because smear slide analysis indicated the absence of significant numbers of radiolarians or diatoms. The de-carbonated samples were subsampled, soaked in Calgon®**,** and left overnight on a shaker table before being analysed at NOCS on a Malvern Mastersizer 2000 with an Autosampler 2000 attached. Four runs of a standard (in house standard A1) were analysed alongside these samples. Initial inspection of the results indicated that the vast majority of the detrital sediment in the drifts at the Site U1411 EOT interval was <20 μm. To examine the coarse detrital fraction more closely, the same 23 samples were then re-run after wet sieving at 20 μm (each fraction was weighed first). Furthermore, some studies have suggested that the Mastersizer, which uses a laser to estimate the diameter of grains suspended in a fluid, can over-estimate the size of very fine particles compared to other techniques, especially when there is a high volume of fine material (Konert and Vandenberghe, 1997). Focusing on the >20 μm fraction therefore could prevent any distortion of the result. For all measurements, data were binned into ¼ϕ intervals during processing (Eq. 2.1).

To examine whether the instrument was correctly characterising the finer sediments, a further split of each de-carbonated sample (un-sieved) was sent to Kristen Chilton at Virginia Tech University, where a Sedigraph was used to analyse the fine fraction for each sample (<63 μm), again using ¼ϕ bins. The Sedigraph calculates the size of particles in this fraction from their settling velocity, and is generally considered to better characterise fine particles compared to the Mastersizer (which does not effectively characterize clay particles <1 μm), but cannot analyse sand-sized particles (Konert and Vandenberghe, 1997; Mccave et al., 2006; Molinaroli et al., 2000).

3.2.4 Spectral analysis of grain flux record

Initial inspection of the grain count, coarse fraction wt%, and 63-150 μm wt% records for the U1411 EOT interval appeared to show a cyclical nature, particularly in the Earliest Oligocene. To explore the dominant periodicity of these cycles, the astrochron package (in R) was used to perform spectral analysis on the grain flux record (Meyers, 2014, 2012; Rahim, 2014; Thomson, 1982). For the purposes of this investigation, the record was analysed both in the depth domain and in the time domain using an un-tuned age model based on the shipboard identification of magnetostratigraphic datum tie points (Norris et al., 2014). Each dataset was first resampled to obtain a regular sampling interval (8 cm, equivalent to ~2.7 kyr), and then the linear trend was subtracted using the *detrend* function in the astrochron package (Meyers, 2014). The multi-taper method (MTM) was then used to identify the dominant frequencies for each de-trended dataset. The periods of frequencies that exceeded a >99% confidence interval were then calculated; for the analyses run in the depth domain, periods were calculated using an average sedimentation rate for the interval of 3 cm/kyr.

As the suspected cyclicity becomes more prominent in the youngest part of the EOT interval, the Matlab application 'A cross wavelet and wavelet coherence toolbox' was used to perform wavelet analysis across the interval of study – again using both a depth scale and the magnetostratigraphic age model (Grinsted et al., 2004; Jevrejeva et al., 2003; Torrence and Compo, 1998; Torrence and Webster, 1999). Initial inspection of the results showed changes in the dominant periodicities above ~140 m CCSF/33.3 Ma, and so the interval above this point was re-analysed in isolation.

During the ongoing development of an astronomically tuned age model for the interval, precessional and 100 kyr eccentricity cycles have been identified in high-resolution X-Ray Fluorescence (XRF) Zr/Rb records (Bohaty & Liebrand, unpublished data). As the drift sediments through the interval are dominated by clay and fine silt, the XRF data should reflect changes in the fine material, and so comparing it to spectral analysis of the grain count time series could help to reveal whether they are both controlled by the same pacing. As such, the Zr/Rb XRF ratio was analysed using MTM and wavelet analysis as described above to provide a direct comparison, again

using both the depth scale and magnetostratigraphic age model. It was resampled at 8 cm (~2.7 kyr) intervals to match the resolution of the flux record, and linear trends were removed as above.

3.2.5 Provenance of detrital coarse fraction vs. rest of drift deposit

As established in Chapter 2, the Pb isotope analysis of sand-sized feldspars from Sites U1411 and U1406 suggests a local source, rather than Greenland. Here this work is expanded on further by exploring how the Nd and Sr isotopic signature of the coarse detrital fraction (>63 μm) compares with the bulk of the drift deposit (i.e., 0-20 μm). Crucially, Nd and Sr isotopes are generally analysed on either the bulk detrital fraction, or on specific grain size ranges of the detrital fraction, unlike Pb. There is also a detailed understanding of the isotopic composition of North Atlantic terranes for both Nd, which is usually expressed as $\varepsilon Nd_{(t)}$, or $^{143}Nd/^{144}Nd$, and Sr, expressed as $^{87}Sr/^{86}Sr$ (Farmer et al., 2003; Hemming et al., 1998). X-ray diffraction (XRD) analysis of clay minerals can also reveal changes in the provenance of the finest (<2 μm) component of the Site U1411 drift deposits (Ehrmann, 1998).

3.2.5.1 Nd: sample preparation, column chemistry, and isotopic analysis

Ten unprocessed sediment samples were taken for bulk detrital Nd isotopic analysis from the Site U1411 EOT interval. The carbonate in these samples was dissolved using excess 10% acetic acid, and the samples were then cleaned with Milli-Q. A centrifuge was then used to ensure that the fine fraction was not lost during the cleaning process. It was not deemed necessary to remove biogenic silica (Section 3.2.3). After de-carbonation, the samples were mixed with sodium hexametaphosphate to deflocculate the clay component, and were left on a shaker table for 24 hours. Each sample was then wet-sieved through a 63-μm mesh, and both the coarse and fine fraction were dried and retained. The coarse fraction contained pyrite, which if authigenic could possibly influence the detrital Nd. To combat this issue, pyrite grains were picked out of the samples; this removed pyrite was then analysed along with the other samples to confirm that it was authigenic. For each sample, the coarse and fine fractions were analysed separately (the fine fraction was first run through a 20 μm sieve, as the detrital sand grains in the coarse fraction were also present as coarse silt in the fine fraction). Including the pyrite, therefore, there were 21 samples to analyse in total.

These samples were then transferred into 3ml Teflon pots and leached on a hot plate at 140°C with 6M hydrochloric acid (HCl) for two hours and left overnight. They were then washed several times with Milli-Q water in preparation for digestion. The samples were each digested with 20 µl sub-boiled nitric acid (HNO_3) and 160 µl of 27M hydrofluoric acid (HF) on a hot plate for 24 hours. They were then evaporated to dryness and cleaned with a few drops of concentrated HCl and HNO_3 (evaporated after each step) ready for column separation.

The column chemistry required to isolate Nd involves two column passes; the first uses AG50-X8 200-400 mesh cation columns, whereas the second uses LN Spec columns. For the first column pass, each Nd subsample was dried down and then dissolved in 100 µl of 1.75M HCl. The columns were conditioned with 2ml of 1.75M HCl, then each sample was loaded and washed in with a further 100 µl of 1.75M HCl. 1.5ml of 1.75M HCl was passed through to elute Fe followed by 2ml of 2M HNO_3 to elute Ba. 1.5ml of 6M HNO_3 was then added to free the Nd, and this was collected, dried down, and then dissolved in 0.3ml of 0.2M HCl ready for the second columns. These were conditioned with 1.5ml of 0.2M HCl. The samples were loaded and then washed in with three passes of 100 µl of 0.2M HCl. 2 ml of 0.2M HCl was added to elute Ba, before the Nd was collected by adding 4ml of 0.2M HCl. The collected fraction was then dried down ready for mass spectrometry.

Each sample was sub-sampled and screened prior to isotopic analysis, and was analysed via a Multi Collector Inductively Coupled Plasma Mass Spectrometer (MC-ICP-MS; Thermo Scientific Neptune) at NOCS following the methods of Lang et al., (2014). External error was calculated at two standard deviations for each sample run. All of the samples analysed delivered useable results, however during sample preparation some material was lost from several of the 0-20 µm samples, leading to higher error.

3.2.5.2 Sr: sample preparation, column chemistry and isotopic analysis

Splits of the same samples prepared for Nd column chemistry were also analysed for Sr isotopic analysis, after being prepared as described above for Nd. The samples were screened prior to column chemistry to determine the volumes of each sample necessary to obtain enough Sr for isotopic analysis. The subsamples were dried down and then dissolved in 200 µl of sub-boiled (SB) 3M HNO_3. Columns containing Sr-Spec resin were prepared by being flushed with two alternating 1.5 ml runs of Milli-Q and SB 3M HNO_3. The columns were then conditioned with a further 1.5 ml of SB 3M HNO_3, the sample was added and washed in with 200 µl of SB 3M HNO_3, and then a further 2ml of HNO_3 was added to elute the sample. 1.5 ml of water was then added to the columns and the Sr was collected before being dried down ready for loading.

Prior to isotopic analysis, the stubs required to load each sample into the mass spectrometer were cleaned in boiling H_2O_2 for 45 minutes; a Ta filament was then soldered onto each stub and the stubs were placed into a vacuum for one hour. Five stubs at a time were then loaded onto a multiloader. Each dried sample was dissolved in 1.5 µl of 1M HCl, and 1 µl of activator was added to each filament and dried at 0.6 amps. The dissolved samples were then added to each filament and dried down ready for analysis. Six standards (NBS 987) were also prepared in the same way. All of the stubs were analysed using a Thermofisher Triton Multicollector Thermal Isolation Mass Spectrometer (TIMS) at NOCS. External error was calculated to two standard deviations. Of the original 21 samples run, only nine returned useable data. The remaining material for each of the 11 samples that did not run was re-screened and re-run, returning a further six useable values (i.e., 15 of 21 samples in total).

3.2.5.3 Data analysis

The aim of characterising Nd and Sr isotopic composition of the Site U1411 detrital fraction was twofold. First, to study whether the provenance of the coarse fraction differed from the majority of the fine drift sediment throughout the interval; and second, to determine where the different size fractions were sourced from by comparing them to provenance data from the North Atlantic. As such, it was necessary to collate previously published $^{143}Nd/^{144}Nd$ and $^{87}Sr/^{86}Sr$ data for the North Atlantic provinces. The studies identified were separated into three regions: Scandinavia, North America, and Greenland. The data from these studies were then

grouped into terranes of differing age within each of these groups (see Appendix B for references). A study by Farmer et al., (2003) also analysed Nd and Sr isotope ratios on glaciomarine sediment from several areas in the North Atlantic, including Greenland and the Gulf of St. Lawrence.

Much of the previous work characterising the North Atlantic terranes reports Nd in the format of εNd, which expresses the sample $^{143}Nd/^{144}Nd$ in terms of its deviation from the $^{143}Nd/^{144}Nd$ of CHUR (CHondritic Uniform Reservoir) (Farmer et al., 2003).

$$\varepsilon Nd_{sample} = \left[\frac{\left(^{143}Nd/_{144}Nd\right)sample}{\left(\frac{^{143}Nd}{^{144}Nd}\right)CHUR} - 1\right] \times 10000 \quad (3.3)$$

The $^{143}Nd/^{144}Nd$ of CHUR has evolved through time, with the present day value (used to calculate $\varepsilon Nd_{(0)}$) being 0.512638. The $^{143}Nd/^{144}Nd$ ratios from all of the amassed references were converted to $\varepsilon Nd_{(0)}$, along with the data from this study, to allow them to be compared, following the practice of previous studies (Farmer et al., 2003; Lang et al., 2014).

3.2.5.4 Clay mineral analysis

Analysing the dominant clay minerals present in the <2 μm fraction can help to establish provenance changes in the fine material being delivered to the drift. 19 samples from the Site U1411 EOT interval were prepared for XRD analysis. Carbonate was removed following the same process outlined in Section 3.2.3, and then each sample was shaken with de-ionised water and sodium hexametaphosphate to deflocculate clay minerals. Samples were then allowed to settle and Stokes' law was used to isolate the clay particles, based on their settling velocity (Gibbs et al., 1971). 10% magnesium chloride was then added to each sample, and they were centrifuged at 2000 rpm for two minutes and decanted. De-ionised water was then added, each sample was centrifuged and decanted again, and then a small amount of each sample was smeared evenly onto a glass slide. Each sample was then analysed on a Phillips Xpert Pro Diffractometer at NOCS, using a cobalt anode x-ray tube and a scanning step of 1.2°. For the purposes of this thesis, the relative proportions of four major clay minerals were calculated: smectite, illite, chlorite, and kaolinite.

3.3 Results and discussion

3.3.1 Relationships between grain flux and bulk carbonate isotope stratigraphy

Detrital sand grains were present in the 63-150 μm fraction in every sample at Site U1411, although very few grains >150 μm were found (Section 2.2.3). The grain flux record from Site U1411 showed relatively low levels in the latest Eocene, rising into the earliest Oligocene (Figure 3.2). This increase occurs in two major steps, one at ~33.9 Ma and another, larger step at ~33.6 Ma. There also appears to be an initial, possibly transient, increase at ~34.3 Ma. These steps are also seen in the weight % of the 63-150 μm fraction, suggesting that the material in this size range is dominated by detrital sand, rather than carbonate, for example (Figure 3.2).

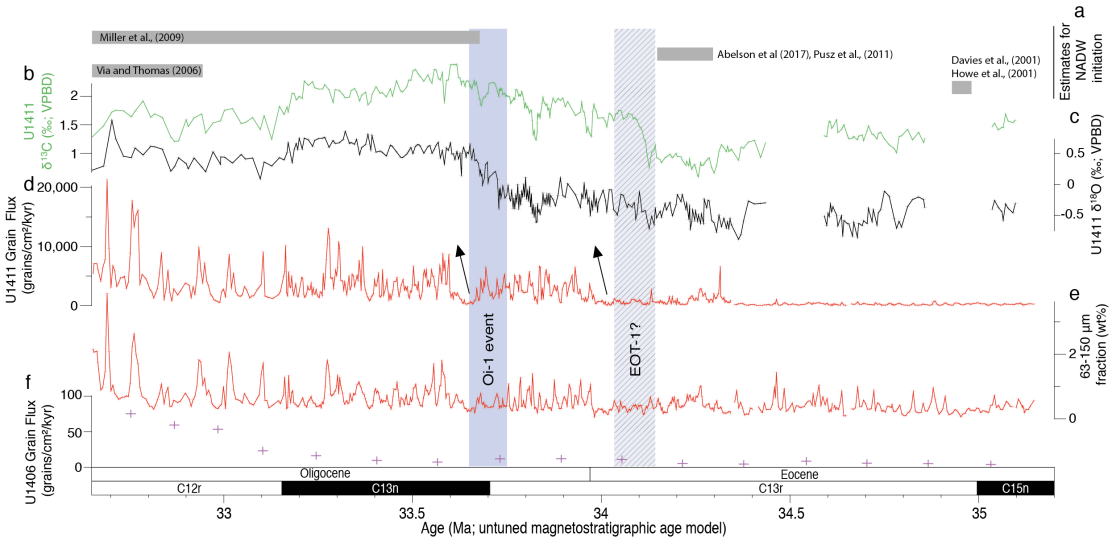

Figure 3.2: a) estimates for the initiation or intensification of North Atlantic Deep Water. Changes across the EOT of b) bulk carbonate $\delta^{13}C$, c) bulk carbonate $\delta^{18}O$, d) detrital sand grain flux and e) the weight of the 63-150 μm fraction from IODP Site U1411, and e) detrital sand grain flux from site U1406 (see Appendix C for data). The untuned age models used for both sites were created using shipboard placing of magnetostratigraphic datums (Norris et al., 2012).

The bulk carbonate $\delta^{18}O$ isotope record shows a positive shift of ~0.7‰, from 33.65 to 33.75 Ma, coinciding with the C13n/C13r magnetic reversal (Figure 3.2). This is interpreted to be the globally recognised Oi-1 shift. Benthic foraminiferal records from other sites have also identified a precursor shift, or EOT-1, but this is not visible in the bulk carbonate record from this site; it may be revealed by the eventual construction of a $\delta^{18}O_{bf}$ record (Coxall and Pearson, 2007; Katz et al., 2008; Miller et

al., 2009; Scher et al., 2011). The bulk carbonate $\delta^{13}C$ isotope record shows a large positive shift of 1‰ at 34.1 Ma. An ongoing investigation has tentatively placed the EOT-1 at this position (S. Bohaty, pers. comm.), based on the fact that a similar $\delta^{13}C$ shift is seen at the Massignano core, the global stratotype section and point (GSSP) for the EOB, and occurs alongside the EOT-1 oxygen isotope step at the site (Jovane et al., 2009; Silva and Jenkins, 1993). The EOB at Site U1411 is currently placed at a depth of 159.155-159.115 m CCSF (~33.95 Ma for the age model used in this study), based on the last occurrence of the planktic foraminifera genus *Hantkenina,* (H. Coxall, pers. comm.).

Of the two main steps identified in the Site U1411 grain flux record, the first appears to coincide with the EOB, after the interpreted placing of the EOT-1 step (Figure 3.2). The second step shift in the flux record occurs after the Oi-1 event, with both steps in the flux record lagging the end of the interpreted positions of the two oxygen isotope steps by ~ 50 ka. The current understanding of the relative contributions of glacioeustatic sea level change and temperature change for the two steps suggests that the Oi-1 step was dominantly a result of ice formation, whereas EOT-1 also featured a temperature component. Given the response of the grain flux to these $\delta^{18}O_{bf}$ steps, glacioeustasy might then seem like a potential mechanism to explain the sand flux record. This also fits in with a recently published reconstruction of Cenozoic sedimentation on the SENR, which does not infer a major or sudden change in bottom current strength, or in delivery of material to Site U1411, across the EOT interval (Boyle et al., 2017). If the flux of the detrital sand was being controlled by sediment changes linked to glacioeustatic sea level fall, then the two-step nature of the grain flux increase suggests that there is an ice volume component to both of the $\delta^{18}O_{bf}$ steps commonly identified in EOT intervals (Houben et al., 2012; Katz et al., 2008; Miller et al., 2009). This does though raise again the question of why there is no obvious EOT-1 step in the bulk carbonate $\delta^{18}O$ at Site U1411. If the majority of the $\delta^{18}O_{bf}$ change elsewhere is due to cooling deep water, which may not have been experienced at Site U1411, then the smaller ice volume component could have been lost in the bulk carbonate $\delta^{18}O$, which is also influenced by planktic foraminifera and calcareous nannofossils.

Aside from sedimentary change driven by glacioeustatic sea level fluctuations, the other likely driver of the changes in detrital sand grain flux seen at Site U1411 is the formation or intensification of North Atlantic Deep Water (NADW). There is a range of predictions as to the timing of NADW initiation (Figure 3.2); based on both tectonic changes and ice sheet growth (Section 1.1.5). One interpretation is that the subsidence of the Greenland Scotland Ridge, a result of the suppression of the Iceland Plume, allowed cold, dense water formed in the Greenland-Iceland-Norway seas to overflow into the North Atlantic (Abelson et al., 2008). Most estimations suggest that this overflow occurred prior to the EOT (Figure 3.2) (Abelson and Erez, 2017; Davies et al., 2001; Howe et al., 2001; Pusz et al., 2011), though Via and Thomas (2006) date it to ~1 Myr after the Oi-1 shift. Miller et al., (2009) however argue that Antarctic glaciation drove changes in North Atlantic circulation once the ice cap reached the coastline; IRD evidence suggests this didn't occur until the Oi-1 shift (Miller et al., 2009; Scher et al., 2011).

A bottom current was evidently flowing around the SENR prior to the EOT, because the drifts here began developing in the Eocene, in line with evidence for an earlier initiation of NADW (Borrelli et al., 2014; Boyle et al., 2017). It may be that this bottom current intensified across the EOT due to the drivers described above, however, and that this could be responsible for the increases in detrital sand flux at Site U1411 (Figure 3.2). If increases in NADW strength are controlling the timing of the steps in grain flux record, then this does not fit with the interpretation of Pusz et al., (2011) that NADW formed prior to the EOT-1 step, or of Via and Thomas (2006), whose interpretation lags the grain flux steps by ~1 Myr. As Miller et al., (2009) tie NADW intensification to the formation of Antarctic ice, it is difficult to separate glacioeustatic sea level change and ocean current strength as the drivers for the second step identified in the detrital sand flux record, but their interpretation cannot explain the first detrital sand flux step (Figure 3.2).

3.3.2 Evidence for a separate, local source for the detrital sand component

The GSD analysis of the Site U1411 >1 μm detrital fraction displays a bimodal distribution, with a potential third, smaller peak between 1-2 μm (Figure 3.3d). It is important to stress that the instrument (Malvern Mastersizer) used to analyse these sediments measures has a practical minimum grain size of 1 μm; Sedigraph analysis of the same samples at Virginia Tech has suggested that ~60% of the detrital material in these samples consists of clay particles below this size (Romans and Chilton, in preparation). As such it would be wrong to suggest that the second, coarser peak analysed here (at ~3-4 μm) contains the majority of the detrital material making up the drift deposit at Site U1411, only that it is separate from the first (at ~7-10 μm). The coarser of the two peaks appears to increase in magnitude going up-core and also migrates, becoming coarser in the younger samples. At the same time, the finer peak decreases in magnitude to the point that it becomes a 'shoulder' on the side of the second peak (Figure 3.3d). All of the samples analysed have a left-skewed distribution, with an elongated coarse 'tail' extending from ~20 to ≤160 μm. It is within this tail that the detrital sand, the focus of this study, lies (Figure 3.3c). Furthermore, it appears that the size of this tail increases from the oldest to the youngest sample. It is interesting that the maximum grain size appears to vary only slightly up-core, and instead the 'thickness' of the tail increases in younger sediments. If the increase in detrital grains was a result of an increase in current strength, then the upper grain size limit of the sediment being deposited should also have increased, assuming no change in the source material, and that coarser grains were present in the source material.

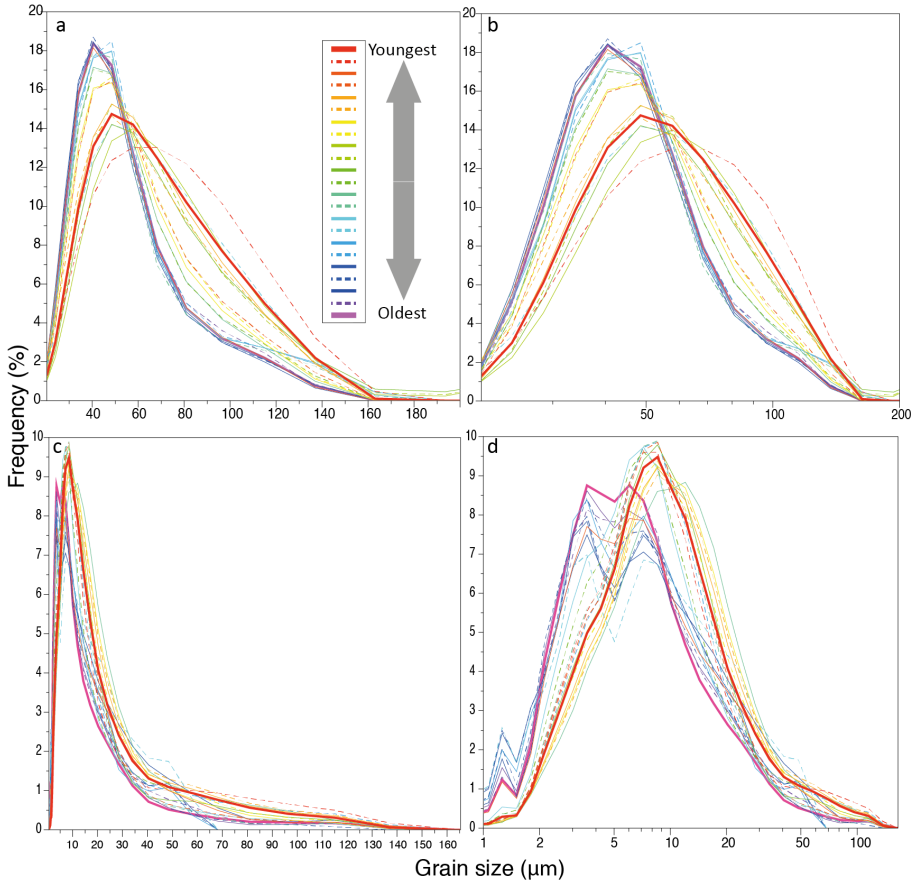

Figure 3.3: Grain size distributions from Site U1411 detrital fractions: a) and b) display the analysis of the >20 µm fraction plotted on a normal and log scale, c) and d) display the analysis of the >1 µm fraction in the same way. Each curve represents one sample; they are coloured in order of depth/age (see Appendix C.3 for data).

The >20 µm GSD profiles for each sample display an uni-modal distribution, and are left-skewed with a coarse tail, as also seen in the full GSD profiles (Figure 3.3a, b). This peak decreases in magnitude going up-core, while also becoming both coarser and broader. The coarse tail also becomes more pronounced, and accounts for a higher proportion of the total distribution.

The estimation of the >63 µm fraction from the >1 µm GSD analysis follows both the grain flux and coarse fraction wt% records (Figure 3.4c, d). It appears to fluctuate until the Oi-1 step, after which it increases by ~1%. The peak grain size of the coarser peak identified in Figure 3.3 (vertical blue lines on GSD plots in Figure 3.4e) also increases up-core, though again there is some fluctuation. Peak grain size increases at the initial jump in grain flux (~34.3 Ma), before again increasing across the Oi-1 event. The position of the first peak/shoulder does not appear to change but decreases in magnitude as the second peak becomes coarser (Figure 3.4e). As with

the >1 µm GSD runs, the peak grain size in each >20 µm GSD run (Figure 3.4f, red vertical bars) matches the grain flux record for the interval. Both show a step-increase after the Oi-1 event, and a transient increase at ~34.3 Ma. The coarse tail of these >20 µm GSD runs also appears to increase in volume up-section (Figure 3.4f, blue shaded areas).

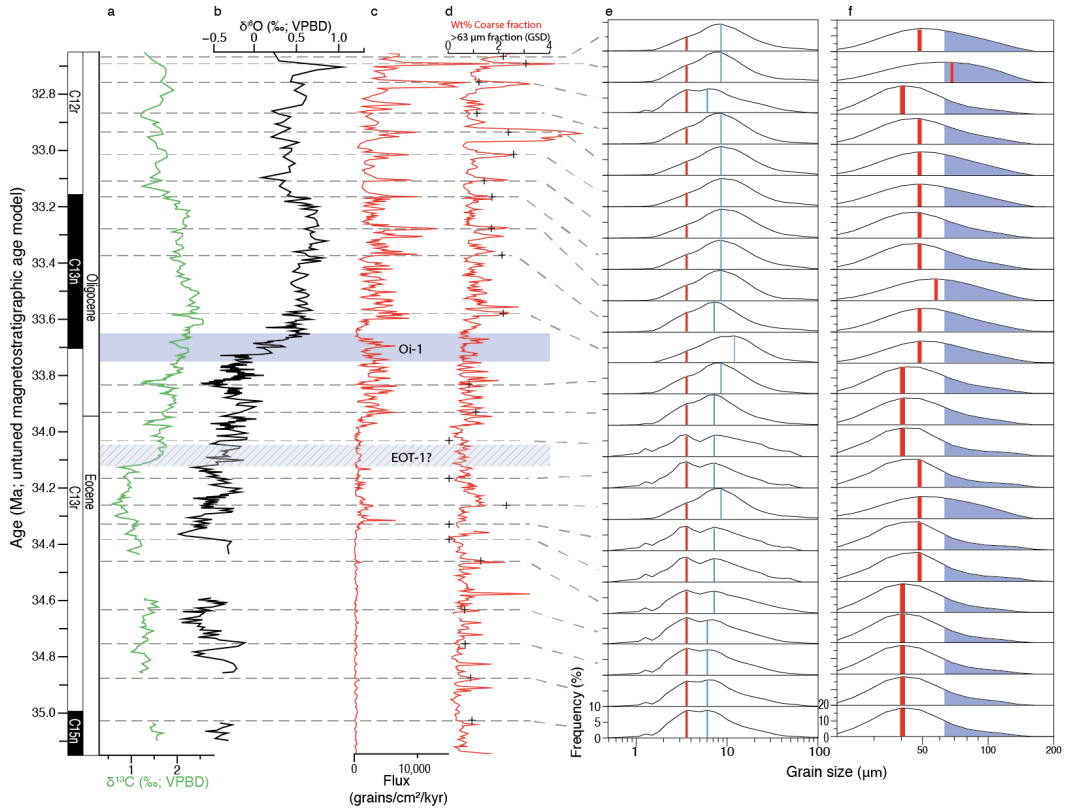

Figure 3.4: Stratigraphic locations of GSD samples (dashed lines), shown against bulk carbonate a) carbon and b) oxygen isotopes; c) grain flux; and d) weight% coarse fraction, calculated both from weighing samples (red line) and from GSD analysis (crosses). E) GSD profiles for the >1 µm fraction for each sample; red and blue vertical bars indicate positions of the first and second peaks referenced in text respectively. F) GSD profiles for the >20 µm fraction for each sample; red vertical bar on each profile indicates peak grain size, shaded blue area shows the proportion of each GSD profile > 63 µm.

The presence of a bimodal distribution in the GSD analysis suggests that the coarse detrital material present at Site U1411 (and U1406) is not the coarse tail of a single fine-grained sediment source carried by the bottom current responsible for the majority of the SENR drift deposits. The grain size analysis of the full detrital fraction displays a bimodal distribution, suggesting that the coarser material is derived from a separate source to the bulk of the drift. If all of the material had been transported the same distance, by the same current, and from the same source then a unimodal smoothed-out peak would be expected instead (Hass, 2002). This secondary peak

could represent a secondary source of sediment being transported by the bottom current, at a position proximal to the site of deposition. If this secondary source was being added to the bottom current very close to the SENR, this might explain why the material has not been fully sorted into the rest of the current's sediment load. A local source for the detrital material in the coarser peak ties in well with the Pb isotope provenance analysis featured in Section 2.3.2 (Figure 2.6). The idea that the coarser material is derived from a different source to the fine-grained drift deposits can be explored further by assessing the provenance of both components using Nd and Sr isotopes and clay mineralogy.

Stratigraphically, the $^{87}Sr/^{86}Sr$ data from the coarse (>63 μm) detrital fraction shows a very slight overall increase going across the EOT, however it actually decreases across the Oi-1 event (Figure 3.5c). This decrease is seen more clearly in the <20 μm data, which here falls below the coarse fraction data (at ~ 33.6 Ma), but otherwise features higher values. Excluding the data point that records this decrease, the <20 μm fraction records an overall increasing trend across the EOT interval. The majority of this increase occurs above ~33.1 Ma, below which there is little change (aside from the decrease at ~33.6 Ma described above). The fine fraction has a higher variability (~0.016) than the coarse fraction (~0.007).

It is important to consider that the $^{87}Sr/^{86}Sr$ of detrital material has been found to vary as a function of grain size, even if the source of the grains remains the same (Dasch, 1969; Meyer et al., 2011). Meyer et al., (2011) recorded a difference in $^{87}Sr/^{86}Sr$ of 0.004-0.006 between two adjacent size fractions (0-10 μm vs. 10-40 μm), whereas Dasch (1969) demonstrated that the difference in $^{87}Sr/^{86}Sr$ between the <20 μm and >74 μm fractions can be >0.1. For Site U1411 EOT interval, the difference between the $^{87}Sr/^{86}Sr$ of the <20 μm and >63 μm fractions ranges from 0.002 to 0.007, so it may be that, when corrected for grain size, the sources of the two size fractions could be indistinguishable from each other, could share the same source, or it could be that the difference between the two is slight. Here the Nd data may prove to be more useful. Detrital $\varepsilon Nd_{(0)}$ data from different size fractions has been shown to only shift in relation to changes of the source of the material and should be consistent within different size fractions if both come from same source (Goldstein et al., 1984; Meyer et al., 2011).

Unlike the $^{87}Sr/^{86}Sr$ data of the two size fractions, the $\varepsilon Nd_{(0)}$ data shows a clear separation between the <20 μm and coarse fraction data for the majority of the EOT interval, with the <20 μm fraction showing lower values (Figure 3.5e). In the Earliest Oligocene (~33 Ma), the two records converge as a result of an increase in the <20 μm fraction of ~10 $\varepsilon Nd_{(0)}$, before both fractions then decrease by ~5 $\varepsilon Nd_{(0)}$. Prior to this convergence, there is little in the way of an overall trend in either the <20 μm or coarse fractions. Note, however, that there is a sharp increase in the <20 μm fraction $\varepsilon Nd_{(0)}$ at ~ 33.6 Ma, which corresponds with a decrease in the $^{87}Sr/^{86}Sr$ <20 μm fraction data as described above (see arrows). As with the $^{87}Sr/^{86}Sr$ data, this increase represents a convergence towards the $\varepsilon Nd_{(0)}$ values of authigenic pyrite. The variability for the coarse fraction samples is much lower than the <20 μm fraction (~8 versus ~15 $\varepsilon Nd_{(0)}$ respectively), which again is in line with the $^{87}Sr/^{86}Sr$ data.

The pyrite analysed shows an $^{87}Sr/^{86}Sr$ value of 0.7091. This is very similar to that of modern seawater (0.709), and to an authigenic manganese nodule from the North-West Atlantic (0.7092-0.7099) (Dasch, 1969). The $\varepsilon Nd_{(0)}$ of the pyrite is -11.31, which again is within the range of seawater $\varepsilon Nd_{(0)}$ in the modern Atlantic ocean of -12±2 (Piepgras and Wasserburg, 1987, 1980), implying that the pyrite is authigenic. It may well be that the inclusion of authigenic minerals (especially in the <20 μm fraction; efforts were made to remove pyrite from the coarse fraction) affected the <20 μm fraction values of $\varepsilon Nd_{(0)}$ and $^{87}Sr/^{86}Sr$ (Figure 3.5). XRF and QEMSCAN data (Section 2.2.3.1) suggest authigenic pyrite increased significantly at ~33.5 Ma (Figure 3.5d).

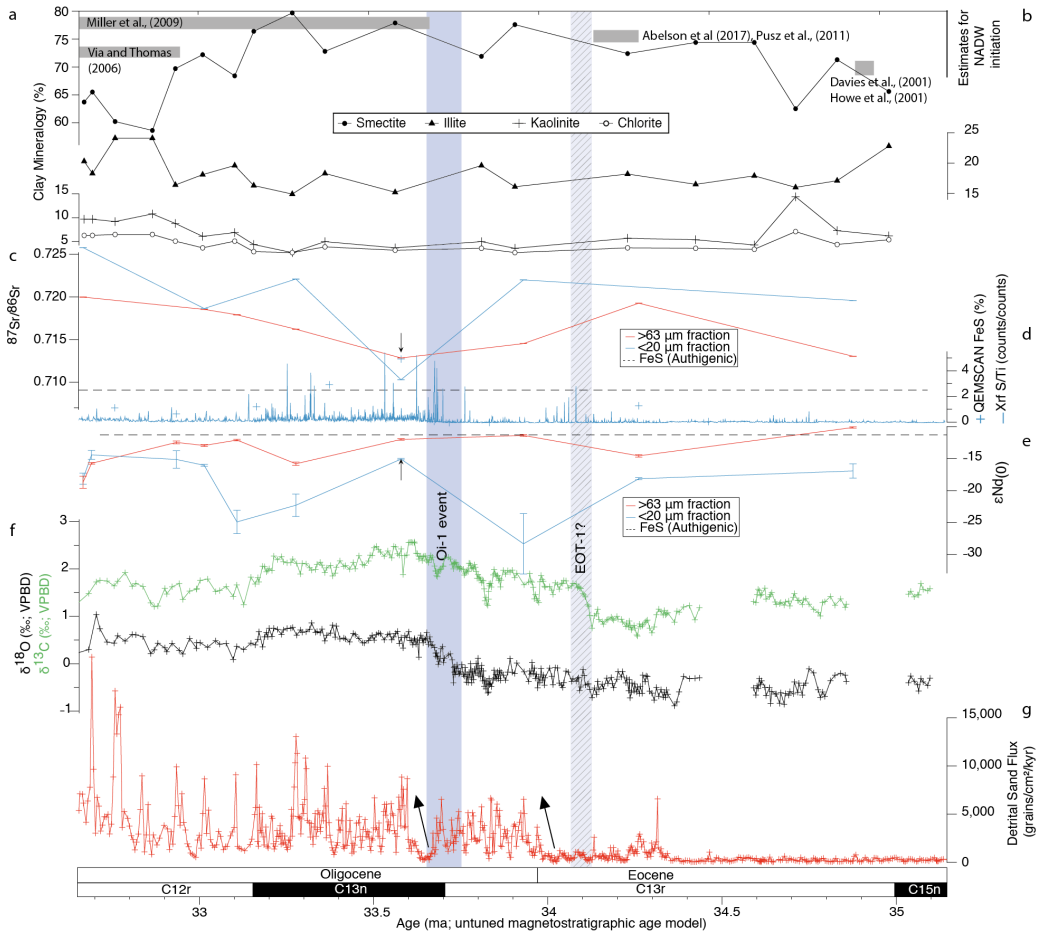

Figure 3.5: Stratigraphic variations in a) clay mineralogy, c) $^{87}Sr/^{86}Sr$, d) QEMSCAN and XRF proxies for pyrite, e) $\varepsilon Nd_{(0)}$, f) bulk carbonate stable isotopes and g) detrital sand grain flux across the Site U1411 EOT interval. Arrows at ~ 33.6 Ma indicate inferred influence on $^{87}Sr/^{86}Sr$ and $\varepsilon Nd_{(0)}$ isotope ratios by authigenic minerals- see text for explanation (see Appendix B for data). Estimations for the onset/intensification of NADW are also displayed (b).

Combining the $\varepsilon Nd_{(0)}$ and $^{87}Sr/^{86}Sr$ of the coarse and <20 µm fraction data from the Site U1411 EOT interval shows that the <20 µm fraction data generally has a higher $^{87}Sr/^{86}Sr$ and lower $\varepsilon Nd_{(0)}$ than the coarse fraction data, though there is overlap between the two, particularly for $^{87}Sr/^{86}Sr$ (Figure 3.6). When comparing this data to published data from North Atlantic terranes, the Site U1411 coarse detrital grains display $\varepsilon Nd_{(0)}$ and $^{87}Sr/^{86}Sr$ values that appear to best match data from Scandinavia and North America, specifically the Proterozoic-age Grenville province terrane. This is in agreement with the Pb isotope data from feldspars featured in Section 2.3.2. In contrast, however, the <20 µm fraction data is skewed towards lower $\varepsilon Nd_{(0)}$ and higher $^{87}Sr/^{86}Sr$ values more similar to Archean-age terranes in North America and Greenland (Figure 3.6).

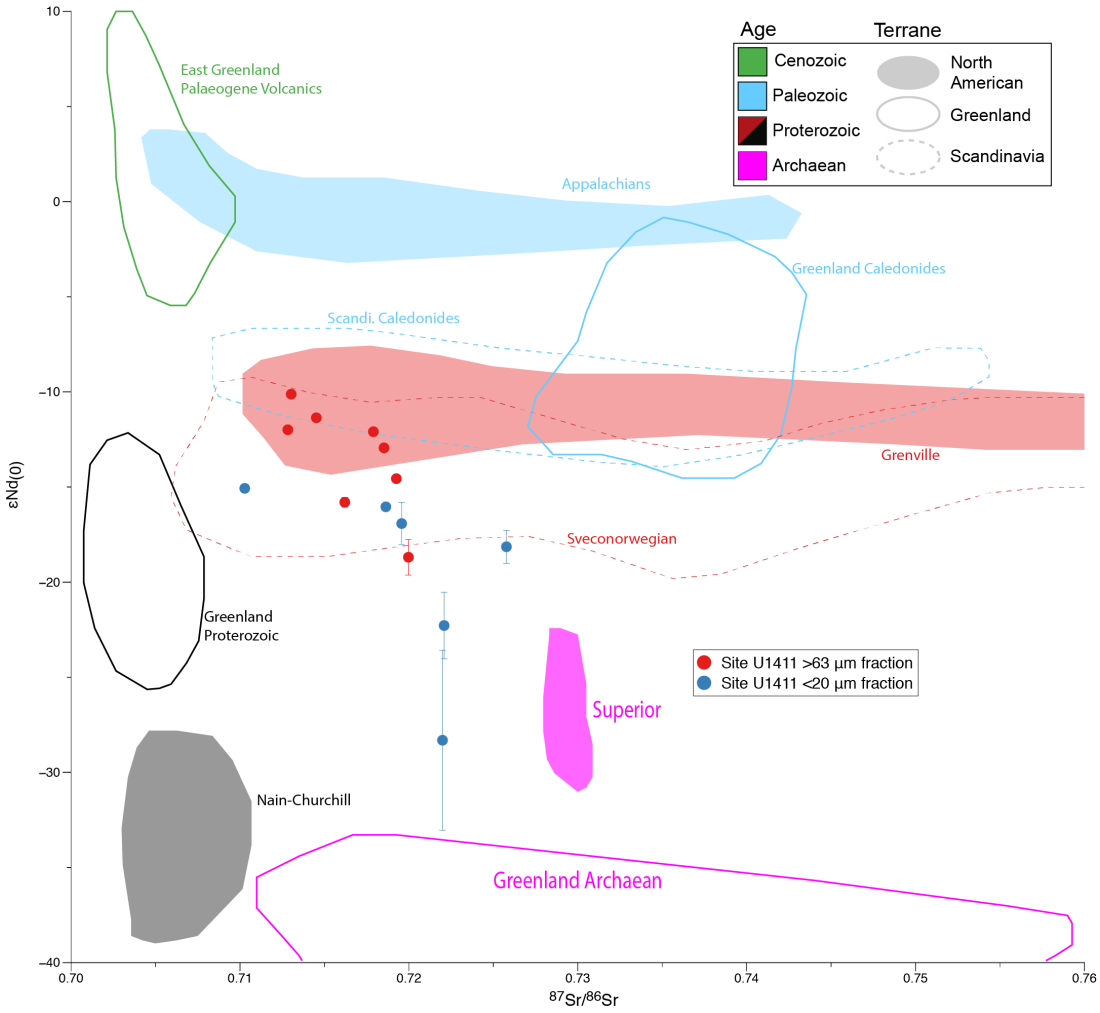

Figure 3.6: Cross plot of $^{87}Sr/^{86}Sr$ and $\varepsilon Nd_{(0)}$ isotope data of coarse and fine fraction detrital grains from Site U1411, plotted alongside published terrane data for the main North Atlantic provinces as displayed in Figure 2.1 (See Appendix B for references).

As detailed above, $\varepsilon Nd_{(0)}$ is likely to be a more useful tool than $^{87}Sr/^{86}Sr$ in determining the provenance of different grain size fractions (Figure 3.7). The coarse fraction $\varepsilon Nd_{(0)}$ data from Site U1411 matches fine glaciomarine sediment from the Norwegian Strait, and both coarse and fine sediment from the Gulf of St Lawrence (GSL), local to the SENR. Note that the $\varepsilon Nd_{(0)}$ of both size fractions for the GSL sediments are indistinguishable, but only the coarse fraction data from Site U1411 matches this data (Figure 3.7).

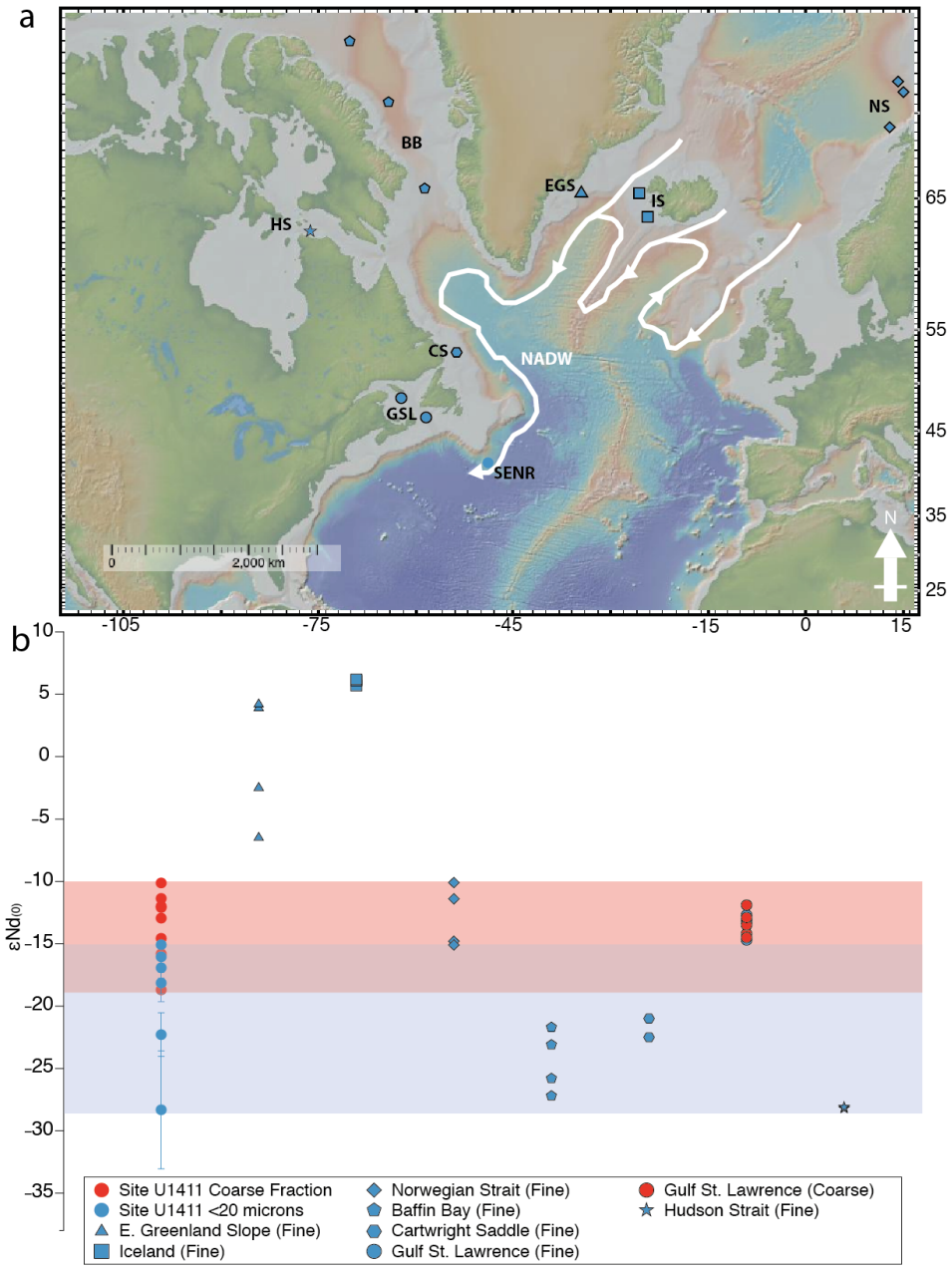

Figure 3.7: a) Location of fine-grained glaciomarine sediments from the North Atlantic in relation to the SENR and the modern flow-path of NADW. Bathymetric base map is from GeoMapApp (http://www.geomapapp.org). b) Range of $\varepsilon Nd_{(0)}$ isotope data of coarse (red) and fine (blue) fraction detrital grains from Site U1411, compared to $\varepsilon Nd_{(0)}$ isotope data from glaciomarine sediments (Farmer et al., 2003).

The $\varepsilon Nd_{(0)}$ of the Site U1411 <20 µm fraction older than 33 Ma overlaps with fine glaciomarine sediment from Hudson Strait, Baffin Bay, and the Cartwright Saddle. This suggests that the fine material that comprises the majority of the drift deposits at Site U1411 was transported from further north than the coarse material (Figures 3.5, 3.7). The $^{87}Sr/^{86}Sr$ and coarse fraction $\varepsilon Nd_{(0)}$ values converge later (~33 Ma) than the step-like increases in detrital sand flux (34 & 33.6 Ma), and the relative proportions of clay minerals also only show a significant trend after ~33 Ma (Figure 3.5a, e). This

separation may provide further evidence therefore that the driver behind the detrital coarse fraction is separate from the bottom current responsible for the clay and fine silt component. The change in the latter, seen at ~ 33 Ma, may represent an increase in bottom current intensity occurring after the EOT, as predicted by Via and Thomas (2006) (Figure 3.5a).

The decrease in smectite, and corresponding increase in chlorite and illite, after ~33 Ma implies the source for the clay component at Site U1411 is changing from a humid environment, featuring chemical weathering, to a cooler environment featuring more physical weathering (Figure 3.5a) (Diester-Haass and Zahn, 2001; Ehrmann, 1998). Previously published clay mineral analysis of Eocene and Oligocene sediments from the Labrador shelf and central Labrador Sea show lower smectite (11-54% vs. 60-80% for Site U1411) and higher illite (18-41% vs. 15-25% for Site U1411), and so the change in clay mineralogy after 33 Ma may reflect a stronger bottom current carrying clay minerals from colder environments to the north, featuring enhanced physical weathering (Hiscott, 1984). Alternatively, however, the change might represent global cooling leading to changes in weathering at the source region, without necessarily implying a change in provenance (Liu et al., 2009). The merging of <20 μm and coarse fraction $\varepsilon Nd_{(0)}$ values appears to occur at the same time that the clay mineralogy is changing (after ~33 Ma).

The <20 μm $\varepsilon Nd_{(0)}$ samples younger than 33 Ma overlap fine glaciomarine sediment from the Gulf of St Lawrence (Figure 3.7), rather than reflecting a more distal source, as the clay mineralogy seems to suggest. This could reflect that, as the delivery of coarse material from local sources increases up-core, silt being delivered from the same source as the coarse fraction may be overprinting the initial, more distal source of the <20 μm $\varepsilon Nd_{(0)}$ samples. The >1 μm GSD profiles (Figure 3.3) show that a large proportion of the coarser peak is also in the <20 μm fraction (though it should be remembered that ~60% of the drift material is <1 μm). Confusingly, however, the predicted clay mineral response to the input of fine sediment from areas more local to the SENR after 33 Ma would be an increase in smectite (i.e. a more southerly source, hence more chemical/less physical weathering). It is possible that though some of the silt in the <20 μm $\varepsilon Nd_{(0)}$ samples may be coming from sources proximal to the SENR,

insufficient clay is being inputted to significantly affect the mineralogy of the <2 μm fraction, which is dominated by material from more distal sources.

It appears difficult to precisely determine therefore whether the changes in clay mineralogy and Nd isotopes of fine material at ~33 Ma represent a reorganisation of bottom currents, but it does appear that the detrital clay and fine silt in the Site U1411 EOT interval is being controlled by a different driver and supplied by different source areas to the coarse detrital fraction. Nd isotopic analysis of fish teeth, alongside benthic foraminiferal carbon isotopes, might better reveal the nature of any deep-water current changes over the SENR (Pusz et al., 2011; Scher and Martin, 2008).

3.3.3 Contour currents or turbidity flows as a mode of deposition

The previous chapter concluded that coarse detrital grains from Sites U1411 and U1406 were not iceberg-rafted, and that they likely came from local North American provinces. Given the nature of the drift deposits in which they were deposited, and the changes in oceanography and sea level predicted across the EOT, these detrital grains therefore likely reflect either change in the intensity of the bottom current or local change in sediment supply as a result of sea level change.

It is unlikely that downslope processes, such as turbidity currents or debris flows, were directly delivering this detrital sand to the sites as the Site U1411 drift is perched on the SENR, rather than at the base of the Grand Banks, and the drill site is sheltered from transport of material down the spine of the ridge by a seamount (Figure 3.1) (Boyle et al., 2017). Furthermore, sedimentary structures typical of transport by turbidity currents in core sections, such as Bouma sequences, are absent (Bouma, 1962). However, these may have been subsequently destroyed by bioturbation. Pb isotope analysis (Section 2.3.2) argues against a downslope source as this suggests that material at Site U1406 comes from the same source as U1411 across the EOT interval. Site U1406, sitting on an isolated seamount, is more bathymetrically isolated from downslope deposition of sand than Site U1411. The flux record here still shows that there is sand throughout the interval, and that it increases across the EOT as at Site U1411, although the volume of sand being deposited at Site U1406 is two orders of magnitude lower than at Site U1411 (Figure

3.2). These observations are consistent with sediment being carried by a bottom current flowing from the north, being deposited as the current hits the northern flank of the SENR (Site U1411). As a result very little material was carried across the SENR and past this bathymetric feature and on to Site U1406.

The relationship between the flux record and the isotope stratigraphy across the EOT suggests glacioeustatically-controlled sedimentation changes are controlling the detrital sand rather than current strength. However, the GSD data presented here, combined with further work by Brian Romans and Kristin Chilton on the Site U1411 fine fraction (in preparation), does not suggest a step-increase in current strength across the EOT at Site U1411. The interpretation of seismic facies on the SENR does point towards an intensification of current strength at depth (>5000 mbsl) at this time however (Boyle et al., 2017).

As the bathymetry and the relationship between sites U1411 and U1406 appear to rule out downslope sand deposition as a direct method of delivery and there is little evidence for changes in current strength being the sole control of the delivery of coarse material, it is possible therefore that a combination of the two exists: that nearby off-shelf deposition (influenced by glacioeustasy) emplaces detrital material into the bottom current, which then transports it a short distance onto the SENR.

Glacioeustatic sea level change, especially influential after the Oi-1 shift, could result in increased off-shelf transport of sediment by, for example, turbidity currents. This could then be incorporated into the nepheloid layer of the bottom current at the base of the slope, and carried a short distance to deposition centres on the ridge. Modern day studies have demonstrated that turbidites are capable of transporting sediment from the shelf break all the way to the abyssal plain, and that this material can then be entrained and carried short distances by the nepheloid layer (Amos and Gerard, 1979; Gardner et al., 2017). A further study has also documented the combination of turbidites and current transportation in depositing (albeit fine) material onto the tops of the Fogo Seamounts nearby to the SENR and J-Anomaly Ridge (Figure 3.1), which are much more isolated even than Site U1406, rising some 1000 m from the surrounding seafloor (Alaf, 1987). Another study of Pleistocene sediments from the J-

anomaly Ridge reports sea-level controlled turbidite delivery into the nepheloid layer (Piper et al., 1994).

3.3.4 Relative pacings of the coarse detrital fraction and the fine-grained drift deposits

The de-trended U1411 flux record of the Site U1411 EOT interval appears to show a cyclical nature, particularly in the Earliest Oligocene, before ~33.3 Ma (Figure 3.8). There also appears to be cyclicity in the Zr/Rb XRF data for the same interval.

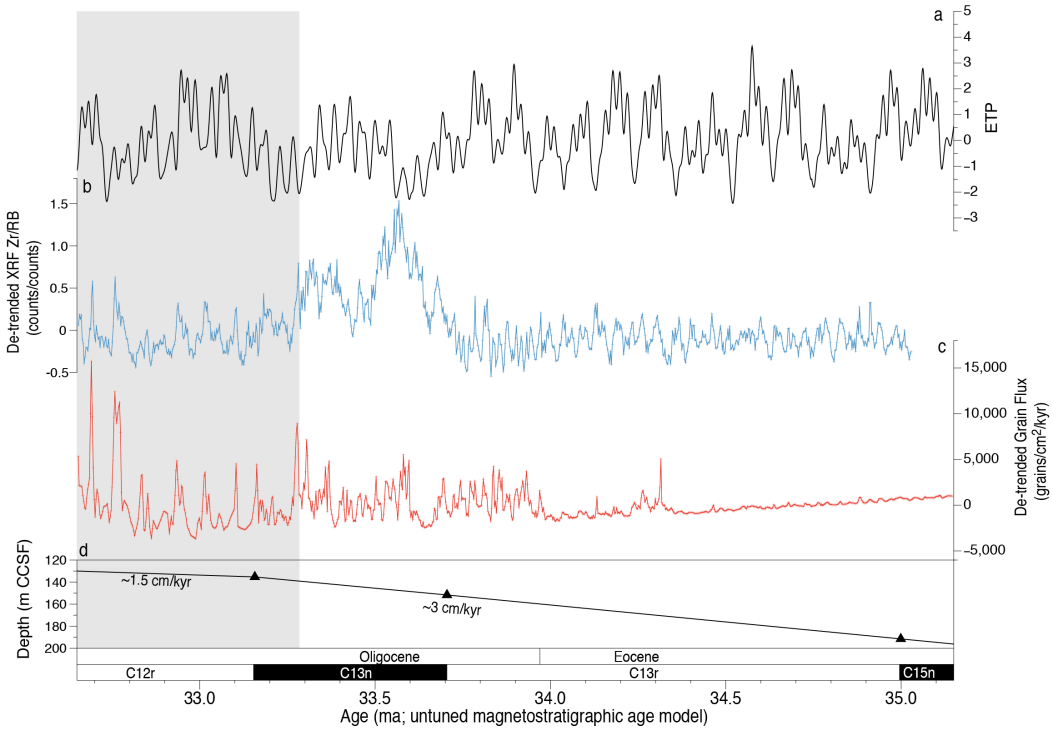

Figure 3.8: a) an arbitrary mix of eccentricity, tilt (obliquity), and precession, plotted alongside b) de-trended Zr/Rb XRF data and c) de-trended detrital sand grain flux across the EOT interval at Site U1411. d) The age-depth plot used to create the untuned ages for spectral analysis is also shown. The Black horizontal bar in panel c indicates the interval in which prominent cyclicity is apparent (Laskar et al., 2004; Wade and Pälike, 2004).

MTM spectral analysis of the de-trended grain flux record for the EOT interval in the age domain (Figure 3.9b) shows four peaks that reach the 99% CI in the window of expected orbital periodicities. According to the shipboard magnetostratigraphic age model, these indicate cycles with periods of ~78-89, 36-39, 24, and 20 kyr. The MTM analysis of this record in the depth domain also shows cycles that exceed the 99% CI (Figure 3.9f). Assuming a sedimentation rate of 3 cm/kyr these return periods of 42-46 kyr and 24 kyr. This rate was obtained as an average of the linear sedimentation

rate for the entire interval, based on magnetostratigraphic datums (Figure 3.8). These peaks likely correlate to the second and third peaks identified in the age domain.

MTM spectral analysis of the interval younger than ~33.3 Ma identifies several of the cycles also present in the full interval of the age-domain flux record (72-80, 34-39, and 20 kyr), again above the 99% CI (Figure 3.9a). There are two cycles above the 99% CI in the depth domain (Figure 3.9e). Using a sedimentation rate of 1.5 cm/kyr (this matches the interval that featured extensive cyclicity; see age-depth plot in Figure 3.8), these return periods of 68-79 and 36-39 kyr, which correlate to the first and second peaks in the age domain.

MTM spectral analysis of the Zr/Rb EOT interval in the age domain did not reveal any peaks above the 99% CI in the target window, however there was one peak between the 95-99% corresponding to a ~31 kyr cycle (Figure 3.9c). The MTM spectral analysis in the depth domain identified one peak above the 99% CI, corresponding to a cycle of 22-23 kyr, assuming a sedimentation rate of 3cm/kyr (Figure 3.9g). There was also a peak above the 95% CI, but below the 99% CI, at ~31 kyr.

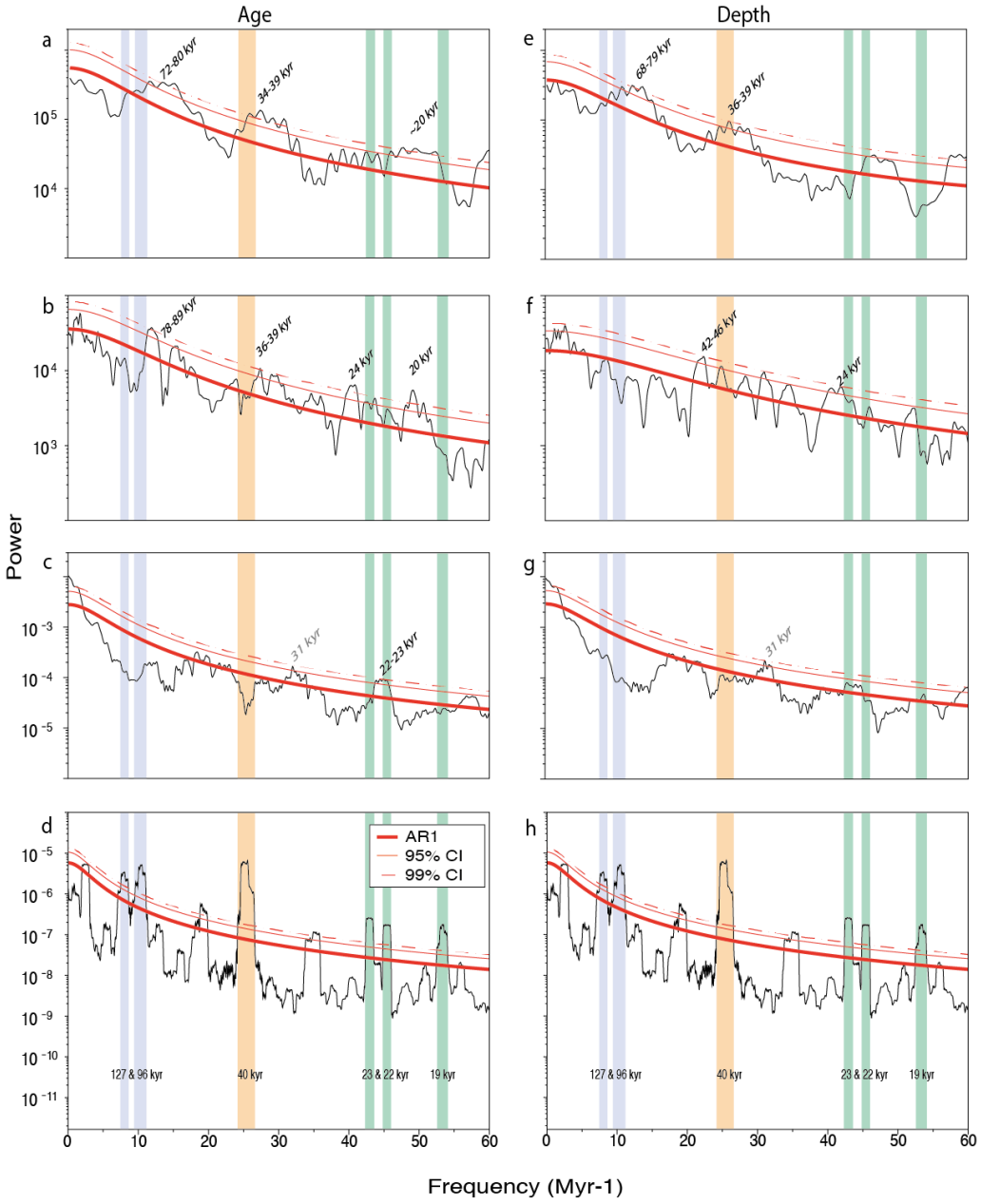

Figure 3.9: MTM periodograms in the age domain of a) grain flux record above 33.3 ma, b) full flux record, c) Zr/Rb XRF record, and d) arbitrary ETP mix. Panels e-h display spectral analysis of the same data in the depth domain. The green, yellow, and blue vertical bars in each panel show the frequencies of precession, obliquity, and eccentricity cycles interpreted from the spectral analysis of the ETP mix in Figure 3.8.

Wavelet analysis of the grain flux record in the age domain across the EOT (Figure 3.10b) reveals higher frequency cycles (aligned to precessional peaks) that appear intermittently from 34 Ma; ~35-40 kyr cycles then appear at ~ 33.3 Ma, aligning with the obliquity peak. ~80-90 kyr cycles first appear at ~33.15 Ma, these appear to be slightly shorter than the expected eccentricity cycles. Wavelet analysis of the same interval in the depth domain is broadly in agreement, however here there is no ~80-

90 kyr cycle detected above the 95% CIs (Figure 3.11b). Wavelet analysis of the <33.3 Ma interval in age and depth domains both intermittently show periodicities that line up with precessional cycles, and both appear to show obliquity cycles above ~32.85 Ma/130.5 m CCSF (Figures 3.10a & 3.11a). The wavelet analysis on the depth domain for this interval also identifies the ~70-80 kyr cyclicity over the same area as the age domain, unlike in the wavelet analysis of the full EOT interval.

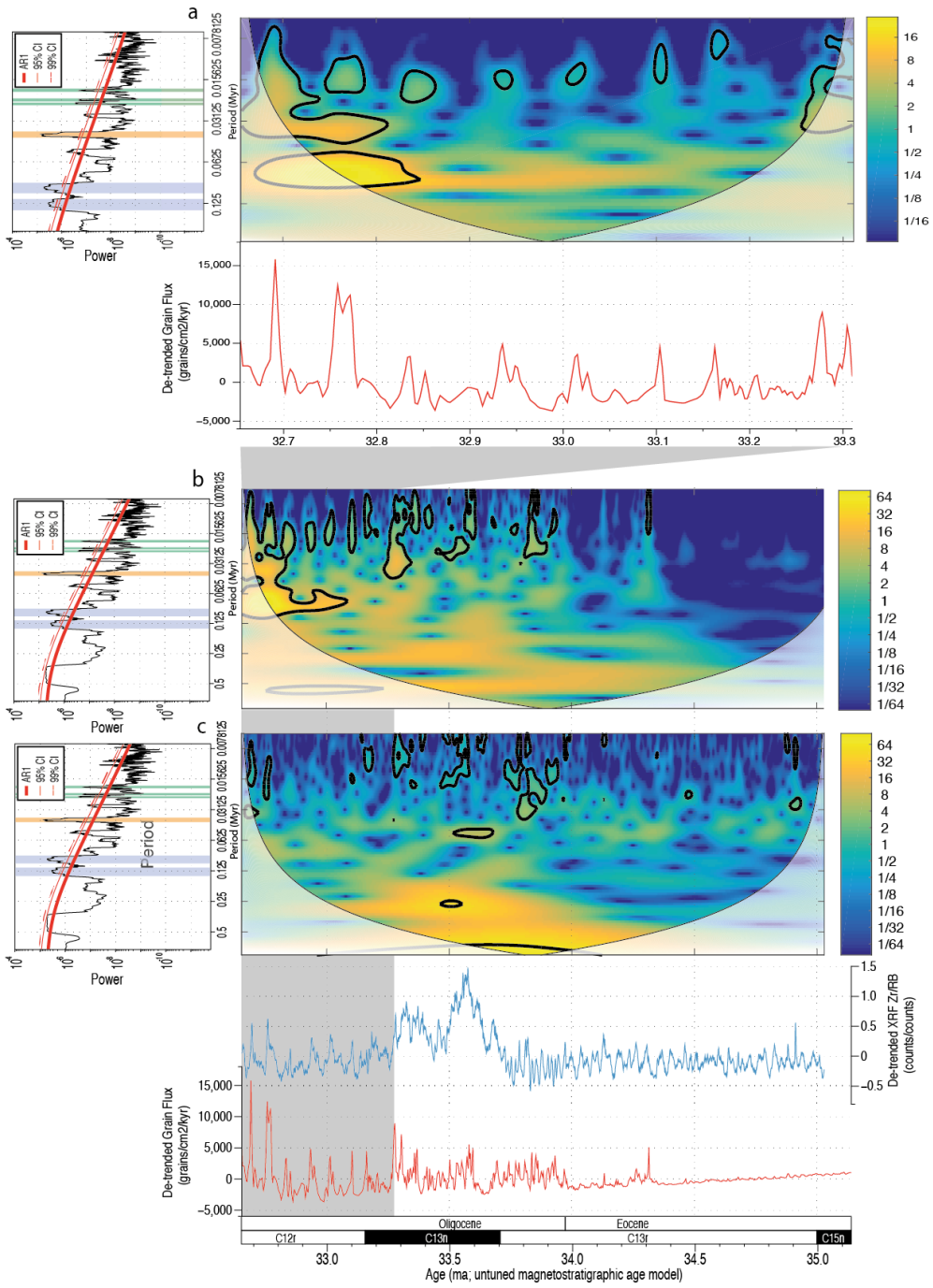

Figure 3.10: Wavelet analyses in the age domain of a) grain flux record after 33.3 ma, b) grain flux record across the EOT interval, and c) Zr/Rb XRF record across the EOT interval. A periodogram of the ETP mix is displayed against each panel to highlight key periods.

Wavelet analysis of the Zr/Rb in age and depth domains reveals that the periodicities identified by MTM spectral analysis dominantly occur above 160 m CCSF/after ~34 Ma (Figures 3.10c and 3.11c). In both analyses, there is very little periodicity above ~31 kyr, and there is no evidence of the ~70-80 ka periodicity in the youngest part of the study interval in the flux record. There are only sporadic suggestions of obliquity-like cyclicity above the 95% CI.

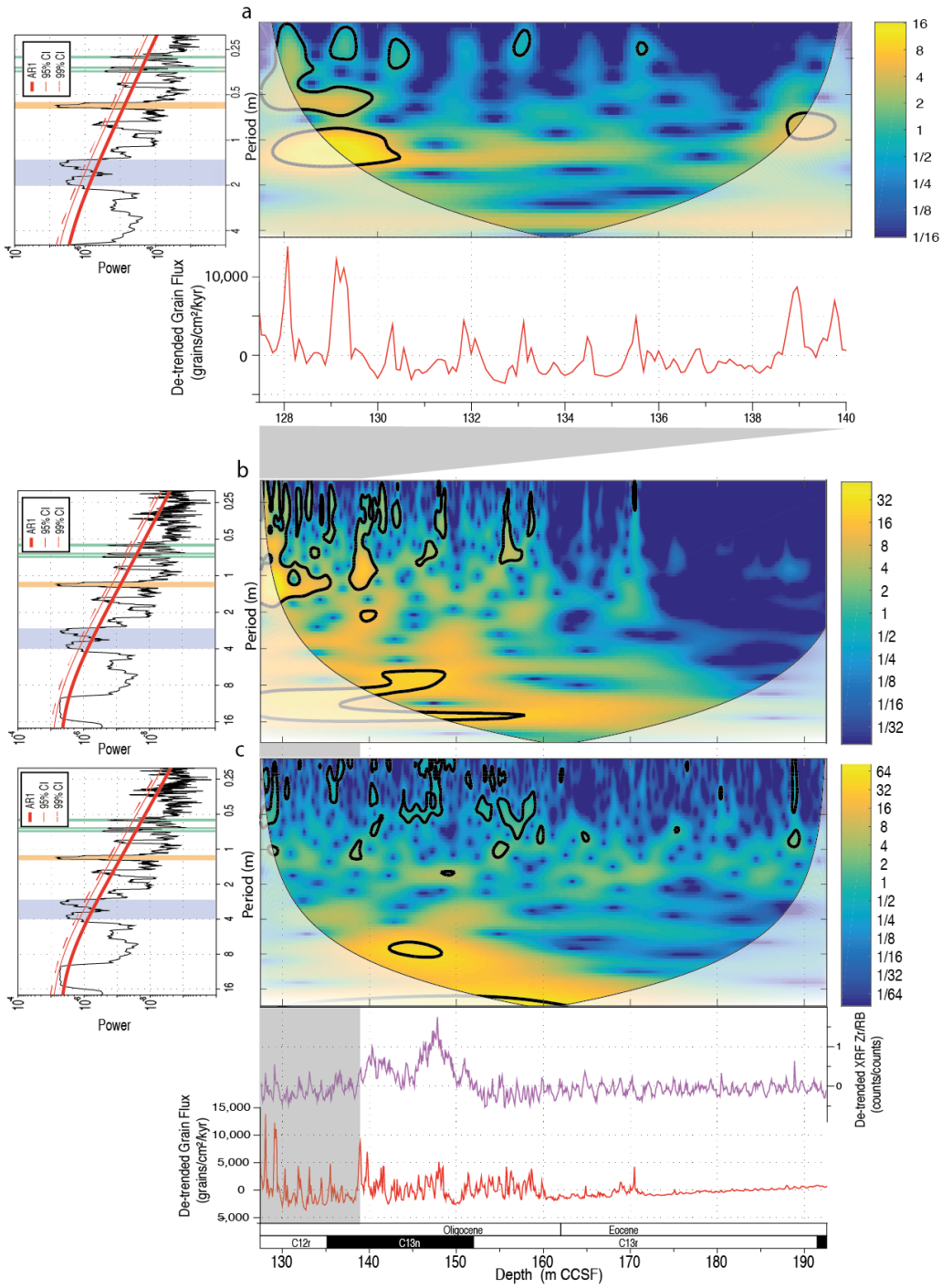

Figure 3.11: Wavelet analyses in the depth domain of a) grain flux record above 33.3 Ma, b) grain flux record across the EOT interval, and c) Zr/Rb XRF record across the EOT interval. A periodogram of the ETP mix is displayed against each panel to highlight key periods.

It appears that precessional cycles are present in both the Zr/Rb and grain flux records, particularly above ~160 m CCSF/33.9 Ma. Assuming that Zr/Rb reflects variations in deposition of the bulk of drift material (i.e., clay and fine silt), it would therefore seem that another influence is responsible for the lower frequency cyclicity also seen in the sand flux record. This apparent disparity also fits in with the bimodal distribution seen in the grain size distribution of the detrital component, and differing provenance of fine and coarse material (Section 3.3.2).

The presence of ~40 kyr cycles in this interval, as identified by MTM and wavelet spectral analysis of both the depth and age domains, suggests that above this point the flux record is being influenced by obliquity cycles, while the bulk of the drift is still being paced by precession. The 70-80 kyr cyclicity might, therefore, be picking up a 'double beat' of the obliquity signal, though allowing for changes in sedimentation rate this may in fact be a 100 kyr eccentricity signal (Huybers and Wunsch, 2005). This observation is significant as the potential obliquity-influenced cyclicity only occurs in the earliest Oligocene after the Oi-1 event, i.e. after a large (~70 m) fall in eustatic sea level (Miller et al., 2009). It may be that this sea level fall altered sedimentation patterns on the shelf-break at the nearby Grand Banks, leading to more sand being eroded and transported off-shelf, before being carried to the site. Obliquity-dominated eustatic sea level change, also featuring the eccentricity cycles, has been identified elsewhere in the N. Hemisphere in the Early Oligocene (Abels et al., 2007). The fact that the detrital sand seen at Site U1411 appears to require transport by bottom currents for a short distance, rather than being directly deposited by downslope sedimentation, may explain why the precessional cycles seen in the Zr/Rb record are also present the in the grain flux record.

It should be stressed that the age model used here is currently un-tuned, and there is uncertainty on the accuracy of the sedimentation rates. It is therefore difficult to be definitive on the source of the periodicities. The wavelet analysis for example appears to suggest a 'migration' in the periodicity of the interpreted processional cycles (Figure 3.10a). Even if the age model, and hence the sedimentation rates, change however, there are still cycles that exist in the flux record but not in the Zr/Rb, suggesting a difference in the mode of delivery for the detrital sand compared to the bulk of the drift deposits.

3.4 Conclusions

Analysis of the sand flux, grain size distribution, cyclicity, and provenance of the Site U1411 detrital component appears to reveal a complex combination of eustatically controlled sedimentation changes and bottom current controlled drift deposition. The flux of detrital sand across the EOT appears to represent the coarse tail of a sediment source separate from the majority of the fine sediment being carried by the bottom current, based on differing GSDs, Nd isotopic signatures, and dominant cyclicity (Hass, 2002; Prins et al., 2002).

The observation that the flux record appears to increase step-wise across the EOT, with the largest step being after the Oi-1 event, suggests that glacioeustatic sea level change may be the driving factor controlling sediment delivery from local shelf-edges to the nepheloid layer (Alaf, 1987; Piper et al., 1994). This is supported the differing cyclicity in the sand flux record compared to the rest of the drift, which appears to show 41 ka obliquity and potentially 100 ka eccentricity cycles, similar to another sedimentation record from the Early Oligocene (Abels et al., 2007). The step-like increase of the grain flux record suggests that, if the interpretation of glacioeustasy as a driver of grain flux is correct, there was a two-step increase in ice volume across the EOT. The EOT-1 step is difficult to identify in the bulk carbonate oxygen isotope record for Site U1411; only the Oi-1 shift is clearly visible. This is perhaps surprising given the step-like nature of the grain flux; the development of a benthic foraminiferal isotope record may better resolve the isotope stratigraphy.

There is little evidence in the clay mineral analysis and fine fraction Nd and Sr isotopes for a change in bottom current intensity prior to, or directly in time with, the EOT, as interpreted by previous studies (Abelson and Erez, 2017; Pusz et al., 2011) though there may be evidence for a change in circulation ~33 Ma, in broad agreement with a study by Via and Thomas (2006). The confidence of this interpretation could be improved however by increasing the resolution of these proxies.

The identification of this record of off-shelf sand deposition is important as it suggests that the off-shelf transport of sediment occurred by the end of the EOT in the Northwest North Atlantic, controlled by eustatic change, and demonstrates the far-reaching effects of the formation of Antarctic ice over the EOT. The fine fraction (and

fine sand) from this sediment was re-distributed by bottom currents, which may have left behind a coarser lag deposit of potential interest as a hydrocarbon reservoir.

Understanding that some of the silt fraction at Site U1411 may have been derived from a secondary source, and not influenced purely by bottom current intensity, is also important if attempts are to be made at calculating bottom current intensity via the sortable silt proxy (Hass, 2002; McCave et al., 1995; Mulder et al., 2013). This analysis, combined with the conclusions of Chapter 2, also suggests that caution should be shown when interpreting detrital sand at a site as IRD, even when the downslope delivery of sediment does not appear to have a direct influence over sediment deposition at a given site.

Chapter 4 Cenozoic changes in sea level, sedimentation and morphology in the Newfoundland Basin and Southeast Newfoundland Ridge

4.1 Introduction

To fully understand the significance of the climate signals held by the Site U1411 interval across the Eocene Oligocene Transition (EOT), and indeed other sites from Expedition 342, it is necessary to frame them in a broader regional context of Cenozoic oceanographic, sea level, and sedimentary change. It is also important to consider that the bathymetry and palaeogeographic location of the region at the time of study may well have differed significantly from the present day. Here, this task is achieved by analysing seismic profiles and well log data (wireline/lithology and palaeobathymetry), and using these to inform the Halliburton Neftex® plate tectonic model, which is then used to generate a palaeogeographic Digital Elevation Model (DEM) of the region for the Eocene-Oligocene Boundary (EOB) (Vérard et al., 2015).

The study region for this chapter consists of the Southeast Newfoundland Ridge (SENR), the area of abyssal plain directly to the north — referred to hereon as the Newfoundland Basin, and the adjacent continental slope and shelf to the west (the Grand Banks) and north (the Flemish Cap) (Tucholke et al., 1989). The Newfoundland Basin lies over transitional continental crust, with the continent-ocean boundary (COB) marked by the J-anomaly to the East. The J-Anomaly is the oldest identified oceanic crust magnetic anomaly in the region, and is thought to have formed between anomalies M0 and M1, giving it a Barremian-Aptian age (126-128.6 Ma) (Austin et al., 1989; Gradstein et al., 2012; Tucholke et al., 1989; Tucholke and Ludwig, 1982). The Newfoundland margin itself separated from the Iberian margin through multiple phases of rifting that ended in the late Aptian (~114 Ma) (Peron-Pinvidic et al., 2010). The final rifting phase also saw the emplacement of sills in the Newfoundland Basin, and the development of widely traceable erosional unconformity known as the 'U' or Avalon unconformity. Since these events occurred, the Newfoundland margin and basin has been tectonically inactive, though may have undergone deformation

through Dynamic Topography (Section 1.14) (Austin et al., 1989; Peron-Pinvidic et al., 2010; Péron-Pinvidic et al., 2007).

The basement of the SENR, unlike the Newfoundland basin, is oceanic; the ridge is thought to have been formed by magma supplied by a mantle plume lying under the rifting zone between the Barremian and earliest Aptian (chrons M4-M0) (Tucholke et al., 2007; Tucholke and Ludwig, 1982). Fragments of diagenetically altered coral recovered from Integrated Ocean Drilling Program (IODP) Site 1407, dated to the Albian age, imply that the SENR was exposed to meteoric waters shortly after its formation (Norris et al., (2014). Since the Late Cretaceous, Cenozoic-age sediments have been deposited in the Newfoundland basin and plastered onto the SENR, under the influence of changing oceanographic conditions, depositional regimes on the Grand Banks, and sea level change. A succession of drifts have been characterised on the SENR, but how these sediments relate to contemporary sedimentation in the Newfoundland Basin remains unknown (Boyle et al., (2017).

Well data:

Aside from IODP Exp. 342, there is little available material that is of EOT-age from IODP resources along the Newfoundland Margin. This is especially true on the Grand Banks, making it difficult to relate the changes seen on the SENR to any potential sedimentary reorganization in this region. There is however a wealth of data available across the Grand Banks in the form of wells and boreholes drilled for the purposes of hydrocarbon exploration. Although these hydrocarbon industry wells lack the temporal resolution and age control of typical IODP drillsites, they are used here to characterise longer-term sedimentological changes (using lithological interpretations and wireline logs) and depositional environments (using biostratigraphically derived palaeobathymetric interpretations).

Seismic data:

A recently published study developed a seismic-stratigraphic framework for the Cretaceous through present sedimentary succession on the SENR by integrating data from IODP Exp. 342 boreholes with seismic facies interpretations from Cruise KN179-01 (Boyle et al., 2017; Norris et al., 2014). The study identified pre-drift, drift accumulation, and post-drift phases of sedimentation through the Late Cretaceous and Cenozoic, but the lateral extent of these sedimentation changes, and how they relate to oceanographic changes elsewhere in the North Atlantic, merit further investigation. This chapter expands the interpretations made at the SENR to sedimentary changes 'up-stream', along the continental slope and in the Newfoundland Basin, and to other known spatially extensive oceanographic events identified in the North Atlantic. This analysis allows the changes interpreted on the SENR across the EOT to be viewed in relation to the rest of the Cenozoic, and in terms of any up-stream oceanographic change.

Reconstructing palaeogeography:

The interpretation of well and seismic data, together with the Halliburton Neftex® plate tectonic model, are used to reconstruct the palaeogeography and geographic location of the SENR and the Grand Banks, continental slope, and Newfoundland Basin to the North in this chapter. Reconstruction of the SENR at the time of the EOT allows for further exploration of the hypothesis that silt and fine sand were carried up on to the ridge by bottom currents from the Newfoundland Basin, presented in Chapter 3. Furthermore, the model also allows for the reconstruction of the width and geometry of the continental shelf above the SENR and Newfoundland Basin, the location of the palaeo-coastline, and the palaeolatitude of the study area in general. Understanding the geometry of the shelf can inform on the likelihood that sea level change would result in off-shelf deposition, and defining the palaeo-coastline can reveal likely sources of the sediments seen on the SENR (the detrital sand fraction in particular appears to have a local provenance, see Pb isotope data in Section 2.3.2 and Nd isotope data in Section 3.3.2). Placing the study area at the correct palaeolatitude also further informs predictions on the likelihood of sea ice formation, as discussed in Section 2.4.

4.1.1 Aims

The first aim of this chapter is to characterise the changes in sediment facies and depositional environments on the Grand Banks across the EOT, determine whether these are linked to glacioeustatic sea-level change, and explore any impacts on off-shelf deposition.

The focus of this chapter will then move to determining the extent of the pre-drift, drift, and post-drift regimes identified on the SENR, and exploring the relationship with larger-scale oceanographic changes in the Newfoundland Basin.

Finally, interpretations made from well and seismic data will be used to reconstruct the paleogeography of the Newfoundland margin at the time of the EOT, and to explore the magnitude of the contour current required to transport the detrital sand documented in Chapter 3 onto the SENR.

4.2 Methods and materials

4.2.1 Well data exploration of the Grand Banks

As highlighted in this thesis, high-resolution and in-depth analysis of marine sediment recovered from IODP expeditions can provide a multitude of proxies on palaeoclimatic and sedimentary changes with a very good temporal resolution. The issue of spatial resolution, however, represents a key problem, as IODP cores featuring EOT-age sediments in the Northwest North Atlantic are sparse. It would be difficult to ascertain how geographically extensive the changes seen at Site U1411 are using IODP data alone. Furthermore, the interpretation provided in Chapter 3 involved the off-shelf transport of detrital sand across the EOT, but there is currently little material available from IODP expeditions (or similar) from the Grand Banks to help explore this conclusion.

Collaboration with Halliburton Neftex ® allowed this issue to be tackled by accessing their extensive database of industrial wells. Thirty-one wells with Late Eocene to

Early Oligocene sediments were found in the area of interest (Figure 4.1) and were accessed using IC™. For the purposes of this study, the following data were used from these wells, where available: Palaeobathymetry, determined from fossil assemblage data; Lithology, interpreted from wireline logs, and cuttings; and two wireline logs, Gamma-Ray (GR) and Sonic (Δt). These wells were grouped into four areas for convenience: North Grand Banks, Flemish Pass, East Grand Banks, and West Grand Banks (Figure 4.1).

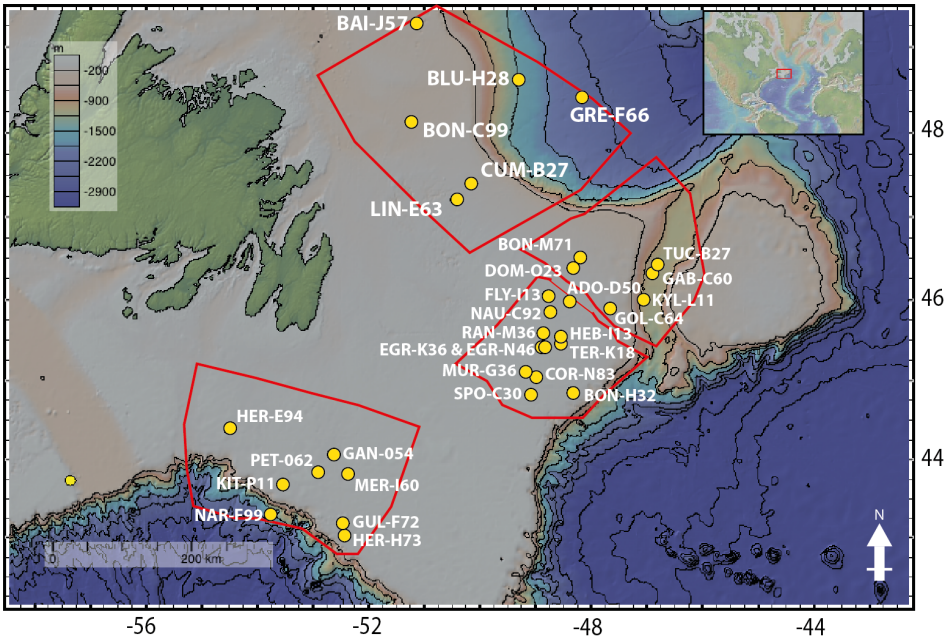

Figure 4.1: Map of the study area showing the locations of the wells used to reconstruct changes in sedimentation and palaeobathymetry across the EOT. The wells were divided into groups to make analysis more manageable (red boxes), from north to south these are: N Grand Banks, Flemish Pass, E Grand Banks and W Grand Banks. Map created using GeoMapApp (http://www.geomapapp.org). See Appendix D for well charts.

4.2.1.1 Paleobathymetry or Depositional Environment

Many of the wells records identified in the Halliburton Neftex® database include interpretations of the palaeobathymetry and/or depositional environment. These interpretations, made by either the exploration companies responsible for drilling each well or by biostratigraphy subcontractors, classify the environment according to water depth using terms such as 'neritic' or 'bathyal'. These interpretations were made by analysing the fossil assemblages in cuttings from each well. However, these cuttings were only taken intermittently, rather than providing a continuous record. Age control was limited to the identification of long-ranging biozones (generally paly

zones based on dinocysts), generally resolving age control to the sub-epoch/stage level (e.g., Late Eocene/Priabonian). As the purpose of this thesis was to investigate spatial changes across the EOT, the approach taken was to characterize the state of the palaeobathymetry and lithology variables for both the Late Eocene (Priabonian) and Early Oligocene (Rupelian), where data were available. A well was only used where these stages or sub-epochs were identified, as it was deemed that wells that only constrained data to the epoch level were not sufficiently accurate.

The Late Eocene and Early Oligocene were then compared, and any changes from the two time-steps were recorded. The various descriptions for each well and each sub-epoch were organized into eight classes, from shallowest to deepest, as follows: marginal-neritic, inner neritic, neritic, outer neritic, neritic-bathyal, upper bathyal, and lower bathyal.

4.2.1.2 Lithology

IC™ was used to identify wells with interpreted lithology data for the Late Eocene and Early Oligocene in the same way as described for palaeobathymetry: the same uncertainties described for the age control of palaeobathymetry interpretations therefore also apply here. The lithological interpretations, made by geophysical consultants on behalf of the original industrial operator, are based upon a combination of analysis of cuttings and petrophysical interpretation of available wireline logs. For this study, these interpretations were grouped into four classifications (from finest to coarsest grain size): shale, siltstone, silty sandstone, and sandstone.

4.2.1.3 Wireline Logs

In addition to interpreted changes in lithology and palaeobathymetry, several of the industrial wells in the database have down-hole records of physical properties, which might also reflect changes in sedimentation/deposition across the EOT. The Gamma Ray tool in particular is commonly used in industrial well logging to characterise changes in lithology (Rider, 2002). Sonic logging can also reflect changes in lithology and effective porosity in the sedimentary column.

The practice of Gamma Ray logging involves lowering a receiver down the well and recording a continuous uphole record of natural gamma radiation. Different lithologies emit varying amounts/spectra, and so the technique can be used to detect changes in sedimentary facies. In particular, shales tend to emit more gamma radiation than sandstones and limestones, due to the presence of potassium in their clay component and the ability of the clay component to absorb thorium and uranium through cation exchange (Rider, 1990). The wells featured in this report have gamma ray records in two different formats: GR API (American Petroleum Institute), and GR usl (unscaled logs). GR API reflects a weighted combination of the contributions of uranium, thorium, and potassium; GR usl is a relative scale used on wireline data from the public domain where the absolute scale was not provided, but trends can still be discerned. Typical GR API values for shale range from 70-150, and sandstone from 15-30 (Morton-Thompson, 1992), though depending on hole conditions sandstone GR API values can reach as high as 169. Shales can have a GR API range of 24-1000 (Rider, 2002).

Sonic logging can also reflect changes in the sedimentary column. The process involves lowering a piezoelectric transmitter downhole along with a receiver; the time taken for sonic waves emitted from the transmitter to travel through the surrounding rock and be recorded by the receiver is referred to as the transit time (Δt or Dt). In the context of lithological changes, changes in Δt reflect changes in lithology, effective porosity, and fluid content (Sheriff and Geldart, 1995). It is a less effective tool for detecting changes in lithology than GR, but can still be useful in discriminating shales and sandstone, for example. Sandstones tend to show Δt values between 55-80 μs/ft, depending on how compact they are, whereas shales show more variability and tend towards higher transit times (60-170 μs/ft) (Rider, 2002). The wireline logging data here was interpreted in terms of % change from the Late Eocene into the Early Oligocene. The advantages of wireline logging in analysing sedimentation changes, over lithology interpretations from cuttings, are that it can record more subtle changes in grain size, and that it provides a continuous down-core record.

4.2.2 Seismic data

The existing interpretation of multi-channel seismic (MCS) profiles from cruise KN179-01 was expanded upon using MCS profiles from cruise RC2510, and further existing interpretations from MCS profiles from cruise EW0007 (Figure 4.2) (Boyle et al., 2017; Shillington et al., 2004; Tucholke et al., 2004). Details of the specific MCS profiles used from each cruise are provided in Appendix E.1.

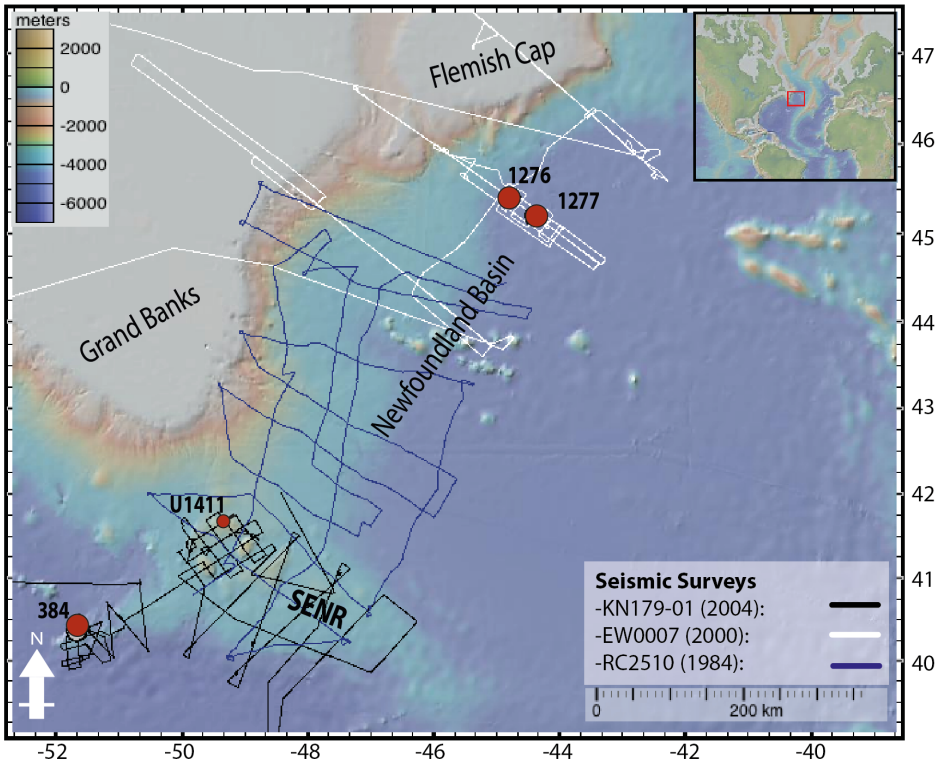

Figure 4.2: Cruise tracks of the three seismic surveys analysed in this study. Relevant IODP & ODP sites are also shown. Map created using GeoMapApp (http://www.geomapapp.org).

4.2.2.1 Seismic cruises

Cruise KN179-01

A previously published interpretation of MCS profiles from the KN179-01 cruise on the SENR, tied to physical property data from IODP Exp. 342, identified the seismic basement as being of Aptian-Albian age. The SENR below this horizon consists of a ridge of oceanic crust that formed during the opening of the Newfoundland-Iberia rift. A pre-drift phase of pelagic sedimentation then occurred during the Late Cretaceous and Palaeocene, which was followed by a series of intervals of drift accumulation through the Cenozoic, and then a pelagic/IRD sequence from the Pliocene to the

present day ('Late contourite phase' in Boyle et al., (2017). In total, five separate seismic horizons were identified by this previous study across the SENR (Boyle et al. 2017). For this study, SEG-Y files from the KN179-01 lines that covered the SENR were loaded into a three-dimensional environment created using the software Petrel®, and the horizons identified by Boyle et al., (2017) were mapped onto the lines to provide a guide for further analysis. Boyle et al., (2017) found that it was possible to further subdivide their third seismic unit (Mid Eocene to Oligocene in age) in some locations, as in some instances the reflectors in the lower part of this unit display more lamination than the upper part. Although not extensively identifiable, this facies shift was mapped where possible to allow comparison with sedimentary/oceanographic changes identified elsewhere in this study.

Cruise RC2510

Several of the MCS profiles shot during cruise RC2510 also cover the SENR, and some locations overlap with the lines from KN179-01. This allows for the potential to correlate the acoustic basement, pre-drift, drift, and post-drift seismic sequences in lines from both cruises (Figure 4.2). Crucially, as well as extending the coverage of the seismic interpretation of the SENR, the RC2510 cruise lines also allowed this interpretation to be extended to cover the continental slope and deep ocean to the North, which is the interpreted direction from which the drift deposits were derived. Analysis of these profiles to date has focused on identifying the placement of the ocean-continent boundary along the J-anomaly or characterising the nature of Newfoundland-Iberia rifting, largely ignoring the Cenozoic cover (Austin et al., 1989; Tucholke et al., 1989).

Unlike KN179-01, there are no intersecting drill-holes with which to directly date any seismic horizons identified, but it is possible to correlate horizons of known age where the cruise crosses with KN179-01. The profiles were inspected to confirm that their resolution was sufficient to capture the seismic horizons and facies identified in KN179-01. SEG-Y files of the MCS profiles from RC2510 were then imported into the Petrel® project and these horizons were mapped digitally.

Cruise EW0007

Cruise EW0007 focuses on three extended MCS profiles extending from the Grand Banks and Flemish Cap, across the shelf break, and down onto the Newfoundland Basin. The central profile aligns with Ocean Drilling Program (ODP) Site 1276 and so the seismic facies and horizons identified on this profile have been assigned ages based on analysis of the sediments cored. Sediments were only recovered from this Site from the crust to just above the EOB however, meaning that from the Oligocene to present the seismic horizons cannot be dated. Instead, loose interpretations on the major sedimentary bodies present have been made via comparison with other areas along the Northwest Atlantic margin (Shillington et al., 2004; Tucholke et al., 2004). This thesis extended the interpretation of these facies to the other MCS profiles shot during EW0007, at which point it was then possible to correlate with the northernmost MCS profiles shot during cruise RC2510, in a similar way as was done with KN179-01 above (Figure 4.2). SEG-Y files from both cruises were integrated into the existing Petrel® project, and the relevant horizons were mapped.

4.2.2.2 Data analysis

The horizons identified both on the SENR and Newfoundland Basin were mapped across the Petrel® project. Seismic horizons and units identified on the SENR and in the Newfoundland Basin were distinguished by using *R* (e.g., Horizon R1) to signify the Southeast Newfoundland *Ridge* and *B* (e.g., Unit B2) to signify the Newfoundland *Basin*. The depths in two-way travel time (TWT, ms) of each horizon were then exported, and the thickness of each seismic unit identified was calculated along each profile (again in TWT). This data was used to generate isochron maps covering the extent of each unit, using the data package R®.

4.2.3 Reconstruction of EOT palaeobathymetry

4.2.3.1 Data preparation

Two facets of the analysis presented in this chapter were used to create a Digital Elevation Model (DEM) for the SENR, continental shelf, and Newfoundland Basin at the time of the EOT. Palaeobathymetry and/or depositional environment data from industrial wells were used where an interpretation was available for the Earliest Oligocene. This information helps to reconstruct the location of the palaeo-coastline

and shelf edge. Analysis of the Petrel® seismic project described above provided the basis for reconstructing the palaeobathymetry of the SENR and Newfoundland Basin. Specifically, Horizon B4/A^U was used. For profiles where this horizon was absent, the depth of the next deepest horizon was used. For this assembled horizon, the two-way travel time (TWT, ms) between the sediment surface and the horizon was calculated across all available seismic profiles.

4.2.3.2 TWT to depth conversion and isostatic correction

To utilise the seismic data in the EOT palaeobathymetric model, it was first necessary to depth convert the data from TWT. The depth to the seafloor was calculated using the TWT of the sediment surface calculated from the Petrel® project, assuming that seawater has a constant velocity of 1480 m s^{-1}. Unfortunately, there was no downhole logging of physical properties during IODP Exp. 342, and so the velocity of the overlying sediment was calculated using discrete P-wave Caliper (PWC) measurements taken during the expedition (Norris et al., 2014) across several sites. Interpolation of the PWC data as a function of depth gives the following linear relationship:

$$V_p\ (m\ s^{-1}) = 0.3916 \cdot z\ (m) + 1501 \quad (4.1)$$

Here V_p is P-wave velocity, and z is depth. V_p (m s^{-1}) can then be integrated to obtain a relationship between TWT and depth, which can then be rearranged to allow the calculation of z as a function of TWT:

$$TWT\ (s) = 5.107 \cdot ln(2.609{\times}10^{-4} \cdot z\ (m)\ + 1) \quad (4.2)$$

$$z\ (m) = 3833\left(e^{0.1958(TWT(s))}\ - 1\right) \quad (4.3)$$

Having calculated the present-day depth of the EOT horizon, it is then possible to remove any overlying sediments and hence bathymetric features resulting from post EOT processes. However, in removing the post EOT sediments it is necessary to account for isostatic impacts. Assuming Airy Isostasy this can be calculated as follows:

$$w_t = w_0 + \frac{\rho_m - \bar{\rho}_s}{\rho_m - \rho_w} z_s \quad (4.4)$$

Here, w_t is palaeobathymetry, w_0 is present-day bathymetry, z_s is the thickness of the sediment being removed, ρ_m is the mantle density (3300 kg m^{-3}), ρ_w is the density of seawater (1030 kg m^{-3}), and $\bar{\rho}_s$is the average density of the sediment. $\bar{\rho}_s$ can be calculated as a product of the grain density (ρ_g) and mean porosity ($\bar{\varphi}$) of the sediment:

$$\bar{\rho}_s = \rho_g(1 - \bar{\varphi}) + \bar{\varphi}\rho_w \quad (4.5)$$

Mean porosity can be calculated using:

$$\bar{\varphi} = \frac{\varphi_0}{cz_s} * (1 - e^{-cz_s}) \quad (4.6)$$

Where φ_0 is porosity at z=0, and c is a decay constant that can be obtained from a best-fit exponential trend of porosity with depth:

$$\varphi = \varphi_0 e^{-cz_s} \quad (4.7)$$

For this study, c was calculated to be -1.070e^{-3} using shipboard moisture and density (MAD) readings taken during IODP Exp. 342 (Norris et al., 2014). The depth conversion of the seismic horizons and the calculation of the isostatic impact on palaeobathymetry were performed at Halliburton Neftex® by Graham Baines.

4.2.3.3 3D palaeogeographic reconstruction

The final 3D palaeogeographic construction of the study area was performed at Halliburton Neftex® following the methods of Vérard et al., (2015); Halliburton Neftex®'s own palaeogeographic maps and geodynamic plate tectonic model, and the bathymetric interpretations obtained from well data in this study, were used to define the coastline and the shelf edge position. The Halliburton Neftex® Geodynamic Earth Model was used to situate the generated palaeobathymetry at its palaeolatitude and longitude at the time of the EOT.

4.3 Results and discussion

4.3.1 Well data exploration of the Grand Banks

4.3.1.1 Palaeobathymetry or depositional environment

In the Late Eocene, the sites closest to the Flemish Pass and Northern Grand Banks indicate deeper palaeobathymetry (outer neritic to bathyal) than those along the East and West Grand Banks, closer to the SENR (marginal-middle neritic, Figure 4.3a). In the Early Oligocene, by comparison, the Flemish Pass and East Grand Banks appear to be shallower than the Eocene, but no change is recorded across the North and West Grand Banks (Figure 4.3b). Overall, little change is recorded in the wells featuring interpretations for both the Late Eocene and Early Oligocene, though two show a trend towards shallower palaeoenvironments across the EOB, and one shows a deepening trend (Figure 4.4).

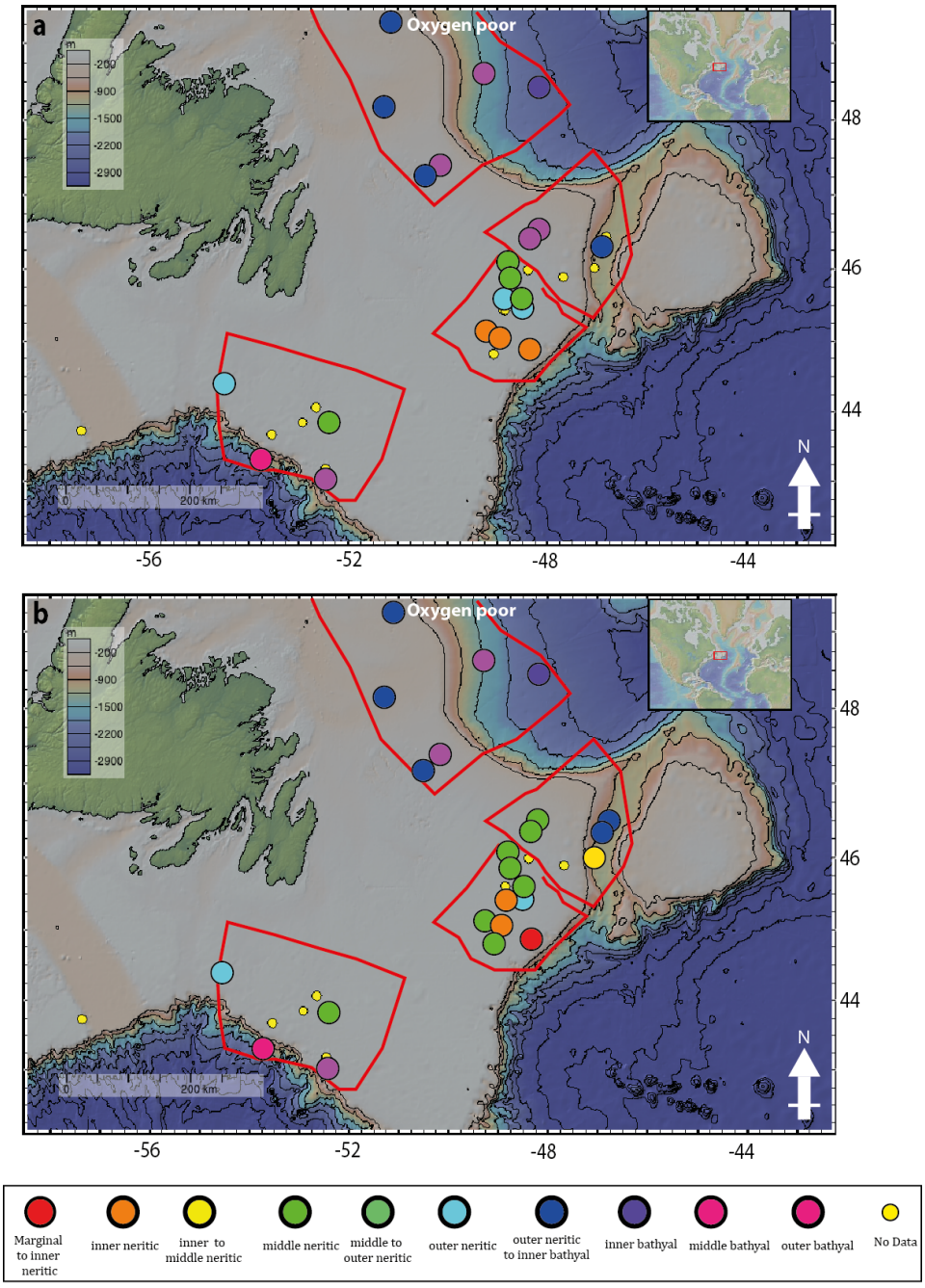

Figure 4.3: Spatial extent of different palaeobathymetry classes identified in a) the Late Eocene and b) the Early Oligocene. For identification of each well, see Figure 4.1.

Some care is needed with these interpretations, as the temporal resolution and terminology of the industry data used can vary. Palaeoenvironments were often recorded as a range, such as 'neritic-bathyal', and it was often difficult to interpret whether this reflects an environment that is transitional or instead the uncertainty in the initial interpretation. Where this was an issue, interpretations of changes from the Late Eocene to Early Oligocene were marked as being tentative, for example in the East Grand Banks (Figure 4.4). The lack of agreement in the palaeoenvironmental

changes recorded in the wells may also partially relate to the data quality. As an example, due to the poor sampling resolution available from cuttings, the positions of stratigraphic boundaries (such as the EOB) are sometimes extrapolated. This is the case for the position of the EOB in the log suggesting a deepening trend into the Oligocene (Murre G67). As such, if a better age model were available for Murre G67, it is possible that the EOB trend would be similar to those shown in the other wells (Supp. Figure D3).

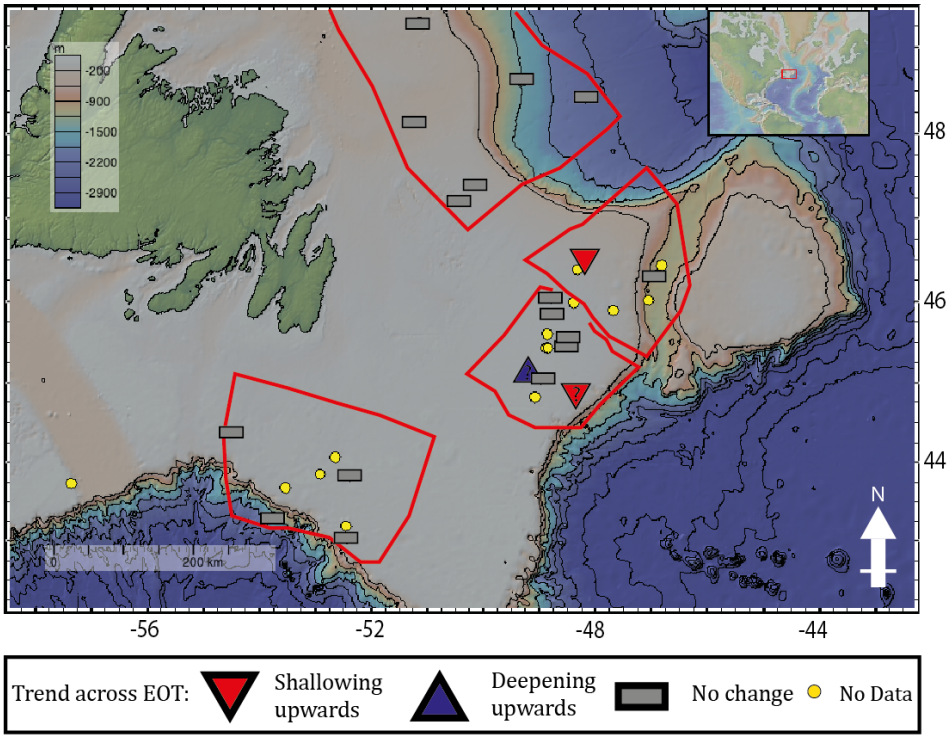

Figure 4.4: Trends observed across the EOB for palaeobathymetry, where data were available for both the Late Eocene and Early Oligocene in each well. Question mark indicates a tentative interpretation, see text for further detail.

4.3.1.2 Lithology

In the Late Eocene, shale was the most common and widespread lithology (Figure 4.5a), with the only exceptions being one record of sandstone in the West Grand Banks (Merganser I60, Supp. Figure D4), and one sandstone and one siltstone in the North Grand Banks (Linnet E63 and Bai Verte J57 respectively, Supp. Figure D1). In the Early Oligocene, shale was still the most common lithology (Figure 4.5b), however one additional well in the North Grand Banks records silty sandstone deposition (Bonavista C99, Supp. Figure D1), as do one well each in the West Grand Banks (Gull F72, Supp. Figure D1) and East Grand Banks (Spoonbill C30, Supp. Figure D3). In

addition to this, two wells (Flying Foam_I13 and Hebron_I13, Supp. Figure D3) in the East Grand Banks also preserve an Oligocene Sandstone (OSS) member over the EOB (Figure 4.5b). Note that the identification of this member is recorded as a separate parameter to interpreted lithology in IC™, as the two wells in question do not have recorded interpretations for lithology.

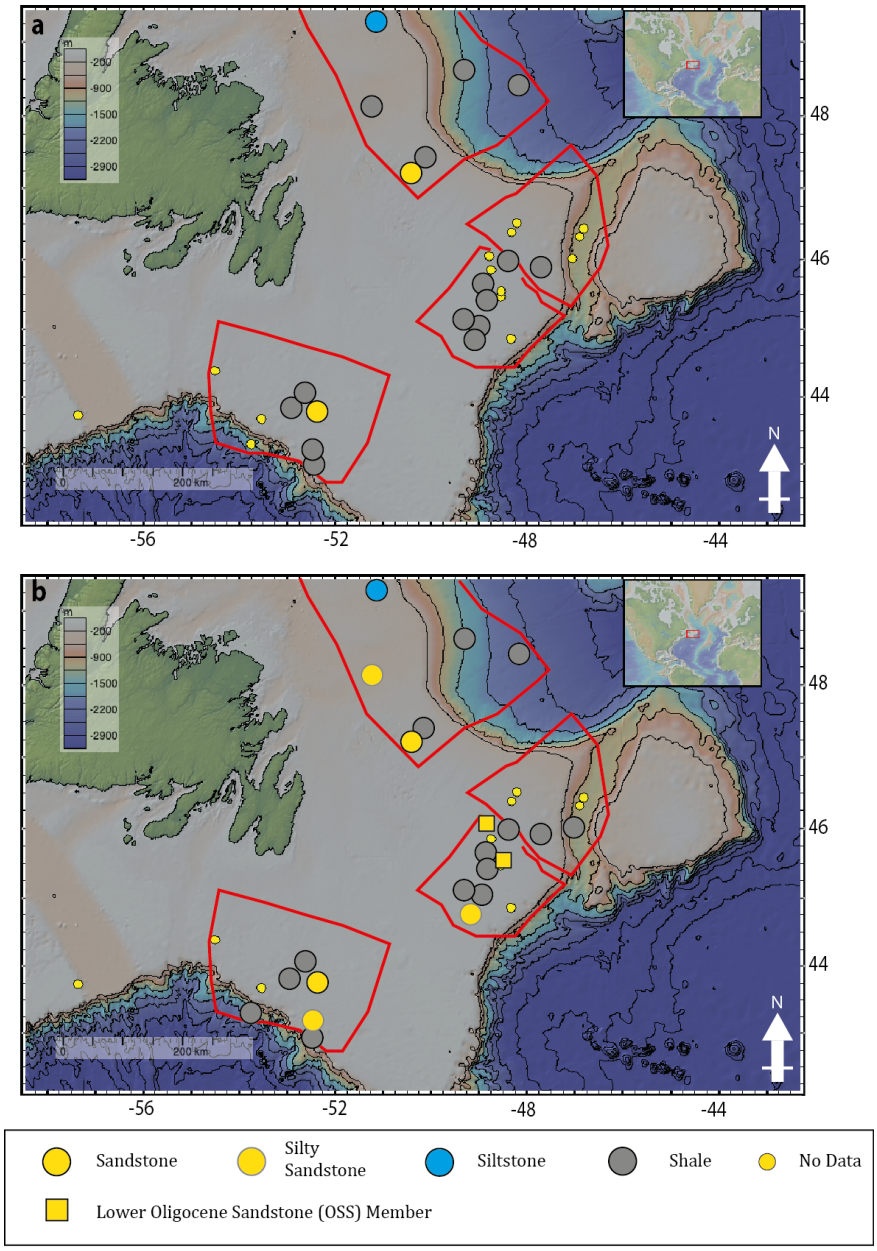

Figure 4.5: Spatial extent of different lithology classes identified in a) the Late Eocene and b) Early Oligocene. For identification of each well see Figure 4.1.

The majority of wells with lithological interpretations above and below the EOB showed no trend across the boundary, however coarsening upwards trends were present in one well each in the North, East, and West Grand Banks (Figure 4.6). As

detailed for trends in palaeobathymetry above, the issue of uncertainty in placing boundaries arises from the use of cuttings.

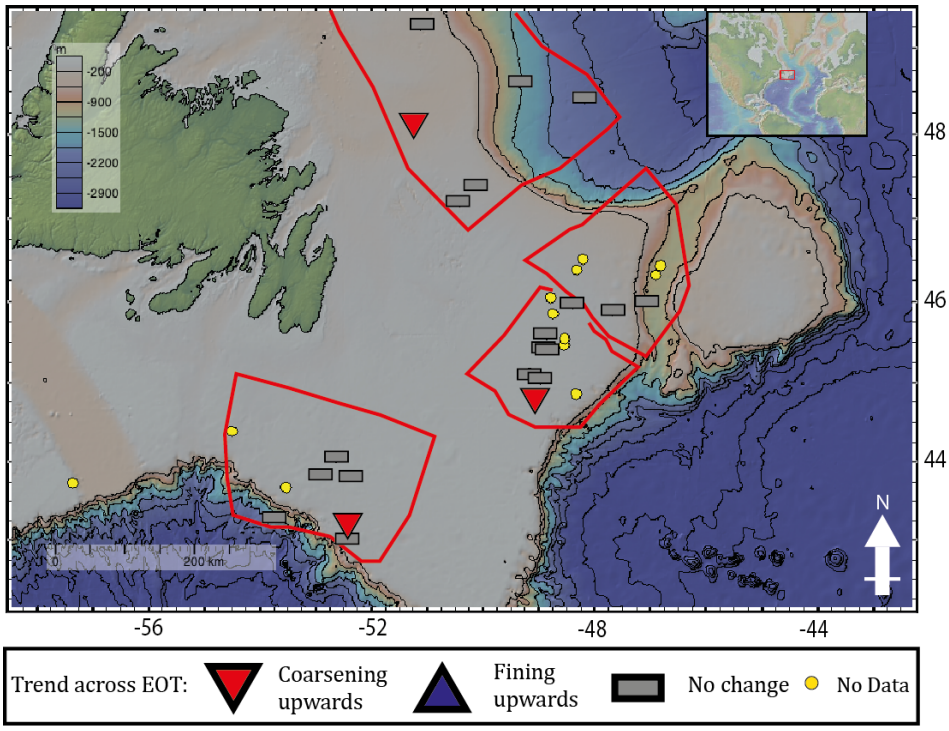

Figure 4.6: Trends observed across the EOB for interpreted lithology, where data were available for both the Late Eocene and Early Oligocene in each well.

4.3.1.3 Wireline Logs

There is significant variation in GR values across the EOB, with both increases and decreases seen along the Grand Banks; no data were available for the Flemish Pass. The majority of wells (9 of 16) show a decrease in GR, suggesting a decrease in clay content and an increase in grain size (Figure 4.7a). There is also a lack of uniformity in the trends seen in the Sonic logs across the EOT, with five wells recording a relative decrease (i.e., a faster response), five showing no change, and two recording an increase (Figure 4.7b). Taken together, there is a general decrease in both variables, particularly in the East and West Grand Banks.

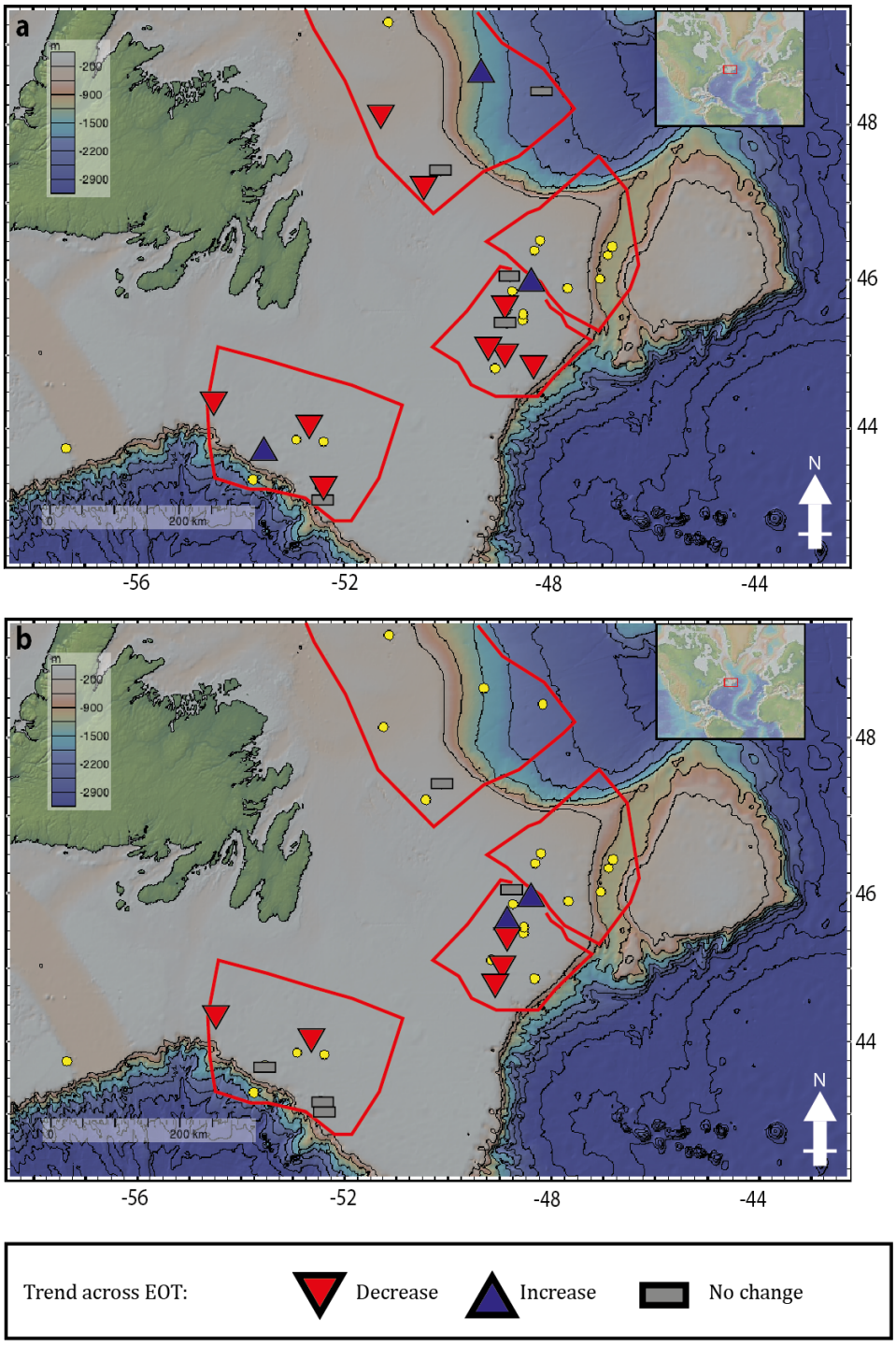

Figure 4.7: Trends in a) GR and b) Sonic logging from the Late Eocene to Early Oligocene.

4.3.1.4 Overall trends in well data

When considered in combination, the lithology and wireline log data demonstrate a general coarsening-up trend across the study area, consistent with forced regression and progradation associated with a sea level drop (Simmons, 2012). This implied sea level drop could also be the result of normal progradation, with the filling of accommodation space by sediments resulting in an apparent drop in sea level, but

this would require the presence of large deltaic systems, for which there is no evidence; the dominant palaeobathymetric environment suggests the area is inner to middle neritic (Figure 4.3). Furthermore, the link between a coarsening trend and sea level drop is not ubiquitous; it could also represent changes in palaeocurrent intensity, or changes in sediment supply. It is also possible in the sequence stratigraphic framework for sea level to fall without necessarily resulting in a coarsening in lithology if the shoreline of the progradation system is muddy (Figure 3.2). It is perhaps surprising that there is not more widespread agreement between the lithological and wireline logging trends. The record of interpreted lithology for each well has a low degree of sensitivity — only four different lithologies were identified in the study area — so it may be that the down-core gamma ray changes across the EOT may pick up changes in lithology that are too subtle to warrant a change from shale to sandstone, for example.

The palaeobathymetry data provide some support for the idea that the coarsening trend across the EOT is a result of sea level fall, with two wells showing a shallowing trend across the EOT (Figure 4.4). Furthermore, more wells in the Earliest Oligocene document marginal to middle neritic environments than the Latest Eocene, with the reverse being true for outer-neritic to outer-bathyal environments (Figure 4.3). The lack of a more unified signal, as discussed in Section 4.3.1.1, may be due to the poor sample resolution for this variable, which is derived entirely from biostratigraphic analysis intermittent cuttings. Furthermore, the eight palaeobathymetric classes interpreted account for a wide range of water depths, from shoreline to basin floor. As such, sea level change on the order of ~50 m, as predicted for the EOT, might not necessarily result in a change of bathymetric class (Coxall et al., 2005; Houben et al., 2012; Katz et al., 2008; Miller et al., 2008).

Site U1411, on the SENR, contains a record of lithic sand that increases dramatically across the EOT, as discussed in Chapter 3. The grain size and provenance signal of this sand suggests that it must have been sourced locally, and it is interpreted to be the result of off-shelf transport in response to glacioeustatic sea level fall associated with the EOT. It is inferred that this lithic material is then transported to its (relatively

isolated) position on the ridge by bottom currents. The morphology of the drift suggests the sediment was transported from the north (in agreement with modern day flow paths), which suggests that the most likely source of the lithic material is the eastern shelf of the Grand Banks or the Flemish Cap. This area appeared to become shallower across the EOT, which may reflect the glacioeustatic effect of the formation of Antarctic ice, and three wells showed evidence of sandstones in this area in the Earliest Oligocene (including where the OSS member is recorded across the EOB). This sand may represent progradation related to sea level fall, and its proximity to the shelf break fits with the idea that it could be transported off-shelf and incorporated into the drift deposits on the SENR (Figures 4.3 & 4.5).

The idea that eustatic sea level change is influencing the observed changes, however, is complicated by the lack of consistency in the responses recorded (Figure 3.2). The Newfoundland margin has been passive, without any major tectonic events, since the late Aptian (114 Ma). More localised tectonic activity could have influenced changes in sedimentation or relative sea level, in addition to eustatic change, but there is little evidence of this occurring (Péron-Pinvidic et al., 2007). As discussed in section 1.1.4 however, even supposedly passive margins can experience dynamic topography, though this is unlikely to have had an effect on sea level on the same scale as glacioeustasy across the EOT (Moucha et al., 2008). It is more likely that variation is related to the complications associated with temporal inaccuracy and/or poor resolution from cuttings.

4.3.2 Seismic data

4.3.2.1 Mapping of seismic horizons and facies between cruises

The five seismic facies (Unit R1-Unit R5), separated by six horizons (Horizon R1-Horizon R6), identified previously on the SENR on cruise KN-179-1 were also identified in cruise RC2510 (Figures 4.8 & 4.9). As described in section 4.2.2.1, the internal horizon within Unit R3 was also identified intermittently within the KN-179-1 profiles, although this horizon was very difficult to identify in the RC2510 profiles. Where present, the sections of Unit R3 above and below this horizon were noted as Unit R3b and R3a respectively. The varying structure of the acoustic basement, which features several seamounts and other structures, meant that the lateral extent of any given reflection was relatively short. This was counteracted though by the high frequency of cross-points between profiles of the two cruises on the SENR (Figure 4.2).

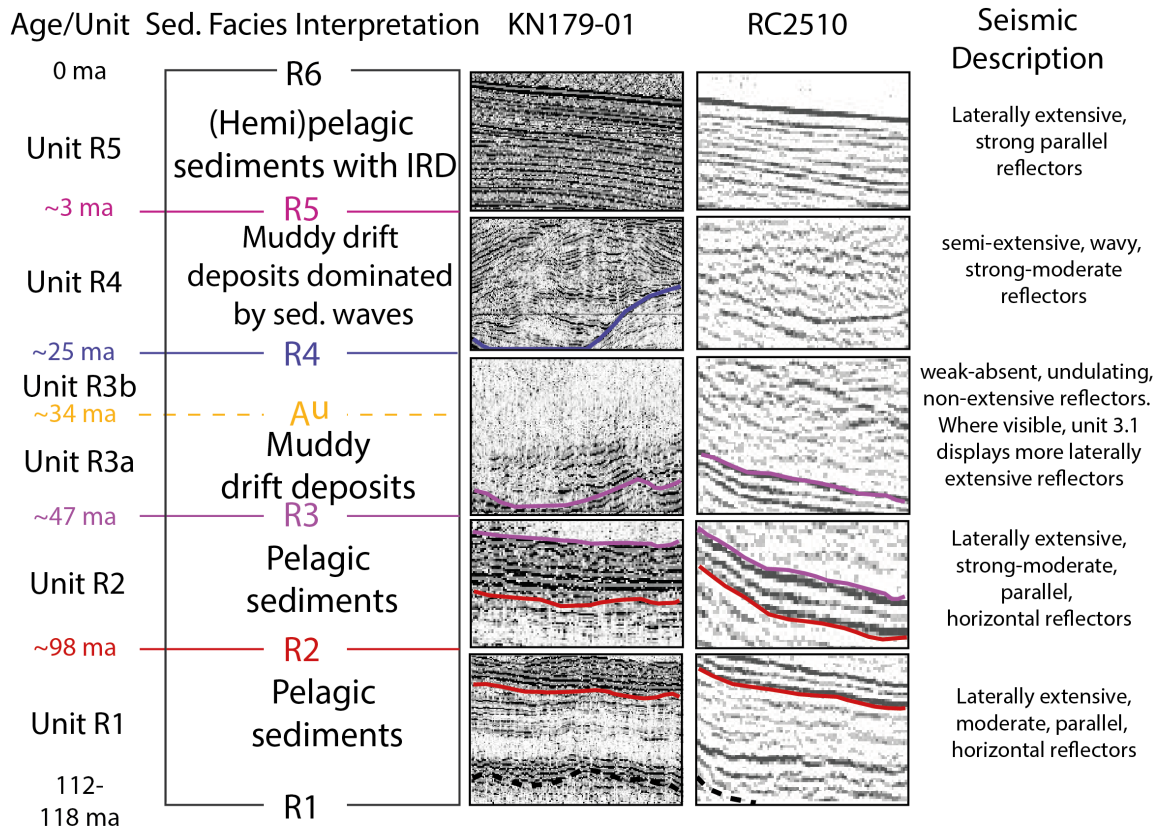

Figure 4.8: Characterisation of seismic facies and horizons present on the SENR. Ages come from correlation with IODP drill sites from exp. 342 (Boyle et al. 2007). Examples for each cruise come from the profiles shown in Figure 4.9.

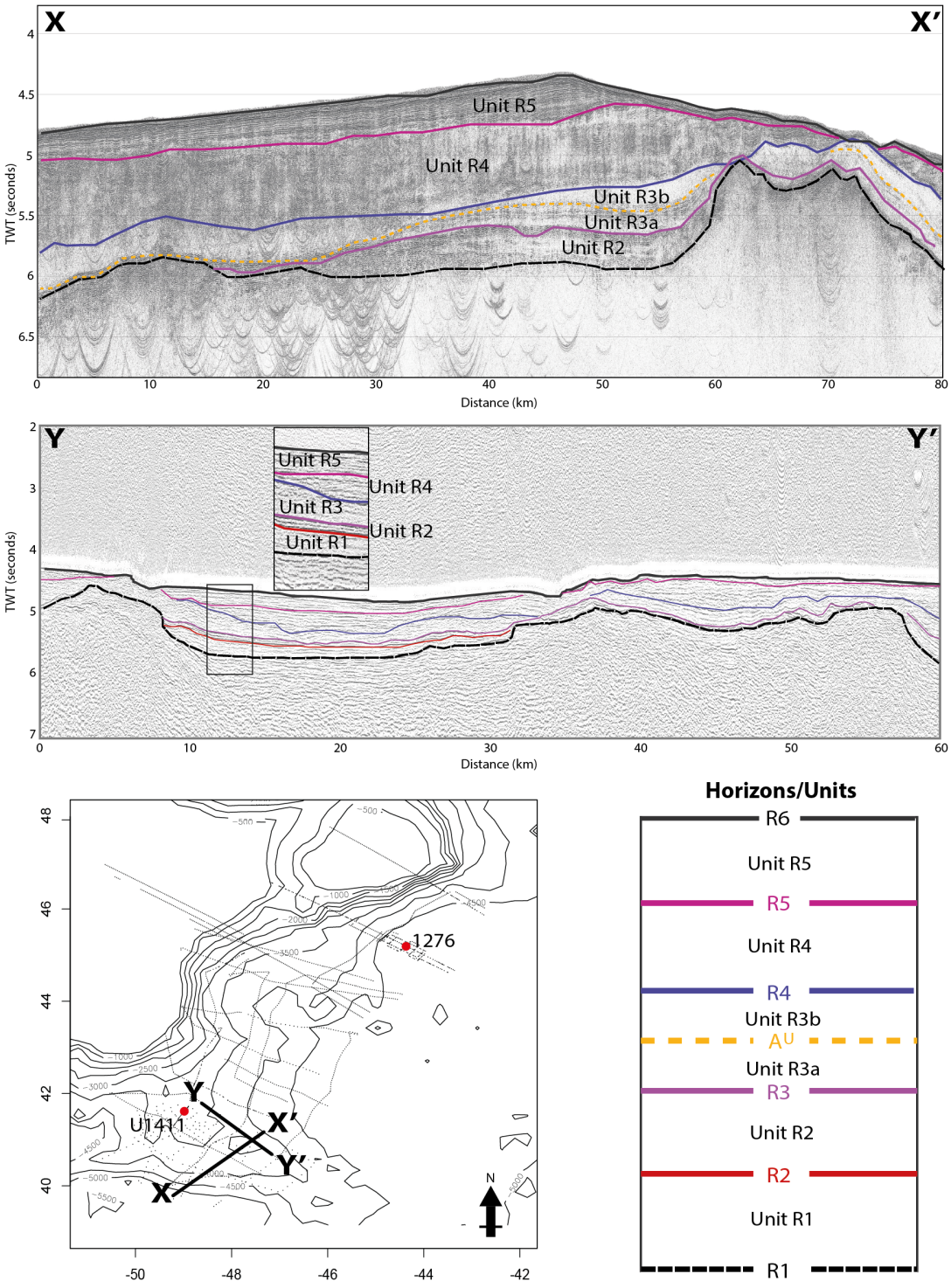

Figure 4.9: Seismic interpretation of Line 43, KN-179-1 (X-X'), and Line nb-12, RC2510 (Y-Y') on the SENR.

Six seismic facies (Unit B1-Unit B6) and seven horizons (Horizon B1-Horizon B7) were identified in the Newfoundland Basin, where the profiles of cruises EW0007 and RC2510 intersect (Figures 4.10 & 4.11). The facies identified here were more laterally extensive than on the SENR, although the average distance between cross-points was lower. It was again possible to trace horizons and identify different seismic facies

across the two cruises. Units B2 and B3, together spanning ~34-98 Ma, were recognizable together as a laterally extensive 'package' of very prominent parallel reflectors, but it was sometimes difficult to distinguish one from the other (Figures 4.10 & 4.11).

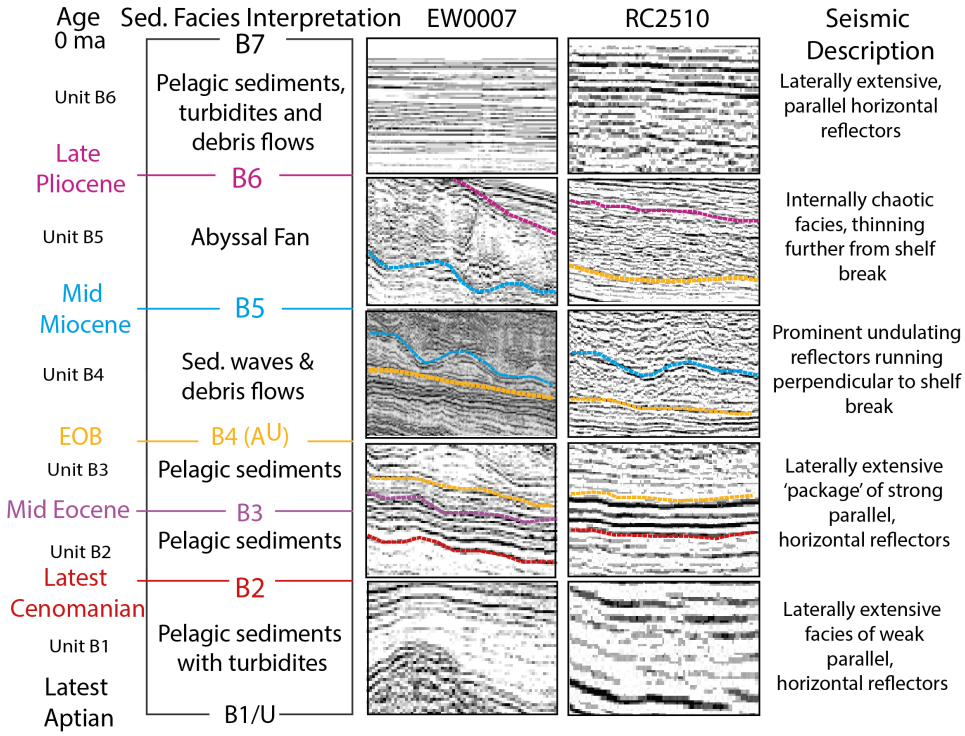

Figure 4.10: Seismic facies identified in Cruises EW0007 & RC2510 in the Newfoundland Basin. Ages come from correlation with ODP drill sites from leg 210 (Shillington et al. 2007), but are inferred above horizon B4. Examples for each cruise come from the profiles shown in Figure 4.11.

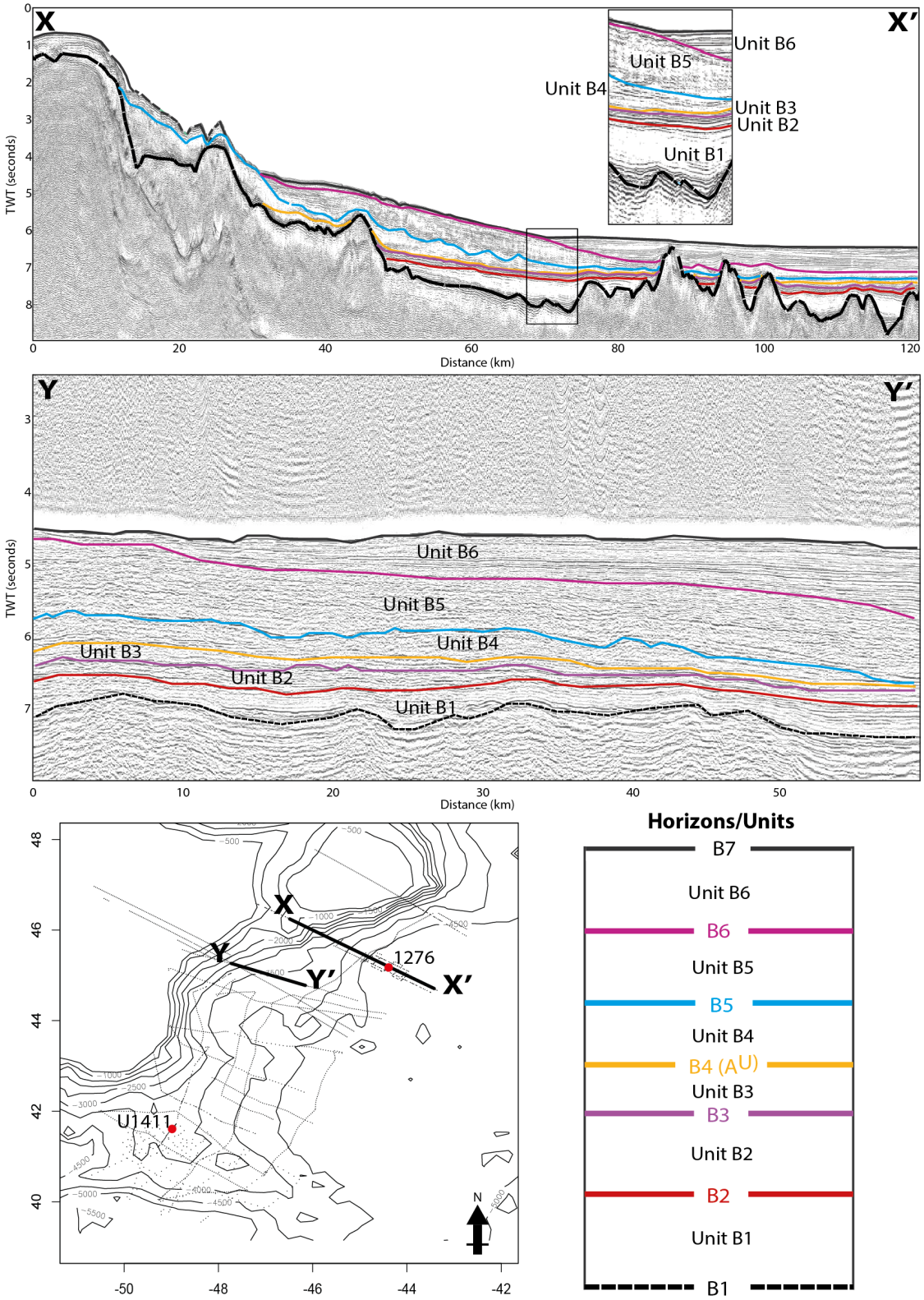

Figure 4.11: Seismic interpretation of Line 2mcs, EW0007 (X-X'), and Line nb-1, RC2510 (Y-Y') in the Newfoundland Basin.

4.3.2.2 Correlation of horizons between the SENR and the Newfoundland Basin

The ages attributed to several of the horizons identified on the Newfoundland Basin, through previous correlation between EW0007 line 2mcs and ODP Site 1276, show similarity to the ages attributed to horizons R1-R5 identified on the SENR (Boyle et al., 2017; Shillington et al., 2004). This correlation between the timing of sedimentation changes occurring on the SENR and those happening on the Newfoundland Basin to the north, allows for some of these horizons to be tentatively linked between the two areas of study (Figure 4.12). These correlations cannot be made with absolute certainty without well control, particularly for Cruise RC2510 and for Horizons B5-B6 from the Newfoundland Basin, which were not sampled during the drilling of Site 1276 (Shillington et al., 2004; Tucholke et al., 2004). Five seismic horizons (including the water-sediment interface) were tentatively interpreted to extend across both the SENR and the Newfoundland Basin. Horizon B5 on the Newfoundland Basin and Horizon R4 on the SENR, however, do not appear to correlate with other horizons across the study area. Four seismic units were tentatively interpreted to have developed contemporaneously both on the SENR and in the Newfoundland Basin, bound by the correlated horizons (Figure 4.12).

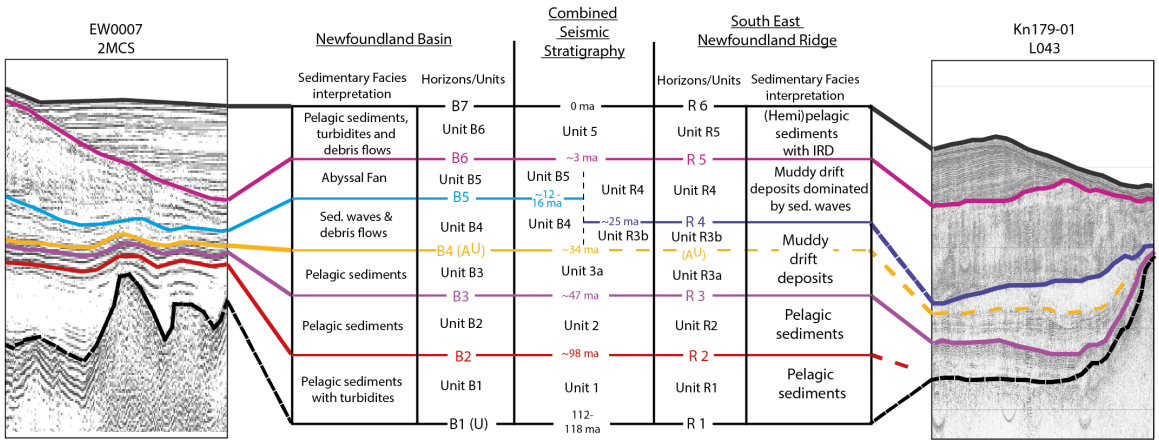

Figure 4.12: Comparison between ages of horizons and nature of seismic units identified in the Newfoundland Basin (left hand side) and the SENR (right hand side), giving the combined seismic stratigraphic framework for this chapter.

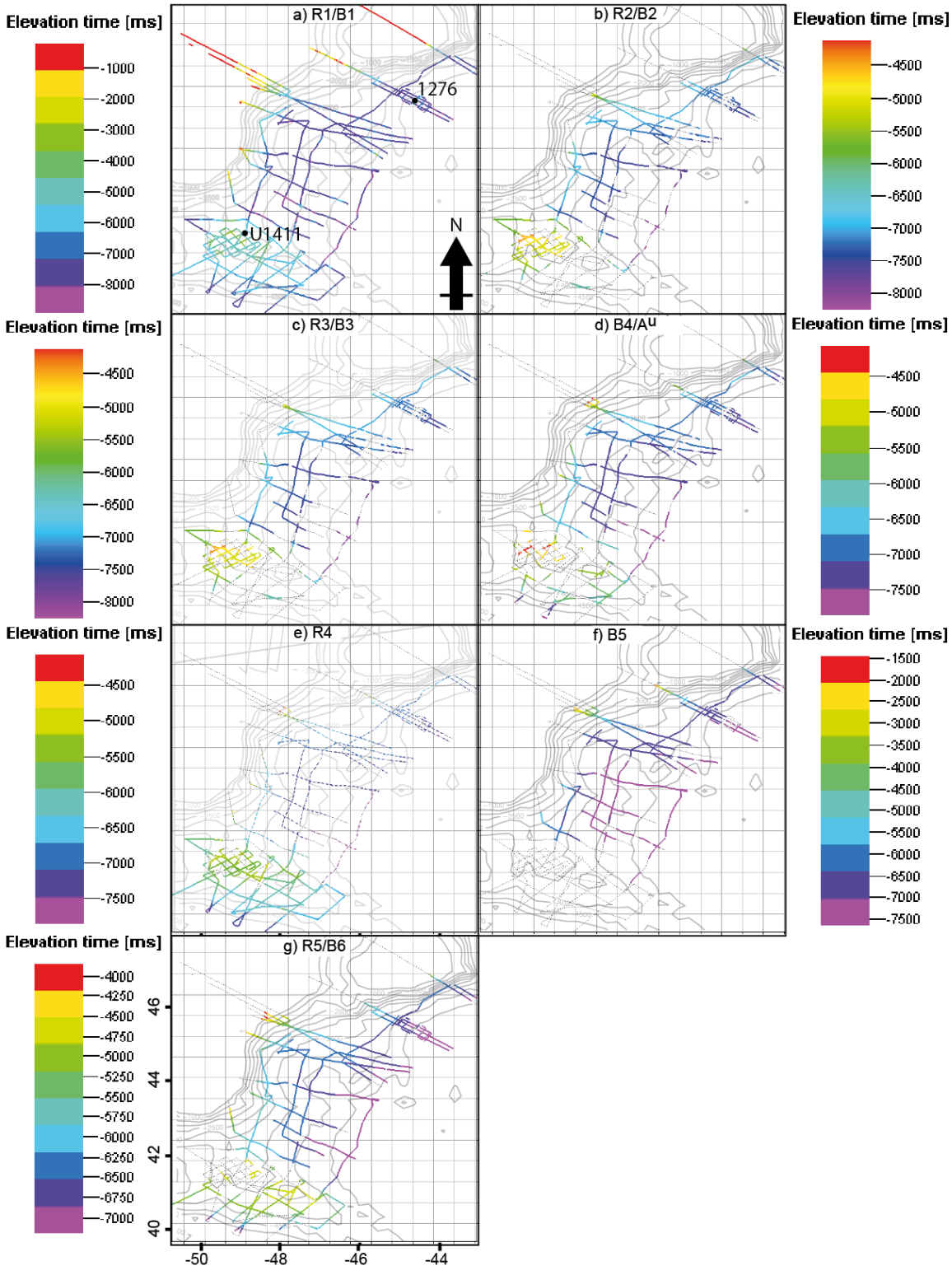

Figure 4.13: Extent of seismic horizons mapped in Petrel® across the Newfoundland Basin and SENR (see Appendix E for further information). The depth to each horizon from sea level is shown via colour scale.

Horizon R1/B1 (Acoustic Basement): The base of Unit R1 on the SENR, Horizon R1 is defined by the acoustic basement, composed of the volcanic basement of the ridge (i.e., oceanic crust). This crust is estimated to have formed during the early

Albian/late Aptian, ~112-118 Ma (Norris et al., 2014; Tucholke and Vogt, 1979; Tucholke et al., 1989). To the north of the SENR, the Newfoundland Basin is underlain by deformed continental crust — it lies to the west of the COB, marked here by the J-anomaly. As a result, the deepest sediments here are much older than on the SENR: the Salar Basin, which skirts the base of the continental slope, contains Triassic-to-Jurassic-age evaporites, whereas closer to the COB a mix of syn-rift sedimentary and volcanic fill is intertwined with a zone of complex faulted basement blocks (Tucholke et al., 1989). The prominent and laterally extensive U reflection lies above these sediments (Tucholke et al., 1989). It is associated with a strong erosional episode that in many areas has removed all underlying sediments to the volcanic basement, and also corresponds with the emplacement of sills in the northernmost part of the study area covered by EW0007, related to rifting along the Newfoundland-Iberia margin (Austin et al., 1989; Deemer et al., 2009; Keen and de Voogd, 1988; Peron-Pinvidic et al., 2010; Quigley, 2005). As the U reflection roughly corresponds to the age of the volcanic basement of the SENR, and in many places is the deepest easily traceable horizon in seismic profiles across the Newfoundland Basin, it was used as the de-facto acoustic basement for cruises EW0007 and RC2510 (Horizon B1) (Shillington et al., 2004; Tucholke et al., 2006) (Figure 4.13a).

Horizon R2/B2: The age of Horizon R2 on the SENR—interpreted from correlation with IODP Exp. 342 holes (Cenomanian, ~98 Ma)—broadly correlates with that given to Horizon B2 in the Newfoundland Basin, obtained from Site 1276 (Boyle et al., 2017; Shillington et al., 2004; Tucholke et al., 2004) (Figure 4.13b).

Horizon R3/B3: Horizon R3 on the SENR is dated as Mid-Eocene (Lutetian, ~47 Ma), and marks the change from pelagic sedimentation in Unit R2 to drift accumulation in Units R3 and R4 (Boyle et al., 2017). Although there is no corresponding drastic sedimentation change interpreted in the Newfoundland Basin, Horizon R3 does broadly correlate to a Horizon B3, which was identified in EW0007 to be of Middle Eocene age (Shillington et al., 2004; Tucholke et al., 2004) (Figure 4.13c).

Horizon B4/A^U: Horizon B4 in the Newfoundland Basin was interpreted to correlate with the widespread Horizon A^U by correlation with sediments from IODP Site 1276 (Shillington et al., 2004). This horizon marks a Late Eocene to Early Oligocene erosional unconformity along the Nova Scotia and U.S. East coast margins, and correlates with other erosional unconformities throughout the North Atlantic attributed to the onset of strong deep-water currents (Figure 1.4) (Tucholke and Mountain, 1986, 1979b). On the SENR, Horizon B4/A^U corresponds to a change in sedimentation identified within Unit R3, is interpreted by Boyle et al., (2017) to represent a decrease in current intensity over the SENR as the core of the bottom current deepened. However, this change was not widely identifiable in many of the MCS profiles over the SENR, particularly in profiles from cruise RC2510 (Figure 4.13d).

Horizon R4: This horizon, which on the SENR is dated to ~25 Ma, marks an increase in the accumulation rate of drift deposition on the ridge, combined with an inferred decrease in current intensity (Figure 4.13e) (Boyle et al., 2017). It is interesting that R4, which is one of the most easily identifiable horizons over the SENR, is not represented by a contemporary sedimentary change in the Newfoundland Basin. It may be that, as the Newfoundland Basin is exposed to downslope sediment deposition from the continental slope (unlike the SENR), any evidence of sedimentary change from bottom current variability was overridden by increased turbidite input driven by Oligocene sea level change (Miller et al., 2008; Pekar et al., 1997).

Horizon B5: This horizon marks the top of Unit B4 and the base of Unit B5 in the Newfoundland Basin (Figure 4.18f). The age predicted for this horizon is Mid-Miocene, based on the identification of similar seismic units along the North American margin, but the horizon itself was not sampled at ODP Site 1276 (Tucholke et al., 2004). It does not appear to have a corresponding horizon on the SENR, although the age control for the Neogene at IODP site 342 was not good enough to characterize the KN-179-01 profiles for this interval (Boyle et al., 2017).

Horizon R5/B6: On the SENR, Horizon R5 marks the end of drift accumulation in the late Pliocene (~3 Ma) and the re-establishment of pelagic sedimentation, now combined with ice-rafted debris (Boyle et al., 2017). This horizon is contemporary with the predicted age for Horizon B6 for the Newfoundland Basin, although as with the Horizon B5 there was no sampling from ODP Site 1276 (Tucholke et al., 2004) (Figure 4.13g).

Horizon R6/B7 (Sediment Surface): This horizon separates Unit 5 below with the water column above. It is the most laterally extensive horizon (other than the acoustic basement), as there are very few areas that do not have at least a thin cover of sediments from Unit 5. This horizon therefore represents the modern seabed across most of the study area.

4.3.2.3 Spatial and temporal differences in sedimentation

The development of isochron maps for the correlated seismic units and horizons presented in this study allows for comparisons to be made between the sedimentation patterns occurring on the SENR and those occurring along Newfoundland Basin. As stated in Section 4.3.2.2, four seismic units were tentatively interpreted to have developed contemporaneously both on the SENR and in the Newfoundland Basin; these were termed Unit 1, Unit 2, Unit 3a, and Unit 5. Units B4 and B5 in the Newfoundland Basin, and Units R3b and R4 on the SENR, do not appear to have formed contemporaneously (Figure 4.12). The variation seen within each identified unit is analysed below:

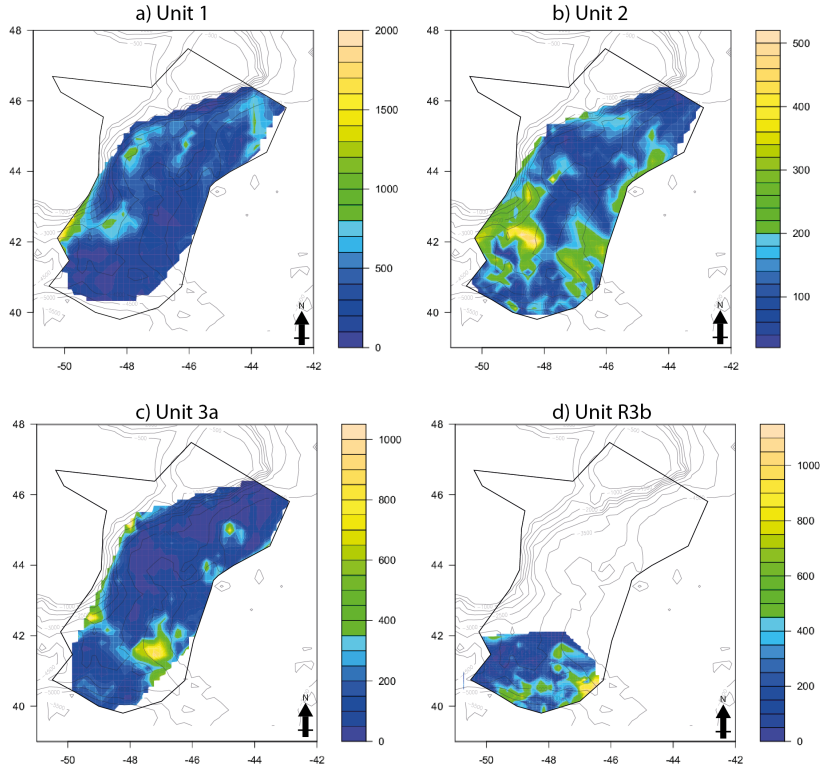

Figure 4.14: Isochron maps for a) Unit 1, b) Unit 2, c) Unit 3a, and d) Unit R3b. Thickness in TWT (ms).

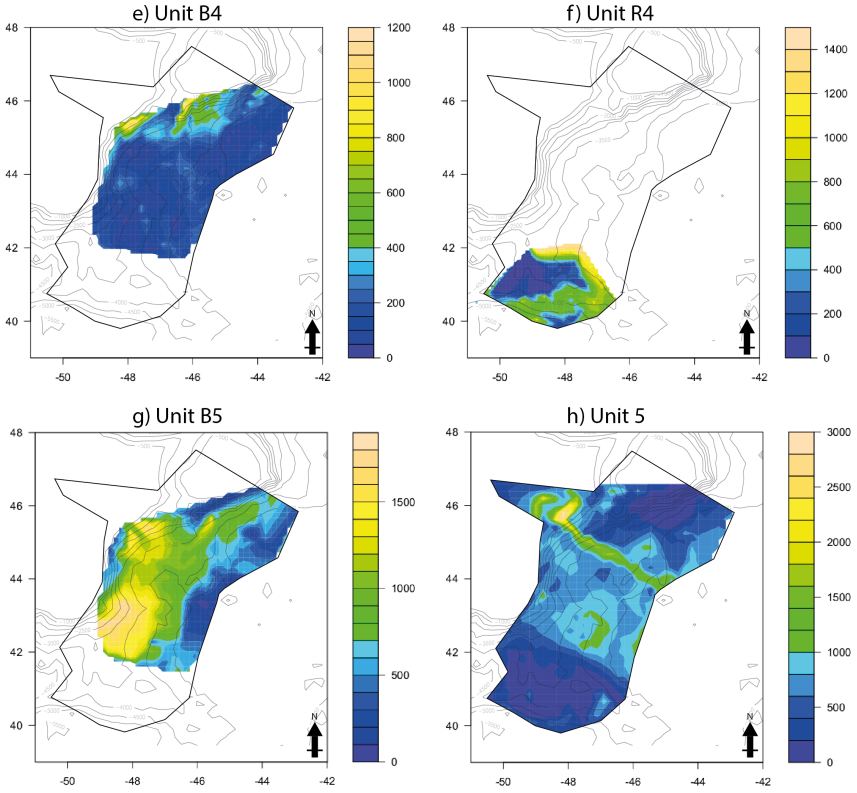

Figure 4.15: Isochron maps for a) Unit B4, b) Unit R4, c) Unit B5, and d) Unit 5. Thickness in TWT (ms).

Unit 1: This unit (Figure 4.14a), which consists of largely pelagic sediments both on the SENR and the Newfoundland Basin, shows a generally uniform, thin-to-absent (~0-300 ms) distribution across both areas. It is early Albian/late Aptian to Cenomanian in age. Areas of thicker accumulation across this interval include the northern edge of the bridge between the SENR and the Grand Banks, and close to the base of the Continental shelf near the Flemish Pass. The relatively uniform accumulation fits with the interpretation that there was no significant bottom current flowing along the slope and up onto the SENR during this interval (Boyle et al., 2017; Davies et al., 2001). Variations in thickness within this unit in the Newfoundland Basin may be controlled by sporadic off-shelf deposition from the continental shelf, as turbidites are identified in sediments of this age at Site 1276 (Shillington et al., 2004).

Unit 2: The Isochron for Unit 2 has the smallest range in thickness of all the units analysed in this report (0-500 ms, Figure 4.14b). This unit, which is Cenomanian to Mid-Eocene in age, exhibits more spatial variation than Unit 1, showing thicker accumulation along the northwestern end of the SENR (200-500 ms). On the SENR, sediment accumulation through Unit 2 is interpreted to be carbonate-dominated pelagic sedimentation, and here it is at its thickest over the shallowest areas of the ridge, suggesting the CCD may be influencing accumulation (Boyle et al., 2017; Tucholke and Vogt, 1979). In the Newfoundland Basin, this unit appears to increase in thickness further away from the continental slope (up to 300 ms). These sediments in the Newfoundland Basin are interpreted to have been dominantly deposited by turbidite and debris flows (Shillington et al., 2004).

Unit 3a: This unit on the SENR marks the onset of drift accumulation in the Mid-Eocene, and this is reflected by the thickness of sediment on the northern flank of the ridge (Figure 4.14c, up to 1000 ms). The contemporary sedimentation occurring over the Newfoundland Basin is much thinner, rarely exceeding 200 ms in thickness; here the sediments are identified as hemipelagic mudstone and claystone (Shillington et al., 2004). Pelagic sedimentation generally has slower sedimentation rates than drift accumulation, which may explain the differences in thickness. The differing thicknesses across this interval between the two areas may also be due to the erosion

(or at least non-deposition) of fine material across the Newfoundland Basin by the current influencing sedimentation on the SENR. The position of the thickest drift accumulation, on the northern flank of the ridge, suggests that the current responsible was flowing from the north (Figure 4.14c).

Unit R3bB: The sediment accumulation over the SENR during this interval is of a similar thickness to during Unit 3a (500-1000 ms). It appears that the main area of deposition moved slightly further down the ridge during Unit 3, across the EOT, and also spread across the axis of the ridge (Figure 4.14d). The difficulty in identifying the A^U Horizon on the SENR hampers this interpretation, however (Figure 4.13d).

Unit B4: This unit begins to form in the Newfoundland Basin around the time of the EOT, alongside Unit R3b on the SENR. Its base is bounded by Horizon B4/A^U (Shillington et al., 2004). This horizon marks an episode of erosion by abyssal currents elsewhere in the North Atlantic, and on the SENR marks a change in the depositional nature of Unit 3 as described above (Tucholke and Mountain, 1986). The effects of bottom current erosion, signified by the A^U Horizon, stretch several hundred km from the base of the slope along the U.S. East coast margin, similar to the distribution seen here (Figure 4.15e) (Mountain and Tucholke, 1985; Tucholke and Mountain, 1986). In the area of Newfoundland Basin analysed in this chapter, a thick sedimentary succession (in some places up to 1000 ms) overlies horizon A^U along the continental slope below the Flemish Cap and eastern Grand Banks (Figure 4.15e). This unit is interpreted to contain material delivered by turbidity and debris flows (Tucholke et al., 2004). It is worth noting that, following the formation of an extensive Antarctic ice cap across the EOT, subsequent sea level fluctuations through the Oligocene, driven by ice volume changes, may have driven the transportation and deposition of off-shelf sediment during this interval (Lear et al., 2008; Miller et al., 2008; Miller and Fairbanks, 1983).

The thickness of the unit adjacent to the shelf break could be explained by the downslope addition of sediment. The coarser material from this downslope activity, would not have travelled far from the continental slope and would have been hard for the current to entrain, whereas finer material may have been either entrained or subsequently eroded by bottom currents (Dalrymple et al., 1992; McCave and Hall, 2006; Stow and Faugères, 2008; Viana et al., 1998b). The morphology of this unit may also have been controlled by bottom currents – Tucholke et al., (2004) identified sediment waves of 1-8 km wavelength in EW0007 line 2mcs, and interpreted that they represented the action of bottom currents (Figures 4.16 & 4.17). As noted by Faugères et al., (1999) however, sediment waves of this wavelength can occur in both turbidite and contourite deposits. In the case of turbidites, these waves form transverse to flow direction, whereas in contourites they can form either transverse or oblique to the flow, suggesting that turbidity currents may in fact have been the cause (Faugères et al., 1999; Stow et al., 2009). The analysis of further profiles in this thesis, however, identified sediment waves that are both perpendicular and parallel to the continental slope, again with wavelengths of ~1-8 km (Figures 4.16 & 4.17). Therefore, it may be that both contour and turbidity currents are responsible (Faugères et al., 1999; Stow et al., 2009).

The overall shape of the sedimentary unit can also help to determine whether contour currents, turbidity currents, or both were responsible for its morphology. This unit appears to extend along the continental slope and continental rise for several hundred kilometres, a trend commonly seen in continental slope contourites (Figure 4.16) (Hernández-Molina et al., 2008). It is also possible that this unit represents a turbidite fan that has since been modified and extended along-slope by bottom currents, such as the Hikurangi Fan Drift (Faugères et al., 1999). This unit has since been buried under further sedimentation, making it difficult to comment further on its morphology. This problem is exacerbated by the poor spatial coverage afforded from seismic profiles, and the relatively poor resolution of said profiles — the intended purpose of cruise EW0007 was to study the ocean-continent boundary rather than Paleogene sedimentation.

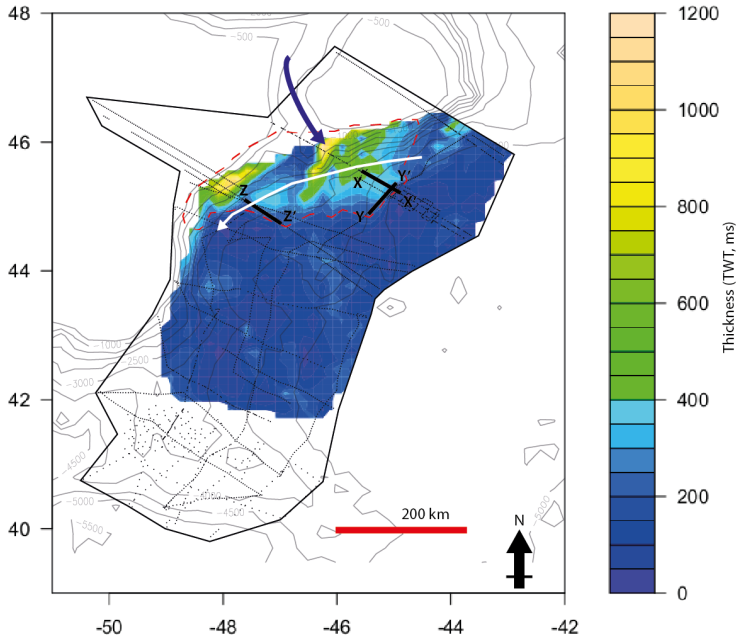

Figure 4.16: Enlarged view of isochron map for Unit B4, showing inferred location of mixed turbidite-contourite system (red dashed line). Blue arrow signifies off-shelf deposition and white arrow signifies action of bottom currents in elongating unit along the continental margin.

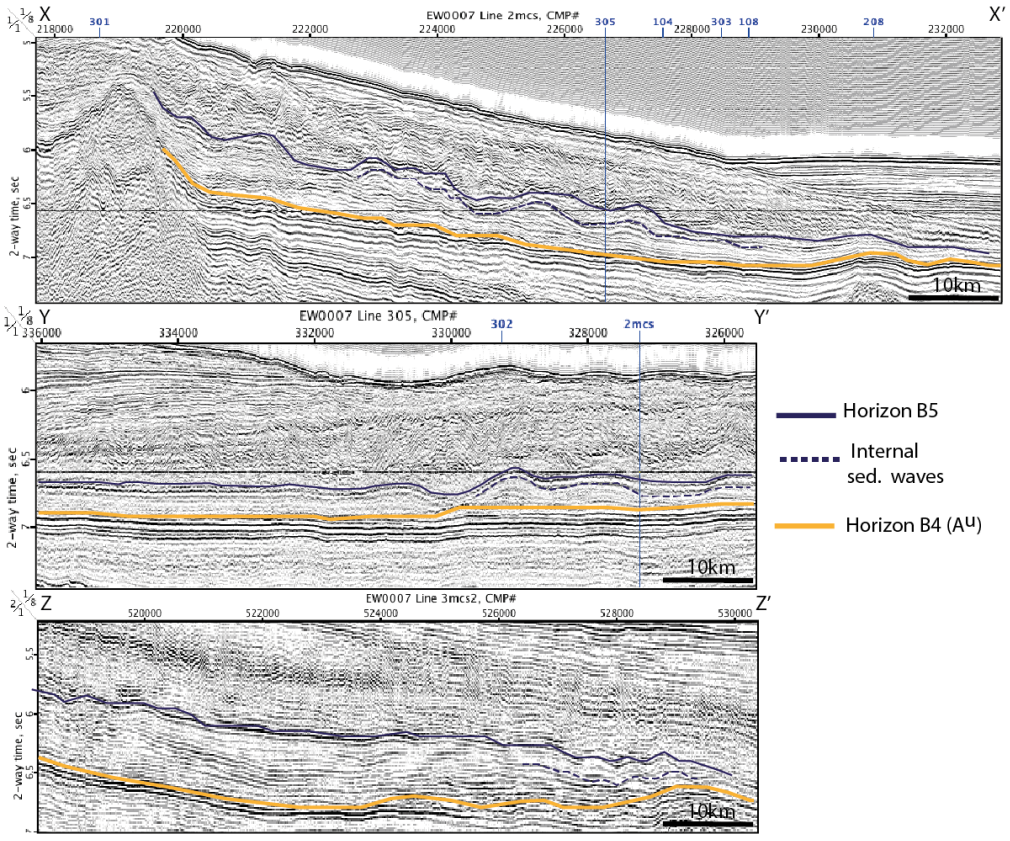

Figure 4.17: Seismic profiles X-X', Y-Y', and Z-Z' from Figure 4.19, showing sediment waves visible both as top of unit and internally. These sediment waves exist both parallel (in Y-Y') and perpendicular (X-X', Y-Y') to the continental shelf.

Unit R4: This unit was only identified on the SENR, where it is marked by an intensification of the drift accumulation first identified in Unit 3a (Boyle et al., 2017). Compared to Unit 3a and Unit R3b, the distribution of thick (>1000 ms) sediments here is more extensive, coats both the northern and southern flanks of the ridge, and deposition generally appears to be in shallower areas, more proximal to the Grand Banks (Figure 4.15f). This change in distribution is in agreement with the isochron maps created by Boyle et al. (2017).

Unit B5: This unit, which is similar to those identified elsewhere on the North Atlantic U.S. east coast margin, is interpreted to be of Miocene-Pliocene age (Mountain and Tucholke, 1985; Tucholke et al., 2004). Its base, though poorly constrained, does not appear to correlate with sedimentary changes on the SENR, and lies somewhere within Unit R4. The formation of the fan is thought to have been controlled by a global sequence of margin progradation (Bartek et al., 1991). It is perhaps unsurprising therefore that this unit does not correlate with changes on the SENR, where deposition is controlled instead by variations in current intensity. Its thickness is greatest along the continental shelf, where it reaches >1500 ms, decreasing to <200 ms at the eastern-most extent of the study area (Figure 4.15g).

Though the drift accumulation rate at the SENR was at its highest during the deposition of this unit over the Newfoundland Basin, the current strength on the ridge during this time is interpreted to have been lower than in Unit R3 (Boyle et al., 2017). This reduction of current intensity on the SENR is attributed to climatic warming reducing the production of NADW. If it was also experienced over the Newfoundland Basin, this could explain why it was possible for such a thick, extensive unit to form along the continental slope, where previously such deposition may have been limited by erosion from bottom currents (Campbell and Mosher, 2016; Mountain and Tucholke, 1985).

Unit 5: The base of Unit 5 marks the end of drift accumulation on the SENR in the Late Pliocene, and on the Newfoundland Basin marks the top of the formation of the abyssal fan in Unit B5. Horizon B6 here marks a widespread period of erosion also identified in Nova Scotia and along the U.S. east coast margin (Campbell and Mosher, 2016; Mountain and Tucholke, 1985). This erosion is attributed to global cooling in the Late Pliocene, which led to increased bottom water production in the high Northern Latitudes and the establishment of the modern deep water configuration in the North Atlantic (Boyle et al., 2017; Campbell and Mosher, 2016). Across the SENR, drift deposition was replaced by a relatively thin (<400 ms) accumulation of pelagic sediments, as the bottom current previously responsible for drift deposition moved to deeper water (Boyle et al., 2017). Ice-rafted debris (IRD) is also prevalent in these sediments. The ridge is isolated from downslope deposition from the Grand Banks, but across the Newfoundland Basin to the north Unit 5 consists of a thick (~600-1600 ms) laterally extensive succession of debris flows and turbidite deposits (Figure 4.15h). This extensive downslope deposition is likely a result of sea level and sedimentary changes driven by Northern Hemisphere glaciation through the Pliocene (Bailey et al., 2013; Raymo, 1994).

4.3.3 EOT palaeobathymetry

The palaeoDEM generated in collaboration with Halliburton Neftex® for the EOT shows several significant differences compared to the modern day bathymetry of the same area (Figures 4.18, 4.19). Firstly, the ridge itself was situated at a palaeolatitude of ~38-39°N across the EOT, compared to its modern latitude of ~41-42°N. This makes the possibility that sedimentation on the ridge was under the influence of sea ice at the time, as discussed in Chapter 2, even less likely; at its modern day latitude, and with a colder climate than during the Oligocene, the SENR today lies at the southern extent of the current North Atlantic sea ice regime (Deser et al., 2002; Eldrett et al., 2009). As the DEM is a model, there is uncertainty associated with the reconstruction, particularly of the bathymetry, which should be noted.

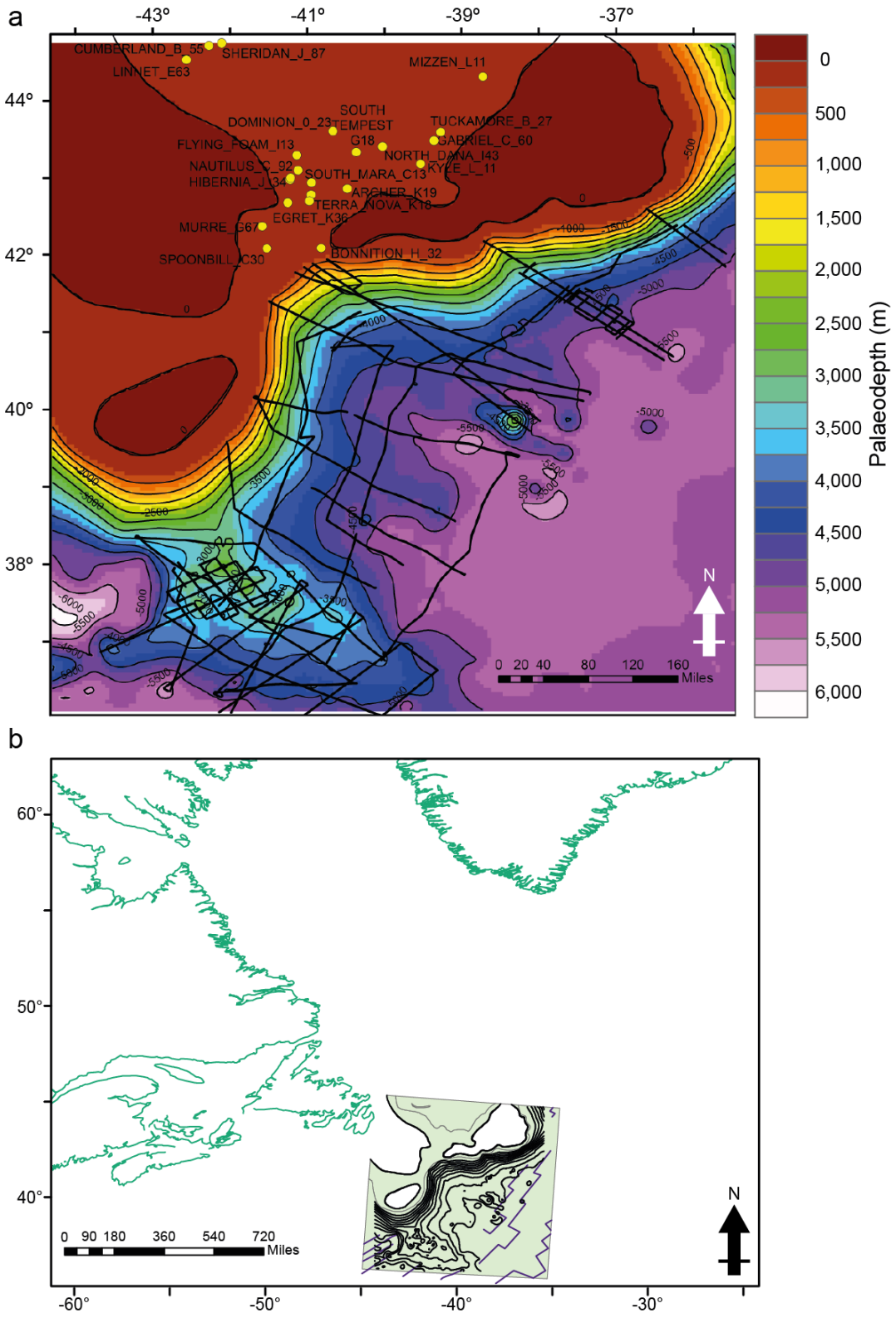

Figure 4.18: a) Reconstructed palaeogeography of the study area for the Latest Eocene-Earliest Oligocene. Thick black line denotes the palaeo-coastline. The locations of the exploration wells (yellow circles) and seismic profiles (black lines) used are also shown. b) The location of the DEM area in the North Atlantic.

Another major difference is the change in the location of the palaeo-coastline (Figure 4.18a). Across the EOT, there was land above sea level within ~160 km of the SENR, and the continental shelf was rarely wider than ~65 km along the Grand Banks. In comparison, the modern day SENR is ~580 km away from the Newfoundland coast, and the shelf of the Grand Banks is ~480 km wide.

The Continental slope to the North of the SENR appears to be steeper across the EOT, compared to the modern day; this is likely a result of the absence of the Miocene-age abyssal fan identified in the seismic interpretation presented in this chapter (Figure 4.15). This proximal coastline, and the narrower shelf across the EOT may have made off-shelf sediment transport more sensitive to sea level change, as discussed in Chapter 3, in the context of the glacioeustatic response to Antarctic ice formation (Harris and Wiberg, 2002).

The palaeobathymetry interpretations from industrial wells (Figure 4.18) appear to define a north-to-south trending channel, possibly analogous to the modern day Flemish Pass. This could have guided the transport of sediment off-shelf; it lines up with the thickest accumulations of sediment indicated for the 'sediment wave' unit identified above (Figure 4.16). It should be noted, however, that the precise morphology of the coastline here is likely to be biased, as the distribution of wells with available data is far from even, so there may have been other channels (Figure 4.18a). The possibility that sand was being deposited off-shelf, as discussed in Chapter 3, is increased by the presence of Oligocene-age sandstone identified in the lithology logs of the wells Linnet_E36, Spoonbill_C30 and Egret_K36, and the identification of the Oligocene Sandstone (OSS) member at the EOB in wells Flying Foam_I13 and Hebron_I13 (Figures 4.5b & 4.18). The complex nature of the modelled topography on the Grand Banks across the EOT may explain why the somewhat simplified predictions made for the responses to SL change of well log data in this chapter were not uniformly observed.

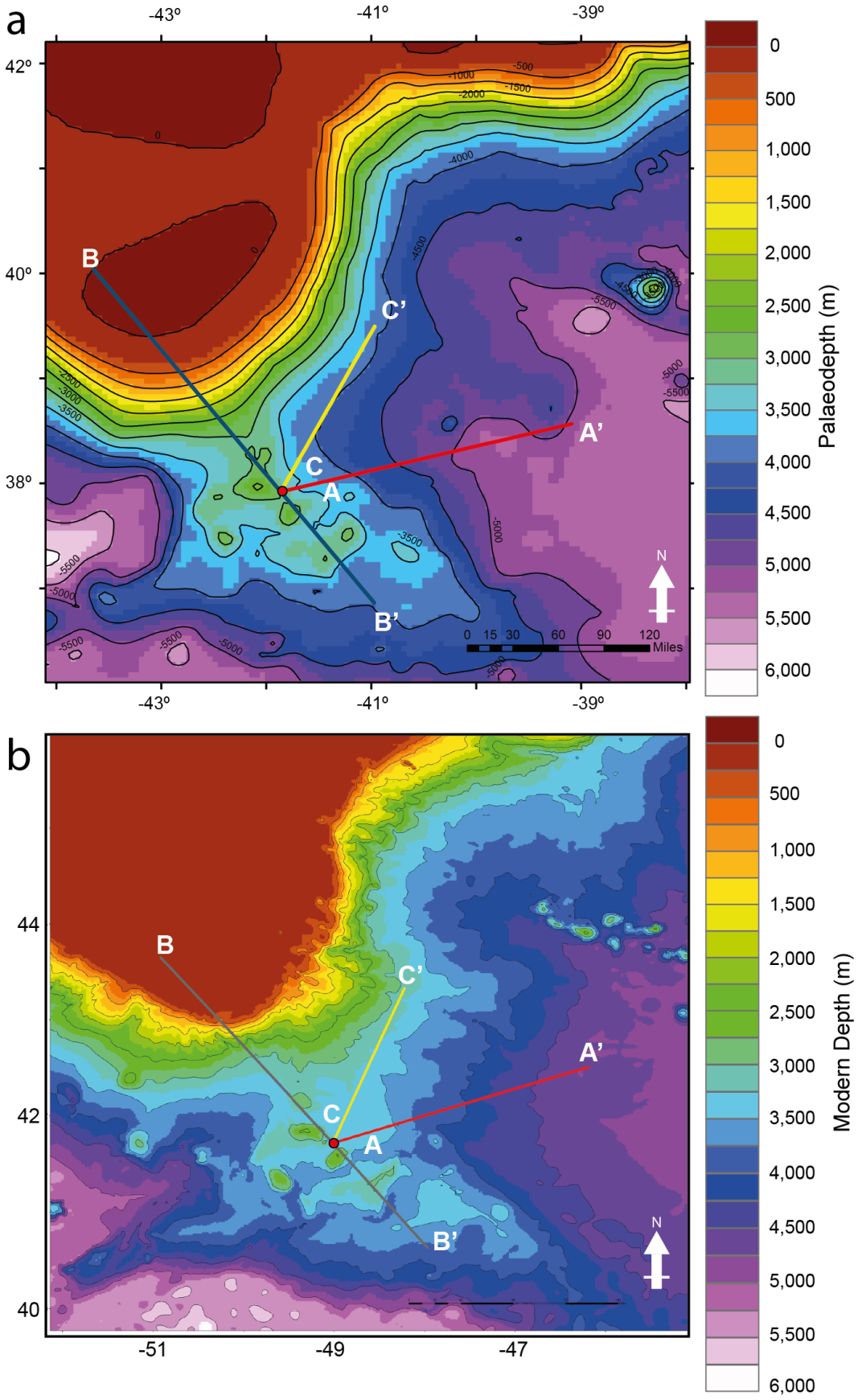

Figure 4.19: Comparison between a) the modelled palaeobathymetry of the SENR, Newfoundland basin, and Grand Banks across the EOB, and b) the modern day bathymetry of the same area. Bathymetric profiles of A-A', B-B' and C-C' are displayed in Figure 4.20.

The shape of the SENR itself does not appear to have changed significantly; the seamounts still exist as bathymetric highs, and shield the drift from downslope movement (Figure 4.19). Depth profiles taken along transects A-A', B-B', and C-C' allow further characterization of the bathymetric changes that the SENR has undergone since the EOT (Figure 4.19, 4.20). Transects A-A' and C-C' both start at the location of Site U1411 (and hence the EOT-Age drift deposit studied in Chapter 3 of this thesis); transect B-B' also intersects this location (red point on Figure 4.19).

Transect A-A' shows that the drift at Site U1411 is now ~300 m deeper than at its time of deposition (Figure 4.20a). Transect A-A' assumes the approach of the bottom current responsible for drift accumulation came from the east-north-east, which is based on the location of the drift in relation to the seamount to its north, and the thickest accumulation of sediment in Unit R3b (Figure 4.14d), which is to the east of Site U1411. At the time of the EOT, this approach would have involved an increase in elevation of ~2200 m from the Newfoundland Basin, across a distance of ~220 km (i.e., a 1% incline). The modern equivalent over the same distance involves an elevation change of ~1000 m and an incline of ~0.5%. Transect B-B' shows that the slope of the Grand Banks down to the SENR was relatively wider and more shallow in the EOT, compared to modern bathymetry (Figure 4.20b); the seamounts are still identifiable in each case. Transect C-C' assumes that the current responsible for drift accumulation followed the contours of the base of the Grand Banks and approached the SENR from the North, as it does today (Section 1.2.2; Figures 4.19a, 4.20c). In the modern day, this approach is relatively level; the continental slope immediately to the north of the SENR is wider than during the EOT, as is the meeting between the SENR and the base of the Grand Banks (Figure 4.19). During the EOT, this approach would have involved an elevation change of ~900 m over a distance of ~70 km, giving an incline of ~1.3%.

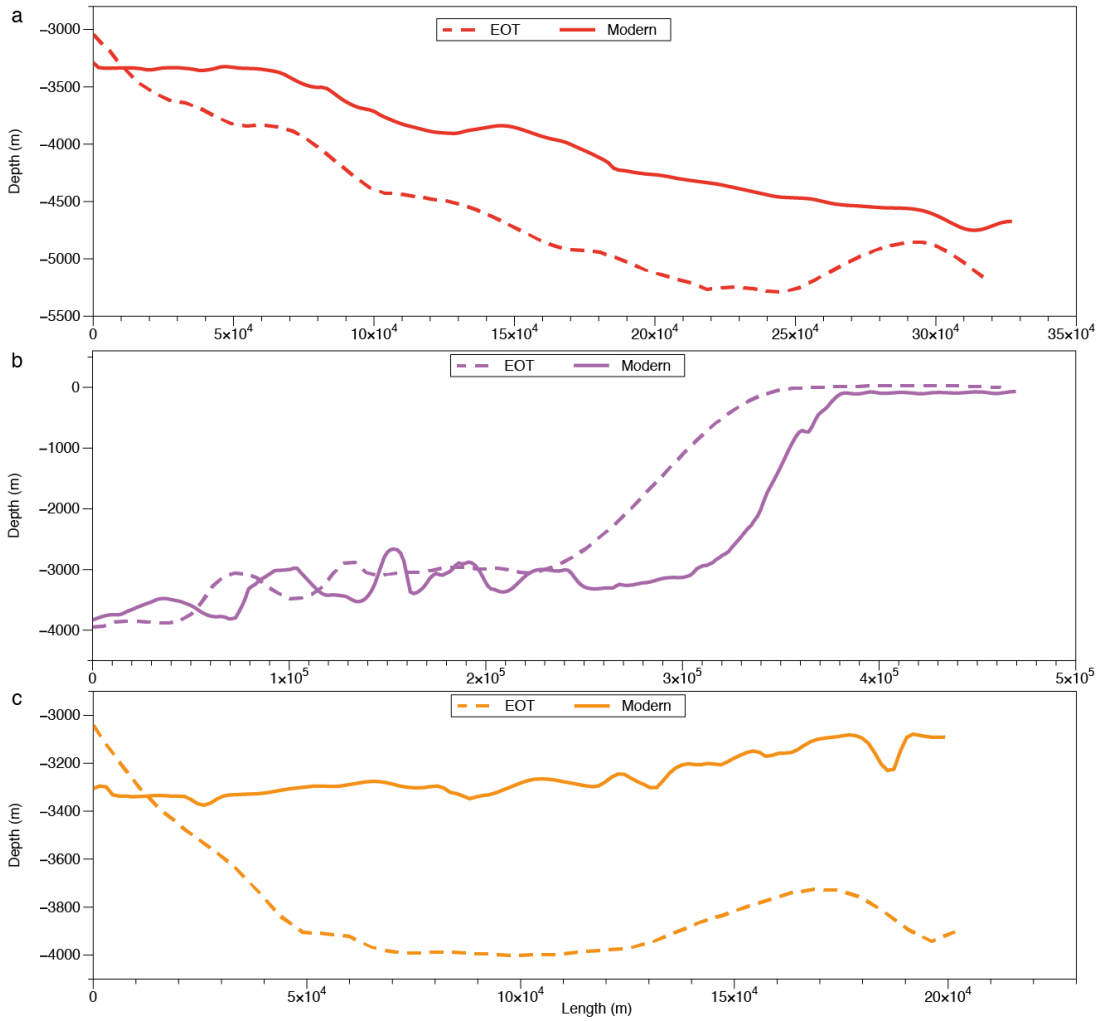

Figure 4.20: Bathymetry profiles for transects a) A-A', b) B-B', and c) C-C' as displayed in Figure 4.20. In each plot, the dashed line shows the EOB palaeobathymetry and the solid line shows the modern-day bathymetry.

It is possible, using these transects, to make some broad predictions of the strength of bottom current required to carry fine sand (as identified in Chapter 3) up-slope onto the SENR. This first requires an estimation of bottom current velocity along a horizontal profile (i.e., the abyssal plain prior to the current reaching the ridge).

The widely used Hjulstrom Curve (Figure 4.21a) relates the erosion and deposition of sediment (with the density of quartz) of varying diameter to the mean flow velocity (Hjulstrom, 1939; McCave, 1984; Miller et al., 1977). However, the accuracy of the depositional predictions of this diagram has been challenged; the low threshold for deposition of fine-grained deposition does not take into account the entrapment of falling sediment in a viscous sublayer that exists directly above the sediment surface (Le Roux, 2005; McCave and Swift, 1976). As such, the deposition of suspended material can in fact occur when flow speed drops below the critical erosion velocity

(McCave, 1984; McCave and Swift, 1976). The grain size distribution analysis presented in Chapter 3 of this thesis suggests the vast majority of the sand deposited on the SENR was <160 μm (Figure 3.4), grains of this size would require a current speed of ~20 cm s^{-1} to be eroded/transported, given the considerations of McCave (1984) as detailed above (Figure 4.21a).

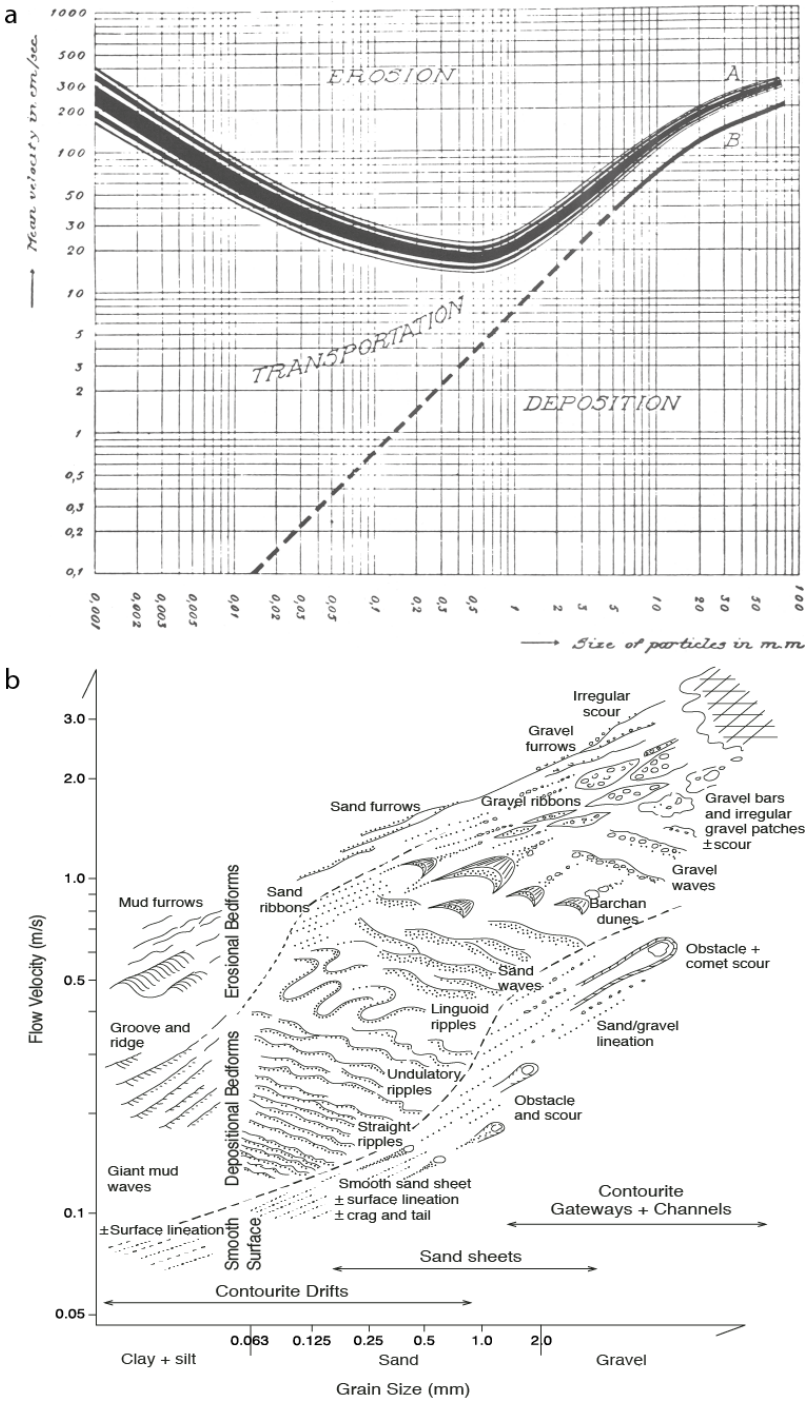

Figure 4.21: a) Hjulstrom curve, showing erosion, transportation and deposition thresholds for quartz-density sediments as a relationship between flow velocity and grain diameter, from Hjulstrom (1939). b) Bedform-velocity matrix for bedforms developing under bottom current systems, related to flow velocity and mean grain size, from Stow et al (2009).

The current velocity in the Newfoundland Basin at the time of the EOT can also be roughly estimated by bedform observations. The A^U horizon, which is widespread in the Newfoundland Basin, represents the erosion of sea-floor sediment. According to Hjulstrom's curve this would have required flow speeds of ≥20 cm s^{-1}, though this assumption is complex for cohesive sediment (<10 μm) (Hjulstrom, 1939; McCave, 1984). In the Oligocene, the km-scale sediment waves identified in Unit B4 above the A^U horizon (Figure 4.17) are predicted to occur under bottom-current velocities from 5-25 cm s^{-1} in the matrix constructed by Stow et al (2009) (Figure 4.21b).

These two predictions of (horizontal) bottom-current velocity are broadly in agreement, suggesting that it is possible that the bottom-current velocity during the EOT interval over the Newfoundland Basin was high enough to transport the detrital sand identified at Site U1411 on the SENR. Changes in the slope of the sediment surface under a flow can affect the critical flow velocity compared to horizontal flow, however. The relationship between horizontal critical flow velocity, (U_{c0}), and critical flow velocity for a slope ($U_{c\alpha}$) was theorised by Allen (1982) to be:

$$\frac{U_{C\alpha}}{U_{C0}} = 1.3204\sqrt{sin(\phi + \alpha)} \quad (4.8)$$

Here, α is the slope of the bed (degrees), and ϕ is the pivot angle, or internal friction angle for the sediment, taken to be 35° (Allen, 1982). This theory was tested experimentally for rounded quartz sand across a range of slope angles, and was supported by the data (particularly up to slopes of +14°) (Whitehouse and Hardisty, 1988). Equation 4.8 was used to calculate $U_{c\alpha}$ for the profiles along transects A-A' and C-C' (for both modern and EOT bathymetry), assuming a U_{c0} of 20 cm s^{-1} (Figure 4.22), showing that the effect of the slope of the SENR caused a minor (<1 cm s^{-1}) increase in the flow velocity required to carry the sand grains in question, relative to horizontal flow. For both profiles, the $U_{c\alpha}$ required near the SENR across the EOT was higher than for the modern day.

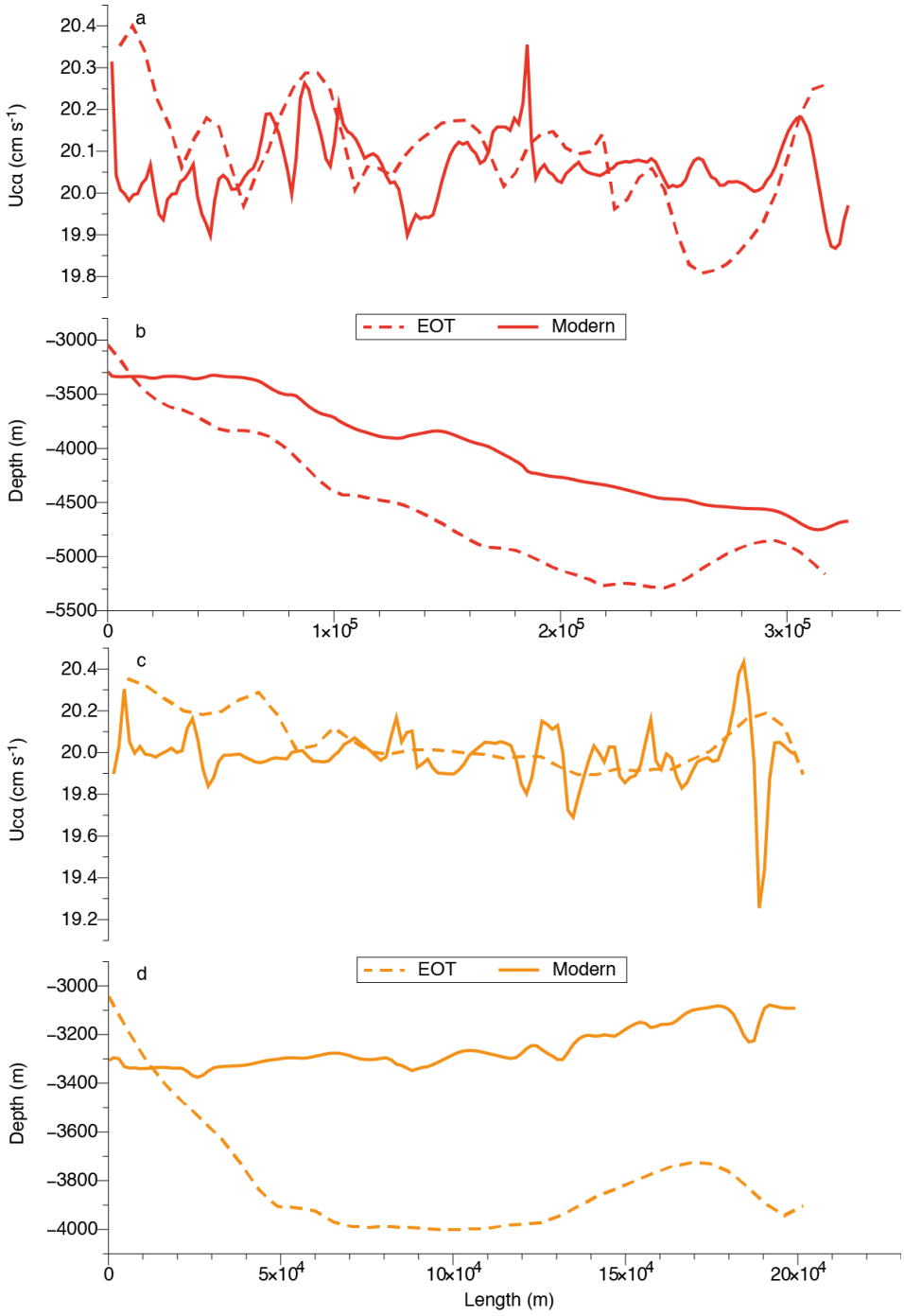

Figure 4.22: a) Critical flow velocity for slope of profile A-A', assuming a horizontal flow velocity of 20 cm s^{-1}, b) bathymetry of profile A-A', c) critical flow velocity for slope of profile C-C', assuming a horizontal flow velocity of 20 cm s^{-1}, d) bathymetry of profile C-C'. In each panel the dashed line represents the EOT reconstruction from Figure 4.20a and the solid line is the modern bathymetry from Figure 4.20b.

The modern day DWBC has a mean southerly flow of ~5-10 cm s^{-1}, but deep (>4000m) currents along the western North Atlantic margin can be highly variable; they were found to average 30 cm s^{-1} over a two-week period along the Nova Scotia continental rise (Gardner et al., 2017; Richardson et al., 1981). Modern day

measurements along the base of the continental slope in the Labrador Sea document bottom-current flow >20 cm s^{-1}, bottom currents of ~10 cm s^{-1} have been measured in the Newfoundland basin, and the Western Boundary Upper Current (WBUC) on the SENR has been measured at 30 cm s^{-1} less than 50 km from Site U1411 (Clarke et al., 1980; Cochonat et al., 1989; Rabinowitz and Eittreim, 1974).

4.4 Conclusions

4.4.1 Sedimentary changes on the Grand Banks

Although none of the variables analysed showed a uniform response across the EOT, there does appear to be an overall shallowing trend suggested by palaeobathymetry interpretations, and a coarsening trend suggested by lithology and wireline log data, focused over the Eastern Grand Banks and Flemish Pass, to the North of the SENR. These observations appear to suggest a drop in sea level corresponding to a lowstand systems tract. Though the apparent sea level drop could also be explained by accommodation space being filled up during progradation, this would require the presence of extensive deltas, for which there is no evidence. The variability of responses across the whole study area is likely down to issues with the temporal accuracy of using cuttings, but may also suggest that there were also small-scale tectonic changes occurring over the EOT in addition to eustatic sea level change, resulting in a more complex sea level response.

4.4.2 Changes in sedimentation through the Cenozoic- the SENR vs. the Newfoundland Basin

This chapter documents a concordant change in sedimentation patterns along the North West Atlantic margin, where it appears that through the Cretaceous and Cenozoic, the depositional changes occurring on the SENR were often linked to the Newfoundland Basin and continental slope to the north.

- During the Late Cretaceous through to the Mid-Eocene (Units 1-2), accumulation was relatively slow across the entire study area; pelagic accumulation was focused in shallower areas of the SENR, while the downslope delivery of sediments augmented thin pelagic successions across the Newfoundland Basin.

- As the accumulation of thick (>1000 ms) drifts began over the SENR in the Middle Eocene, sediment accumulation on the Newfoundland Basin remained slow. Across the Eocene Oligocene Boundary, the presence of the A^U horizon provides evidence that the bottom current controlling deposition on the SENR was eroding fine sediments across the Newfoundland Basin. The significant lateral extent of this erosional unconformity implies that it is unlikely there are any potential EOT-aged sedimentary records from the Newfoundland Basin. The extent of the A^U horizon, and other equivalent Late Eocene/Early Oligocene erosional unconformities such as R4, TE, and T35 (Figure 1.4) throughout the North Atlantic, highlights how vital and unique the expanded EOT interval on the SENR truly is. As erosion along the Newfoundland margin largely took place at depths >4000 m, the bathymetry of the SENR allowed the EOT interval to survive intact (Boyle et al., 2017). More generally, this example highlights the palaeoclimatic importance of the influence of bathymetric features on the formation of contourite drifts- which can preserve expanded sequences at times where widespread oceanographic changes might lead to erosion in more typical continental slope contourites (Hernández-Molina et al., 2008).
- The increase in bottom current intensity going into the Oligocene also appears to have influenced the formation of a thick (400-1000 ms) succession of contourite and turbidite deposits along the continental slope of the Eastern Grand Banks and the Flemish Cap. This unit (Unit B4) contains sediment waves, suggesting moderation by bottom currents (Davies et al., 2001; Lear et al., 2008; Miller and Fairbanks, 1983). In comparison to the Newfoundland Basin, the sedimentary change seen across the EOT on the SENR is less pronounced. Boyle et al., (2017) interpreted a slight decrease in current intensity on the ridge, in response to the implied deepening of the bottom current across the interval.
- Heading into the Miocene, sedimentation on the SENR continued to be controlled by bottom currents, but in the Newfoundland Basin, progradation of sediments from the shelf led to the formation of a thick (>1500 ms) fan deposit. The reduced influence of the bottom current on sedimentation over the plain may have also been due to an interpreted decrease in current

intensity along the North American margin (Boyle et al., 2017; Campbell and Mosher, 2016).

- In the Late Pliocene, global cooling, Northern Hemisphere Glaciation, and the associated increase in the production of NADW, led to the end of drift accumulation on the SENR (Boyle et al., 2017; Campbell and Mosher, 2016; Raymo, 1994). The SENR is isolated from downslope deposition, and its sediment cover is thin (0-400 ms) and consists of pelagic sediments and IRD. In contrast, this interval saw the accumulation of thick (>1500 ms) turbidites along the continental slope and Newfoundland Basin to the north.

4.4.3 The palaeobathymetry of the Newfoundland Basin over the EOT

The palaeobathymetric model generated in this study suggests that during the EOT, the SENR was proximal to a continental shelf that was much narrower than at the present day, and that its arrangement was such that off-shelf deposition may have occurred to the north. It documents that the SENR rose further above the Newfoundland Basin to the north than it does today, but that the gradient of this rise would not have been a significant impediment to the transportation of fine quartz sand (as identified in Chapter 3) onto the ridge. The bottom current velocities required to entrain and transport this sand are similar to those estimated from the presence of the A^U erosional unconformity across the EOT, and from giant sediment waves identified in the Newfoundland Basin during the Oligocene. They are also comparable to modern-day measurements of bottom current velocities.

Chapter 5 Conclusions

This thesis is constructed around three major themes. The first of these themes, Chapter 2, focuses on establishing whether there was extensive Northern Hemisphere Glaciation at the time of the Eocene Oligocene Transition (EOT), synchronous with Antarctic glaciation. The second theme of this thesis, Chapter 3, explores signals of palaeoclimatic, oceanographic, and sea-level change across the high-resolution EOT interval recovered at Integrated Ocean Drilling Program (IODP) Site U1411 on the Southeast Newfoundland Ridge (SENR). Finally, Chapter 4 investigates the sedimentological development of the Cenozoic drift sequence on the SENR within the broader context of the Newfoundland Margin.

5.1 Summary of main findings

5.1.1 Was there an extensive ice-rafting regime in the North Atlantic over the EOT, signifying bipolar glaciation?

The controversial hypothesis of bipolar Cenozoic glaciation suggests that significant ice caps formed across the EOT in both the Antarctic and the Northern Hemisphere (Tripati et al., 2008), contrary to modelled CO_2 thresholds (DeConto et al., 2008). A large part of this hypothesis rests on the discovery of an EOT succession of ice-rafted debris (IRD) at Ocean Drilling Program (ODP) Site 913 offshore of east Greenland (Eldrett et al., 2007). Tripati et al., (2008) interpreted this IRD to represent iceberg rafting from a Greenland ice cap. The location of this site, however, proximal to the Greenland coastline, combined with the absence of other EOT-age IRD records in the North Atlantic, raises the possibility that it might only represent isolated mountain outlet glaciers rather than an ice cap (Eldrett et al., 2007). The results of this thesis, which explored three further North Atlantic EOT-age detrital sediment records, suggest that while the EOT interval at Site 913 does represent an example of glacially sourced ice rafting, there is no evidence for a larger ice-rafting regime extending into the North Atlantic (i.e., there is no evidence for significant bipolar glaciation across the EOT). Instead, the IRD identified at Site 913 likely represents ice rafting from a local tidewater glacier on east Greenland, the influence of which did not extend into the North Atlantic.

Detrital grains identified at Sites U1411 and U1406 on the SENR were originally interpreted by members of the IODP Expedition 342 shipboard party to be a further record of IRD across the EOT (Norris et al., 2014). The analysis presented in this thesis on the surface textures of quartz grains from these sites, however, suggests that, along with those from ODP Site 647 in the Labrador Sea, these grains were transported in a sub-aqueous environment. They differ from those found at Site 913 and from the Pleistocene interval at Site U1411, which were transported by icebergs (Section 2.3.4). Provenance analysis of the Site U1411 and U1406 grains also showed that they derived from terranes local to the Newfoundland Margin, rather than Greenland (Sections 2.3.2 & 3.3.2).

CT-scanning shows that the loosely compacted detrital clasts identified at the Site U1411 EOT interval, originally suggested to have been ice-rafted dropstone clasts similar to those seen at Site 913, are instead products of post-depositional bioturbation (Norris et al., 2014): their three-dimensional structure reflects a network of inter-connected silt-lined burrows. Inspection of low-latitude drift deposits also revealed similar features, confirming that they can be formed outside of areas under the influence of ice rafting (Section 2.3.1).

5.1.2 Is the surface textural analysis of quartz grains sensitive to changes in grain size?

The results of analysis on the sensitivity of surface textures to grain size, as featured in Chapter 2, emphasise a need for caution when comparing quartz surface texture analyses from different studies, especially if the size fractions in each are not consistent. Quartz grains from both of the sites sampled for this thesis displayed increasing roundness with increasing grain size, and the same trend is also visible for the frequency of chemical surface textures. Krinsley and Doornkamp (2011) suggest that quartz grains larger than 200 μm (2.32 ϕ) display surface textures in a different way to smaller grains. This interpretation is borne out by the results of this thesis, particularly in terms of roundness and chemical surface textures (Section 2.3.3).

5.1.3 Does the detrital sand flux at Site U1411 represent changes in sea level, current intensity, or both?

Detrital sands deposited in sediments of EOT age appear to represent a separate sediment source to the majority of the fine material being carried by the bottom current responsible for drift accumulation on the SENR, based on differing grain size distributions, Nd isotopic signatures, and dominant cyclicity (Hass, 2002; Prins et al., 2002).

The grain flux record increases step-wise across the EOT, similarly to several existing benthic foraminiferal $\delta^{18}O$ records for the interval (though it should be noted that the EOT-1 step was not easily identifiable in the bulk carbonate $\delta^{18}O$ record for Site U1411 as presented in this thesis). The largest increase in grain flux follows the Oi-1 event, suggesting that glacioeustatic sea level change may be the driving factor controlling sediment delivery from local shelf-edges to the nepheloid layer (Section 3.3.1) (Alaf, 1987; Piper et al., 1994). The sand flux record also appears to show 41 ka obliquity and potentially 100 ka eccentricity cycles, similar to another sea level-controlled sedimentation record from the early Oligocene (Abels et al., 2007). Site U1411 (and Site U1406, which also shows an increase in detrital sand flux across the EOT) are bathymetrically isolated from direct downslope sand transport. Therefore, the sand must have been transported up onto the ridge by bottom currents after it was ejected off-shelf. The Nd isotopic signature of the sand fraction suggests it originated from sources closer to the site of deposition than the fine fraction (i.e., it has been transported over a shorter distance). This interpretation is also supported by grain size distribution analysis of the detrital fraction, which shows a bimodal distribution (Section 3.3.2).

There is little evidence in the clay mineral analysis and fine fraction Nd and Sr isotopes for a change in bottom current intensity prior to, or directly in time with, the EOT, as interpreted by previous studies (Abelson and Erez, 2017; Pusz et al., 2011) though there may be evidence for a change in circulation ~33 Ma, in broad agreement with a study by Via and Thomas (2006). The confidence of this interpretation could be improved, however, by increasing the resolution of these proxies.

5.1.4 How did Sedimentation on the Grand Banks Change across the EOT?

Commercial well records of interpreted lithology, wireline log data, and interpreted palaeobathymetry were used to analyse sedimentary and palaeobathymetric change on the Grand Banks across the EOT. Although none of the variables analysed showed a uniform response across the EOT across all wells, there does appear to be evidence for sea level fall over the Grand Banks across the interval. In particular, there is an overall shallowing upwards trend suggested by palaeobathymetry interpretations, and a coarsening upwards trend suggested by lithology and wireline log data, focused over the Eastern Grand Banks and the Flemish Pass, to the north of the SENR. These observations are consistent with a fall in sea level corresponding to a lowstand systems tract. Though the apparent sea level fall could also be explained by accommodation space being filled up during progradation, this would require the presence of extensive deltas, for which there is no evidence. The variability of the response across the whole study area is likely attributable to issues with the temporal accuracy of using cuttings, but may also suggest that there were also small-scale tectonic changes occurring over the EOT in addition to eustatic sea level change, resulting in a more complex sea level response.

5.1.5 How was sedimentation on the SENR and in the Newfoundland Basin affected by changes in sea level and bottom current change through the Cenozoic

Analysis of seismic profiles covering the SENR and the Newfoundland Basin showed that through the Cenozoic, depositional changes occurring in these two locations were often linked. Prior to the Mid-Eocene, accumulation was relatively slow across the entire study area; pelagic accumulation was focused in shallower areas of the SENR, while the downslope delivery of sediments augmented thin pelagic successions across the Newfoundland Basin. While the accumulation of thick (>1000 ms) drifts began over the SENR in the Mid-Eocene, sediment accumulation in the Newfoundland Basin remained slow.

Across the Eocene Oligocene Boundary, the presence of the A^U horizon in the Newfoundland Basin provides evidence that the bottom current controlling

deposition on the SENR was now strong enough to erode fine sediments in the basin. Glacioeustatic sea level fall across the EOT, controlled by Antarctic Ice Sheet formation, also appears to have increased off-shelf deposition into the Newfoundland Basin going into the Oligocene, as shown by evidence of turbidity and debris flows in sediments along the continental slope of the Eastern Grand Banks and Flemish Cap. These sediments also contain sediment waves suggesting moderation by bottom currents, and they may represent a mixed contourite-turbidite drift (Davies et al., 2001; Lear et al., 2008; Miller and Fairbanks, 1983). In comparison to the Newfoundland Basin, the sedimentary change seen across the EOT on the SENR is less pronounced, with a slight decrease in current intensity on the ridge interpreted in response to the implied deepening of the bottom current across the interval (Boyle et al., 2017). Though erosion along the Newfoundland margin, and across the North Atlantic as a whole, appears to have been widespread across the EOT, the bathymetry of the SENR appears to have allowed the EOT interval here to survive intact (Boyle et al., 2017).

During the Miocene, sedimentation on the SENR continued to be controlled by bottom currents. In the Newfoundland Basin, however, prograding sediments from the continental shelf led to the formation of a thick (>1500 ms) and laterally extensive fan deposit. The increasing influence of sea level change on off-shelf deposition, driven by fluctuations in the volume of a large Antarctic ice cap, may have driven this progradation and overshadowed the influence of the bottom currents on sedimentation in the basin. There may have also been a decrease in current intensity along the North American margin (Boyle et al., 2017; Campbell and Mosher, 2016; Miller et al., 1991).

Global cooling, expanding Northern Hemisphere glaciation, and the associated increase in the production of NADW led to the end of drift deposition on the SENR in the Late Pliocene. This was replaced by the accumulation of thin (0-400 ms) pelagic sediments and IRD (Boyle et al., 2017; Campbell and Mosher, 2016; Raymo, 1994). In contrast, this interval saw the accumulation of thick (>1500 ms) turbidites along the continental slope and the Newfoundland Basin to the north.

5.1.6 How did the geography of the SENR, Grand Banks, and Newfoundland Basin across the EOT differ from the modern day, and how hoes this affect the feasibility of sediment transport onto the ridge?

The creation of a palaeogeographic Digital Elevation Model (DEM) for an EOT time slice of the Newfoundland Margin revealed several key differences between the modern day bathymetry of the same region. The model generated suggests that the SENR during the EOT was proximal to a continental shelf that was much narrower than at present day, and that its arrangement was such that off-shelf deposition would have occurred to the north of the SENR, into the Newfoundland Basin. It documents that the SENR rose further above the Newfoundland Basin to the north than it does today, but that the gradient of this rise would not have been a significant impediment to the transportation of fine quartz sand (as identified in Chapter 3) onto the ridge. The bottom current velocities required to entrain and transport this sand are similar to those estimated from the presence of the A^U erosional unconformity across the EOT, and from giant sediment waves identified in the Newfoundland Basin during the Oligocene. They are also comparable to modern-day measurements of bottom current velocities in the Labrador Basin, Newfoundland Basin, and the SENR.

5.2 Future considerations

Caution is needed when looking for evidence of ice rafting:

The analysis presented in Chapter 2 shows that caution should be used when interpreting detrital sand at any given site as IRD, even when the downslope delivery of sediment does not appear to have a direct influence over sediment deposition at a given site. In particular, the mm-scale loosely compacted detrital clasts identified at Site U1411, which at first glance appear quite convincingly to be dropstones, are shown here to be post-depositional features.

Future estimates of EOT ice volume from North Atlantic sites:

The Site U1411 bulk carbonate $\delta^{18}O$ record for the EOT presented in this thesis differs from existing benthic foraminiferal $\delta^{18}O$ records for the interval, which feature a two-step shift (EOT-1 and Oi-1 event); it only appears to record the Oi-1 event. The

detrital grain flux record from Site U1411, however, does appear to have a step-like nature. Though beyond the scope of this thesis, the development of a high-resolution benthic foraminiferal oxygen isotope record for Site U1411 will better resolve whether the EOT-1 step exists at this site. This record will also allow, with accompanying foraminiferal Mg/Ca ratios, for the ice volume associated with each step to be estimated. The relatively shallow depth of Site U1411 will hopefully circumnavigate the CCD-related complications that were encountered when analysing the Pacific EOT Mg/Ca record from ODP Site 1218 (Coxall et al., 2005; Lear et al., 2008).

Further analysis of provenance of Site U1411 & U1406 detrital sand fraction:

One of the findings from this thesis is that the detrital sand seen on the SENR is not transported from a large Greenland ice cap, via iceberg rafting; it appears to be more locally sourced. Possible source regions include Late Eocene to Early Oligocene sandstone bodies on the Eastern Grand Banks, and reworked sediments from the Newfoundland Basin. This interpretation could be taken further by Pb isotope analysis of feldspars from further EOT-age North Atlantic intervals, any available material from ODP Site 1276 in the Newfoundland Basin, and any remaining rock cuttings from industrial wells on the Eastern Grand Banks.

Considerations for Hydrocarbon exploration:

The conclusion that the detrital sand flux record at Site U1411 reflects off-shelf sand deposition is important because it suggests that the off-shelf transport of sediment occurred by the end of the EOT in the Northwest North Atlantic, controlled by eustatic change, and demonstrates the far-reaching effects of the formation of Antarctic ice over the EOT. The fine fraction (and fine sand) from this sediment was re-distributed by bottom currents, which may have left behind a coarser deposit of potential interest as a hydrocarbon reservoir. The identification of giant sediment waves during the Oligocene in the Newfoundland Basin, for example, suggests the reworking of sediments by bottom currents. The possibility of a sizeable Oligocene-age drift deposit in the Newfoundland Basin could have significant implications for deep-water

hydrocarbon exploration if this unit is able to provide a potential reservoir. This unit is of particular hydrocarbon interest because it overlies Cretaceous-age sediments featuring black shales that have total organic carbon (TOC) contents of up to 12% (Arnaboldi and Meyers, 2006). Potential hydrocarbon source rocks have also been identified in the Salar Basin, which underlies the Newfoundland Basin (Wielens et al., 2006). Better age control and sedimentological data is needed however, particularly on the sediments filling the Newfoundland Basin after the Latest Eocene (Shillington et al., 2004). Further seismic exploration of the Newfoundland Basin, at a resolution akin to Cruise KN179-01, is also essential to better reveal the nature of Paleogene sedimentation in this region.

Predicting palaeocurrent intensity through the sortable silt proxy:

Understanding that some of the silt fraction at Site U1411 may have been derived from a secondary source, and hence that its flux may not be influenced purely by bottom current intensity, is important if attempts are to be made to calculate bottom current intensity via the sortable silt proxy (Hass, 2002; McCave et al., 1995; Mulder et al., 2013). A greater understanding of the relative contributions of the two sources of material to the SENR drifts could be achieved by higher resolution grain size distribution analysis than presented in this thesis, coupled by accompanying high-resolution Nd isotope and QEMSCAN analysis of the differing size fractions.

The bioturbation recorded at Site U1411 (burrow features, originally thought to be ice-rafted lithic clasts) may also provide a proxy with which to study changes in palaeocurrent intensity. The increased oxygenation and sediment supply afforded by contourite currents can lead to enhanced burrow formation, though the relationship is as yet poorly understood (Uchman and Wetzel, 2011; Wetzel and Uchman, 2012). In other sediments, bioturbation intensity has also been used as a proxy for the oxygenation of the depositional environment. Further work to establish a record of the abundance of the burrow features may help to better understand oceanographic change through the interval (Frey, 2012).

5.3 Wider implications

The conclusion presented in Chapter two, that detrital lithic grains found in the Northwest Atlantic do not represent a widespread iceberg-rafting regime, has wider implications for the controversial hypothesis of bipolar glaciation (Tripati et al., 2005; 2008). It appears that northern hemisphere glaciation to the same extent as seen in the Pliocene or Pleistocene did not exist across the EOT, implying that IRD seen along the East Greenland Shelf are the result of ice rafting from localised glaciers rather than an ice cap (Bailey et al., 2012; Eldrett et al., 2007). The results highlight two points to take forward for future IRD studies. Firstly, the presence of detrital sand grains and/or clasts should not be interpreted as evidence of ice rafting without detailed examination (e.g. of their texture, size, and/or provenance), even in locations where downslope transport of sediments is not apparent or feasible. As a follow up to this thesis, it might be wise to consider using the lessons learned to create a checklist or identification guide to be used during IODP expeditions when attempting to identify IRD. Secondly, even in scenarios where detrital grains can be reasonably described as IRD, as is the case for the Site 913 EOT interval, their presence should be taken only to represent localised tidewater glaciers in the absence of other evidence, rather than a potential ice cap.

Chapter three highlighted that the detrital sand record seen on the SENR across the EOT was the result of a complex combination of several processes. In particular, grain size, geochemical Nd-Sr, and time series analyses suggest that the sand was transported from a different source (and potentially through a different process) to the finer components of the drift sediments that plaster the ridge. This complexity should be borne in mind when attempts are made to relate the accumulation of the drift deposits to changes in bottom current intensity, through the sortable silt proxy for example (Hass, 2002; McCave et al., 1995).

Chapter four of this thesis can be viewed as a case study for collaboration between the UK-IODP (via university-led research and analysis of IODP-derived material) and an industry partner (in this case via the database and earth system modelling capabilities of Halliburton Neftex®). The hydrocarbon well and seismic data provided

by Halliburton Neftex® were used to explore the spatial extent of the climate signals interpreted at ODP and IODP sites along the Newfoundland Margin, and accessing Halliburton Neftex®'s modelling capabilities allowed for the generation of an EOT-aged palaeoDEM in which the IODP-obtained data could be situated. In return, through part-funding this studentship Halliburton Neftex® were able to influence the generation of new proxy records from a high-resolution IODP-recovered sedimentary interval, and can use the data generated to contribute to the accuracy of their models.

5.4 Concluding remarks

This thesis features an extensive exploration of the sedimentary and palaeoclimatic signals of the EOT in the North West Atlantic, with specific attention paid to the SENR and Newfoundland Basin. No support is found for the suggestion that bipolar glaciation occurred across the EOT, rather the sedimentary record is most consistent with the conclusions of Eldrett et al., (2007), that ice formation was limited to a small tidewater glacier local to east Greenland, unable to produce icebergs capable of rafting detrital material into the North Atlantic at the scale seen much later into the Cenozoic. Instead, the sedimentary record of the SENR reveals a complex combination of off-shelf deposition influenced by Antarctic-driven glacioeustatic sea-level fall and bottom current-controlled sediment transport.

Appendix A SEM Grain surface analysis

A.1 Surface texture descriptions

Texture	Type	Description
Breakage Blocks	M	Removal of large, blocky portions of original grain via physical impact with other grains or ice.
Conchoidal fractures	M	Distinctive curved breakage surface; do not follow separation planes. A result of grain-to-grain contact.
Straight or arcuate step	M	Fractures that feature distinct repeated steps, incorporating several planes of separation.
Isolated cusps/ v impact pits	M	Isolated pits found on grain surface, caused by the sharp corner of another grain impacting on the surface.
Other Fractures	M	Irregular and isolated cracks that run across grain, ignoring planes of separation.
Striations/Grooves	M	Superficial scratches on grain surface caused by the sharp edge of a separate grain being dragged across it.
Edge abrasion	M	Fresh grain edge is broken and chipped by grain-to-grain impacts.
Upturned plates	M	Edges of overlying plates have been exposed.
Silica dissolution	C	Amorphous dissolution of the original silica of grain surface
Micro-layering	C	Forms through successive precipitation of thin diagenetic silica layers
Silica precipitation	C	Amorphous covering of diagenetic silica, can cover other surface features and give grain a smooth appearance and low relief
Adhering particles	C	Fragments of foreign material that have been chemically stuck to the surface of the grain, e.g. by silica cement
Chemical v shaped pits	C	Similar to mechanical impact pits, but are formed by dissolution of silica. They often have a distinctive V-shape.

Table A : Descriptions of mechanical (m) and chemical (c) surface textures used in this thesis

A.2 Abundance of quartz surface textures

Texture	Interval			
	Site 647 EOT	**Exp. 342 EOT**	**Site 913 EOT**	**Site U1411 Pleistocene**
Breakage Blocks	30.19	38.28	35.14	22.77
Conchoidal Fractures	64.15	58.59	83.24	77.23
Arc Step-like Fractures	33.96	29.69	37.30	36.63
Straight Step-like Fractures	24.53	16.41	20.00	16.83
Isolated Fractures	7.55	17.97	35.68	11.88
Mechanical Impact Pits	32.08	36.72	72.43	63.37
Gouges/Striations	47.17	40.63	59.46	64.36
Edge Abrasion	47.17	55.47	46.49	71.29
Upturned Plates	50.94	34.38	28.11	39.60
Microlayering	13.21	25.78	2.70	1.98
Chemical v-pits	54.72	42.97	31.89	18.81
Adhering Particles	18.87	38.28	16.76	11.88
Silica Precipitation	92.45	84.38	70.27	65.35
Silica Dissolution Y/N	83.02	67.97	62.16	46.53
Dissolution- Rare-Absent	1.89	7.03	71.35	16.83
Dissolution- Present	15.09	25.00	24.86	39.60
Dissolution- Common	54.72	44.53	38.38	32.67
Dissolution- Pervasive	28.30	23.44	23.78	13.86
Relief-Low -	54.72	42.19	10.81	7.92
Relief-Medium	37.74	42.97	50.27	55.45
Relief-High	7.55	14.06	38.38	39.60
Roundness-Very Angular	3.77	4.69	6.49	20.79
Roundness-Angular	13.21	16.41	23.78	40.59
Roundness-Sub-Angular	24.53	22.66	44.86	19.80
Roundness-Sub-Rounded	47.17	28.91	16.76	11.88
Roundness-Rounded	9.43	20.31	5.95	6.93
Roundness-Well Rounded	1.89	6.25	2.16	0.00

Table A 1: Abundance of surface textures on quartz sand grains for the four intervals featured in this thesis

Texture	Sample, IODP Nomenclature				
	913-1	913-2	913-3	913-4	913-4
	B20R 3W 37-43	B22R 2W 107-110	B24R 1W 107-110	B24R 2W 80-83	B26R 4W 20-22
Breakage Blocks	44.44	22.73	37.50	43.24	28.57
Conchoidal Fractures	82.22	79.55	87.50	86.49	82.86
Arc Step-like Fractures	35.56	43.18	54.17	27.03	31.43
Straight Step-like Fractures	8.89	31.82	33.33	21.62	8.57
Isolated Fractures	35.56	43.18	29.17	37.84	28.57
Mechanical Impact Pits	53.33	79.55	75.00	78.38	80.00
Gouges/Striations	64.44	70.45	45.83	51.35	57.14
Edge Abrasion	42.22	43.18	45.83	51.35	51.43
Upturned Plates	24.44	27.27	25.00	32.43	31.43
Microlayering	4.44	4.55	0.00	0.00	2.86
Chemical v-pits	31.11	25.00	37.50	27.03	42.86
Adhering Particles	8.89	18.18	20.83	13.51	25.71
Silica Precipitation	68.89	81.82	62.50	67.57	65.71
Silica Dissolution Y/N	60.00	61.36	62.50	45.95	51.43
Dissolution- Rare-Absent	13.33	4.55	8.33	10.81	8.57
Dissolution- Present	26.67	36.36	29.17	43.24	40.00
Dissolution- Common	44.44	43.18	45.83	35.14	42.86
Dissolution- Pervasive	15.56	18.18	16.67	10.81	8.57
Relief-Low -	11.11	13.64	4.17	10.81	11.43
Relief-Medium	53.33	52.27	50.00	45.95	48.57
Relief-High	35.56	36.36	45.83	37.84	40.00
Roundness-Very Angular	6.67	0.00	12.50	10.81	5.71
Roundness-Angular	26.67	22.73	25.00	16.22	28.57
Roundness-Sub-Angular	37.78	56.82	33.33	51.35	40.00
Roundness-Sub-Rounded	22.22	13.64	20.83	10.81	17.14
Roundness-Rounded	4.44	6.82	4.17	8.11	5.71
Roundness-Well Rounded	2.22	0.00	4.17	2.70	2.86

Table A 2: Surface textural analysis of quartz grains from ODP Site 913 for intra-site comparison

Appendix A

Texture	Sample, IODP Nomenclature				
	U1411-1	U1411-2	U1411-3	U1411-4	U1411-4
	B2H 1W 100-102	B2H 2W 116-118	B2H 3W 135-137	B2H 4W 133-135	B2H 5W 146-148
Breakage Blocks	30.77	17.39	29.63	12.00	23.53
Conchoidal Fractures	80.77	82.61	70.37	76.00	82.35
Arc Step-like Fractures	30.77	39.13	40.74	36.00	41.18
Straight Step-like Fractures	19.23	34.78	11.11	4.00	5.88
Isolated Fractures	7.69	17.39	11.11	12.00	0.00
Mechanical Impact Pits	69.23	56.52	51.85	76.00	64.71
Gouges/Striations	61.54	60.87	66.67	68.00	52.94
Edge Abrasion	57.69	65.22	88.89	72.00	76.47
Upturned Plates	46.15	30.43	37.04	44.00	64.71
Microlayering	3.85	4.35	0.00	0.00	5.88
Chemical v-pits	15.38	8.70	18.52	32.00	17.65
Adhering Particles	7.69	4.35	14.81	20.00	11.76
Silica Precipitation	69.23	73.91	59.26	60.00	58.82
Silica Dissolution Y/N	42.31	52.17	40.74	52.00	58.82
Dissolution- Rare-Absent	19.23	4.35	29.63	12.00	11.76
Dissolution- Present	46.15	47.83	29.63	36.00	29.41
Dissolution- Common	34.62	34.78	25.93	36.00	41.18
Dissolution- Pervasive	7.69	17.39	14.81	16.00	17.65
Relief-Low -	11.54	8.70	0.00	12.00	0.00
Relief-Medium	50.00	56.52	66.67	48.00	52.94
Relief-High	46.15	39.13	33.33	40.00	47.06
Roundness-Very Angular	26.92	21.74	22.22	12.00	11.76
Roundness-Angular	30.77	47.83	44.44	40.00	58.82
Roundness-Sub-Angular	11.54	26.09	22.22	20.00	23.53
Roundness-Sub-Rounded	15.38	0.00	11.11	20.00	5.88
Roundness-Rounded	15.38	4.35	0.00	8.00	0.00
Roundness-Well Rounded	0.00	0.00	0.00	0.00	0.00

Table A 3: Surface textural analysis of quartz grains from IODP Site U1411 for intra-site comparison

Texture	Grain Size Bin (Φ)				
	3-2.5	**2.5-2**	**2-1.5**	**1.5-1**	**1-0.5**
Breakage Blocks	31.25	43.33	31.37	42.50	52.38
Conchoidal Fractures	81.25	70.00	78.43	77.50	76.19
Arc Step-like Fractures	18.75	13.33	19.61	30.00	23.81
Straight Step-like Fractures	12.50	6.67	19.61	25.00	23.81
Isolated Fractures	18.75	13.33	29.41	25.00	28.57
Mechanical Impact Pits	25.00	33.33	60.78	67.50	76.19
Gouges/Striations	43.75	36.67	58.82	45.00	57.14
Edge Abrasion	93.75	83.33	66.67	70.00	71.43
Upturned Plates	18.75	30.00	35.29	67.50	28.57
Microlayering	0.00	3.33	1.96	5.00	4.76
Chemical v-pits	6.25	23.33	35.29	45.00	28.57
Adhering Particles	6.25	16.67	15.69	22.50	14.29
Silica Precipitation	25.00	53.33	58.82	77.50	61.90
Silica Dissolution Y/N	6.25	46.67	47.06	57.50	61.90
Dissolution- Rare-Absent	43.75	20.00	23.53	5.00	9.52
Dissolution- Present	50.00	33.33	29.41	37.50	28.57
Dissolution- Common	6.25	20.00	37.25	45.00	47.62
Dissolution- Pervasive	0.00	26.67	9.80	12.50	14.29
Relief-Low -	18.75	6.67	9.80	2.50	14.29
Relief-Medium	37.50	60.00	54.90	65.00	28.57
Relief-High	43.75	33.33	35.29	35.00	52.38
Roundness-Very Angular	18.75	16.67	17.65	10.00	23.81
Roundness-Angular	81.25	36.67	25.49	22.50	28.57
Roundness-Sub-Angular	0.00	33.33	23.53	52.50	33.33
Roundness-Sub-Rounded	0.00	13.33	21.57	7.50	4.76
Roundness-Rounded	0.00	0.00	11.76	7.50	4.76
Roundness-Well Rounded	0.00	0.00	0.00	0.00	4.762

Table A 4: Surface textural analysis of quartz grains from different size fractions of sample 913 B24R 2W, 80-83 cm

Appendix A

Texture	Grain Size Bin (Φ)				
	2.5-2	**2-1.5**	**1.5-1**	**1-0.5**	**0.5-0**
Breakage Blocks	60.00	33.33	22.86	59.09	31.25
Conchoidal Fractures	90.00	80.00	85.71	81.82	87.50
Arc Step-like Fractures	50.00	23.33	25.71	54.55	31.25
Straight Step-like Fractures	0.00	26.67	11.43	18.18	18.75
Isolated Fractures	10.00	13.33	8.57	9.09	12.50
Mechanical Impact Pits	40.00	63.33	82.86	90.91	93.75
Gouges/Striations	60.00	63.33	57.14	68.18	62.50
Edge Abrasion	90.00	80.00	57.14	86.36	68.75
Upturned Plates	40.00	60.00	48.57	59.09	50.00
Microlayering	0.00	6.67	11.43	9.09	6.25
Chemical v-pits	30.00	20.00	54.29	31.82	68.75
Adhering Particles	10.00	10.00	22.86	13.64	31.25
Silica Precipitation	40.00	73.33	74.29	72.73	62.50
Silica Dissolution Y/N	60.00	60.00	54.29	45.45	50.00
Dissolution- Rare-Absent	20.00	13.33	14.29	13.64	18.75
Dissolution- Present	20.00	26.67	31.43	40.91	31.25
Dissolution- Common	50.00	40.00	37.14	36.36	43.75
Dissolution- Pervasive	10.00	20.00	17.14	9.09	6.25
Relief-Low -	0.00	3.33	17.14	9.09	18.75
Relief-Medium	60.00	46.67	54.29	36.36	31.25
Relief-High	40.00	50.00	28.57	54.55	50.00
Roundness-Very Angular	30.00	20.00	5.71	18.18	0.00
Roundness-Angular	40.00	40.00	28.57	45.45	31.25
Roundness-Sub-Angular	10.00	30.00	34.29	13.64	31.25
Roundness-Sub-Rounded	20.00	6.67	14.29	13.64	12.50
Roundness-Rounded	0.00	3.33	14.29	9.09	12.50
Roundness-Well Rounded	0.00	0.00	2.86	0.00	12.50

Table A 5: Surface texture analysis of quartz grains from different size fractions of sample U1411 B1H 1W, 37-39cm

Appendix B Provenance data for Exp. 342 and North Atlantic source areas

Hole Core	Sec.	Interval (cm)	Qz	Pf	Af	Bt	Mt	Ch	Sm	It	Kt	oc	Gt	Ga	Al	Ru	To	Py
C6	4	113-114	66	6.7	6.2	0.4	4.0	0.6	2.0	3.7	3.9	3.7	0.5	0.3	0.4	0.2	0.5	1.4
B15	1	89-90	62	9.3	6.3	0.2	2.8	0.4	4.0	4.8	3.3	4.6	0.4	0.4	0.5	0.2	0.4	0.8
B15	4	22-23	63	9.0	6.3	0.4	3.1	0.4	2.2	4.6	2.8	4.6	0.7	0.3	0.4	0.2	0.4	1.4
B16	1	137-138	64	7.9	5.7	0.7	2.4	0.3	2.4	3.9	2.3	4.1	1.9	0.2	0.5	0.2	0.3	3.2
C8	3	77-78	64	7.4	5.4	0.4	2.1	0.3	2.1	3.7	2.2	4.3	1.7	0.3	0.4	0.2	0.3	5.4
B17	2	11-12	65	8.6	5.3	0.3	3.3	0.5	2.2	4.7	3.0	4.7	0.6	0.3	0.5	0.2	0.5	0.2
B17	5	143-144	46	7.9	5.2	1.1	9.5	1.4	7.2	6.5	5.2	5.4	0.9	0.8	0.9	0.2	1.3	0.1
B17	4	46-47	59	7.6	5.5	0.7	3.7	0.6	4.7	5.1	4.5	5.9	1.6	0.3	0.5	0.2	0.5	0.1
B18	5	113-114	60	9.1	6.5	0.2	2.7	0.4	2.3	4.7	4.3	7.0	0.2	0.4	0.5	0.2	0.4	1.5
B11	3	49-50	55	8.6	6.4	0.5	4.3	0.7	3.2	5.1	5.8	8.1	0.5	0.4	0.4	0.2	0.7	0.0

Qz=Quartz, Pf= Plagioclase feldspar, Af= Alkali feldspar, Bt=Biotite, Mt= Muscovite, CH= Chlorite, Sm= Smectite, It=Illite, Kt= Kaolinite/Dictite, oc=Other clays, Gt= Glauconite, Ga= Garnet, Al= Amphibole, Ru= Rutile/Anatase, To= Tourmalines, Py= Pyrite

Table B 1: Mineralogical composition (%) of detrital sand from Site U1411 EOT interval

Appendix B

Interval	Hole	Core	Section	Top (cm)	Bottom (cm)	$^{208}Pb/^{204}Pb$	$^{207}Pb/^{204}Pb$	$^{206}Pb/^{204}Pb$
Site U1411								
Mid O	B	7	1	20	22	37.7820	15.5069	18.0249
Mid O	B	7	2	26	28	37.4879	15.5041	17.7885
Mid O	B	7	4	2	4	37.5131	15.4508	17.7261
Mid O	B	7	8	16	18	37.7944	15.4711	17.7305
Early O	C	6	3	77.5	79	37.8455	15.4949	18.0563
Early O	C	6	4	14.5	16	37.2248	15.3484	17.2627
Early O	C	6	4	122.5	124	37.9323	15.5630	18.1569
Early O	B	15	1	38.5	40	37.2479	15.4052	17.4829
Early O	B	15	1	126.5	128	37.7565	15.5431	18.2501
Early O	B	15	3	50.5	52	37.8255	15.5022	18.0224
Early O	B	15	3	142	144	38.0821	15.5424	18.3254
Early O	B	15	4	106.5	108	37.5712	15.4588	17.7395
Early O	C	7	5	22.5	24	37.7310	15.4810	17.8836
Early O	C	7	6	42.5	44	38.4333	15.5652	18.5255
Early O	B	16	2	99	100.5	37.2800	15.4387	17.4845
Early O	B	16	3	143	144.5	37.8481	15.5215	17.9992
EOT	C	8	3	130.5	132	37.5017	15.5847	17.9805
EOT	C	8	6	53	55	38.0634	15.6043	18.8368
EOT	B	17	3	127	128.5	38.2179	15.5750	18.6969
EOT	B	17	4	24	26	37.9854	15.5253	18.1196
EOT	B	18	1	14.5	16	37.1360	15.4456	17.4641
EOT	B	18	3	26.5	28	37.9814	15.5491	17.9833
EOT	B	18	5	26.5	28	38.2312	15.5785	18.2516
Late E	C	11	3	50.5	52	37.7480	15.5557	18.1491
Late E	C	11	5	50.5	52	37.6748	15.4902	17.7664
Late E	B	19	4	130.5	132	37.2053	15.4280	17.2979
Late E	C	12	3	70.5	72	37.4434	15.4600	17.5863
Late E	B	20	3	54.5	56	38.0216	15.5397	18.02170
Site U1406								
Mid O	A	17	3	60	62	37.3099	15.4262	17.4751
Early O	C	21	3	45	47	37.9289	15.5290	18.0851

Early O	C	22	2	82	84	38.0624	15.5872	19.1763
Early O	C	22	5	36	38	38.1598	15.5887	18.4181
EOT	B	24	1	144	146	37.6412	15.4378	17.6947

Table B 2: Pb isotope data for Sites U1411 and U1406 analysed in this thesis

Region	**Terrane**	**Reference**
Greenland	Archaean	(Baadsgaard et al., 1986a)
		(Kamber et al., 2003)
		(Robertson, 1986)
	Palaeoproterozoic	(Connelly and Thrane, 2005)
	Caledonian	(Hansen and Friderichsen, 1989)
North America	Superior	(Carignan et al., 1993)
		(Gariépy and Allègre, 1985)
		(Doe, 1976)
		(Stevenson et al., 1999)
		(Tilton and Kwon, 1990)
		(Hinchey and Hattori, 2007)
		(Tilton and Steiger, 1969)
		(Henry et al., 1998)
	Grenville	(Aleinikoff et al., 1993)
		(Ashwal and Wooden, 1989)
		(DeWolf and Mezger, 1994)
		(Zartman and Wasserburg, 1969)
		(Gariépy et al., 1990)
	Appalachians	(Ayuso and Bevier, 1991)
		(LeHuray, 1986)
		(Tomascak et al., 1996)
		(Vitrac et al., 1981)
	Churchill	(Sinha, 1970)
	Proterozoic	(Ripley et al., 1998)
Scandinavia	Archaean	(Halla, 2005)
		(Halla and Heilimo, 2009)
		(Vidal et al., 1980)

	Svecofennian	(Andersson et al., 2001)
	Sveconorwegian	(Andersen et al., 1994)
		(Andersen, 1997)
		(Barling et al., 2000)
		(Cosca et al., 1998)
		(Weis, 1986)
		(Andersen et al., 2001)
	Caledonian	(Birkeland et al., 1993a)
		(Birkeland et al., 1993b)
Britain & Ireland	UK & Irish Granites	(Blaxland et al., 1979)
		(Tyrrell et al., 2006)
		(Tyrrell et al., 2007)
	Irish Grampians	(Tyrrell et al., 2007)
	UK North Atlantic Igneous Province	(Dickin and Jones, 1983)

Table B 3: Sources for Pb isotopes from feldspars for North Atlantic Terranes

Fraction	Hole	Core	Sect.	Top (cm)	Bot. (cm)	$^{87}Sr/^{86}Sr$	$^{143}Nd/^{144}Nd$	$\varepsilon Nd_{(0)}$
Coarse	C	6	3	120	121	0.719973±18.1	0.511679	-18.70±0.94
Coarse	C	6	4	9	10	-	0.511831	-15.74±0.14
Coarse	B	15	1	89	90	-	0.511999	-12.47±0.22
Coarse	B	15	2	73	74	0.718527±6.92	0.511974	-12.95±0.16
Coarse	B	15	3	72	73	0.717898±18	0.512018	-12.10±0.12
Coarse	C	7	4	145.5	146.5	0.716205±15.8	0.511828	-15.81±0.26
Coarse	C	8	3	77	78	0.712832±7.02	0.512023	-12.00±0.12
Coarse	C	9	3	101.5	102.5	0.714519±8.19	0.512055	-11.37±0.15
Coarse	B	18	5	113	114	0.719258±6.65	0.511891	-14.57±0.20
Coarse	C	12	3	49	50	0.713032±11.6	0.512119	-10.13±0.11
Fine	C	6	3	120	121	0.725777±8.54	0.511707	-18.15±0.87
Fine	C	6	4	9	10	-	0.511899	-14.42±0.70
Fine	B	15	1	89	90	-	0.511862	-15.13±1.36
Fine	B	15	2	73	74	0.718635±8.91	0.511815	-16.05±0.15
Fine	B	15	3	72	73	-	0.511362	-24.90±1.83
Fine	C	7	4	145.5	146.5	0.722088±14	0.511495	-22.29±1.75
Fine	C	8	3	77	78	0.710282±8.1	0.511865	-15.08±0.12
Fine	C	9	3	101.5	102.5	0.721991±17	0.511186	-28.32±4.73
Fine	B	18	5	113	114	-	0.511708	-18.15±0.17
Fine	C	12	3	49	50	0.719573±9.25	0.511770	-16.93±1.11
Site U1411 Authigenic Pyrite						0.709091±7.02	0.512058	-11.31±0.18

Table B 4: Nd and Sr isotopes from Site U1411 EOT interval, Coarse= >63 μm, Fine= <20 μm, Error given to 2sd ($x10^{-6}$ for Sr)

Region	Terrane	Reference
Greenland	Archaean	(Baadsgaard et al., 1986b)
		(Kalsbeek et al., 1987)
		(Jacobsen and Dymek, 1988)
	Proterozoic	(Brown et al., 2003)
		(Kalsbeek and Taylor, 1985)
		(McCulloch and Wasserburg, 1978)
	Caledonides	(Stendal and Frei, 2008)
	East Greenland Paleogene Volcanics	(Bernstein et al., 1998)
		(Saunders et al., 1999)
		(Hansen and Nielsen, 1999)
		(Morton and Parson, 1988)
		(Andreasen et al., 2004)
North America	Nain-Churchill	(McCulloch and Wasserburg, 1978)
		(Ashwal et al., 1986)
	Grenville	(Marcantonio et al., 1990)
		(Ashwal et al., 1986)
		(Ashwal and Wooden, 1989)
	Appalachian	(Whalen et al., 1996)
	Superior	(Ashwal et al., 1986)
Scandinavia	Sveconorwegian	(Andersen, 1997)
		(Barling et al., 2000)
		(Andersen et al., 2001)
	Caledonides	(Birkeland et al., 1993b)

Table B 5: Sources for Nd and Sr isotope data for North Atlantic terranes

Hole	Core	Type	Section	Half	Interval (cm)	Clay Mineral Proportion (%)			
						Smectite	Illite	Kaolinite	Chlorite
C	6	H	3	W	120-121	65.6	22.8	6.2	5.4
C	6	H	4	W	9-10	71.3	17.1	7.3	4.4
C	6	H	4	W	113-114	62.5	16	14.4	7.1
C	6	H	6	W	40-41	74.4	17.9	4.3	3.4
B	15	H	1	W	89-90	74.4	16.5	5.4	3.6
B	15	H	2	W	73-74	72.4	18.2	5.7	3.7
B	15	H	3	W	72-73	77.6	16.1	3.6	2.7
B	15	H	4	W	22-23	71.9	19.6	5	3.6
C	7	H	4	W	145.5-146.5	77.9	15.2	3.7	3.2
B	16	H	1	W	137-138	72.8	18.3	5	3.9
C	8	H	3	W	77-78	79.7	14.9	2.7	2.7
B	17	H	4	W	46-47	76.4	16.3	4.4	2.9
C	9	H	3	W	101.5-102.5	68.4	19.6	6.9	5.1
B	18	H	5	W	113-114	72.2	18.1	6.1	3.7
C	11	X	3	W	49-50	69.7	16.4	8.8	5.1
B	19	H	3	W	9.5-10.5	58.6	24.1	10.8	6.5
B	19	H	4	W	83-84	60.2	24.1	9.2	6.5
C	12	X	3	W	49-50	65.5	18.3	9.7	6.3
B	20	H	2	W	77-78	63.7	20.3	9.7	6.3

Table B 6: X-Ray Diffraction Clay mineral analysis of samples from the Site U1411 EOT interval.

Appendix C Grain Flux & Size Distribution Records:

C.1 Link to Site U1411 grain flux record (table too large to include):

https://drive.google.com/open?id=0BwxbTgHAvuATa2lBb0hETDlmZ0U

C.2 Link to Site U1406 grain flux record (table too large to include):

https://drive.google.com/open?id=0BwxbTgHAvuATYlBSWDZxT29lRTg

C.3 Link to Site U1411 grain size distribution analysis data (table too large to include):

https://drive.google.com/open?id=0BwxbTgHAvuATcGZPSllVaTc3OEE

Appendix D Well charts for the Grand Banks

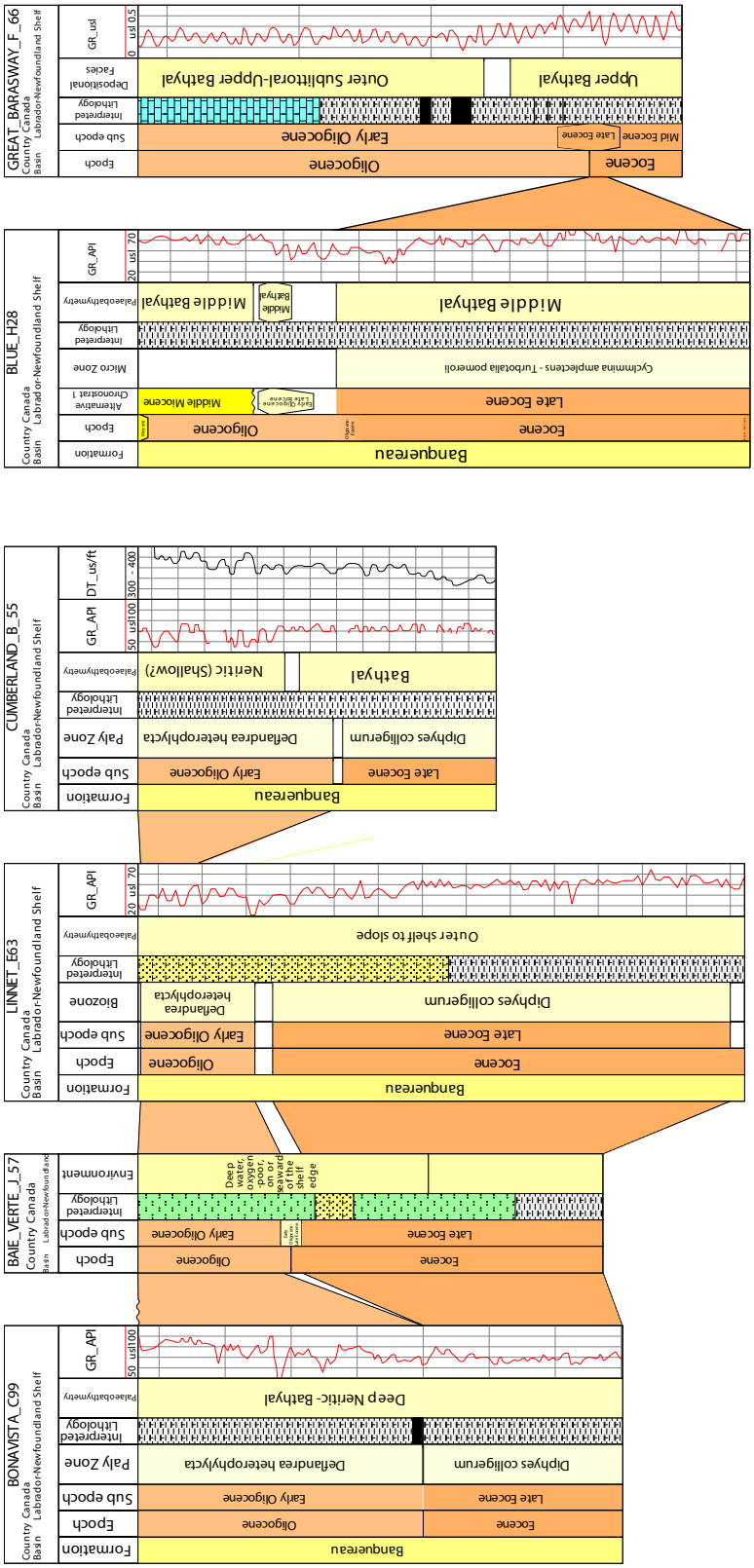

Supplementary Figure D1: Well charts showing lithology and palaeobathymetry interpretations and wireline logging data for the North Grand Banks region (see Fig. 4.1)

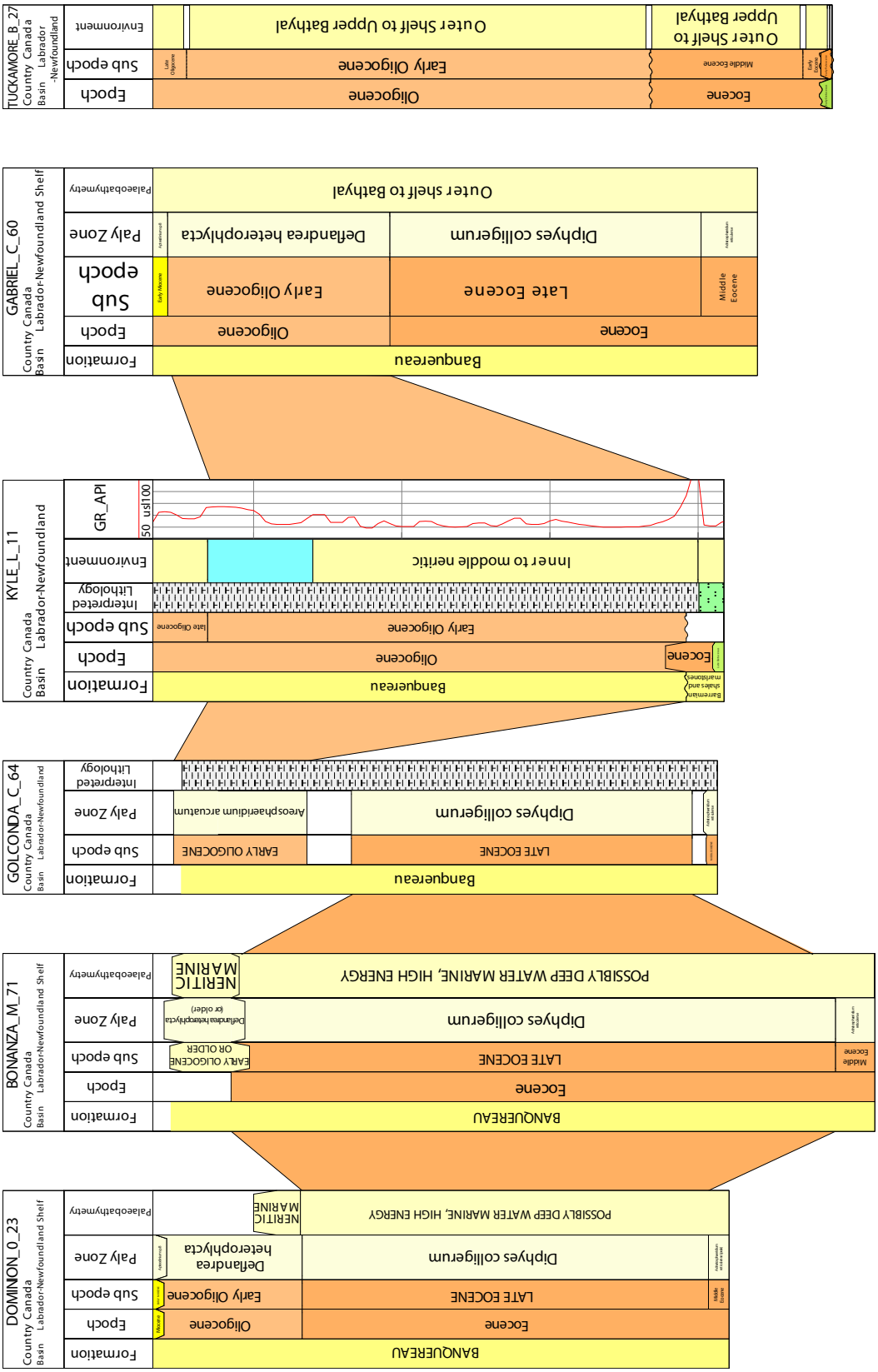

Supplementary Figure D2: Well charts showing lithology and palaeobathymetry interpretations and wireline logging data for the Flemish Cap region (see Fig 4.1)

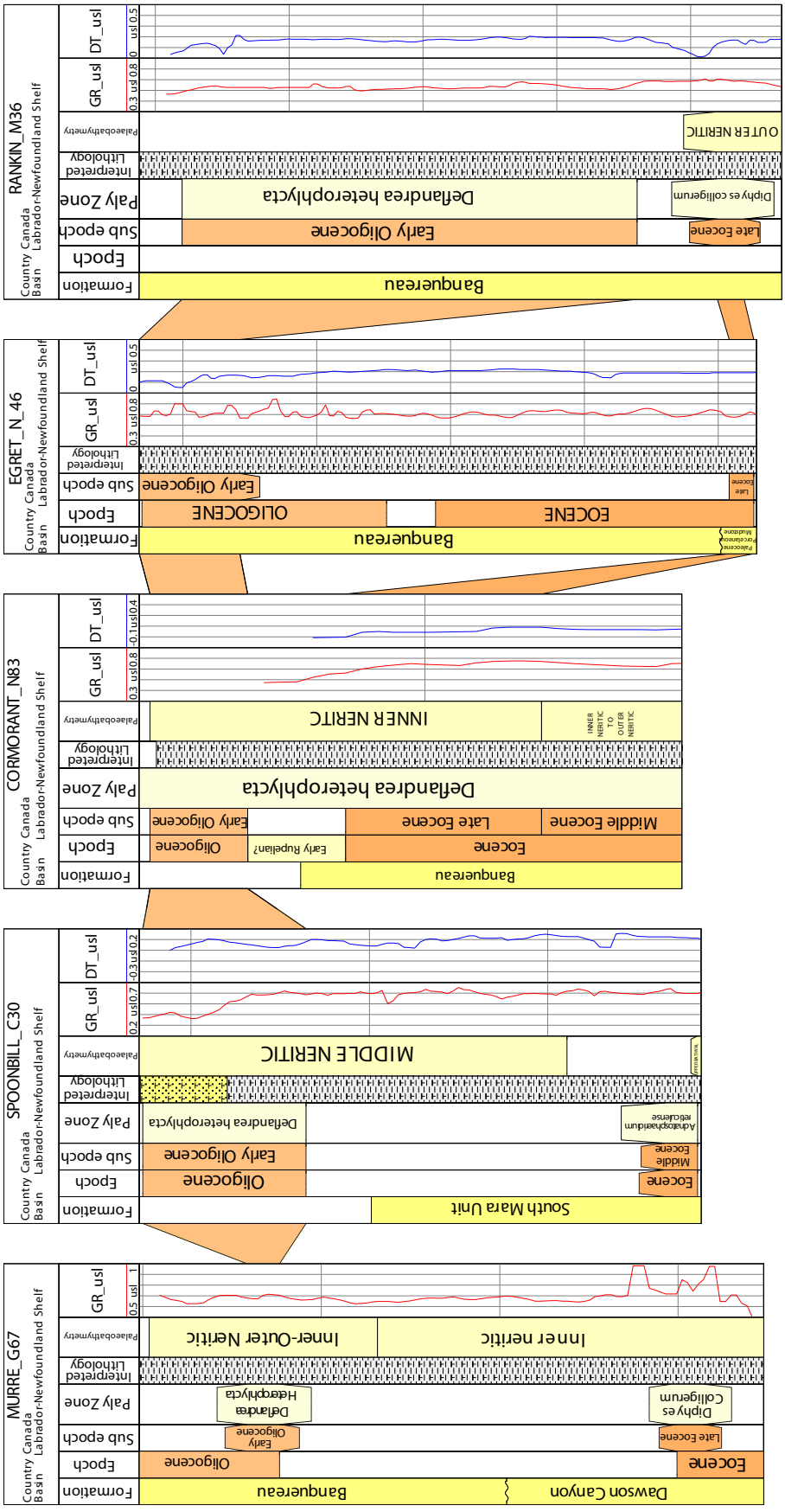
RANKIN_M36
Country Canada
Basin Labrador-Newfoundland Shelf
DT_usl
GR_usl
Palaeobathymetry
Interpreted Lithology
Paly Zone
Sub epoch
Epoch
Formation
OUTER NERITIC
Delflandrea heterophlycta
Dityes colligerum
Late Eocene
Early Oligocene
Banquereau
EGRET_N_46
Country Canada
Basin Labrador-Newfoundland Shelf
DT_usl
GR_usl
Interpreted Lithology
Sub epoch
Epoch
Formation
Early Oligocene
Late Eocene
OLIGOCENE
EOCENE
Banquereau
CORMORANT_N83
Country Canada
Basin Labrador-Newfoundland Shelf
DT_usl
GR_usl
Palaeobathymetry
Interpreted Lithology
Paly Zone
Sub epoch
Epoch
Formation
INNER NERITIC
Delflandrea heterophlycta
Middle Eocene
Late Eocene
Early Oligocene
Oligocene
Early Rupelian?
Eocene
Banquereau
SPOONBILL_C30
Country Canada
Basin Labrador-Newfoundland Shelf
DT_usl
GR_usl
Palaeobathymetry
Interpreted Lithology
Paly Zone
Sub epoch
Epoch
Formation
MIDDLE NERITIC
Delflandrea heterophlycta
Middle Eocene
Early Oligocene
Oligocene
Eocene
South Mara Unit
MURRE_G67
Country Canada
Basin Labrador-Newfoundland Shelf
GR_usl
Palaeobathymetry
Interpreted Lithology
Paly Zone
Sub epoch
Epoch
Formation
Inner-Outer Neritic
Inner neritic
Dityes Colligerum
Late Eocene
Delflandrea Heterophlycta
Early Oligocene
Eocene
Oligocene
Banquereau
Dawson Canyon

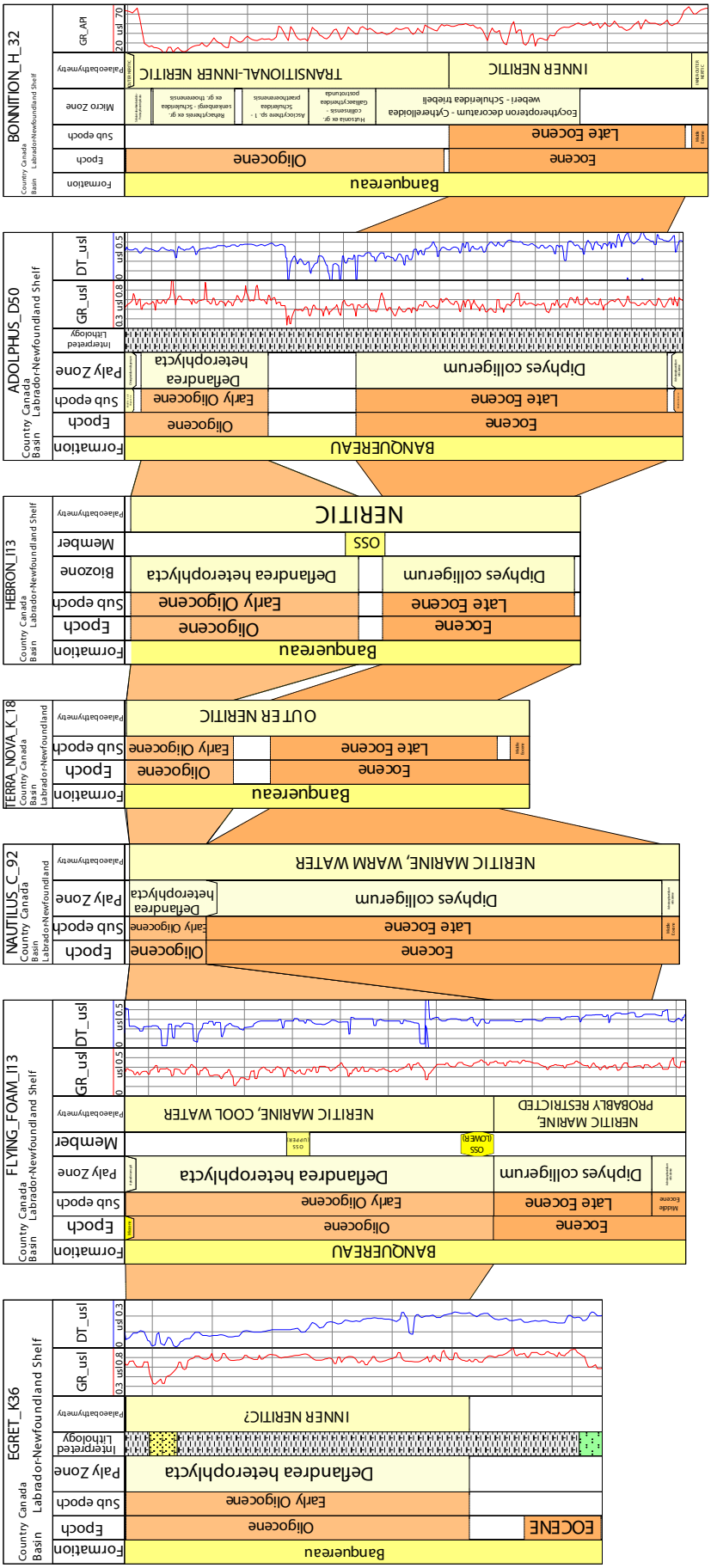

Supplementary Figure D3: Well charts showing lithology and palaeobathymetry interpretations and wireline logging data from the East Grand Banks region (see Fig 4.1).

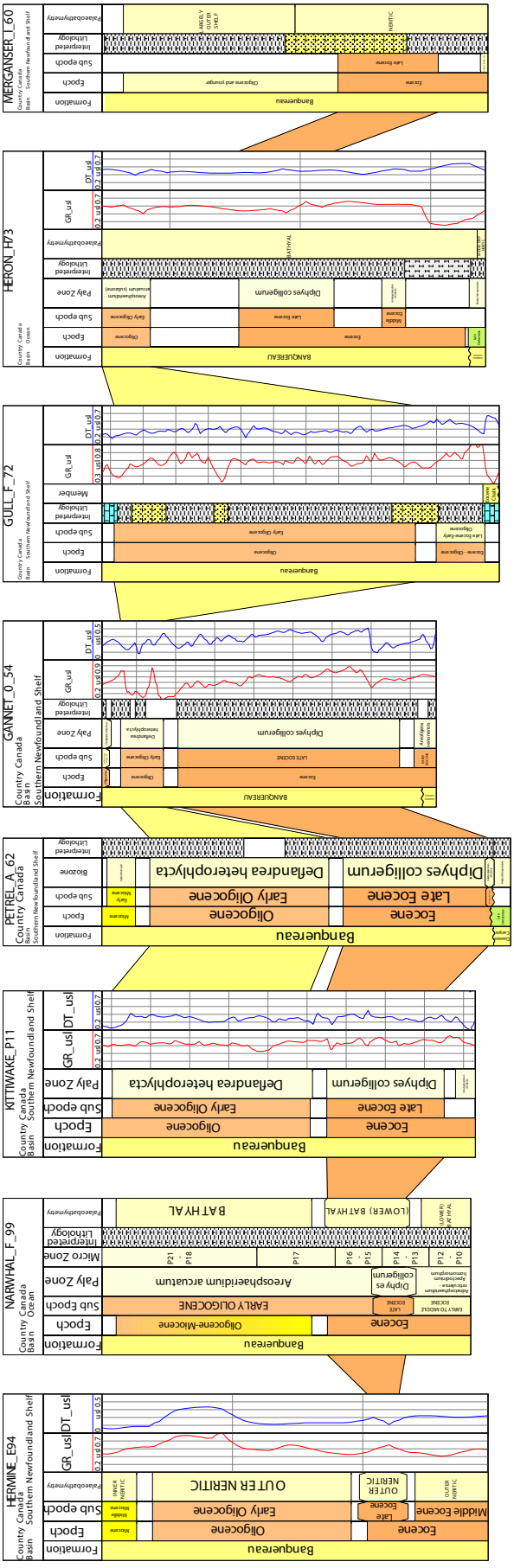

Supplementary Figure D4: Well charts showing lithology and palaeobathymetry interpretations and wireline logging data from the West Grand Banks region (see Fig 4.1)

Appendix E Seismic Interpretations

E.1 Seismic interpretation of SENR and Newfoundland Basin

A copy of the Petrel project created during the seismic interpretation in this thesis is available from the link below, loading the project correctly requires the SEG-Y files for each seismic profile listed below in E.2:

https://drive.google.com/open?id=0BwxbTgHAvuATZWQ5NUpkSmo0eXM

E.2 SEG-Y files for Petrel project

Migration SEG-Y files for Cruise KN179-01 can be downloaded from the following link; multi-channel seismic profiles L020 to L056 were used for this thesis:

http://www-udc.ig.utexas.edu/sdc/cruise.php?cruiseIn=kn179-01

Migration SEG-Y files for Cruise RC2510 can be downloaded from the following link; multi-channel seismic profiles nb01-a to nb32 were used for this thesis:

http://www-udc.ig.utexas.edu/sdc/cruise.php?cruiseIn=rc2510

Migration SEG-Y files for Cruise EW0007 can be downloaded from the following link; multi-channel seismic profiles 101 to 403 were used for this thesis:

http://www-udc.ig.utexas.edu/sdc/cruise.php?cruiseIn=ew0007

Bibliography

Aagaard, K., Swift, J.H., Carmack, E.C., 1985. Thermohaline circulation in the Arctic Mediterranean Seas. J. Geophys. Res. 90, 4833–4846. doi:10.1029/JC090iC03p04833

Abels, H.A., Simaeys, S.V., Hilgen, F.J., Man, E.D., Vandenberghe, N., 2007. Obliquity-dominated glacio-eustatic sea level change in the early Oligocene: evidence from the shallow marine siliciclastic Rupelian stratotype (Boom Formation, Belgium). Terra Nova 19, 65–73. doi:10.1111/j.1365-3121.2006.00716.x

Abelson, M., Agnon, A., Almogi-Labin, A., 2008. Indications for control of the Iceland plume on the Eocene–Oligocene "greenhouse–icehouse" climate transition. Earth Planet. Sci. Lett. 265, 33–48. doi:10.1016/j.epsl.2007.09.021

Abelson, M., Erez, J., 2017. The onset of modern-like Atlantic meridional overturning circulation at the Eocene-Oligocene transition: Evidence, causes, and possible implications for global cooling. Geochem. Geophys. Geosystems 18, 2177–2199. doi:10.1002/2017GC006826

Abreu, V.S., Haddad, G.A., 1998. Glacioeustatic Fluctuations: The Mechanism Linking Stable Isotope Events and Sequence Stratigraphy from the Early Oligocene to Middle Miocene, in: Graciansky, P.-C. de, Hardenbol, J., Jaquin, T., Vail, P.R. (Eds.), Mesozoic and Cenozoic Sequence Stratigraphy of European Basins, SEPM Special Publication. SEPM (Society for Sedimentary Geology), Tulsa, pp. 245–259.

Alaf, M., 1987. Late Quaternary plume, nepheloid and turbidite sedimentation and effect of the Gulf Stream near the tail of the Grand Banks, Newfoundland. Mar. Geol. 74, 277–290. doi:10.1016/0025-3227(87)90054-5

Aleinikoff, J.N., Walter, M., Kunk, M.J., Hearn, P.P., 1993. Do ages of authigenic K-feldspar date the formation of Mississippi Valley-type Pb-Zn deposits, central and southeastern United States?: Pb isotopic evidence. Geology 21, 73–76. doi:10.1130/0091-7613(1993)021<0073:DAOAKF>2.3.CO;2

Allen, J.R.L., 1982. Simple models for the shape and symmetry of tidal sand waves: (1) Statically stable equilibrium forms. Mar. Geol. 48, 31–49. doi:10.1016/0025-3227(82)90128-1

Amos, A.F., Gerard, R.D., 1979. Anomalous bottom water south of the grand banks suggests turbidity current activity. Science 203, 894–897. doi:10.2307/1747885

Anagnostou, E., John, E.H., Edgar, K.M., Foster, G.L., Ridgwell, A., Inglis, G.N., Pancost, R.D., Lunt, D.J., Pearson, P.N., 2016. Changing atmospheric CO2 concentration was the primary driver of early Cenozoic climate. Nature 533, 380–384. doi:10.1038/nature17423

Andersen, T., 1997. Radiogenic isotope systematics of the Herefoss granite, South Norway: an indicator of Sveconorwegian (Grenvillian) crustal evolution in the Baltic Shield. Chem. Geol. 135, 139–158. doi:10.1016/S0009-2541(96)00095-2

Andersen, T., Andresen, A., Sylvester, A.G., 2001. Nature and distribution of deep crustal reservoirs in the southwestern part of the Baltic Shield: evidence from Nd, Sr and Pb isotope data on late Sveconorwegian granites. J. Geol. Soc. 158, 253–267. doi:10.1144/jgs.158.2.253

Andersen, T., Hagelia, P., Whitehouse, M.J., 1994. Precambrian multi-stage crustal evolution in the Bamble sector of south Norway: Pb isotopic evidence from a Sveconorwegian deep-seated granitic intrusion. Chem. Geol. 116, 327–343. doi:10.1016/0009-2541(94)90023-X

Andersson, U.B., Neymark, L.A., Billström, K., 2001. Petrogenesis of Mesoproterozoic (Subjotnian) rapakivi complexes of central Sweden: implications from U–Pb zircon ages, Nd, Sr and Pb isotopes. Earth Environ. Sci. Trans. R. Soc. Edinb. 92, 201–228. doi:10.1017/S0263593300000237

Andreasen, R., Peate, D.W., Brooks, C.K., 2004. Magma plumbing systems in large igneous provinces: Inferences from cyclical variations in Palaeogene East Greenland basalts. Contrib. Mineral. Petrol. 147, 438–452. doi:10.1007/s00410-004-0566-2

Andrews, J., 2000. Icebergs and Iceberg Rafted Detritus (IRD) in the North Atlantic: Facts and Assumptions. Oceanography 13, 100–108. doi:10.5670/oceanog.2000.19

Arnaboldi, M., Meyers, P.A., 2006. Data report: Multiproxy geochemical characterization of OAE-related black shales at Site 1276, Newfoundland Basin, in: Tucholke, B.E., Sibuet, J.-C., Klaus, A. (Eds.), Proc. ODP, Sci. Results. Ocean Drilling Program, College Station, TX, pp. 1–18.

Ashwal, L.D., Wooden, J.L., 1989. River Valley pluton, Ontario: A late-Archean/early-Proterozoic anorthositic intrusion in the Grenville Province. Geochim. Cosmochim. Acta 53, 633–641. doi:10.1016/0016-7037(89)90006-9

Ashwal, L.D., Wooden, J.L., Emslie, R.F., 1986. Sr, Nd and Pb isotopes in Proterozoic intrusives astride the Grenville Front in Labrador: Implications for crustal contamination and basement mapping. Geochim. Cosmochim. Acta 50, 2571–2585. doi:10.1016/0016-7037(86)90211-5

Austin, J.A., Tucholke, B.E., Uchupi, E., 1989. Upper Triassic—Lower Jurassic salt basin southeast of the Grand Banks. Earth Planet. Sci. Lett. 92, 357–370. doi:10.1016/0012-821X(89)90060-5

Ayer, E.A., Laine, E.P., 1982. Seismic stratigraphy of the northern Bermuda Rise. Mar. Geol. 49, 169–186. doi:10.1016/0025-3227(82)90035-4

Ayuso, R.A., Bevier, M.L., 1991. Regional differences in PB isotopic compositions of feldspars in plutonic rocks of the northern Appalachian Mountains, U.S.A., and Canada: A geochemical method of terrane correlation. Tectonics 10, 191–212. doi:10.1029/90TC02132

Baadsgaard, H., Nurman, A.P., Rosing, M., Bridgwater, D., Longstaffe, F.J., 1986a. Alteration and metamorphism of Amitsoq gneisses from the Isukasia area, West Greenland: Recommendations for isotope studies of the early crust. Geochim. Cosmochim. Acta 50, 2165–2172. doi:10.1016/0016-7037(86)90071-2

Baadsgaard, H., Nutman, A.P., Bridgwater, D., 1986b. Geochronology and isotopic variation of the early Archaean Amitsoq gneisses of the Isukasia area, southern

West Greenland. Geochim. Cosmochim. Acta 50, 2173–2183. doi:10.1016/0016-7037(86)90072-4

Bailey, I., Foster, G.L., Wilson, P.A., Jovane, L., Storey, C.D., Trueman, C.N., Becker, J., 2012. Flux and provenance of ice-rafted debris in the earliest Pleistocene sub-polar North Atlantic Ocean comparable to the last glacial maximum. Earth Planet. Sci. Lett. 341–344, 222–233. doi:10.1016/j.epsl.2012.05.034

Bailey, I., Hole, G.M., Foster, G.L., Wilson, P.A., Storey, C.D., Trueman, C.N., Raymo, M.E., 2013. An alternative suggestion for the Pliocene onset of major northern hemisphere glaciation based on the geochemical provenance of North Atlantic Ocean ice-rafted debris. Quat. Sci. Rev. 75, 181–194. doi:10.1016/j.quascirev.2013.06.004

Barker, P.F., Carlson, R.L., Johnson, D.A., 1983. Initial Reports of the Deep Sea Drilling Project, 72, Initial Reports of the Deep Sea Drilling Project. U.S. Government Printing Office. doi:10.2973/dsdp.proc.72.1983

Barling, J., Weis, D., Demaiffe, D., 2000. A Sr-, Nd-and Pb-isotopic investigation of the transition between two megacyclic units of the Bjerkreim–Sokndal layered intrusion, south Norway. Chem. Geol. 165, 47–65. doi:10.1016/S0009-2541(99)00163-1

Barnes, P.W., Reimnitz, E., Fox, D., 1982. Ice Rafting of Fine-Grained Sediment, a Sorting and Transport Mechanism, Beaufort Sea, Alaska. J. Sediment. Res. 52, 493-502.

Bartek, L.R., Vail, P.R., Anderson, J.B., Emmet, P.A., Wu, S., 1991. Effect of Cenozoic ice sheet fluctuations in Antarctica on the stratigraphic signature of the Neogene. J. Geophys. Res. Solid Earth 96, 6753–6778. doi:10.1029/90JB02528

Bell, D.B., Jung, S.J.A., Kroon, D., 2015. The Plio-Pleistocene development of Atlantic deep-water circulation and its influence on climate trends. Quat. Sci. Rev. 123, 265–282. doi:10.1016/j.quascirev.2015.06.026

Bennett, M.R., Doyle, P., Mather, A.E., 1996. Dropstones: their origin and significance. Palaeogeogr. Palaeoclimatol. Palaeoecol. 121, 331–339. doi:10.1016/0031-0182(95)00071-2

Berggren, W.A., Kent, D.V., Swisher III, C.C., Aubry, M.-P., 1995. A revised Cenozoic geochronology and chronostratigraphy. Geochronol. Time Scales Glob. Stratigr. Correl. 129–212. doi:10.2110/pec.95.04.0129

Bernard, T., Steer, P., Gallagher, K., Szulc, A., Whitham, A., Johnson, C., 2016. Evidence for Eocene–Oligocene glaciation in the landscape of the East Greenland margin. Geology 44, 895–898. doi:10.1130/G38248.1

Bernstein, S., Kelemen, P.B., Tegner, C., Kurz, M.D., Blusztajn, J., Brooks, C.K., 1998. Post-breakup basaltic magmatism along the East Greenland Tertiary rifted margin. Earth Planet. Sci. Lett. 160, 845–862. doi:10.1016/S0012-821X(98)00132-0

Birkeland, A., Ihlen, P.M., Bjorlykke, A., 1993a. The sources of metals in sulfide deposits in the Helgeland nappe complex, north-central Norway; Pb isotope evidence. Econ. Geol. 88, 1810–1829. doi:10.2113/gsecongeo.88.7.1810

Birkeland, A., Nordgulen, Ø., Cumming, G.L., Bjørlykke, A., 1993b. Pb Nd Sr isotopic constraints on the origin of the Caledonian Bindal Batholith, central Norway. Lithos 29, 257–271.

Blaxland, A.B., Aftalion, M., van Breemen, O., 1979. Pb isotopic composition of feldspars from Scottish Caledonian granites, and the nature of the underlying crust. Scott. J. Geol. 15, 139–151.

Bohaty, S.M., Zachos, J.C., Delaney, M.L., 2012. Foraminiferal Mg/Ca evidence for Southern Ocean cooling across the Eocene–Oligocene transition. Earth Planet. Sci. Lett. 317–318, 251–261. doi:10.1016/j.epsl.2011.11.037

Bond, G., Heinrich, H., Broecker, W., Labeyrie, L., McManus, J., Andrews, J., Huon, S., Jantschik, R., Clasen, S., Simet, C., Tedesco, K., Klas, M., Bonani, G., Ivy, S., 1992. Evidence for massive discharges of icebergs into the North Atlantic ocean during the last glacial period. Nature 360, 245–249. doi:10.1038/360245a0

Borrelli, C., Cramer, B.S., Katz, M.E., 2014. Bipolar Atlantic deepwater circulation in the middle-late Eocene: Effects of Southern Ocean gateway openings. Paleoceanography 29, 2012PA002444. doi:10.1002/2012PA002444

Boulila, S., Galbrun, B., Miller, K.G., Pekar, S.F., Browning, J.V., Laskar, J., Wright, J.D., 2011. On the origin of Cenozoic and Mesozoic "third-order" eustatic sequences. Earth-Sci. Rev. 109, 94–112. doi:10.1016/j.earscirev.2011.09.003

Bouma, A.H., 1962. Sedimentology of some Flysch deposits; a graphic approach to facies interpretation. Elsevier Pub. Co., Amsterdam; New York.

Boyle, P.R., Romans, B.W., Tucholke, B.E., Norris, R.D., Swift, S.A., Sexton, P.F., 2017. Cenozoic North Atlantic deep circulation history recorded in contourite drifts, offshore Newfoundland, Canada. Mar. Geol. 385, 185–203. doi:10.1016/j.margeo.2016.12.014

Brown, P.E., Dempster, T.J., Hutton, D.H.W., Becker, S.M., 2003. Extensional tectonics and mafic plutons in the Ketilidian rapakivi granite suite of South Greenland. Lithos 67, 1–13. doi:10.1016/S0024-4937(02)00212-8

Campbell, D.C., Mosher, D.C., 2016. Geophysical evidence for widespread Cenozoic bottom current activity from the continental margin of Nova Scotia, Canada. Mar. Geol., The contourite log-book: significance for palaeoceanography, ecosystems and slope instability 378, 237–260. doi:10.1016/j.margeo.2015.10.005

Carignan, J., Gariépy, C., Machado, N., Rive, M., 1993. Pb isotopic geochemistry of granitoids and gneisses from the late Archean Pontiac and Abitibi Subprovinces of Canada. Chem. Geol. 106, 299–315. doi:10.1016/0009-2541(93)90033-F

Clarke, R.A., Hill, H.W., Reiniger, R.F., Warren, B.A., 1980. Current System South and East of the Grand Banks of Newfoundland. J. Phys. Oceanogr. 10, 25–65. doi:10.1175/1520-0485(1980)010<0025:CSSAEO>2.0.CO;2

Cochonat, P., Ollier, G., Michel, J.L., 1989. Evidence for slope instability and current-induced sediment transport, the RMS Titanic wreck search area, Newfoundland rise. Geo-Mar. Lett. 9, 145–152. doi:10.1007/BF02431041

Connelly, J.N., Thrane, K., 2005. Rapid determination of Pb isotopes to define Precambrian allochthonous domains: An example from West Greenland. Geology 33, 953–956. doi:10.1130/G21720.1

Cosca, M.A., Mezger, K., Essene, E.J., 1998. The Baltica-Laurentia connection: Sveconorwegian (Grenvillian) metamorphism, cooling, and unroofing in the Bamble sector, Norway. J. Geol. 106, 539–552. doi:10.1086/516040

Coxall, H.K., Pearson, P.N., 2007. The Eocene-Oligocene transition, in: Williams, M., Haywood, A.M., Gregory, F.J., Schmidt, D.N. (Eds.), Deep-Time Perspectives on Climate Change: Marrying the Signal from Computer Models and Biological Proxies. Geological Society, London, pp. 351–387.

Coxall, H.K., Wilson, P.A., Pälike, H., Lear, C.H., Backman, J., 2005. Rapid stepwise onset of Antarctic glaciation and deeper calcite compensation in the Pacific Ocean. Nature 433, 53–57. doi:10.1038/nature03135

Cristini, L., Grosfeld, K., Butzin, M., Lohmann, G., 2012. Influence of the opening of the Drake Passage on the Cenozoic Antarctic Ice Sheet: A modeling approach. Palaeogeogr. Palaeoclimatol. Palaeoecol. 339–341, 66–73. doi:10.1016/j.palaeo.2012.04.023

Curry, J.A., Schramm, J.L., Ebert, E.E., 1995. Sea Ice-Albedo Climate Feedback Mechanism. J. Clim. 8, 240–247. doi:10.1175/1520-0442(1995)008<0240:SIACFM>2.0.CO;2

Dalrymple, R.W., LeGresley, E.M., Fader, G.B.J., Petrie, B.D., 1992. The western Grand Banks of Newfoundland: Transgressive Holocene sedimentation under the combined influence of waves and currents. Mar. Geol. 105, 95–118. doi:10.1016/0025-3227(92)90184-J

Darby, D.A., 2014. Ephemeral formation of perennial sea ice in the Arctic Ocean during the middle Eocene. Nat. Geosci. 7, 210–213. doi:10.1038/ngeo2068

Darby, D.A., 2003. Sources of sediment found in sea ice from the western Arctic Ocean, new insights into processes of entrainment and drift patterns. J. Geophys. Res. Oceans 108, 3257. doi:10.1029/2002JC001350

Dasch, E.J., 1969. Strontium isotopes in weathering profiles, deep-sea sediments, and sedimentary rocks. Geochim. Cosmochim. Acta 33, 1521–1552. doi:10.1016/0016-7037(69)90153-7

Davies, R., Cartwright, J., Pike, J., Line, C., 2001. Early Oligocene initiation of North Atlantic Deep Water formation. Nature 410, 917–920. doi:10.1038/35073551

DeConto, R.M., Pollard, D., 2003. Rapid Cenozoic glaciation of Antarctica induced by declining atmospheric CO_2. Nature 421, 245–249. doi:10.1038/nature01290

DeConto, R.M., Pollard, D., Wilson, P.A., Pälike, H., Lear, C.H., Pagani, M., 2008. Thresholds for Cenozoic bipolar glaciation. Nature 455, 652–656. doi:10.1038/nature07337

Deemer, S., Hall, J., Solvason, K., Lau, K.H., Louden, K., Srivastava, S., Sibuet, J.-C., 2009. Structure and development of the southeast Newfoundland continental passive margin: derived from SCREECH Transect 3. Geophys. J. Int. 178, 1004–1020. doi:10.1111/j.1365-246X.2009.04162.x

Deser, C., Holland, M., Reverdin, G., Timlin, M., 2002. Decadal variations in Labrador Sea ice cover and North Atlantic sea surface temperatures. J. Geophys. Res. Oceans 107, 3–1. doi:10.1029/2000JC000683

Dethleff, D., Kuhlmann, G., 2010. Fram Strait sea-ice sediment provinces based on silt and clay compositions identify Siberian Kara and Laptev seas as main source regions. Polar Res. 29, 265–282. doi:10.1111/j.1751-8369.2010.00149.x

DeWolf, C.P., Mezger, K., 1994. Lead isotope analyses of leached feldspars: Constraints on the early crustal history of the Grenville Orogen. Geochim. Cosmochim. Acta 58, 5537–5550. doi:10.1016/0016-7037(94)90248-8

Dickin, A.P., Jones, N.W., 1983. Isotopic evidence for the age and origin of pitchstones and felsites, Isle of Eigg, NW Scotland. J. Geol. Soc. 140, 691–700. doi:10.1144/gsjgs.140.4.0691

Dickson, R.R., Brown, J., 1994. The production of North Atlantic Deep Water: Sources, rates, and pathways. J. Geophys. Res. Oceans 99, 12319–12341. doi:10.1029/94JC00530

Diester-Haass, L., Zahn, R., 2001. Paleoproductivity increase at the Eocene–Oligocene climatic transition: ODP/DSDP Sites 763 and 592. Palaeogeogr. Palaeoclimatol. Palaeoecol. 172, 153–170.

Doe, B.R., 1976. Lead isotope data bank; 2,624 samples and analyses cited (USGS Numbered Series No. 76–201), Open-File Report. U.S. Geological Survey.

Duarte, C.S., Viana, A.R., 2007. Santos Drift System: stratigraphic organization and implications for late Cenozoic palaeocirculation in the Santos Basin, SW Atlantic Ocean. Geol. Soc. Lond. Spec. Publ. 276, 171–198. doi:10.1144/GSL.SP.2007.276.01.09

Dunhill, G., 1998. Comparison of sea-ice rafted debris; grain size, surface features, and grain shape (USGS Numbered Series No. 98–367), Open-File Report. U.S. Geological Survey.

Edgar, K.M., Wilson, P.A., Sexton, P.F., Suganuma, Y., 2007. No extreme bipolar glaciation during the main Eocene calcite compensation shift. Nature 448, 908–911. doi:10.1038/nature06053

Ehrmann, W., 1998. Implications of late Eocene to early Miocene clay mineral assemblages in McMurdo Sound (Ross Sea, Antarctica) on paleoclimate and ice dynamics. Palaeogeogr. Palaeoclimatol. Palaeoecol. 139, 213–231. doi:10.1016/S0031-0182(97)00138-7

Eicken, H., Gradinger, R., Gaylord, A., Mahoney, A., Rigor, I., Melling, H., 2005. Sediment transport by sea ice in the Chukchi and Beaufort Seas: Increasing importance due to changing ice conditions? Deep Sea Res. Part II Top. Stud. Oceanogr., The Western Arctic Shelf-Basin Interactions (SBI) Project The Western Arctic Shelf-Basin Interactions (SBI) Project 52, 3281–3302. doi:10.1016/j.dsr2.2005.10.006

Eldrett, J.S., Greenwood, D.R., Harding, I.C., Huber, M., 2009. Increased seasonality through the Eocene to Oligocene transition in northern high latitudes. Nature 459, 969–973. doi:10.1038/nature08069

Eldrett, J.S., Harding, I.C., Firth, J.V., Roberts, A.P., 2004. Magnetostratigraphic calibration of Eocene–Oligocene dinoflagellate cyst biostratigraphy from the Norwegian–Greenland Sea. Mar. Geol. 204, 91–127. doi:10.1016/S0025-3227(03)00357-8

Eldrett, J.S., Harding, I.C., Wilson, P.A., Butler, E., Roberts, A.P., 2007. Continental ice in Greenland during the Eocene and Oligocene. Nature 446, 176–179. doi:10.1038/nature05591

Expedition 318 Scientists, 2010. Wilkes Land Glacial History: Cenozoic East Antarctic Ice Sheet evolution from Wilkes Land margin sediments. IODP Prelim. Rep. 318, 99. doi: 10.2204/iodp.pr.318.2010

Farmer, G.L., Barber, D., Andrews, J., 2003. Provenance of Late Quaternary ice-proximal sediments in the North Atlantic: Nd, Sr and Pb isotopic evidence. Earth Planet. Sci. Lett. 209, 227–243. doi:10.1016/S0012-821X(03)00068-2

Faugères, J.-C., Stow, D.A.V., 2008. Chapter 14 Contourite Drifts: Nature, Evolution and Controls, in: Rebesco, M., Camerlenghi, A. (Eds.), Developments in Sedimentology. Elsevier, pp. 257–288. doi:10.1016/S0070-4571(08)10014-0

Faugères, J.-C., Stow, D.A.V., Imbert, P., Viana, A., 1999. Seismic features diagnostic of contourite drifts. Mar. Geol. 162, 1–38. doi:10.1016/S0025-3227(99)00068-7

Frey, R.W., 2012. The Study of Trace Fossils: A Synthesis of Principles, Problems, and Procedures in Ichnology. Springer Science & Business Media, New York.

Fulthorpe, C.S., Miller, K.G., Camoin, G.F., Kominz, M.A., 2008. Drilling to decipher long-term sea-level changes and effects—a joint consortium for Ocean Leadership, ICDP, IODP, DOSECC, and Chevron workshop. Sci Drill 6, 19–28. doi:https://doi.org/10.2204/iodp.sd.6.02.2008

Gale, A.S., Huggett, J.M., Pälike, H., Laurie, E., Hailwood, E.A., Hardenbol, J., 2006. Correlation of Eocene–Oligocene marine and continental records: orbital cyclicity, magnetostratigraphy and sequence stratigraphy of the Solent Group, Isle of Wight, UK. J. Geol. Soc. 163, 401–415. doi:10.1144/0016-764903-175

Gardner, W.D., Tucholke, B.E., Richardson, M.J., Biscaye, P.E., 2017. Benthic storms, nepheloid layers, and linkage with upper ocean dynamics in the western North Atlantic. Mar. Geol. 385, 304–327. doi:10.1016/j.margeo.2016.12.012

Gariépy, C., Allègre, C.J., 1985. The lead isotope geochemistry and geochronology of late-kinematic intrusives from the Abitibi greenstone belt, and the

implications for late Archaean crustal evolution. Geochim. Cosmochim. Acta 49, 2371–2383. doi:10.1016/0016-7037(85)90237-6

Gariépy, C., Verner, D., Doig, R., 1990. Dating Archean metamorphic minerals southeast of the Grenville front, western Quebec, using Pb isotopes. Geology 18, 1078–1081. doi:10.1130/0091-7613(1990)018<1078:DAMMSO>2.3.CO;2

Gasson, E., Lunt, D.J., DeConto, R., Goldner, A., Heinemann, M., Huber, M., LeGrande, A.N., Pollard, D., Sagoo, N., Siddall, M., Winguth, A., 2013. Uncertainties in the modelled CO2 threshold for Antarctic glaciation. Clim. Past Discuss. 9, 5701–5745. doi:10.5194/cpd-9-5701-2013

Gibbs, R.J., Matthews, M.D., Link, D.A., 1971. The relationship between sphere size and settling velocity. J. Sediment. Res. 41, 7–18. doi:10.1306/74D721D0-2B21-11D7-8648000102C1865D

Goldner, A., Herold, N., Huber, M., 2014. Antarctic glaciation caused ocean circulation changes at the Eocene-Oligocene transition. Nature 511, 574–577. doi:10.1038/nature13597

Goldstein, S.L., Onions, R.K., Hamilton, P.J., 1984. A Sm-Nd isotopic study of atmospheric dusts and particulates from major river systems. Earth Planet. Sci. Lett. 70, 221–236. doi:10.1016/0012-821X(84)90007-4

Gonthier, E.G., Faugères, J.C., Stow, D.A.V., 1984. Contourite facies of the Faro Drift, Gulf of Cadiz. , in: Stow, D.A., Piper, D.J.W. (Eds.), Fine-grained Sediments: Deep-water Processes and Facies, Geol. Soc. Lond. Spec. Publ. 15, 275-292. doi:10.1144/GSL.SP.1984.015.01.18

Gradstein, F.M., Ogg, J.G., Schmitz, M., Ogg, G., 2012. The Geologic Time Scale 2012. Elsevier, Boston.

Grinsted, A., Moore, J.C., Jevrejeva, S., 2004. Application of the cross wavelet transform and wavelet coherence to geophysical time series. Nonlinear Process. Geophys. 11, 561–566. doi:10.5194/npg-11-561-2004

Gwiazda, R.H., Hemming, S.R., Broecker, W.S., 1996. Tracking the sources of icebergs with lead isotopes: The provenance of ice-rafted debris in Heinrich layer 2. Paleoceanography 11, 77–93. doi:10.1029/95PA03135

Halla, J., 2005. Late Archean high-Mg granitoids (sanukitoids) in the southern Karelian domain, eastern Finland: Pb and Nd isotopic constraints on crust-mantle interactions. Lithos, Geodynamic Controls on Adakite, TTG and Sanukitoid Genesis: Implications for Models of Crust Formation 79, 161–178. doi:10.1016/j.lithos.2004.05.007

Halla, J., Heilimo, E., 2009. Deformation-induced Pb isotope exchange between K-feldspar and whole rock in Neoarchean granitoids: Implications for assessing Proterozoic imprints. Chem. Geol. 265, 303–312. doi:10.1016/j.chemgeo.2009.04.007

Hansen, B.T., Friderichsen, J.D., 1989. The influence of recent lead loss on the interpretation of disturbed U-Pb systems in zircons from igneous rocks in East Greenland. Lithos 23, 209–223. doi:10.1016/0024-4937(89)90006-6

Hansen, H., Nielsen, T.F.D., 1999. Crustal contamination in Palaeogene East Greenland flood basalts: plumbing system evolution during continental rifting. Chem. Geol. 157, 89–118. doi:10.1016/S0009-2541(98)00196-X

Haq, B.U., Hardenbol, J., Vail, P.R., others, 1987. Chronology of fluctuating sea levels since the Triassic. Science 235, 1156–1167. doi:10.1126/science.235.4793.1156

Hardenbol, J., Thierry, J., Farley, M.B., Jacquin, T., Graciansky, P.-C. de, Vail, P.R., 1999. Mesozoic and Cenozoic Sequence Chronostratigraphic Framework of European Basins. SEPM Society for Sedimentary Geology, pp. 3–13.

Harris, C.K., Wiberg, P., 2002. Across-shelf sediment transport: Interactions between suspended sediment and bed sediment. J. Geophys. Res. Oceans 107, 8–1. doi:10.1029/2000JC000634

Hass, H.C., 2002. A method to reduce the influence of ice-rafted debris on a grain size record from northern Fram Strait, Arctic Ocean. Polar Res. 21, 299–306. doi:10.1111/j.1751-8369.2002.tb00084.x

Hebbeln, D., 2000. Flux of ice-rafted detritus from sea ice in the Fram Strait. Deep Sea Res. Part II Top. Stud. Oceanogr. 47, 1773–1790. doi:10.1016/S0967-0645(00)00006-0

Hegewald, A., Jokat, W., 2013. Relative sea level variations in the Chukchi region-Arctic Ocean-since the late Eocene. Geophys. Res. Lett. 40, 803–807. doi:10.1002/grl.50182

Helland, P.E., Holmes, M.A., 1997. Surface textural analysis of quartz sand grains from ODP Site 918 off the southeast coast of Greenland suggests glaciation of southern Greenland at 11 Ma. Palaeogeogr. Palaeoclimatol. Palaeoecol. 135, 109–121. doi:10.1016/S0031-0182(97)00025-4

Hemming, S.R., Broecker, W.S., Sharp, W.D., Bond, G.C., Gwiazda, R.H., McManus, J.F., Klas, M., Hajdas, I., 1998. Provenance of Heinrich layers in core V28-82, northeastern Atlantic: 40Ar/39Ar ages of ice-rafted hornblende, Pb isotopes in feldspar grains, and Nd–Sr–Pb isotopes in the fine sediment fraction. Earth Planet. Sci. Lett. 164, 317–333. doi:10.1016/S0012-821X(98)00224-6

Henry, P., Stevenson, R.K., Gariépy, C., 1998. Late Archean Mantle Composition and Crustal Growth in the Western Superior Province of Canada: Neodymium and Lead Isotopic Evidence from the Wawa, Quetico, and Wabigoon Subprovinces. Geochim. Cosmochim. Acta 62, 143–157. doi:10.1016/S0016-7037(97)00324-4

Hernández-Molina, F.J., Llave, E., Stow, D.A.V., 2008. Chapter 19 Continental Slope Contourites. Dev. Sedimentol., Contourites 60, 379–408. doi:10.1016/S0070-4571(08)10019-X

Hernandez-Molina, F.J., Stow, D.A.V., Alvarez-Zarikian, C.A., Acton, G., Bahr, A., Balestra, B., Ducassou, E., Flood, R., Flores, J.-A., Furota, S., Grunert, P., Hodell, D., Jimenez-Espejo, F., Kim, J.K., Krissek, L., Kuroda, J., Li, B., Llave, E., Lofi, J., Lourens, L., Miller, M., Nanayama, F., Nishida, N., Richter, C., Roque, C., Pereira, H., Goni, M.F.S., Sierro, F.J., Singh, A.D., Sloss, C., Takashimizu, Y., Tzanova, A., Voelker, A., Williams, T., Xuan, C., 2014. Onset of Mediterranean outflow into the North Atlantic. Science 344, 1244–1250. doi:10.1126/science.1251306

Hinchey, J.G., Hattori, K.H., 2007. Lead isotope study of the late Archean Lac des Iles palladium deposit, Canada: enrichment of platinum group elements by ponded sulfide melt. Miner. Deposita 42, 601–611. doi:10.1007/s00126-007-0129-3

Hiscott, R.N., 1984. Clay mineralogy and clay-mineral provenance of Cretaceous and Paleogene strata, Labrador and Baffin shelves. Bull. Can. Pet. Geol. 32, 272–280.

Hjulstrom, F., 1939. Transportation of Detritus by Moving Water: Part 1. Transportation, in: Recent Marine Sediments, AAPG Special Volumes. pp. 5–31.

Hohbein, M.W., Sexton, P.F., Cartwright, J.A., 2013. Onset of North Atlantic Deep Water production coincident with inception of the Cenozoic global cooling trend: REPLY. Geology 41, e292–e292. doi:10.1130/G34655Y.1

Hohbein, M.W., Sexton, P.F., Cartwright, J.A., 2012. Onset of North Atlantic Deep Water production coincident with inception of the Cenozoic global cooling trend. Geology 40, 255–258. doi:10.1130/G32461.1

Houben, A.J.P., van Mourik, C.A., Montanari, A., Coccioni, R., Brinkhuis, H., 2012. The Eocene–Oligocene transition: Changes in sea level, temperature or both? Palaeogeogr. Palaeoclimatol. Palaeoecol., Cenozoic Evolution of Antarctic Climates, Oceans and Ice Sheets 335–336, 75–83. doi:10.1016/j.palaeo.2011.04.008

Howe, J.A., Stoker, M.S., Woolfe, K.J., 2001. Deep-marine seabed erosion and gravel lags in the northwestern Rockall Trough, North Atlantic Ocean. J. Geol. Soc. 158, 427–438. doi:10.1144/jgs.158.3.427

Huybers, P., Wunsch, C., 2005. Obliquity pacing of the late Pleistocene glacial terminations. Nature 434, 491–494. doi:10.1038/nature03401

Immonen, N., 2013. Surface microtextures of ice-rafted quartz grains revealing glacial ice in the Cenozoic Arctic. Palaeogeogr. Palaeoclimatol. Palaeoecol. 374, 293–302. doi:10.1016/j.palaeo.2013.02.003

Immonen, N., Strand, K., Turunen, S., 2009. Mineralogical evidence of Middle Miocene glacial ice in the central Arctic Ocean sediments. Geophysica 45, 93–101.

Inglis, G.N., Farnsworth, A., Lunt, D., Foster, G.L., Hollis, C.J., Pagani, M., Jardine, P.E., Pearson, P.N., Markwick, P., Galsworthy, A.M.J., Raynham, L., Taylor, K.W.R., Pancost, R.D., 2015. Descent towards the Icehouse: Eocene sea surface cooling

inferred from GDGT distributions. Paleoceanography 2014PA002723. doi:10.1002/2014PA002723

Jacobsen, S.B., Dymek, R.F., 1988. Nd and Sr isotope systematics of clastic metasediments from Isua, West Greenland: Identification of pre-3.8 Ga Differentiated Crustal Components. J. Geophys. Res. Solid Earth 93, 338–354. doi:10.1029/JB093iB01p00338

Jevrejeva, S., Moore, J.C., Grinsted, A., 2003. Influence of the Arctic Oscillation and El Niño-Southern Oscillation (ENSO) on ice conditions in the Baltic Sea: The wavelet approach. J. Geophys. Res. Atmospheres 108, 4577–4687. doi:10.1029/2003JD003417

Jovane, L., Coccioni, R., Marsili, A., Acton, G., 2009. The late Eocene greenhouse-icehouse transition: Observations from the Massignano global stratotype section and point (GSSP). Geol. Soc. Am. Spec. Pap. 452, 149–168. doi:10.1130/2009.2452(10)

Kalsbeek, F., Pidgeon, R.T., Taylor, P.N., 1987. Nagssugtoqidian mobile belt of West Greenland: a cryptic 1850 Ma suture between two Archaean continents—chemical and isotopic evidence. Earth Planet. Sci. Lett. 85, 365–385. doi:10.1016/0012-821X(87)90134-8

Kalsbeek, F., Taylor, P.N., 1985. Isotopic and chemical variation in granites across a Proterozoic continental margin—the Ketilidian mobile belt of South Greenland. Earth Planet. Sci. Lett. 73, 65–80. doi:10.1016/0012-821X(85)90035-4

Kamber, B.S., Collerson, K.D., Moorbath, S., Whitehouse, M.J., 2003. Inheritance of early Archaean Pb-isotope variability from long-lived Hadean protocrust. Contrib. Mineral. Petrol. 145, 25–46. doi:10.1007/s00410-002-0429-7

Katz, M.E., Browning, J.V., Miller, K.G., Monteverde, D.H., Mountain, G.S., Williams, R.H., 2013. Paleobathymetry and sequence stratigraphic interpretations from benthic foraminifera: Insights on New Jersey shelf architecture, IODP Expedition 313. Geosphere 9, 1488–1513. doi:10.1130/GES00872.1

Katz, M.E., Cramer, B.S., Toggweiler, J.R., Esmay, G., Liu, C., Miller, K.G., Rosenthal, Y., Wade, B.S., Wright, J.D., 2011. Impact of Antarctic Circumpolar Current Development on Late Paleogene Ocean Structure. Science 332, 1076–1079. doi:10.1126/science.1202122

Katz, M.E., Miller, K.G., Wright, J.D., Wade, B.S., Browning, J.V., Cramer, B.S., Rosenthal, Y., 2008. Stepwise transition from the Eocene greenhouse to the Oligocene icehouse. Nat. Geosci. 1, 329–334. doi:10.1038/ngeo179

Keen, C.E., de Voogd, B., 1988. The continent-ocean boundary at the rifted margin off eastern Canada: New results from deep seismic reflection studies. Tectonics 7, 107–124. doi:10.1029/TC007i001p00107

Kempema, E.W., Reimnitz, E., Barnes, P.W., 1989. Sea Ice Sediment Entrainment and Rafting in the Arctic. J. Sediment. Res. 59, 308–317. doi:10.1306/212F8F80-2B24-11D7-8648000102C1865D

Kennard, L., Schafer, C., Carter, L., 1990. Late Cenozoic evolution of Sackville Spur: a sediment drift on the Newfoundland continental slope. Can. J. Earth Sci. 27, 863–878. doi:10.1139/e90-089

Kominz, M.A., Browning, J.V., Miller, K.G., Sugarman, P.J., Mizintseva, S., Scotese, C.R., 2008. Late Cretaceous to Miocene sea-level estimates from the New Jersey and Delaware coastal plain coreholes: an error analysis. Basin Res. 20, 211–226. doi:10.1111/j.1365-2117.2008.00354.x

Konert, M., Vandenberghe, J., 1997. Comparison of laser grain size analysis with pipette and sieve analysis: a solution for the underestimation of the clay fraction. Sedimentology 44, 523–535. doi:10.1046/j.1365-3091.1997.d01-38.x

Krinsley, D.H., Donahue, J., 1968. Environmental Interpretation of Sand Grain Surface Textures by Electron Microscopy. Geol. Soc. Am. Bull. 79, 743–748. doi:10.1130/0016-7606(1968)79[743:EIOSGS]2.0.CO;2

Krinsley, D.H., Doornkamp, J.C., 2011. Atlas of Quartz Sand Surface Textures. Cambridge University Press, Cambridge, pp 1-66.

Lang, D.C., Bailey, I., Wilson, P.A., Beer, C.J., Bolton, C.T., Friedrich, O., Newsam, C., Spencer, M.R., Gutjahr, M., Foster, G.L., Cooper, M.J., Milton, J.A., 2014. The

transition on North America from the warm humid Pliocene to the glaciated Quaternary traced by eolian dust deposition at a benchmark North Atlantic Ocean drill site. Quat. Sci. Rev. 93, 125–141. doi:10.1016/j.quascirev.2014.04.005

Larsen, H.C., Saunders, A.D., Clift, P.D., Beget, J., Wei, W., Spezzaferri, S., 1994. Seven Million Years of Glaciation in Greenland. Science 264, 952–955. doi:10.2307/2883753

Laskar, J., Robutel, P., Joutel, F., Gastineau, M., Correia, A.C.M., Levrard, B., 2004. A long-term numerical solution for the insolation quantities of the Earth. Astron. Astrophys. 428, 261–285. doi: 10.1051/0004-6361:20041335

Le Roux, J.P., 2005. Grains in motion: A review. Sediment. Geol. 178, 285–313. doi:10.1016/j.sedgeo.2005.05.009

Lear, C.H., Bailey, T.R., Pearson, P.N., Coxall, H.K., Rosenthal, Y., 2008. Cooling and ice growth across the Eocene-Oligocene transition. Geology 36, 251–254. doi:10.1130/G24584A.1

Lear, C.H., Elderfield, H., Wilson, P.A., 2000. Cenozoic deep-sea temperatures and global ice volumes from Mg/Ca in benthic foraminiferal calcite. Science 287, 269–272. doi:10.1126/science.287.5451.269

Lear, C.H., Rosenthal, Y., Coxall, H.K., Wilson, P.A., 2004. Late Eocene to early Miocene ice sheet dynamics and the global carbon cycle. Paleoceanography 19, PA4015. doi:10.1029/2004PA001039

LeHuray, A.P., 1986. Isotopic evidence for a tectonic boundary between the Kings Mountain and Inner Piedmont belts, southern Appalachians. Geology 14, 784–787. doi:10.1130/0091-7613(1986)14<784:IEFATB>2.0.CO;2

Lisitzin, P.A.P., 2002. Iceberg and Sea-Ice Sedimentation in the North Atlantic — Recent and Past, in: Sea-Ice and Iceberg Sedimentation in the Ocean. Springer Berlin Heidelberg, pp. 337–385.

Liu, Z., Pagani, M., Zinniker, D., DeConto, R., Huber, M., Brinkhuis, H., Shah, S.R., Leckie, R.M., Pearson, A., 2009. Global Cooling During the Eocene-Oligocene Climate Transition. Science 323, 1187–1190. doi:10.1126/science.1166368

Locker, S.D., Laine, E.P., 1992. Paleogene-Neogene depositional history of the middle U.S. Atlantic continental rise: mixed turbidite and contourite depositional systems. Mar. Geol. 103, 137–164. doi:10.1016/0025-3227(92)90013-8

Mackiewicz, N.E., Powell, R.D., Carlson, P.R., Molnia, B.F., 1984. Interlaminated ice-proximal glacimarine sediments in Muir Inlet, Alaska. Mar. Geol., Sedimentation on High-latitude Continental Shelves 57, 113–147. doi:10.1016/0025-3227(84)90197-X

Mahaney, W.C., 1995. Glacial crushing, weathering and diagenetic histories of quartz grains inferred from scanning electron microscopy. Glacial Environ. 1, 487–506.

Mahaney, W.C., Kalm, V., 2000. Comparative scanning electron microscopy study of oriented till blocks, glacial grains and Devonian sands in Estonia and Latvia. Boreas 29, 35–51. doi:10.1111/j.1502-3885.2000.tb01199.x

Mahaney, W.C., Stewart, A., Kalm, V., 2001. Quantification of SEM microtextures useful in sedimentary environmental discrimination. Boreas 30, 165–171. doi:10.1111/j.1502-3885.2001.tb01220.x

Marcantonio, F., McNutt, R.H., Dickin, A.P., Heaman, L.M., 1990. Isotopic evidence for the crustal evolution of the Frontenac Arch in the Grenville Province of Ontario, Canada. Chem. Geol., Development of Continental Crust Through Geological Time 83, 297–314. doi:10.1016/0009-2541(90)90286-G

Masson, D.G., Howe, J.A., Stoker, M.S., 2002. Bottom-current sediment waves, sediment drifts and contourites in the northern Rockall Trough. Mar. Geol. 192, 215–237. doi:10.1016/S0025-3227(02)00556-X

McCave, I.N., 1984. Erosion, transport and deposition of fine-grained marine sediments, in: Stow, D.A., Piper, D.J.W. (Eds.), Fine-grained Sediments: Deep-water Processes and Facies, Geol. Soc. Lond. Spec. Publ. 15, 35–69. doi:10.1144/GSL.SP.1984.015.01.03

McCave, I.N., Hall, I.R., 2006. Size sorting in marine muds: Processes, pitfalls, and prospects for paleoflow-speed proxies. Geochem. Geophys. Geosystems 7, Q10N05. doi:10.1029/2006GC001284

McCave, I.N., Hall, I.R., Bianchi, G.G., 2006. Laser vs. settling velocity differences in silt grainsize measurements: estimation of palaeocurrent vigour. Sedimentology 53, 919–928. doi:10.1111/j.1365-3091.2006.00783.x

McCave, I.N., Manighetti, B., Robinson, S.G., 1995. Sortable silt and fine sediment size/composition slicing: Parameters for palaeocurrent speed and palaeoceanography. Paleoceanography 10, 593–610. doi:10.1029/94PA03039

McCave, I.N., Swift, S.A., 1976. A physical model for the rate of deposition of fine-grained sediments in the deep sea. GSA Bull. 87, 541–546. doi:10.1130/0016-7606(1976)87<541:APMFTR>2.0.CO;2

McCave, I.N., Tucholke, B.E., 1986. Deep current-controlled sedimentation in the western North Atlantic, in: Vogt, P.., Tucholke, B.E. (Eds.), The Western North Atlantic Region, The Geology of North America. Geological Society of America, Boulder, Colo, pp. 451–468.

McCulloch, M.T., Wasserburg, G.J., 1978. Sm-Nd and Rb-Sr Chronology of Continental Crust Formation. Science 200, 1003–1011. doi:10.1126/science.200.4345.1003

Merico, A., Tyrrell, T., Wilson, P.A., 2008. Eocene/Oligocene ocean de-acidification linked to Antarctic glaciation by sea-level fall. Nature 452, 979–982. doi:10.1038/nature06853

Meyer, I., Davies, G.R., Stuut, J.-B.W., 2011. Grain size control on Sr-Nd isotope provenance studies and impact on paleoclimate reconstructions: An example from deep-sea sediments offshore NW Africa. Geochem. Geophys. Geosystems 12, Q03005. doi:10.1029/2010GC003355

Meyers, S.R., 2014. Astrochron: An R Package for Astrochronology.

Meyers, S.R., 2012. Seeing red in cyclic stratigraphy: Spectral noise estimation for astrochronology. Paleoceanography 27, PA3228. doi:10.1029/2012PA002307

Miller, K.G., Browning, J.V., Aubry, M.-P., Wade, B.S., Katz, M.E., Kulpecz, A.A., Wright, J.D., 2008. Eocene–Oligocene global climate and sea-level changes: St. Stephens Quarry, Alabama. Geol. Soc. Am. Bull. 120, 34–53. doi:10.1130/B26105.1

Miller, K.G., Browning, J.V., Pekar, S.F., Sugarman, P.J., 1997. Cenozoic evolution of the New Jersey coastal plain: Changes in sea level, tectonics, and sediment supply. Proc. Ocean Drill. Program Sci. Results 156, 361–373.

Miller, K.G., Fairbanks, R.G., 1983. Evidence for Oligocene–Middle Miocene abyssal circulation changes in the western North Atlantic. Nature 306, 250–253. doi:10.1038/306250a0

Miller, K.G., Kominz, M.A., Browning, J.V., Wright, J.D., Mountain, G.S., Katz, M.E., Sugarman, P.J., Cramer, B.S., Christie-Blick, N., Pekar, S.F., 2005. The Phanerozoic Record of Global Sea-Level Change. Science 310, 1293–1298. doi:10.1126/science.1116412

Miller, K.G., Mountain, G.S., 1996. Drilling and Dating New Jersey Oligocene-Miocene Sequences: Ice Volume, Global Sea Level, and Exxon Records. Science 271, 1092–1095. doi:10.1126/science.271.5252.1092

Miller, K.G., Thompson, P.R., Kent, D.V., 1993. Integrated Late Eocene-Oligocene Stratigraphy of the Alabama Coastal Plain: Correlation of Hiatuses and Stratal Surfaces to Glacioeustatic Lowerings. Paleoceanography 8, 313–331. doi:10.1029/93PA00203

Miller, K.G., Tucholke, B.E., 1983. Development of Cenozoic abyssal circulation south of the Greenland-Scotland Ridge, in: Structure and Development of the Greenland-Scotland Ridge, Nato Conference Series. Springer, pp. 549–589. doi:10.1007/978-1-4613-3485-9_27

Miller, K.G., Wright, J.D., Fairbanks, R.G., 1991. Unlocking the Ice House: Oligocene-Miocene oxygen isotopes, eustasy, and margin erosion. J. Geophys. Res. 96, 6829. doi:10.1029/90JB02015

Miller, K.G., Wright, J.D., Katz, M.E., Wade, B.S., Browning, J.V., Cramer, B.S., Rosenthal, Y., 2009. Climate threshold at the Eocene-Oligocene transition: Antarctic ice

sheet influence on ocean circulation. Geol. Soc. Am. Spec. Pap. 452, 169–178. doi:10.1130/2009.2452(11)

Miller, McCave, I.N., Komar, P.D., 1977. Threshold of sediment motion under unidirectional currents. Sedimentology 24, 507–527. doi:10.1111/j.1365-3091.1977.tb00136.x

Milne, G.A., Mitrovica, J.X., 2008. Searching for eustasy in deglacial sea-level histories. Quat. Sci. Rev. 27, 2292–2302. doi:10.1016/j.quascirev.2008.08.018

Moffa-Sánchez, P., Hall, I.R., Barker, S., Thornalley, D.J.R., Yashayaev, I., 2014. Surface changes in the eastern Labrador Sea around the onset of the Little Ice Age. Paleoceanography 29, 2013PA002523. doi:10.1002/2013PA002523

Molinaroli, E., De Falco, G., Rabitti, S., Portaro, R.A., 2000. Stream-scanning laser system, electric sensing counter and settling grain size analysis: a comparison using reference materials and marine sediments. Sediment. Geol. 130, 269–281. doi:10.1016/S0037-0738(99)00119-0

Molnia, B.F., 1983. Distal glacial-marine sedimentation: abundance, composition, and distribution of North Atlantic Ocean Pleistocene ice-rafted sediment, in: Glacial-Marine Sedimentation. Springer, Boston, MA, pp. 593–626. doi:10.1007/978-1-4613-3793-5_15

Moran, K., Backman, J., Brinkhuis, H., Clemens, S.C., Cronin, T., Dickens, G.R., Eynaud, F., Gattacceca, J., Jakobsson, M., Jordan, R.W., Kaminski, M., King, J., Koc, N., Krylov, A., Martinez, N., Matthiessen, J., McInroy, D., Moore, T.C., Onodera, J., O'Regan, M., Pälike, H., Rea, B., Rio, D., Sakamoto, T., Smith, D.C., Stein, R., St John, K., Suto, I., Suzuki, N., Takahashi, K., Watanabe, M., Yamamoto, M., Farrell, J., Frank, M., Kubik, P., Jokat, W., Kristoffersen, Y., 2006. The Cenozoic palaeoenvironment of the Arctic Ocean. Nature 441, 601–605. doi:10.1038/nature04800

Morton, A.C., Parson, L.M., 1988. Early Tertiary volcanism and the opening of the NE Atlantic. Blackwell Scientific Publications, Oxford.

Morton-Thompson, D.W., Arnold M., 1992. Development Geology Reference Manual. American Association of Petroleum Geologists. doi:10.1306/Mth10573

Moucha, R., Forte, A.M., Mitrovica, J.X., Rowley, D.B., Quéré, S., Simmons, N.A., Grand, S.P., 2008. Dynamic topography and long-term sea-level variations: There is no such thing as a stable continental platform. Earth Planet. Sci. Lett. 271, 101–108. doi:10.1016/j.epsl.2008.03.056

Mountain, G.S., Tucholke, B.E., 1985. Mesozoic and Cenozoic Geology of the U.S. Atlantic Continental Slope and Rise, in: Geologic Evolution Of The United States Atlantic Margin. Van Nostrand Reinhold Co., New York, pp. 293–341.

Mulder, T., Hassan, R., Ducassou, E., Zaragosi, S., Gonthier, E., Hanquiez, V., Marchès, E., Toucanne, S., 2013. Contourites in the Gulf of Cadiz: a cautionary note on potentially ambiguous indicators of bottom current velocity. Geo-Mar. Lett. 33, 357–367. doi:10.1007/s00367-013-0332-4

Müller-Michaelis, A., Uenzelmann-Neben, G., Stein, R., 2013. A revised Early Miocene age for the instigation of the Eirik Drift, offshore southern Greenland: Evidence from high-resolution seismic reflection data. Mar. Geol. 340, 1–15. doi:10.1016/j.margeo.2013.04.012

Myhre, A.M., Thiede, J., Firth, J.V., et al. (Eds.), 1995. Proceedings of the Ocean Drilling Program, 151 Initial Reports, Proceedings of the Ocean Drilling Program. Ocean Drilling Program.

Mysak, L.A., Manak, D.K., Marsden, R.F., 1990. Sea-ice anomalies observed in the Greenland and Labrador seas during 1901–1984 and their relation to an interdecadal Arctic climate cycle. Clim. Dyn. 5, 111–133. doi:10.1007/BF00207426

Newsome, D., Ladd, P., 1999. The use of quartz grain microtextures in the study of the origin of sand terrains in Western Australia. CATENA 35, 1–17. doi:10.1016/S0341-8162(98)00122-2

Norris, R.D., Wilson, P.A., Blum, P., the Expedition 342 Scientists, 2014. Proceedings IODP Leg 342.

Norris, R.D., Wilson, P.A., Expedition 342 Scientists, Whiteside, J., 2012. Integrated Ocean Drilling Program Expedition 342 Preliminary Report. Paleogene

Newfoundland Sediment Drifts, 1 June–30 July 2012. International Ocean Drilling Program Management International, Inc.

Nürnberg, D., Wollenburg, I., Dethleff, D., Eicken, H., Kassens, H., Letzig, T., Reimnitz, E., Thiede, J., 1994. Sediments in Arctic sea ice: Implications for entrainment, transport and release. Mar. Geol., 4th International Conference on Paleoceanography (ICP IV) 119, 185–214. doi:10.1016/0025-3227(94)90181-3

Olsson, R.K., Miller, K.G., Ungrady, T.E., 1980. Late Oligocene transgression of middle Atlantic coastal plain. Geology 8, 549–554. doi:10.1130/0091-7613(1980)8<549:LOTOMA>2.0.CO;2

Pagani, M., Zachos, J.C., Freeman, K.H., Tipple, B., Bohaty, S., 2005. Marked Decline in Atmospheric Carbon Dioxide Concentrations During the Paleogene. Science 309, 600–603. doi:10.1126/science.1110063

Parkinson, C.L., 2000. Recent trend reversals in arctic sea ice extents: Possible connections to the North Atlantic Oscillation. Polar Geogr. 24, 1–12. doi:10.1080/10889370009377684

Pekar, S.F., Christie-Blick, N., Kominz, M.A., Miller, K.G., 2002. Calibration between eustatic estimates from backstripping and oxygen isotopic records for the Oligocene. Geology 30, 903–906. doi:10.1130/0091-7613(2002)030<0903:CBEEFB>2.0.CO;2

Pekar, S.F., Kominz, M.A., 2001. Two-Dimensional Paleoslope Modeling: A New Method for Estimating Water Depths of Benthic Foraminiferal Biofacies and Paleoshelf Margins. J. Sediment. Res. 71, 608–620. doi:10.1306/100600710608

Pekar, S.F., Miller, K.G., Browning, J.V., 1997. New Jersey coastal plain Oligocene sequences. Proc. Ocean Drill. Program Sci. Results 156, 187–206.

Peltier, W.R., Fairbanks, R.G., 2006. Global glacial ice volume and Last Glacial Maximum duration from an extended Barbados sea level record. Quat. Sci. Rev., Critical Quaternary Stratigraphy 25, 3322–3337. doi:10.1016/j.quascirev.2006.04.010

Péron-Pinvidic, G., Manatschal, G., Minshull, T.A., Sawyer, D.S., 2007. Tectonosedimentary evolution of the deep Iberia-Newfoundland margins: Evidence for a complex breakup history. Tectonics 26, TC2011. doi:10.1029/2006TC001970

Peron-Pinvidic, G., Shillington, D.J., Tucholke, B.E., 2010. Characterization of sills associated with the U reflection on the Newfoundland margin: evidence for widespread early post-rift magmatism on a magma-poor rifted margin. Geophys. J. Int. 182, 113–136. doi:10.1111/j.1365-246X.2010.04635.x

Pickart, R.S., 1992. Water mass components of the North Atlantic deep western boundary current. Deep Sea Res. Part Oceanogr. Res. Pap. 39, 1553–1572. doi:10.1016/0198-0149(92)90047-W

Piepgras, D.J., Wasserburg, G.J., 1987. Rare earth element transport in the western North Atlantic inferred from Nd isotopic observations. Geochim. Cosmochim. Acta 51, 1257–1271. doi:10.1016/0016-7037(87)90217-1

Piepgras, D.J., Wasserburg, G.J., 1980. Neodymium isotopic variations in seawater. Earth Planet. Sci. Lett. 50, 128–138. doi:10.1016/0012-821X(80)90124-7

Pinous, O.V., Akhmetiev, M.A., Sahagian, D.L., 1999. Sequence stratigraphy and sea-level history of Oligocene strata of the northern Aral Sea region (Kazakhstan): Implications for glacioeustatic reconstructions. Geol. Soc. Am. Bull. 111, 1–10. doi:10.1130/0016-7606(1999)111<0001:SSASLH>2.3.CO;2

Piper, D.J., 2005. Late Cenozoic evolution of the continental margin of eastern Canada. Nor. J. Geol. Geol. Foren. 85, 305–318.

Piper, D.J.W., Mudie, P.J., Aksu, A.E., Skene, K.I., 1994. A 1 Ma record of sediment flux south of the grand banks used to infer the development of glaciation in southeastern Canada. Quat. Sci. Rev. 13, 23–37. doi:10.1016/0277-3791(94)90123-6

Powers, M.C., 1953. A New Roundness Scale for Sedimentary Particles. J. Sediment. Res. 23, 117–119. doi:10.1306/D4269567-2B26-11D7-8648000102C1865D

Price, G.D., 1999. The evidence and implications of polar ice during the Mesozoic. Earth-Sci. Rev. 48, 183–210. doi:10.1016/S0012-8252(99)00048-3

Prins, M., Jonkers, L., Brummer, G., Dijkstra, N., 2008. Glacial North Atlantic Millennial Scale Ice-rafting Events and Their Influence on Overflow Speed. Did Sea-ice Play a Role as a Source of IRD and Freshwater? AGU Fall Meet. Abstr. 1, 1439.

Prins, M.A., Bouwer, L.M., Beets, C.J., Troelstra, S.R., Weltje, G.J., Kruk, R.W., Kuijpers, A., Vroon, P.Z., 2002. Ocean circulation and iceberg discharge in the glacial North Atlantic: Inferences from unmixing of sediment size distributions. Geology 30, 555–558. doi:10.1130/0091-7613(2002)030<0555:OCAIDI>2.0.CO;2

Prinsenberg, S.J., Peterson, I.K., Narayanan, S., Umoh, J.U., 1997. Interaction between atmosphere, ice cover, and ocean off Labrador and Newfoundland from 1962 to 1992. Can. J. Fish. Aquat. Sci. 54, 30–39. doi:10.1139/f96-150

Pusz, A.E., Thunell, R.C., Miller, K.G., 2011. Deep water temperature, carbonate ion, and ice volume changes across the Eocene-Oligocene climate transition. Paleoceanography 26, PA2205. doi:10.1029/2010PA001950

Quigley, L., 2005. A Seismological Investigation Into the Continental Margin and Lithosphere Extension in the Southeast Newfoundland Basin. Memorial University of Newfoundland.

Rabinowitz, P.D., Eittreim, S.L., 1974. Bottom current measurements in the labrador sea. J. Geophys. Res. 79, 4085–4090. doi:10.1029/JC079i027p04085

Rahim, K., 2014. Applications of Multitaper Spectral Analysis to Nonstationary Data (Thesis). Queen's University at Kingston, Canada.

Raymo, M.E., 1994. The Initiation of Northern Hemisphere Glaciation. Annu. Rev. Earth Planet. Sci. 22, 353–383. doi:10.1146/annurev.ea.22.050194.002033

Rebesco, M., Javier Hernández-Molina, F., Van Rooij, D., Wåhlin, A., 2014. Contourites and associated sediments controlled by deep-water circulation processes: State-of-the-art and future Considerations. Mar. Geol., 50th Anniversary Special Issue 352, 111–154. doi:10.1016/j.margeo.2014.03.011

Reimnitz, E., McCormick, M., Bischof, J., Darby, D.A., 1998. Comparing sea-ice sediment load with Beaufort Sea shelf deposits: is entrainment selective? J. Sediment. Res. 68, 777–787. doi:10.2110/jsr.68.777

Reimnitz, E., McCormick, M., McDougall, K., Brouwers, E., 1993. Sediment export by ice rafting from a coastal polynya, Arctic Alaska, U.S.A. Arct. Alp. Res. 25, 83. doi:10.2307/1551544

Richardson, M.J., Wimbush, M., Mayer, L., 1981. Exceptionally strong near-bottom flows on the continental rise of Nova Scotia. Science 213, 887–888. doi:10.1126/science.213.4510.887

Rider, M.H., 2002. The Geological Interpretation of Well Logs. Rider-French Consulting. Scotland

Rider, M.H., 1990. Gamma-ray log shape used as a facies indicator: critical analysis of an oversimplified methodology, in Hurst, A., Lovell, M.A., Morton, A.C., Geological Applications of Wireline Logs, Geol. Soc. Lond. Spec. Publ. 48, 27–37. doi:10.1144/GSL.SP.1990.048.01.04

Ripley, E.M., Lambert, D.D., Frick, L.R., 1998. Re-Os, Sm-Nd, and Pb isotopic constraints on mantle and crustal contributions to magmatic sulfide mineralization in the Duluth Complex. Geochim. Cosmochim. Acta 62, 3349–3365. doi:10.1016/S0016-7037(98)00235-X

Roberts, D.G., 1975. Marine geology of the Rockall Plateau and Trough. Phil. Trans. R. Soc. Lond. A 278, 447–509. doi:10.1098/rsta.1975.0033

Robertson, S., 1986. Evolution of the late Archaean lower continental crust in southern West Greenland. Geol. Soc. Lond. Spec. Publ. 24, 251–260. doi:10.1144/GSL.SP.1986.024.01.22

Rodríguez-Tovar, F.J., Dorador, J., 2014. Ichnological analysis of Pleistocene sediments from the IODP Site U1385 “Shackleton Site” on the Iberian margin: Approaching paleoenvironmental conditions. Palaeogeogr. Palaeoclimatol. Palaeoecol. 409, 24–32. doi:10.1016/j.palaeo.2014.04.027

Rowley, D.B., 2013. Sea Level: Earth’s Dominant Elevation—Implications for Duration and Magnitudes of Sea Level Variations. J. Geol. 121, 445–454. doi:10.1086/671392

Ruddiman, W.F., 1977. Late Quaternary deposition of ice-rafted sand in the subpolar North Atlantic (lat 40° to 65°N). Geol. Soc. Am. Bull. 88, 1813–1827. doi:10.1130/0016-7606(1977)88<1813:LQDOIS>2.0.CO;2

Saucier, F.J., Roy, F., Gilbert, D., Pellerin, P., Ritchie, H., 2003. Modeling the formation and circulation processes of water masses and sea ice in the Gulf of St. Lawrence, Canada. J. Geophys. Res. Oceans 108, 3269. doi:10.1029/2000JC000686

Saunders, A.D., Kempton, P.D., Fitton, J.G., Larsen, L.M., 1999. Sr, Nd, and Pb isotopes and trace element geochemistry of basalts from the Southeast Greenland margin, in: Proceedings of the Ocean Drilling Program. Scientific Results. Ocean Drilling Program, pp. 77–93.

Scher, H.D., Bohaty, S.M., Smith, B.W., Munn, G.H., 2014. Isotopic interrogation of a suspected late Eocene glaciation. Paleoceanography 29, 628–644. doi:10.1002/2014PA002648

Scher, H.D., Bohaty, S.M., Zachos, J.C., Delaney, M.L., 2011. Two-stepping into the icehouse: East Antarctic weathering during progressive ice-sheet expansion at the Eocene–Oligocene transition. Geology 39, 383–386. doi:10.1130/G31726.1

Scher, H.D., Martin, E.E., 2008. Oligocene deep water export from the North Atlantic and the development of the Antarctic Circumpolar Current examined with neodymium isotopes. Paleoceanography 23, PA1205. doi:10.1029/2006PA001400

Schumacher, J.D., Aagard, K., Pease, C.H., Tripp, B.R., 1983. Effects of a shelf polynya on flow and water properties in the northern Bering Sea. J. Geophys. Res. Oceans 88, 2723–2732. doi:10.1029/JC088iC05p02723

Scott, D.B., Mudie, P.., De Vernal, A., Baki, V., Mackinnon, K.D., Medioli, F., Mayer, L.A., 1989. Lithostratigraphy, biostratigraphy, and stable-isotope stratigraphy of cores from ODP Leg 105 site surveys, Labrador Sea and Baffin Bay. Proc. Ocean Drill. Program Sci. Resu 105, 561–582.

Shcherbina, A.Y., Talley, L.D., Rudnick, D.L., 2003. Direct Observations of North Pacific Ventilation: Brine Rejection in the Okhotsk Sea. Science 302, 1952–1955. doi:10.1126/science.1088692

Shennan, I., Peltier, W.R., Drummond, R., Horton, B., 2002. Global to local scale parameters determining relative sea-level changes and the post-glacial isostatic adjustment of Great Britain. Quat. Sci. Rev., 21, 397–408. doi:10.1016/S0277-3791(01)00091-9

Shennan, S., 1988. Quantifying archaeology. Edinburgh University Press Academic Press, Edinburgh.

Sheriff, R.E., Geldart, L.P., 1995. Exploration Seismology. Cambridge University Press, Cambridge.

Shillington, D.J., Tucholke, B.E., Karner, G.D., Sawyer, D.S., Holbrook, W.S., Delius, H., 2004. Linking core and seismic data without logs: Core-seismic correlation at site 1276, in: Tucholke, B.E., Sibuet, J.-C., Klaus, A. (Eds.), Proceedings of the Ocean Drilling Program.

Silva, I., Jenkins, D., 1993. Decision on the Eocene-Oligocene Boundary Stratotype. Episodes 16, 379–382.

Simmons, M.D., 2012. Chapter 13 - Sequence Stratigraphy and Sea-Level Change, in: The Geologic Time Scale. Elsevier, Boston, pp. 239–267. doi:10.1016/B978-0-444-59425-9.00013-5

Simon, Q., 2007. Analyse sédimentologique et isotopique (Nd & Pb) d'une carotte sédimentaire prélevée dans le Détroit du Danemark (MD99-2322) Implication sur l'évolution de la circulation océanique profonde au cours de l'Holocène. Universite de Liege.

Sinha, A.K., 1970. Model lead and radiometric ages from the Churchill Province, Canadian Shield. Geochim. Cosmochim. Acta 34, 1089–1106. doi:10.1016/0016-7037(70)90164-X

Srivastava, S.P., Arthur, M., Clement, B., et al. (Eds.), 1987. Proceedings of the Ocean Drilling Program, Initial Reports. Ocean Drilling Program.

St. John, K., 2008. Cenozoic ice-rafting history of the central Arctic Ocean: Terrigenous sands on the Lomonosov Ridge. Paleoceanography 23, 1-12. doi:10.1029/2007PA001483

St. John, K., Passchier, S., Tantillo, Brooke, Darby, D., Kearns, L.E., 2015. Microfeatures of modern sea-ice-rafted sediment and implications for paleo-sea-ice reconstructions. Ann. Glaciol. 56, 89–93. doi:10.3189/2015AoG69A586

Stendal, H., Frei, R., 2008. Mineral occurrences in central East Greenland (70°N-75°N) and their relation to the Caledonian orogeny- A Sr-Nd-Pb isotopic study of scheelite. Mem. Geol. Soc. Am. 202, 293–306. doi:10.1130/2008.1202(12)

Stevenson, R., Henry, P., Gariépy, C., 1999. Assimilation–fractional crystallization origin of Archean Sanukitoid Suites: Western Superior Province, Canada. Precambrian Res. 96, 83–99. doi:10.1016/S0301-9268(99)00009-1

Stickley, C.E., St John, K., Koç, N., Jordan, R.W., Passchier, S., Pearce, R.B., Kearns, L.E., 2009. Evidence for middle Eocene Arctic sea ice from diatoms and ice-rafted debris. Nature 460, 376–379. doi:10.1038/nature08163

Stoker, M., Leslie, A., Smith, K., Ólavsdóttir, J., Johnson, H., Laberg, J.S., 2013. Onset of North Atlantic Deep Water production coincident with inception of the Cenozoic global cooling trend: Comment. Geology 41, e291–e291. doi:10.1130/G33670C.1

Stoker, M.S., Weering, T.C.E.V., Svaerdborg, T., 2001. A Mid- to Late Cenozoic tectonostratigraphic framework for the Rockall Trough. Geol. Soc. Lond. Spec. Publ. 188, 411–438. doi:10.1144/GSL.SP.2001.188.01.26

Stow, D.A.V., Faugères, J.-C., 2008. Chapter 13 Contourite Facies and the Facies Model, in: M. Rebesco and A. Camerlenghi (Ed.), Developments in Sedimentology, Contourites. Elsevier, pp. 223–256.

Stow, D.A.V., Hernández-Molina, F.J., Llave, E., Sayago-Gil, M., Río, V.D. del, Branson, A., 2009. Bedform-velocity matrix: The estimation of bottom current velocity from bedform observations. Geology 37, 327–330. doi:10.1130/G25259A.1

Strand, K., Passchier, S., Näsi, J., 2003. Implications of quartz grain microtextures for onset Eocene/Oligocene glaciation in Prydz Bay, ODP Site 1166, Antarctica.

Palaeogeogr. Palaeoclimatol. Palaeoecol. 198, 101–111. doi:10.1016/S0031-0182(03)00396-1

Taylor, R.N., Ishizuka, O., Michalik, A., Milton, J.A., Croudace, I.W., 2015. Evaluating the precision of Pb isotope measurement by mass spectrometry. J Anal Spectrom 30, 198–213. doi:10.1039/C4JA00279B

Thistle, D., Ertman, S.C., Fauchald, K., 1991. The fauna of the HEBBLE site: patterns in standing stock and sediment-dynamic effects. Mar. Geol., Deep ocean sediment transport 99, 413–422. doi:10.1016/0025-3227(91)90053-7

Thomson, D.J., 1982. Spectrum estimation and harmonic analysis. Proc. IEEE 70, 1055–1096. doi:10.1109/PROC.1982.12433

Tilton, G.R., Kwon, S.-T., 1990. Isotopic evidence for crust-mantle evolution with emphasis on the Canadian Shield. Chem. Geol., Development of Continental Crust Through Geological Time 83, 149–163. doi:10.1016/0009-2541(90)90277-E

Tilton, G.R., Steiger, R.H., 1969. Mineral ages and isotopic composition of primary lead at Manitouwadge, Ontario. J. Geophys. Res. 74, 2118–2132. doi:10.1029/JB074i008p02118

Tomascak, P.B., Krogstad, E.J., Walker, R.J., 1996. Nature of the crust in Maine, USA: evidence from the Sebago batholith. Contrib. Mineral. Petrol. 125, 45–59. doi:10.1007/s004100050205

Torrence, C., Compo, G.P., 1998. A Practical Guide to Wavelet Analysis. Bull. Am. Meteorol. Soc. 79, 61–78. doi:10.1175/1520-0477(1998)079<0061:APGTWA>2.0.CO;2

Torrence, C., Webster, P.J., 1999. Interdecadal Changes in the ENSO–Monsoon System. J. Clim. 12, 2679–2690. doi:10.1175/1520-0442(1999)012<2679:ICITEM>2.0.CO;2

Tripati, A., Backman, J., Elderfield, H., Ferretti, P., 2005. Eocene bipolar glaciation associated with global carbon cycle changes. Nature 436, 341–346. doi:10.1038/nature03874

Tripati, A.K., Eagle, R.A., Morton, A., Dowdeswell, J.A., Atkinson, K.L., Bahé, Y., Dawber, C.F., Khadun, E., Shaw, R.M.H., Shorttle, O., Thanabalasundaram, L., 2008. Evidence for glaciation in the Northern Hemisphere back to 44 Ma from ice-rafted debris in the Greenland Sea. Earth Planet. Sci. Lett. 265, 112–122. doi:10.1016/j.epsl.2007.09.045

Tucholke, B.., Vogt, P.., 1979. Western North Atlantic: sedimentary evolution and aspects of tectonic history. Initial Rep. DSDP 43, 791–825.

Tucholke, B.E., Austin, J.A., Uchupi, E., others, 1989. Crustal structure and rift-drift evolution of the Newfoundland Basin, in: Tankard, A.J., Balkwill, H.R. (Eds.), Extensional Tectonics and Stratigraphy of the North Atlantic Margins, 46. AAPG, Tulsa, pp. 247–263.

Tucholke, B.E., Ludwig, W.J., 1982. Structure and origin of the J anomaly Ridge, western North Atlantic Ocean. J. Geophys. Res. Solid Earth 87, 9389–9407. doi:10.1029/JB087iB11p09389

Tucholke, B.E., Mountain, G.S., 1986. Tertiary paleoceanography of the western North Atlantic Ocean, in: The Western North Atlantic Region, The Geology of North America. Geological Society of America, Boulder, Colo, pp. 631–350.

Tucholke, B.E., Mountain, G.S., 1979a. Seismic stratigraphy, lithostratigraphy and paleosedimentation patterns in the North American Basin. Deep Drill. Results Atl. Ocean Cont. Margins Paleoenviron. 3, 58–86.

Tucholke, B.E., Mountain, G.S., 1979b. Seismic stratigraphy, lithostratigraphy and paleosedimentation patterns in the North American Basin. Deep Drill. Results Atl. Ocean Cont. Margins Paleoenviron. 3, 58–86.

Tucholke, B.E., Sawyer, D.S., Sibuet, J.-C., 2007. Breakup of the Newfoundland–Iberia rift. Geol. Soc. Lond. Spec. Publ. 282, 9–46. doi:10.1144/SP282.2

Tucholke, B.E., Sibuet, J.-C., Klaus, A. (Eds.), 2006. Proceedings of the Ocean Drilling Program, 210 Scientific Results, Proceedings of the Ocean Drilling Program. Ocean Drilling Program. doi:10.2973/odp.proc.sr.210.2007

Tucholke, B.E., Sibuet, J.-C., Klaus, A., et al. (Eds.), 2004. Proceedings of the Ocean Drilling Program, 210 Initial Reports, Proceedings of the Ocean Drilling Program. Ocean Drilling Program. doi:10.2973/odp.proc.ir.210.2004

Turgut, S., Eseller, G., 2000. Sequence stratigraphy, tectonics and depositional history in eastern Thrace Basin, NW Turkey. Mar. Pet. Geol. 17, 61–100. doi:10.1016/S0264-8172(99)00015-X

Tyrrell, S., Haughton, P.D., Daly, J.S., 2007. Drainage reorganization during breakup of Pangea revealed by in-situ Pb isotopic analysis of detrital K-feldspar. Geology 35, 971–974. doi:10.1130/G4123A.1

Tyrrell, S., Haughton, P.D.W., Daly, J.S., Kokfelt, T.F., Gagnevin, D., 2006. The use of the common Pb isotope composition of detrital K-feldspar grains as a provenance tool and its application to Upper Carboniferous paleodrainage, northern England. J. Sediment. Res. 76, 324–345. doi:10.2110/jsr.2006.023

Uchman, A., Wetzel, A., 2011. Deep-Sea Ichnology: The Relationships Between Depositional Environment and Endobenthic Organisms. Dev. Sedimentol. 63. doi:10.1016/B978-0-444-53000-4.00008-1

Vail, P.R., 1977. Seismic stratigraphy and global changes of sea level. Bull Am Assoc Pet. Geol Mem 26, 49–212.

Vérard, C., Hochard, C., Baumgartner, P.O., Stampfli, G.M., Liu, M., 2015. 3D palaeogeographic reconstructions of the Phanerozoic versus sea-level and Sr-ratio variations. J. Palaeogeogr. 4, 64–84. doi:10.3724/SP.J.1261.2015.00068

Via, R.K., Thomas, D.J., 2006. Evolution of Atlantic thermohaline circulation: Early Oligocene onset of deep-water production in the North Atlantic. Geology 34, 441–444. doi:10.1130/G22545.1

Viana, A.R., Faugeres, J.C., Kowsmann, R.O., Lima, J.A.M., Caddah, L.F.G., Rizzo, J.G., 1998a. Hydrology, morphology and sedimentology of the Campos continental margin, offshore Brazil. Sediment. Geol., Contourites, Turbidites and Process Interaction 115, 133–157. doi:10.1016/S0037-0738(97)00090-0

Viana, A.R., Faugères, J.-C., Stow, D.A.V., 1998b. Bottom-current-controlled sand deposits — a review of modern shallow- to deep-water environments.

Sediment. Geol., Contourites, Turbidites and Process Interaction 115, 53–80. doi:10.1016/S0037-0738(97)00087-0

Vidal, P., Blais, S., Jahn, B.M., Capdevila, R., Tilton, G.R., 1980. U-Pb and Rb-Sr systematics of the Suomussalmi Archean greenstone belt (eastern Finland). Geochim. Cosmochim. Acta 44, 2033–2044. doi:10.1016/0016-7037(80)90201-X

Vitrac, A.M., Albarede, F., Allègre, C.J., 1981. Lead isotopic composition of Hercynian granitic K-feldspars constrains continental genesis. Nature 291, 460–464. doi:10.1038/291460a0

Wade, B.S., Pälike, H., 2004. Oligocene climate dynamics. Paleoceanography 19, PA4019. doi:10.1029/2004PA001042

Walsh, J.P., Nittrouer, C.A., 2003. Contrasting styles of off-shelf sediment accumulation in New Guinea. Mar. Geol. 196, 105–125. doi:10.1016/S0025-3227(03)00069-0

Wang, J., Mysak, L.A., Ingram, R.G., 1994. Interannual variability of sea-ice cover in Hudson bay, Baffin bay and the Labrador sea. Atmosphere-Ocean 32, 421–447. doi:10.1080/07055900.1994.9649505

Weis, D., 1986. Genetic implications of Pb isotopic geochemistry in the Rogaland anorthositic complex (southwest Norway). Chem. Geol., Isotopes in Geology—Picciotto Volume 57, 181–199. doi:10.1016/0009-2541(86)90102-6

Wentworth, C.K., 1922. A Scale of Grade and Class Terms for Clastic Sediments. J. Geol. 30, 377–392. doi:10.1086/622910

Wetzel, A., Uchman, A., 2012. Hemipelagic and Pelagic Basin Plains, in: Developments in Sedimentology. pp. 673–701. doi:10.1016/B978-0-444-53813-0.00022-8

Whalen, J.B., Jenner, G.A., Longstaffe, F.J., Robert, F., Gariépy, C., 1996. Geochemical and Isotopic (O, Nd, Pb and Sr) Constraints on A-type Granite Petrogenesis Based on the Topsails Igneous Suite, Newfoundland Appalachians. J. Petrol. 37, 1463–1489. doi:10.1093/petrology/37.6.1463

White, L.F., Bailey, I., Foster, G.L., Allen, G., Kelley, S.P., Andrews, J.T., Hogan, K., Dowdeswell, J.A., Storey, C.D., 2016. Tracking the provenance of Greenland-

sourced, Holocene aged, individual sand-sized ice-rafted debris using the Pb-isotope compositions of feldspars and $^{40}Ar/^{39}Ar$ ages of hornblendes. Earth Planet. Sci. Lett. 433, 192–203. doi:10.1016/j.epsl.2015.10.054

Whitehouse, R.J.S., Hardisty, J., 1988. Experimental assessment of two theories for the effect of bedslope on the threshold of bedload transport. Mar. Geol. 79, 135–139. doi:10.1016/0025-3227(88)90162-4

Wielens, J. b. w., Jauer, C. d., Williams, G. l., 2006. Is There a Viable Petroleum System in the Carson and Salar Basins, Offshore Newfoundland? J. Pet. Geol. 29, 303–326. doi:10.1111/j.1747-5457.2006.00303.x

Williams, A.T., Morgan, P., 1993. Scanning electron microscope evidence for offshore-onshore sand transport at Fire Island, New York, USA. Sedimentology 40, 63–77. doi:10.1111/j.1365-3091.1993.tb01091.x

Wold, C.N., 1994. Cenozoic sediment accumulation on drifts in the northern North Atlantic. Paleoceanography 9, 917–941. doi:10.1029/94PA01438

Yashayaev, I., Clarke, A., 2008. Evolution of North Atlantic water masses inferred from Labrador Sea salinity series. Oceanography, 21, 30-45.
doi: 10.5670/oceanog.2008.65

Yokokawa, M., 2001. 7. Sedimentary structures of contourites and turbidites observed by X-radiographic prints: samples from Blake-Bahama outer Ridge and Sohm Abyssal Plain. Proc ODP Sci Results 172.

Zachos, J.C., Dickens, G.R., Zeebe, R.E., 2008. An early Cenozoic perspective on greenhouse warming and carbon-cycle dynamics. Nature 451, 279–283. doi:10.1038/nature06588

Zartman, R.E., Wasserburg, G.J., 1969. The isotopic composition of lead in potassium feldspars from some 1.0 b.y. old North American igneous rocks. Geochim. Cosmochim. Acta 33, 901–942. doi:10.1016/0016-7037(69)90104-5